

Donor-Bridge-Acceptor Systems
with Varying Bridge Units for the Investigation of
Intramolecular and Intermolecular Electron Transfer Processes



Dissertation zur Erlangung des
naturwissenschaftlichen Doktorgrades
der Julius-Maximilians-Universität Würzburg

vorgelegt von

Conrad Kaiser

aus Miltenberg

Würzburg 2014

Eingereicht am: _____

bei der Fakultät für Chemie und Pharmazie

1.Gutachter: _____

2.Gutachter: _____

der Dissertation

1.Prüfer: _____

2.Prüfer: _____

3.Prüfer: _____

des Öffentlichen Promotionskolloquiums

Tag des Öffentlichen Promotionskolloquiums: _____

Doktorurkunde ausgehändigt am: _____

Die vorliegende Arbeit wurde in der Zeit von Juni 2006 bis Februar 2014 am
Institut für Organische Chemie der Universität Würzburg angefertigt

Mein besonderer Dank gilt

Herrn Prof. Dr. Christoph Lambert

für die Vergabe des Themas und das mit vielen Anregungen verbundene Interesse an dieser
Arbeit.

CONTENTS

COPYRIGHT REMARKS

INTRODUCTION..... 1

CHAPTERS

- I) Intramolecular Electron Transfer via Energetically Different Bridge Units in Ferrocene-Hydroquinone Derivative-Gold Model Systems in a Monolayer Environment 4

- II) Intermolecular Electron Transfer Mimicked via Differently Sized Paracyclophanes in Triarylamine-Paracyclophane-Triarylamine Cation/Naphthalene Diimide Model Systems in Solution 107

GENERAL SUMMARY (GERMAN)..... 240

COPYRIGHT REMARKS

Regarding Part II of this thesis, parts of this chapter have already been published in the following articles:

C. Kaiser, A. Schmiedel, M. Holzapfel, C. Lambert *J. Phys. Chem. C* **2012**, 116, 15265-15280.

D. R. Kattnig, B. Mladenova, G. Grampp, C. Kaiser, A. Heckmann, C. Lambert *J. Phys. Chem. C* **2009**, 113, 2983-2995.

ACS extends blanket permission to students to include in their theses and dissertations their own articles, or portions thereof, that have been published in ACS journals or submitted to ACS journals for publication.

INTRODUCTION

In this thesis the influence of specifically tailored bridging units on electron transfer processes (ET) in donor-bridge-acceptor model systems was investigated. These model systems comprised ferrocene-hydroquinone derivative-gold systems in monolayer environments and triarylamine-paracyclophane-triarylamine cation as well as triarylamine-paracyclophane-naphthalene bisimide systems in solution. In the course of this study a broad set of electrochemical and optical techniques were employed. The most important were impedance spectroscopy, UV-Vis-NIR spectroscopy, transient absorption spectroscopy (ns- and fs-range) and time resolved electron paramagnetic resonance spectroscopy provided by *Grampp et al*^[1].

Knowledge concerning ET processes like charge separation, charge transport and charge recombination is crucial for the specific design of new organic compounds and materials for artificial photosynthesis, molecular electronics, photovoltaic and other optoelectronic applications. In this context, ET in molecules or polymer strains as well as in-between them, i.e. intra-and intermolecular ET, must be considered.

The most promising approaches to reach a level of understanding of these ET processes to allow for extrapolation and specific tuning start with the investigation of the elementary electron and charge transfer steps in small model systems.^[2-5] The focus on model systems consisting of single molecules and structured assemblies thereof in defined environments greatly simplifies the investigation of the nature of and basic causal relations regarding the ET processes. Such model systems have to consist of at least a donor or an electrode to provide electrons and an acceptor or an electrode to accept electrons. Aside from the properties of these components, especially the often neglected interconnecting organic structures are of crucial importance, since they can have a very profound effect on the speed and mechanism of the ET processes. This thesis emphasizes the influence of systematic alterations to these so called bridging units on ET processes.

In part I of this work, the impact of synthetically adjusting the energetics of the bridge unit in a donor-bridge-electrode (ferrocene-hydroquinone derivative-gold) set-up arranged within a monolayer on intramolecular ET was investigated. Aside from the influence on the efficiency of the mechanisms, the possibility to deliberately alter the dominating mechanism between superexchange and the highly efficient hopping within a monolayer environment was evaluated.^[6-10]

In part II of this thesis, the effect of introducing differently-sized paracyclophanes as bridging units into donor-bridge-acceptor (triarylamine-paracyclophane-triarylamine cation as well as triarylamine-paracyclophane-naphthalene bisimide) model systems on the ET properties of these systems was studied. Due to their stacked aromatic rings, paracyclophanes provide a through-space pathway and thereby mimic intermolecular ET.^[11-17] Gathering knowledge about intermolecular ET is important, especially since, in functional materials, the performance regarding their applications is often limited by the intermolecular ET between the individual molecules or polymer strains.

A special characteristic of the present work is that the studied model systems go slightly beyond the scope of single molecules and expand into the realm of organic functional materials. In part I, this is achieved by choosing a monolayer environment which provides a dense packing of the inspected molecules which resembles the packing in organic solid state materials more than fully solvated molecules. Furthermore, the setup includes an organic substance/electrode interface as present in many applications. In part II, this expansion is realized by providing through-space pathways via introducing paracyclophanes and thus mimicking intermolecular charge and electron transfer as present in many organic materials.

Due to the diversity of the two approaches, this thesis is divided into two self-contained parts including more specific introductions and summaries.

LITERATURE

- [1] D. R. Kattnig, B. Mladenova, G. Grampp, C. Kaiser, A. Heckmann, C. Lambert *J. Phys. Chem. C* **2009**, 113, 2983–2995.
- [2] J. W. Verhoeven, H. J. van Ramesdonk, M. M. Groeneveld, A. C. Benniston, A. Harriman *ChemPhysChem* **2005**, 6, 2251–2260.
- [3] A. Harriman *Angew. Chem., Int. Ed.* **2004**, 43, 4985–4987.
- [4] A. C. Benniston, A. Harriman, P. Li, J. P. Rostron, H. J. van Ramesdonk, M. M. Groeneveld, H. Zhang, J. W. Verhoeven *J. Am. Chem. Soc.* **2005**, 127, 16054–16064.
- [5] D. M. Guldi *Angew. Chem., Int. Ed.* **2010**, 49, 7844–7846.
- [6] M. D. Newton, J. F. Smalley *Phys. Chem. Chem. Phys.* **2007**, 9, 555–572.
- [7] B. P. Paulson, J. R. Miller, W.-X. Gan, G. Closs *J. Am. Chem. Soc.* **2005**, 127, 4860–4868.
- [8] E. A. Weiss, M. J. Ahrens, L. E. Sinks, A. V. Gusev, M. A. Ratner, M. R. Wasielewski *J. Am. Chem. Soc.* **2004**, 126, 5577–5584.

- [9] E. A. Weiss, J. K. Kriebel, M.-A. Rampi, G. M. Whitesides *Phil. Trans. R. Soc., A* **2007**, 365, 1509–1537.
- [10] E. A. Weiss, M. R. Wasielewski, M. A. Ratner *Molecular Wires: From Design to Properties*, Vol. 257 (Ed. L. DeCola), Springer-Verlag Berlin, Berlin, **2005**, 103–133.
- [11] E. Heilbronner, J. P. Maier *Helv. Chim. Acta* **1974**, 57, 151–159.
- [12] K. A. Lyssenko, M. Y. Antipin, D. Y. Antonov *ChemPhysChem* **2003**, 4, 817–823.
- [13] *Modern cyclophane chemistry*, (Eds.: R. Gleiter, H. Hopf), Wiley-VCH, Weinheim, **2004**.
- [14] G. F. Caramori, S. E. Galembeck *J. Phys. Chem. A* **2007**, 111, 1705–1712.
- [15] S. Grimme *Chem. Eur. J.* **2004**, 10, 3423–3429.
- [16] H.-C. Lin, B.-Y. Jin *J. Phys. Chem. A* **2008**, 112, 2948–2954.
- [17] S. Amthor, C. Lambert *J. Phys. Chem. A* **2006**, 110, 1177–1189.

**I) Intramolecular Electron Transfer via Energetically Different
Bridge Units in Ferrocene-Hydroquinone Derivative-Gold Model
Systems in a Monolayer Environment**

1	INTRODUCTION.....	6
2	PROJECT AIM.....	10
3	THEORETICAL SECTION.....	14
	3.1 FORMATION OF MONOLAYERS	14
	3.2 SURFACE COVERAGE DETERMINATION BY CYCLIC VOLTAMMETRY.....	17
	3.3 CHARGE TRANSFER RATE ACQUISITION BY IMPEDANCE SPECTROSCOPY.....	19
4	RESULTS AND DISCUSSION	24
	4.1 MOLECULES	24
	4.1.1 RETROSYNTHETIC SCHEMES OF MOLECULES A, B AND C	24
	4.1.2 SYNTHESIS OF FERROCENE COMPOUND F3.....	26
	4.1.3 SYNTHESIS OF DIBROMIDE PRECURSORS OF A; B AND C	27
	4.1.4 SYNTHESIS OF A, B AND C.....	29
	4.1.5 CYCLIC VOLTAMMETRY.....	30
	4.2 MONOLAYERS.....	33
	4.2.1 PREPARATION CONDITIONS	33
	4.2.2 MEASUREMENT CONDITIONS	38
	4.2.3 ADAPTED PROTOCOL FOR IMPEDANCE MEASUREMENT ANALYSIS.....	44
	4.2.4 IMPEDANCE MEASUREMENT PARAMETERS	49
	4.2.5 ELECTROCHEMICAL CHARACTERIZATION TEST.....	51
	4.2.6 ELECTROCHEMICAL CHARACTERIZATION.....	55

5	SUMMARY AND CONCLUSION.....	73
6	EXPERIMENTAL SECTION	76
6.1	PREPARATIVE AND ANALYTICAL METHODS	76
6.2	SYNTHESIS	79
6.2.1	SYNTHESIS OF FERROCENE COMPOUND F3.....	79
6.2.2	SYNTHESIS OF DIBROMIDE PRECURSOR OF A.....	82
6.2.3	SYNTHESIS OF DIBROMIDE PRECURSOR OF B.....	83
6.2.4	SYNTHESIS OF DIBROMIDE PRECURSOR OF C.....	85
6.2.5	SYNTHESIS OF A.....	86
6.2.6	SYNTHESIS OF B.....	90
6.2.7	SYNTHESIS OF C.....	94
7	LITERATURE	98
8	STRUCTURAL FORMULA TABLE.....	106

1 INTRODUCTION

In this part of the thesis, the influence of the energetic alignment of the bridge unit on ground-state intramolecular electron transfer (ET) in a donor-bridge-electrode (ferrocene-hydroquinone-gold) setup in the environment of a highly ordered self-assembled monolayer was investigated. The main analysis technique employed was impedance spectroscopy.

Due to the unique properties and versatility of self-assembled monolayers (SAMs), the number of studies utilizing them has been continuously rising in the last decades. Many combinations of molecules and substrates can be used to form such monolayers. However, none even come close to the significance of the one where the molecules are attached via sulfur groups to bulk gold substrates, which was discovered about three decades ago.^[1-3] Because of being so well investigated,^[4] this combination was employed in the present study. An overview of monolayer investigations with an emphasis on recent advances regarding these sulfur-gold monolayers is provided below. To allow for a more detailed review, monolayers used in combination with gold-nanoparticles, nanotubes and graphene sheets will not be addressed here.

Some studies involving monolayers deal with their structure and formation processes.^[5, 6] Current investigations in this field mainly target the thiolate-gold bond^[7-9], whose nature still remains elusive and includes the issue of gold adatom formation^[10-12]. Furthermore, there are many studies targeting applications of SAMs. The main subjects of these are electronics, immobilization of biomolecules and intramolecular ET. Their utilization in electronics comprises organic electronics and molecular electronics.

In organic electronics SAMs are mainly used to alter the properties of interfaces in multilayer devices like light emitting devices, photovoltaics and organic field effect transistors (OFETs). They are predominately attached to the electrodes to lower the contact resistances between them and the active organic layers like semiconductors, light emitting and light harvesting, interjectional hole and charge transport layers. This is achieved by their ability to alter the work functions of the electrode materials due to dipolar and electron push-back effects of the SAMs to thus better match the lowest unoccupied or highest occupied molecular orbitals of the active organic layers. In addition, by tuning the terminal groups of SAMs the wettability and surface energy of the electrodes are altered. The morphology and film thickness and hence the inherent electronic properties of the active organic layers are thereby influenced. In addition, redox centers can be incorporated into the SAMs to enable them to act as electron or hole injection layers. In case of OFETs SAMs on metal oxide gate electrodes are

used to improve the shielding of the conduction channel. Beyond this, SAMs are utilized for the electrochemical stabilization of silver electrodes. Furthermore, the properties of gold electrodes may also be modified via SAMs with zinc oxide layers to allow their utilization as cathodes.^[13-23]

Concerning molecular electronics the SAMs themselves carry the functional units of the devices.^[20] Examples of such molecular electronics applications are unimolecular rectifiers,^[24-28] molecular memory applications,^[29-33] photochromic molecular switches,^[33-40] photovoltaic devices^[41-44] and molecular motors^[45-49].

Regarding the immobilization of biomolecules, SAMs provide an ordered scaffold for the surface attachment of the molecules for sensing, bio catalytic purposes and simplified characterization by electrochemical and surface techniques.

On the subject of biosensors, the most commonly investigated applications are in deoxyribonucleic acid- (DNA-), protein- and immuno- sensing.^[50-57] Recent developments include the enhancement of these techniques^[58-65] and the implementation of fluorophores^[66] as well as extending the range of sensed biomolecules^[67].

As to the concept of creating biocatalytically active surfaces^[68] via employment of SAMs for example hydrogenase^[69], laccase^[70], myoglobin^[71] or cytochrome c oxidase^[72] have been employed as active biomolecules.

The simplified characterization of biomolecules attached to an ordered SAM-scaffold has for instance been exploited for cytochrome c.^[73, 74]

When investigating intramolecular ET, SAMs are used due to their ability to attach the studied molecules directly to an electrode with a uniform conformation and an ordered environment. Thus, the ET can be measured from the electrode through structurally aligned molecular backbones to integrated redox centers or a terminally attached electrode. The knowledge gained helps to understand ET in biological systems and is crucial for tailoring the ET properties of molecules needed for many of the electronic applications mentioned above.

It is commonly assumed that electron transfer through molecular backbones takes place by a mixture of a strongly distance-dependent tunneling mechanism referred to as superexchange and a weakly distance dependent incoherent transport mechanism called hopping. The dominance and efficiency of the mechanisms is, aside from the distance, mainly dependent on the energetic alignment of the work function or energy band of the electrode or the state energy of an integrated redox center which injects the charge and the state energy of the

bridge units' anions or cations. The latter are usually approximated by the energies of the frontier orbitals of the neutral units.^[75-77]

A broad variety of systems with varying backbones integrated into SAM molecules have been investigated. However, in nearly all cases, a domination of the superexchange mechanism with its exponential degrading distance dependence was encountered. Examples include numerous systems with alkane, oligophenylene, oligo(phenyleneethynylene) and oligo(phenylenevinylene), oligoene and oligoyne backbones.^[76]

Nevertheless, in rare cases, the prevalence of the intramolecular hopping mechanism could be determined with high probability. Depending on the applied bias and temperature, a phenylenevinylene derivative may provide such an example.^[78, 79] Recently, hopping was also suggested to be the dominant mechanism in certain beta peptides^[80] and related to the length and energetics of the integrated bases in double stranded peptide nucleic acids.^[81, 82] Furthermore, the hopping mechanism was proposed to be the prevailing mechanism in long peptide alpha helices, enabling efficient electron transport up to 120 Ångströms.^[83-87]

Other examples of recent developments concerning intramolecular ET in SAMs, which have drawn much attention, will be described below.

One case is the in situ alteration of ET rates. This was realized by the integration of azobenzene into the backbone to reversibly modify the structure by ultraviolet-radiation and thus switch the electrochemical characteristics including the ET rates of the system.^[40] Another approach is changing the redox state of the bridge unit by sweeping the applied potential thereby altering the energetics of the bridge states.^[88]

Furthermore, interesting discoveries regarding the nature of intramolecular ET have been made. Concerning alkane backbones, it was found that orbital symmetry can affect ET rates,^[89] that charge carrier tunneling can be mediated by the lowest unoccupied molecular orbital^[90] and that inter-chain tunneling is probably dependent on high molecular tilt angles.^[91] While investigating DNA oligomer backbones with chiral symmetry spin selective charge transport was observed.^[92]

As to ET through anchor groups, for alkane- or phenyl-thiol groups a very efficient interfacial coupling was revealed with ET rates on a time scale of less than 6 fs.^[93, 94]

Another recent subject of investigation is the effect on the ET rates of integrating diluents with endgroups of varying polarity into the SAMs. A highly sophisticated approach was the

controlled placement of the integrated redox centers at fixed points on or above the diluents monolayer surface by employing norbornylogous backbones.^[95-97]

Regarding theoretic analysis of experimental work, recent examples are the calculation of cluster effects in SAMs with a high concentration of terminal redox centers^[98] and the development of a new statistical method for analyzing experimental ET values.^[99]

Aside from these recent examples, in the last few decades numerous studies on intramolecular ET in SAM environments have been carried out. However, despite the accepted knowledge that energetic alignment of the bridge units and terminal redox centers of the investigated systems is crucial to the effectiveness and dominance of the prevailing electron transfer mechanism,^[75-77] studies which approach this issue are scarce. The rare examples emphasize somewhat random variation of the bridge unit's energetics^[81, 100-104]. Thus, systematic energetic alignment remains a hot subject and has therefore been chosen as the main topic of the following part of this thesis.

2 PROJECT AIM

The main goal of this study is to investigate the influence of systematic energetic adjustment of a bridging unit on the rate of intramolecular electron transfer (ET) between a donor and an electrode in a donor-bridge-electrode-setup (see Figure 1). The energetic alignment of the energy states of the system parts is expected to be of crucial importance, since it directly affects the efficiency and dominance of the electron transfer mechanisms. If the oxidized bridge state is positioned far above the oxidized state of the terminal donor, the superexchange mechanism, a one-step tunneling process, dominates. When the oxidized bridge state approaches the oxidized state of the terminal donor, the tunneling barrier decreases and a change of the dominating ET mechanism from superexchange to the more efficient hopping occurs (see Figure 3). While the rise of the ET rate during the lowering of the tunneling barrier is moderate, if the superexchange mechanism dominates, a substantial increase occurs if it changes to the more efficient hopping mechanism, a multistep tunneling mechanism. ^[75-77, 105, 106]

To investigate the influence energetic alignment of the bridge unit, molecules consisting of a protected thiol anchor group, spacers, different bridge units and a terminal donor must be designed (see Figure 1). These molecules must then be synthesized and arranged in dense, highly ordered monolayers on electrodes. Subsequently, the ET rates between the terminal donors of these monolayers and the electrodes are to be determined by impedance spectroscopy.

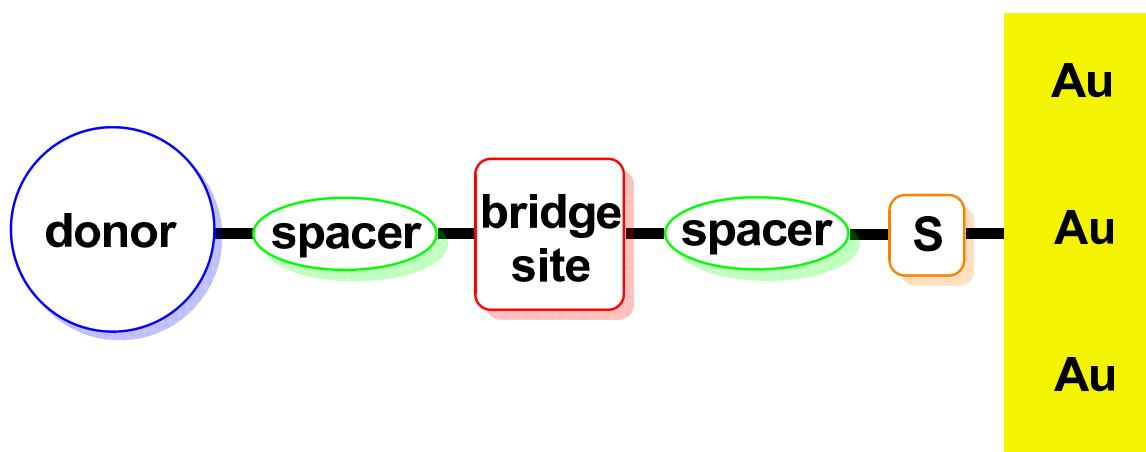


Figure 1. General Model of a schematic target molecule attached to a gold electrode.

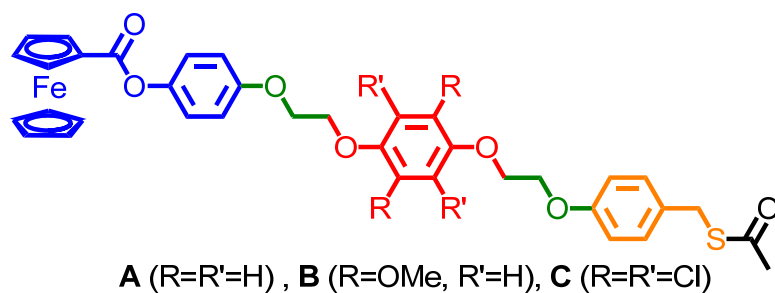
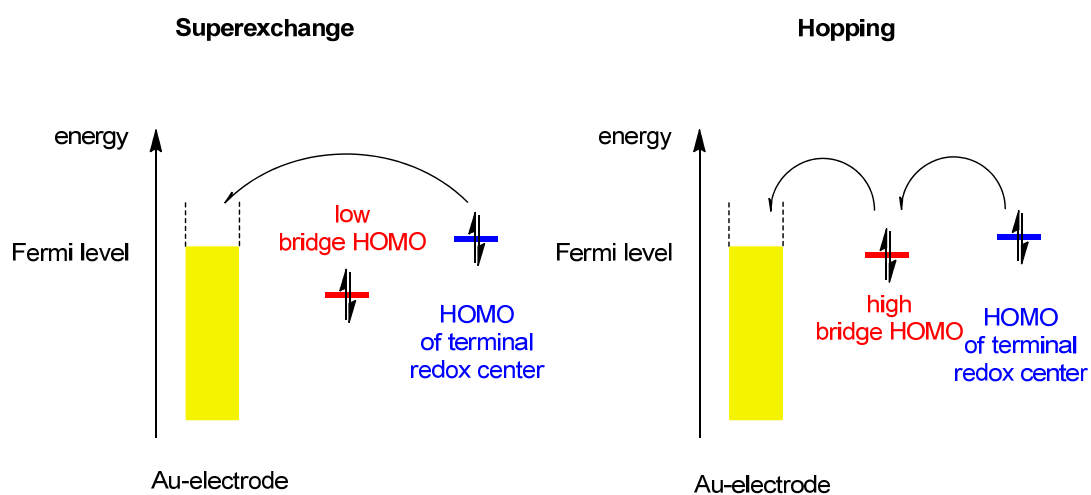


Figure 2. Structural formula of the target molecules.

ORBITAL DIAGRAMM



STATE DIAGRAMM

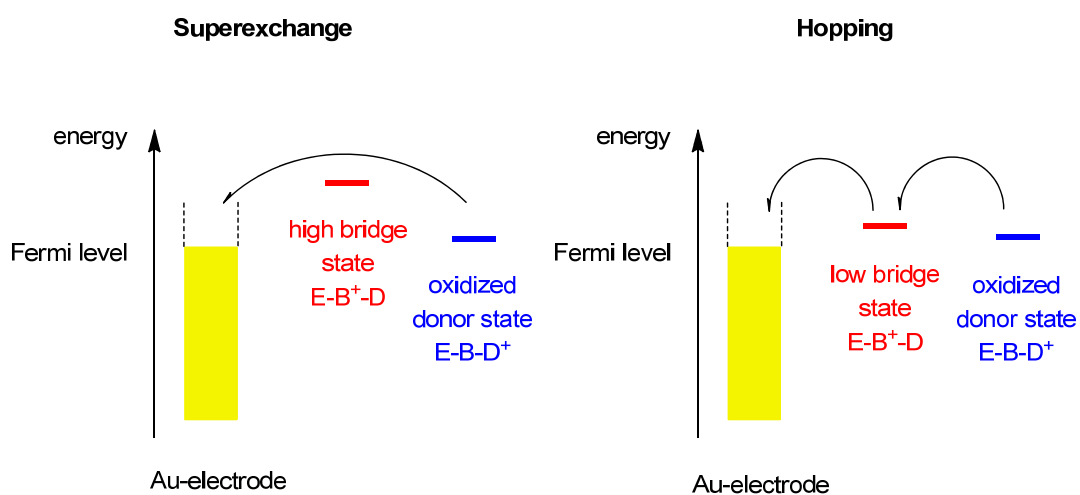


Figure 3. Orbital diagrams and state diagrams of a donor-bridge-electrode arrangement.

The reasons for the choice of the subunits of the target molecules (see Figures 1 and 2) are as follows: Ferrocene was chosen as the donor (redox active terminal group) because of the higher reorganization energy of ferrocene (ca. 0.87 eV^[107] in 1 M perchloric acid in water) compared to triarylamine (ca. 0.2 eV^[108, 109] in acetonitrile), which decelerates the ET rate.^[110] A low ET rate is a main target since the speed of ET rates to be determined by impedance spectroscopy is limited by the cell time constant of the electrochemical cell.^[111, 112] The ferrocene was attached via an ester group since this further slows the ET^[110] without significantly affecting its reorganization energy^[113, 114] (0.85 eV^[111, 112] in 1 M HClO₄). Furthermore, the integration of the ester group has been reported to minimize non-ideal broadening towards higher potentials of the ferrocene redox waves when conducting cyclic voltammetry.^[115] In addition, saturated ethyl-spacers were integrated into the backbone to further decrease the rate of ET.

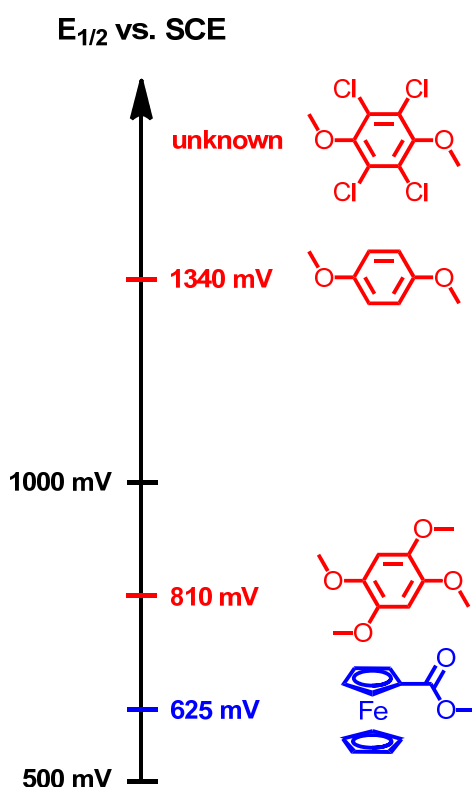


Figure 4. Half-wave potentials given versus a standard calomel electrode of the terminal redox center subunit (blue) determined in tetraethylammonium perchlorate in acetonitrile (0.1 M)^[116] and of the bridge subunits (red) in tetrapropylammonium perchlorate in acetonitrile (0.1 M).^[117]

Hydroquinone derivatives have been selected as bridge units, since many derivatives are known, and some are even commercially available, thus allowing adjusting the oxidized bridge state over a wide potential range. Moreover, the incorporation of hydroquinone units into the backbone of alkyl chains has been confirmed not to hamper dense packing during monolayer formation, but to actually favor a more perpendicular arrangement on the surface.^[118] To enhance the chances of observing significant effects on the ET rates three bridge units with distinct half-wave potentials of the first oxidation of 185 mV (**B**), 715 mV (**A**) and $\gg 715$ mV (**C**) above those of the terminal ferrocene redox center were chosen (see Figures 2 and 4). The half-wave potentials used for this preliminary assessment of the energetic gaps in the target molecules were taken from literature values of simple precursors (see Figure 4).^[116, 117]

Benzylthiol was selected as anchor group because its methyl group increases the flexibility which allows a perpendicular arrangement of the molecules to the substrate surface and ameliorates the structural order and density of the monolayers formed (see Figure 5).^[119] The thiol is protected by an acetyl group to allow for storage of the thiols, which are unstable towards oxidation.^[120, 121]

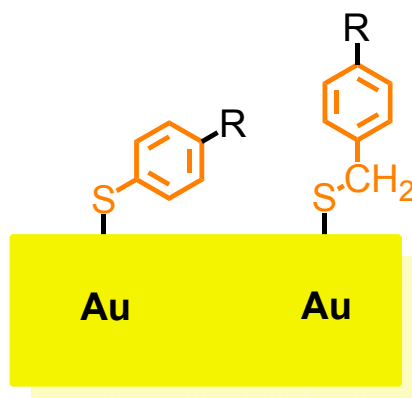


Figure 5. Structural arrangement of different sulfur anchor groups.

Gold has been chosen as substrate, because gold is very inert and therefore electrodes with homogeneous gold surfaces with Au(110) or Au(111) crystal structures can be easily prepared and cleaned.^[9]

3 THEORETICAL SECTION

3.1 FORMATION OF MONOLAYERS

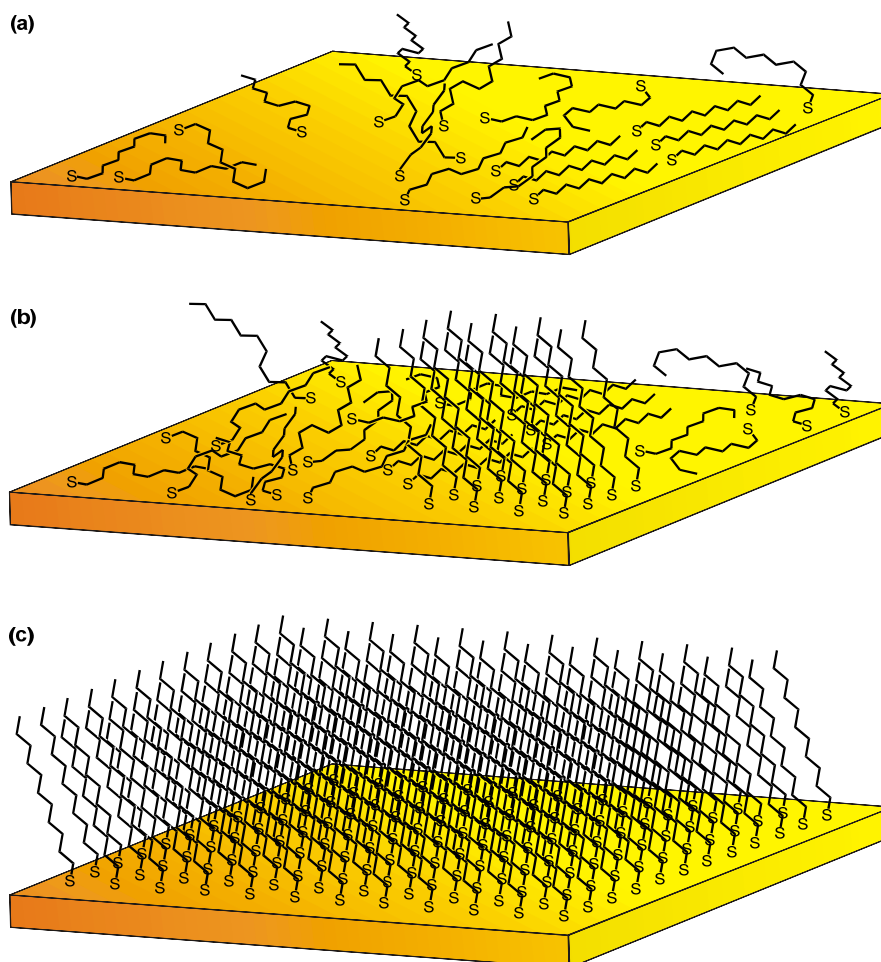


Figure 6. Low (a), intermediate (b) and high (c) density phase of alkane thiol monolayers on Au(111) surface.

Self-assembled monolayers of organic molecules are formed by the spontaneous ordered arrangement of molecules on a substrate surface. For this to take place, the molecules must include at least one element with a high affinity to the substrate. Especially stable monolayers can be achieved by the incorporation of special anchor groups into the molecules which strongly bind to the substrate surface (chemisorption). The corresponding reversible attachment process is called physisorption, whereby the attachment is only realized by weak interactions. Depending on the conditions and the structure of the

employed molecules, they arrange themselves into nearly ideal uniformly ordered monolayers due to intermolecular forces. Within this framework, structurally flexible molecules are usually forced into similar rigid conformations (see Figure 6). The thermodynamic precondition for the formation is, that the lower entropy is compensated by a decrease of enthalpy due to the molecule-surface and intermolecular interactions.^[11] While many well-functioning combinations of anchor groups and substrate exist, the most popular approach to produce chemisorbed monolayers makes use of the strong affinity of sulfur to gold.^[6, 122]

The employment of gold as a substrate is highly favored throughout the literature because gold is very inert, and therefore, homogeneous gold surfaces, most commonly with Au(111) or Au(110) crystal surfaces, can be easily prepared and cleaned. The monolayers are, aside from vapor deposition, mostly generated from the liquid phase, whereby a diluted solution of the molecules with sulfur-containing anchor groups like RSH, RSSR or RSR, where R is an organic rest, is brought in contact with the surface of the gold substrate. The formation of such monolayers is best studied for molecules containing alkyl chains as organic backbones attached via sulfur-containing anchor groups to Au(111) substrates.^[5, 6, 9, 122]

During the formation process such monolayers can be assigned to one of three organization states (see Figure 6). First, a low-density phase is formed where molecules assemble randomly on the surface of the substrate. The attachment is mainly realized via their sulfur groups by either coordinative bonding via the lone pairs of the sulfur in the anchor group or, in the case of free thiols, by creating covalent gold-sulfur bonds. The latter are nearly as strong as gold-gold bonds. In case of long organic backbones, in this phase an alignment primarily parallel to the surface of the substrate is common. However, most molecules studied, like those with alkyl chains as a backbone, bond only weakly via the backbone to the gold surface. Therefore, at standard conditions, an equilibrium with various amounts of at least partially desorbed backbones is generated. Depending on the nature of the backbone and the conditions, the adsorbed molecules might adopt a "lying down" position (to various degrees) on the substrate surface. This formation stage is followed by the second intermediate density phase (see Figure 6), during which the above mentioned equilibrium has made it possible for further molecules to bind with their anchor groups to the surface, thus supplanting the backbones of lying molecules and forcing more and more of them into an upright position. The interactions, typically van der Waals forces, between the backbones in this denser packing result in self-alignment of the backbones above the surface and thus first islands of a uniform 3-dimensional order are formed. In the final high-density phase (see Figure 6), the attachment of stronger bonding anchor groups of additional molecules leads to

a complete replacement of the backbones on the surface. Furthermore, the self-alignment of the backbones has results in an extension of the uniform 3-dimensional order over the complete surface of the substrate. [5, 6, 9, 122]

Of course, the whole formation of monolayers involves multiple processes like island nucleation and growth as well as multiple 2D-phase transitions. Despite this variety of partially parallel mechanisms, many experimental studies have shown that most of the macroscopic average coverage growth process can be well described by applying simple Langmuir kinetics. However, for a more accurate description, the kinetics of each of the detailed processes must be accounted for. Aside from being experimentally challenging, such investigations are further complicated by the fact, that despite the wealth of studies on the subject, not even a consensus on the influence of basic conditions exists. The various contradictions in the literature include effects like alkane backbone length or solvent changes. It should be emphasized that the source for these inconsistencies cannot be tracked down to a certain preparation technique or condition. [122]

In addition, the atomic structure of the actual sulfur gold-interface potentially involving gold adatoms is rarely known. This is especially true if intermediate to high densities of the molecules on the substrate surface lead to concealment of the interface by the molecular backbones. [7-12]

In conclusion, currently many questions regarding the details of monolayer formation remain unresolved. Nevertheless, through reasonable effort including variation of the formation conditions and by assuring a high purity of the molecules, solvent and substrate (usually accomplished through preparation with dry solvents in an inert atmosphere under exclusion of light) uniquely ordered high density monolayers can be created. [123]

3.2 SURFACE COVERAGE DETERMINATION BY CYCLIC VOLTAMMETRY

A main criterion for the quality of monolayers is the surface coverage, measured by the number of molecules attached per area unit, usually given in mol per cm². The surface coverage can, in combination with literature data or calculated values for the densest packing possible, give an estimation of the completeness of a monolayer as well as information about possible multilayer formation.

In the case of monolayers prepared with a single type of molecule, which is redox active, on an electrode surface, there is a simple and effective way to determine this value. It can be done by oxidizing and reducing a certain redox center within the molecules attached to the electrode by conducting cyclic voltammetry. To determine the surface coverage, the charge Q transferred during these redox processes is determined by averaging the integrals of the cathodic and anodic waves (Q_C and Q_A) of a cyclic voltammogram conducted on the monolayer. When integrating the peaks, they must be corrected for the background currents such as the charging of the double layer capacitance as well as a possible slope of the baseline (see Figure 7).^[115]

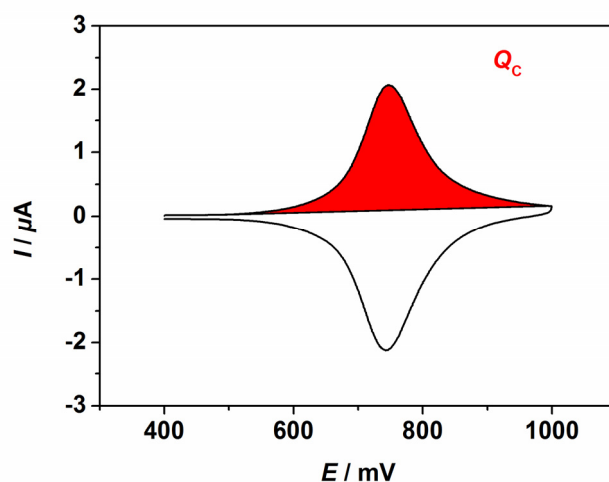


Figure 7. Integration of the charge (Q) transferred during the cathodic wave corrected for background currents in a cyclic voltammogram conducted on a redox active monolayer.

Furthermore, the real surface of the electrodes A has to be determined by multiplying the surface measured by gauging the spherical electrodes with, for example, a light microscope by a factor which accounts for the estimated surface roughness of the electrode substrate.^[124] In addition, the electrons n , which are transferred, when a single chemisorbed molecule is oxidized and reduced, must be known. The only other value needed is F , the Faraday Constant. The surface coverage Γ can then be determined by using the following equation (1).^[115, 125]

$$\Gamma = \frac{Q}{nFA} \quad (1)$$

3.3 CHARGE TRANSFER RATE ACQUISITION BY IMPEDANCE SPECTROSCOPY

Aside from its numerous applications including label-free biosensing, metal corrosion, conducting polymers, dye-sensitized solar cells, semiconductor-conducting polymer interfaces, electrode-electrolyte interfaces, batteries and fuel cells, impedance spectroscopy can be used to investigate electron transfer processes in monolayers.^[126, 127] For this purpose *Creager et al.* developed an especially simple protocol to determine the electron transfer rates between an electrode and redox centers of molecules that are chemisorbed in uniform monolayers to this electrode.^[111] In order to conduct the measurements, this electrode covered with the monolayer has to be integrated as the working electrode into a conventional three-electrode setup in an electrochemical cell. A distinct advantage of the protocol is that only the moduli of the impedances are needed, while the acquisition of the corresponding phase information is not essential. In addition, the number of fitting parameters is reduced to two at a time, in contrast to the conventional complex-plane impedance analysis.^[128] Furthermore, the fitting process is simple enough to be achieved manually. However, the acquisition of impedance data necessary to apply the protocol requires potential range scans at logarithmically distributed frequency points over several orders of magnitude, meaning it is essential that the monolayers are highly stable under the measurement conditions.^[111] However, according to *Lambert et al.*,^[110, 112] the measurement complexity and strain can be reduced by recording a fast scan voltammogram on the investigated monolayers in advance of the impedance measurements. Thus, the half-wave potential of the redox centers within the monolayers and the potential at which no more redox processes of these redox centers occur can be determined in advance. Therefore, since the potential dependence of the double layer capacitance is usually negligible, the potential scans can be reduced to only conducting measurements over the logarithmically distributed frequency points at the half-wave potential (= impedance scan) and at the potential where the faradaic currents vanished (= reference scan). Using this technique, monolayers with limited stability under the measurement conditions can also be investigated.

This adapted protocol is as follows. First, the data from the reference scan is presented by plotting the modulus of the impedance vs. the logarithmic frequency of the alternating current. This form of representation is called a Bode plot (see Figure 8). The gathered data are then analyzed with the help of equivalent circuits, i.e. circuits as simple as possible that match the electrical response of the electrochemical cell during the impedance measurement. In the case of the reference scan, the reference circuit is used (see Figure 9). The resistance (R_u) representing the uncompensated resistance of the electrochemical cell

that equals the modulus of the impedance at the plateau in the high frequency region of the Bode plot (see Figure 8) of the reference scan is thus determined. In addition, the value (C_{dl}) of the double layer capacitance of the electrochemical cell that dominates the response of the cell in the frequency region with the most negative slope of the Bode plot (see Figure 8) is extrapolated to the frequency point at 0.159 Hz. At this frequency point, due to $2\pi f = 1$, the value C_{dl} of the capacitor can be determined as the reciprocal value of the modulus of the corresponding impedance.

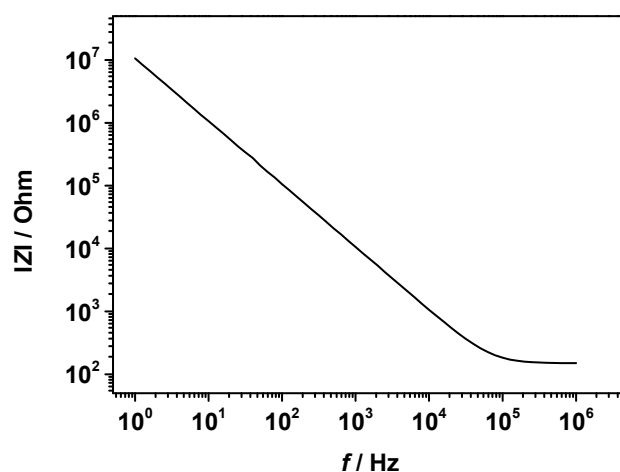




Figure 8. Simulated Bode Plot ($R_u = 150$ Ohm, $C_{dl} = 15.0 \times 10^{-9}$ F) of the response of a redox active monolayer using the reference equivalent circuit (see Figure 9).

Table 1. Circuit elements and their corresponding impedance equations.

Circuit Element	Impedance Equation	Name
	$Z = R$	Resistor
	$Z = -\frac{j}{2\pi f C}$ $j^2 = -1$	Capacitor

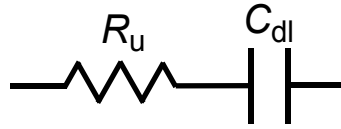


Figure 9. Equivalent circuit used for the fitting the reference scan.

Next, the *ratio* of the moduli of the impedances from the reference scan and the impedance scans are plotted vs. the logarithmic frequency. The result is a sinusoidal curve (see Figure 11). This curve has to be fitted by the simulated *ratio* of the moduli of the impedances of the equivalent circuits corresponding to the reference scan and the impedance scan.

The mathematical expression for this simulation to determine the *ratio* of the moduli of the impedances (see equation 2) is derived by combining the impedances of the individual elements R_u (Z_1), C_{dl} (Z_2), the charge transfer resistance R_{ct} (Z_3) and the adsorption pseudocapacitance C_{ad} (Z_4). They are combined according to common electrical rules regarding their arrangement in the equivalent circuits employed to describe the electrical response during the reference and impedance scan (see Figures 9 and 10).

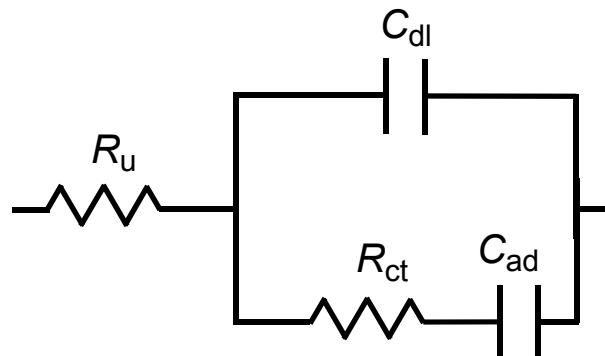


Figure 10. Randles equivalent circuit used for the fitting of the impedance scan.

$$\frac{Z_{ref}}{Z_{imp}} = \frac{Z_1 + Z_2}{Z_1 + \frac{Z_2 Z_3 + Z_2 Z_4}{Z_2 + Z_3 + Z_4}} \quad (2)$$

The impedances within this expression are then replaced by the corresponding impedance equations (see Table 1).

Furthermore, known relations (see equation 3–6), where G_a is the number of redox centers that undergo redox processes during an impedance scan and $ratio_C$ is the maximum value of the $ratio$ in the sinusoidal plot (see Figure 8), are used to simplify the equation.^[129, 130] The resulting formula (see equation 7) is then used to simulate and fit the sinusoidal plot.

$$R_{ct} = \frac{2RT}{F^2 G_a k_{et}} \quad (3)$$

$$C_{ad} = \frac{F^2 G_a}{4RT} \quad (4)$$

$$ratio_C = \frac{C_{ad} + C_{dl}}{C_{dl}} \quad (5)$$

$$G_a = \frac{4RT(ratio_C C_{dl} - C_{dl})}{F^2} \quad (6)$$

$$\left| \frac{Z_{ref}}{Z_{imp}} \right| = \left| \frac{R_u - \frac{j}{2\pi f C_{dl}}}{R_u + \frac{\left(-\frac{j}{2\pi f C_{dl}} \right) \left(\frac{1}{2(ratio_C C_{dl} - C_{dl}) k_{et}} - \frac{j}{2\pi f (ratio_C C_{dl} - C_{dl})} \right)} - \frac{j}{2\pi f C_{dl}} + \frac{1}{2(ratio_C C_{dl} - C_{dl}) k_{et}} - \frac{j}{2\pi f (ratio_C C_{dl} - C_{dl})} \right| \quad (7)$$

In this fitting process, only two parameters, namely $ratio_C$, the maximum value of the $ratio$, and k_{et} , the electron transfer rate per second, must be adapted manually to match the sinusoidal plot (see Figure 11). This can be accomplished in a straightforward manner since $ratio_C$ is mainly dependent on the vertical position of the maximal value of the $ratio$ of the impedances and the electron transfer rate primarily affects the horizontal position of the inflection point of the plot. The advantage of this method is its high simplicity regarding its theory and fitting processes. The main disadvantage is its susceptibility to contamination by non-ideal behavior of monolayers (see Section 4.2.3).

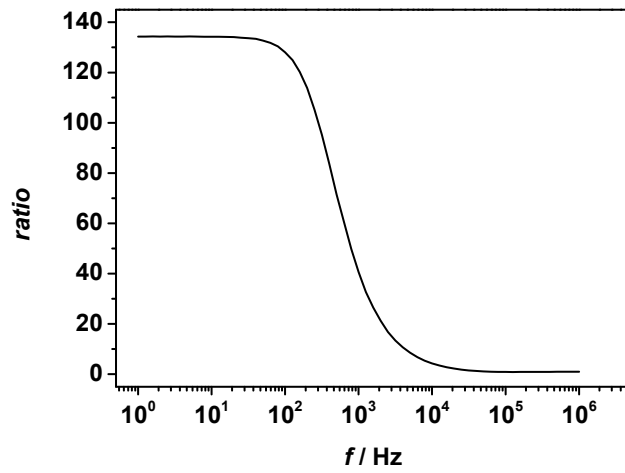


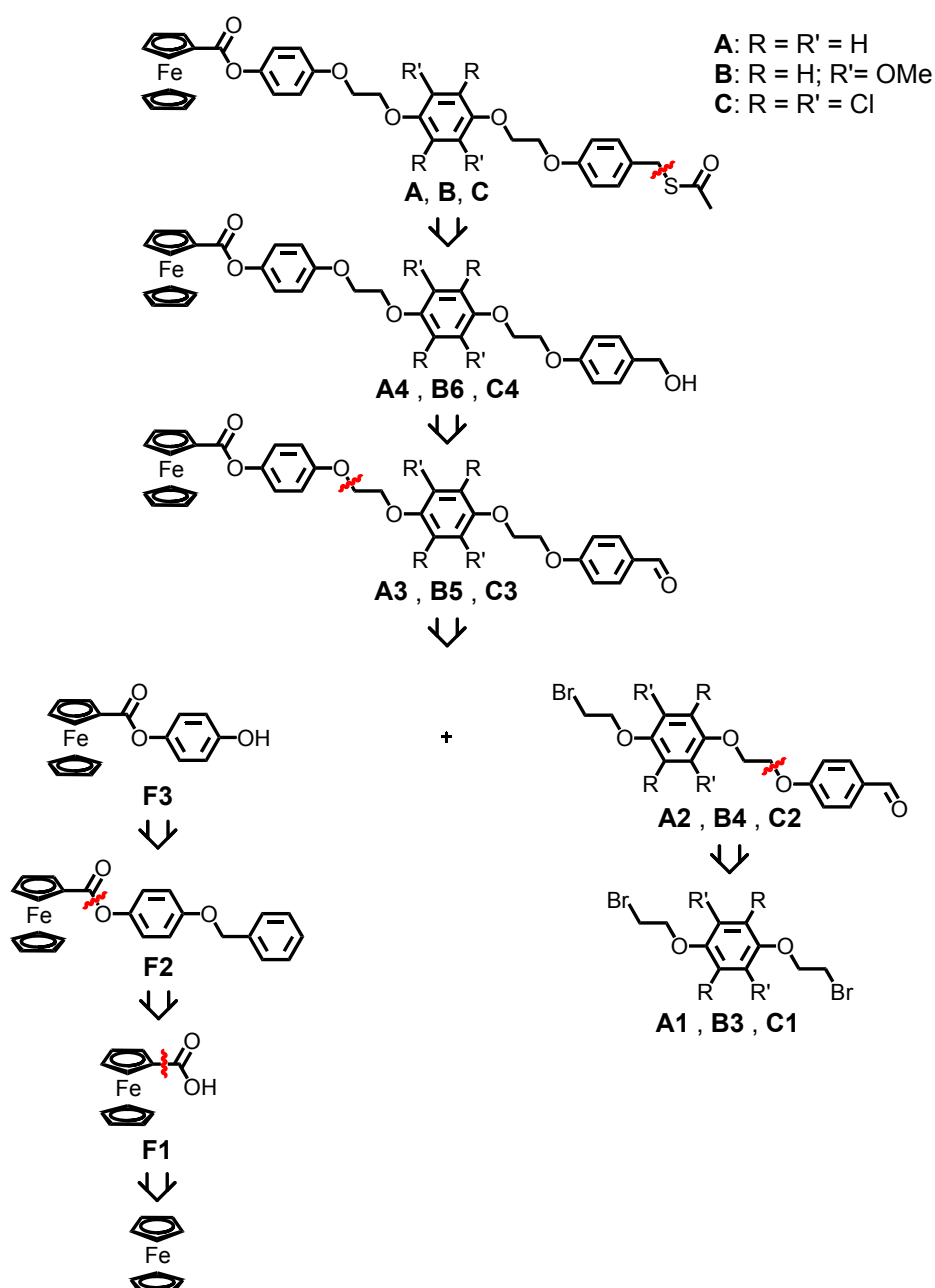
Figure 11. Simulated *ratio* ($= |Z_{ref}|/|Z_{imp}|$) ($R_u = 150$ Ohm, $C_{dl} = 15.0 \times 10^{-9}$ F, $C_{ct} = 2 \times 10^{-6}$ F, $R_{ct} = 100$ Ohm) employing the equivalent circuits (see Figures 9 and 10).

4 RESULTS AND DISCUSSION

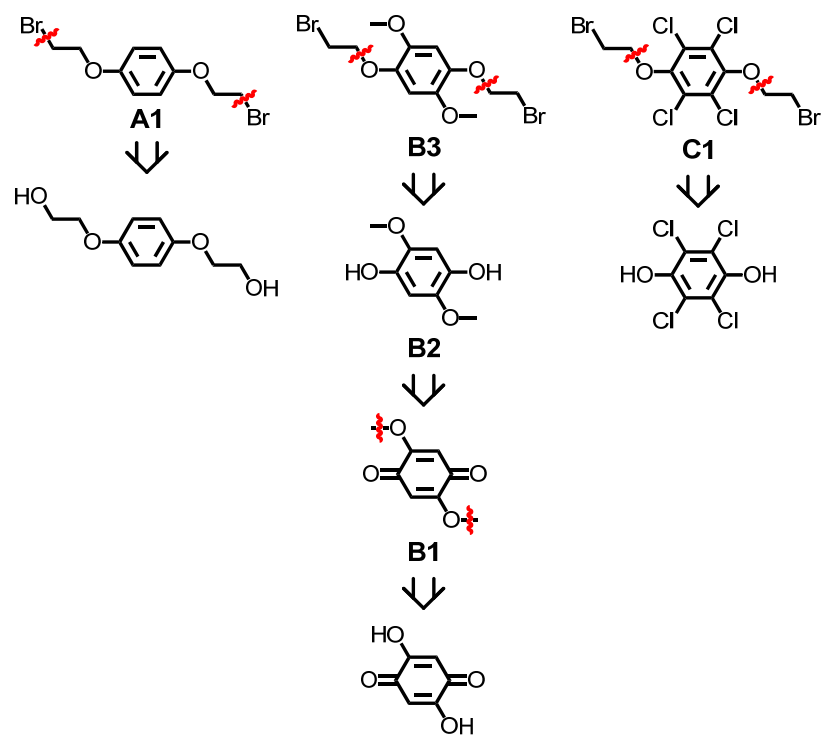
4.1 MOLECULES

4.1.1 RETROSYNTHETIC SCHEMES OF MOLECULES A, B AND C

All target compounds were synthesized according to the retrosynthetic schemes shown (see Schemes 1 and 2).

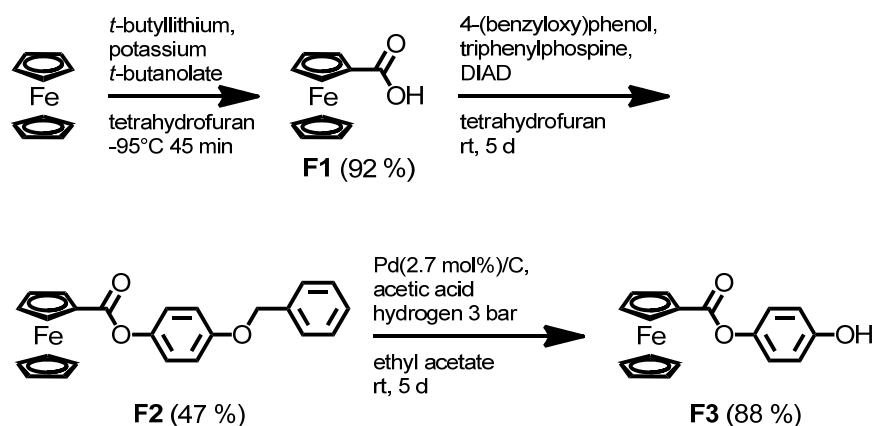


Scheme 1. Retrosynthetic scheme of the synthesis of compounds **A–C**.



Scheme 2. Retrosynthetic scheme of dibromide precursors of compound **A**, **B** and **C**.

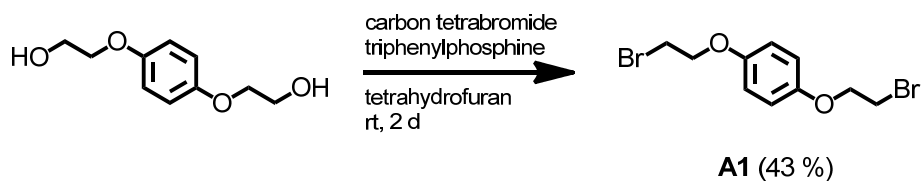
4.1.2 SYNTHESIS OF FERROCENE COMPOUND F3



Scheme 3. Synthetic scheme of ferrocene precursor **F3**.

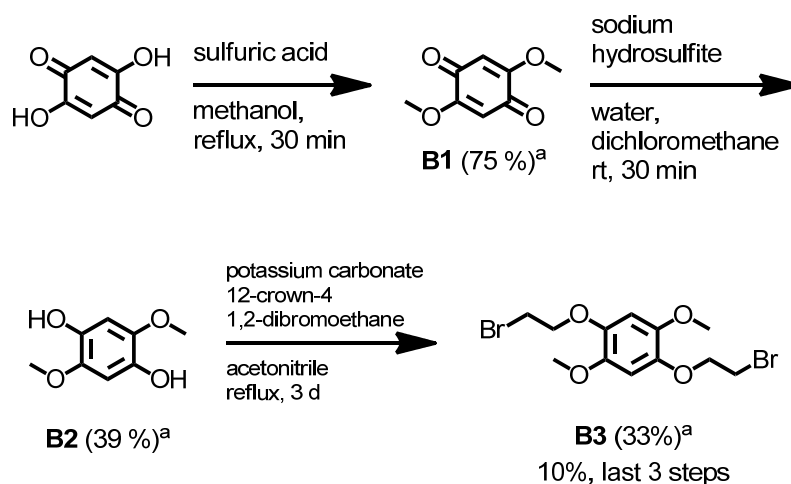
Monolithiation of ferrocene with *tert*-butyllithium and quenching with carbon dioxide yielded compound **F1** (see Scheme 3) in a purity not requiring purification by column chromatography, which can lead to degradation of the product. The following esterification under Mitsunobu reaction conditions introduced a benzyl protected hydroquinone group to produce **F2**. Due to the large amount of triphenylphosphine oxide generated, the purification by column chromatography on silica gel was laborious. In the last step the protection group was removed by Pd-catalyzed reduction to yield **F3** in a purity not requiring purification by column chromatography.

4.1.3 SYNTHESIS OF DIBROMIDE PRECURSORS OF A; B AND C



Scheme 4. Synthetic scheme of precursor **A1**.

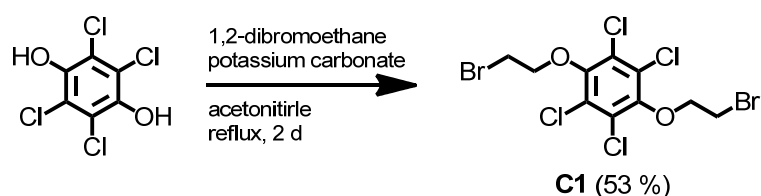
The preparation of the precursor of **A1** (see Scheme 4) was done according to literature methods, which involved laborious purification by column chromatography of the diol.^[131] The precursor was dibrominated in an Apple reaction. Due to the generated triphenylphosphine oxide, large amounts of solvent and silica gel were required during purification by column chromatography.



Scheme 5. Synthetic scheme of precursor **B3**. ^a Yields are estimated by NMR

The synthesis of **B3** is carried out starting with 2,5-dihydroxycyclohexa-2,5-diene-1,4-dione, which in the first step is methylated to form crude **B1** (see Scheme 5). This was followed by a reduction to the crude diol **B2** with sodium hydrosulfite. Then **B2** is directly extended with the

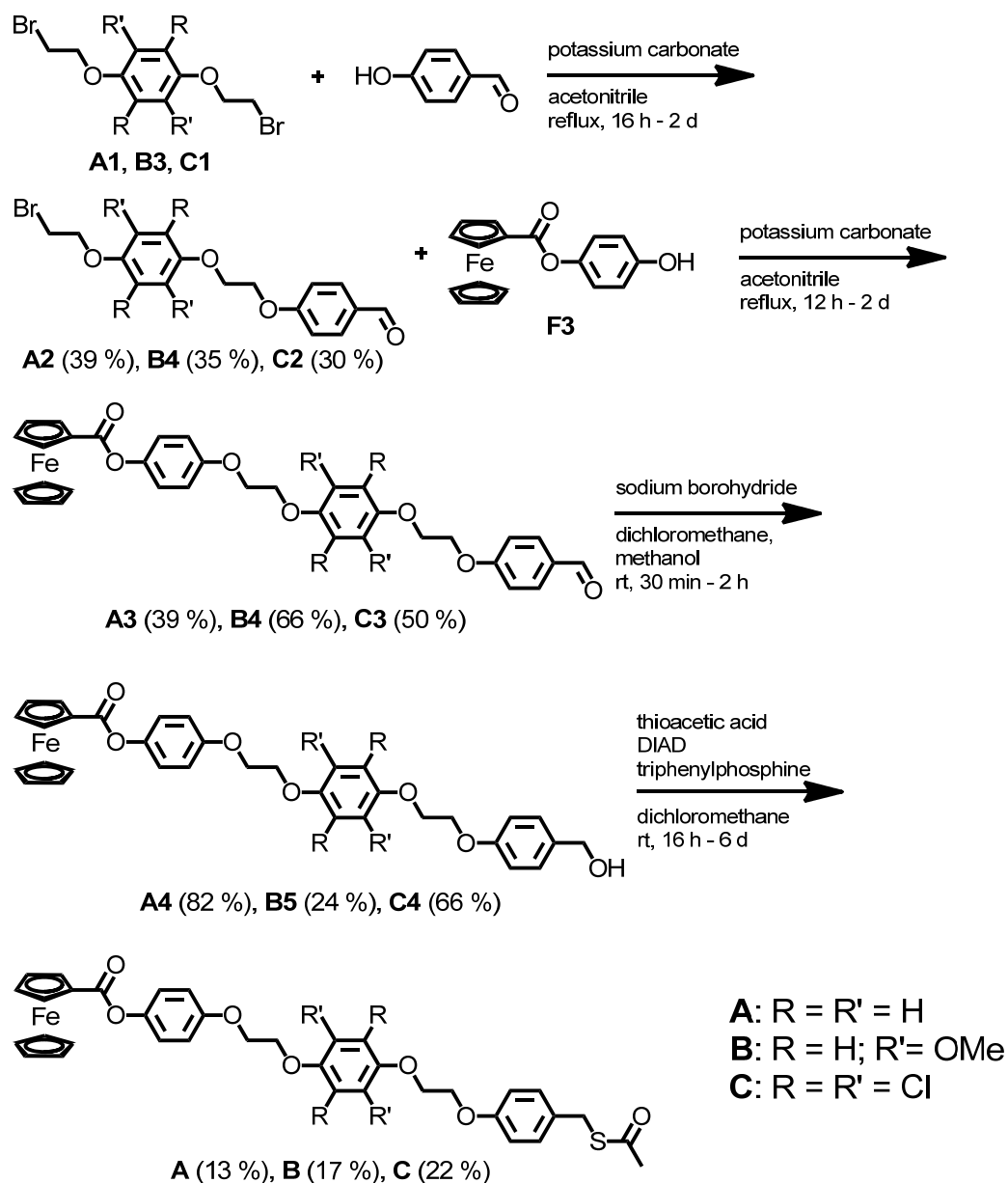
help of an excess of 1,2-dibromoethane to yield **B3**. This change in the synthetic route avoided the intermediate diol, which was used as a precursor for **A1** and therefore also eliminated the need of the laborious purification involved. Furthermore, this also simplified the purification of **B3** because there was no need to remove the triphenylphosphine oxide as in the synthesis of dibromide **A1**.



Scheme 6. Synthetic scheme of precursor **C1**.

C1 was also synthesized by directly extending 2,3,5,6-tetrachlorobenzene-1,4-diol with an excess of 1,2-dibromoethane. Analogous to the synthesis of **B3** (see Scheme 6), the synthesis was shortened by one step and involved a simplified purification (see above).

4.1.4 SYNTHESIS OF A, B AND C



Scheme 7. Synthetic scheme of target compounds **A**, **B** and **C**.

After the generation of the precursor dibromides **A1**, **B3** and **C1**, the synthesis of the target compounds proceeds in a similar manner (see Scheme 7). Consecutively, the aldehyde and then the ferrocene compound **F3** were introduced via nucleophilic substitution. Thereafter, the aldehyde was reduced, and, finally, a Mitsunobu reaction was used to attach an acetyl protected thiol function. Thus, the three target compounds were synthesized in reasonable yields, particularly when considering the limited stability of the ferrocene carboxylic ester.

4.1.5 CYCLIC VOLTAMMETRY

Before the actual target molecules **A**, **B** and **C** were synthesized from the corresponding subunits, the half-wave potentials of the ferrocene unit precursor **F2** and the precursors of the bridge units **B3** and **A1** were determined by cyclic voltammetry. This was done to ensure that the potential gaps between the oxidized states of the terminal and bridge units redox centers in the target molecules remain within the intended distances as determined from the literature values of similar redox centers measured in other set-ups.

The cyclic voltammograms of the precursors show a half-wave potential $E_{1/2}$ of the first oxidation of 275 mV for **F2**, 475 mV for **B3** and 975 mV for **A1** versus ferrocene/ferrocenium (Fc/Fc^+) (see Figures 12-14). A conversion of the literature known half-wave potentials of similar redox centers, which were determined versus a standard calomel electrode, according to Addison *et al.*, made it possible to compare them directly to the obtained values (see Figure 15).^[132]

Although the periphery of the similar redox center is slightly different from the precursors and even though the measurement setup is slightly different than those used for the determination of the literature values, the potential differences were minor. The energetic gaps between the redox centers remained approximately the same with 200 mV for **B3**, 700 mV for **A1** and >700 mV for **C1** (outside the electrolyte solution window).

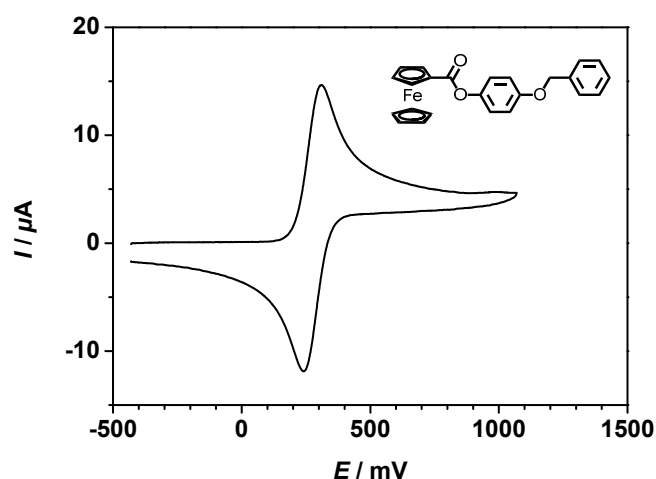


Figure 12. Cyclic voltammogram (CV) of **F2** recorded with a scan rate of 250 mV s^{-1} in tetrabutylammonium hexafluorophosphate in acetonitrile (0.15 M) versus Fc/Fc^+ .

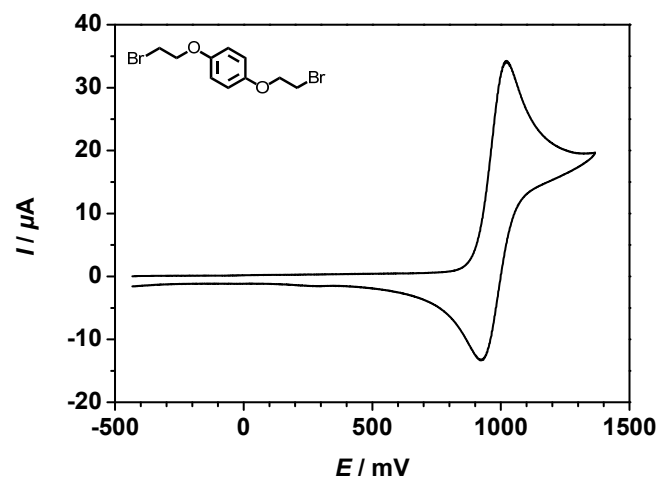


Figure 13. Cyclic voltammogram (CV) of **A1** recorded with a scan rate of 250 mV s^{-1} in tetrabutylammonium hexafluorophosphate in acetonitrile (0.15 M) versus Fc/Fc^+ .

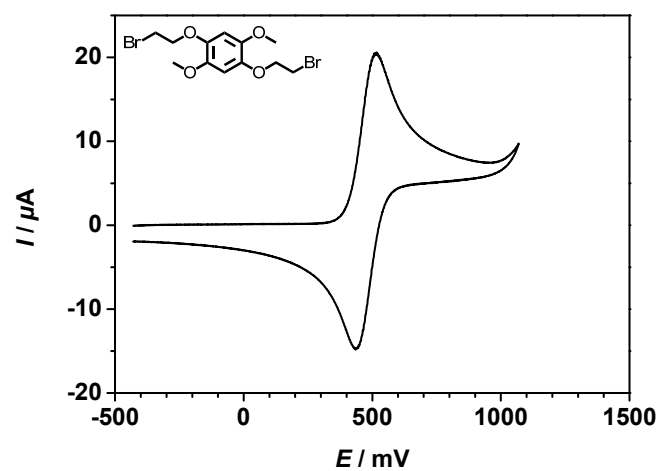


Figure 14. Cyclic voltammogram (CV) of **B3** recorded with a scan rate of 250 mV s^{-1} in tetrabutylammonium hexafluorophosphate in acetonitrile (0.15 M) versus Fc/Fc^+ .

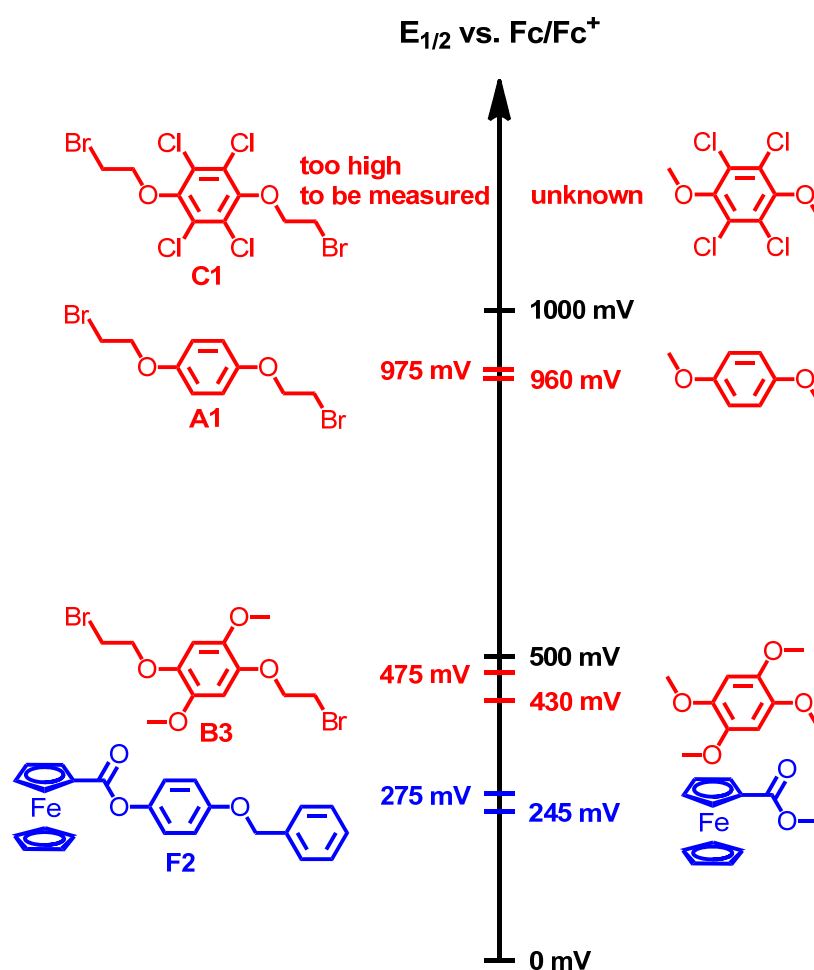


Figure 15. Comparison of the half-wave potentials of first oxidation precursors of the target molecules (left) synthesized within this work (determined in 0.15 M tetrabutylammonium hexafluorophosphate in acetonitrile) vs. those of similar redox centers (right) from literature (bridge units determined in 0.1 M tetrapropylammonium perchlorate and ferrocene unit determined in 0.1 M tetraethylammonium perchlorate in acetonitrile).^[116, 117]

4.2 MONOLAYERS

4.2.1 PREPARATION CONDITIONS

All monolayers electrochemically characterized within this work were prepared on self-made freshly molten and tempered spherical gold electrodes which are known to possess an Au(111) surface.^[133] These electrodes were closely inspected for surface inhomogeneities (see Figure 16) that could be detected by using a conventional light microscope. Although such inhomogeneities did rarely occur, it allowed the preclusion of possibly contaminated measurement data gathered on monolayers, which were of lesser uniformity due to being prepared on these distorted surfaces.

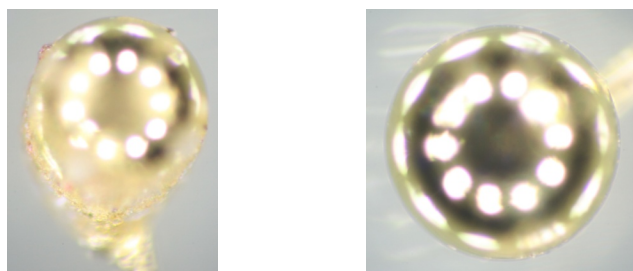


Figure 16. Photo of gold electrodes with (left) and without (right) surface inhomogeneities.

As a hard criterion for the quality of the monolayers prepared throughout this investigation, the surface coverage (see Section 3.2) determined via cyclic voltammetry was employed. Monolayers with a minimum surface coverage of $3.0 \times 10^{-10} \text{ mol} \times \text{cm}^{-2}$, which therefore lie within the region of the theoretical value of $4.5 \times 10^{-10} \text{ mol} \times \text{cm}^{-2}$, that is based on the densest packing of ferrocene groups on an Au(111) surface, were considered of sufficient quality for measurement.^[115]

The target molecules **A**, **B** and **C** used for the preparation of the monolayers were insoluble in ethanol, which is used in most studies as a medium for the assembling of thiols on gold surfaces.^[111, 113, 134-139] Due to their good solubility in tetrahydrofuran, it was used instead of ethanol for this work. This is probably a reasonable choice, since the replacement was verified not to lower the monolayer quality in the preparation of a reference monolayer prepared from a ferrocene terminated alkylthiol provided by *Terfort et al.*^[110] (see Figure 17). This was confirmed by the determination of near identical surface coverages and electron

transfer rates (see below) of monolayers prepared in both solvents. Additionally, the concurrence of the fit of the *ratio* determined from the impedance measurements was of a very high quality for monolayers prepared in either solvent (see below).

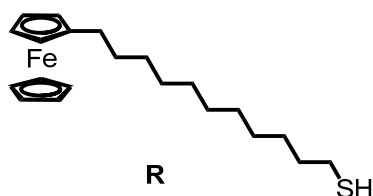


Figure 17. Structure formula of the reference molecule.

Monolayer preparations directly employing the molecules as acetyl protected thiols or disulfides, which have been claimed to form monolayers in some cases,^[140, 141] failed to yield layers of sufficient surface coverage with the target molecules used in this investigation. For example, the surface coverage of monolayers prepared from acetyl protected compounds reached only $0.303 \times 10^{-10} \text{ mol} \times \text{cm}^{-2}$ (average of two monolayers) with molecule **C** after one day and $0.788 \times 10^{-10} \text{ mol} \times \text{cm}^{-2}$ (average of two monolayers) with molecule **A** after two days. When using disulfides of molecule **B** (see preparation of free thiols), the surface coverage reached $2.34 \times 10^{-10} \text{ mol} \times \text{cm}^{-2}$ (average of two monolayers) after three days but did not improve further with a value of $2.32 \times 10^{-10} \text{ mol} \times \text{cm}^{-2}$ (average of two monolayers) after six days. These coverages were considered not sufficient, because in the case of molecule **B**, in the corresponding cyclic voltammograms, the redox processes of the bridge units, while being distorted, remained visible (see Figure 18). As those signals were always suppressed in monolayers of higher coverage, this was interpreted as a sign for non-ideal packing in the monolayers (see Figure 18). A reasonable explanation for this behavior will be given later (see Section 4.2.6).

The reproducibility of the literature technique of an *in situ* base promoted deprotection^[120, 121] of the acetyl capped thiols also did not yield satisfactory results with the target molecules of this work. A sufficient surface coverage could not be achieved within acceptable time spans. For example, with molecule **A** a surface coverage of only $0.835 \times 10^{-10} \text{ mol} \times \text{cm}^{-2}$ was achieved after two days and in a preparation employing molecule **B** surface coverage only reached $2.68 \times 10^{-10} \text{ mol} \times \text{cm}^{-2}$ after three weeks. Again, in the case of the monolayers prepared with molecule **B**, the insufficient quality is substantiated by the visibility of the redox processes of the bridge in their cyclic voltammograms (see Figure 19), which is not typical of

those of sufficient surface coverage (see Figure 19). However, it should be noted that, in the case of the cyclic voltammograms of these monolayers, the direct comparability of the shapes is limited by the employment of different electrolyte solutions in the measurements.

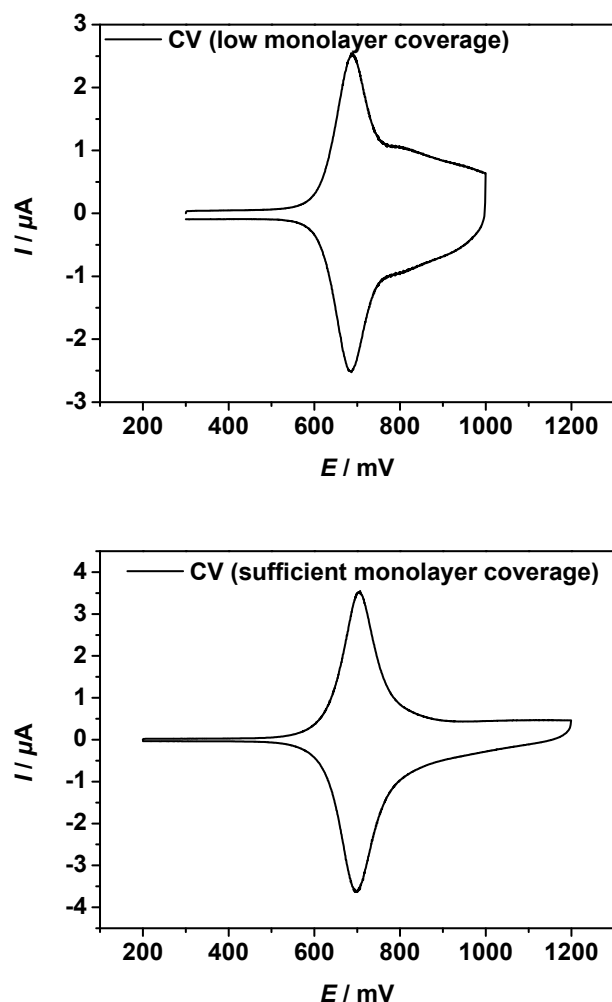


Figure 18. Cyclic voltammograms (CV) of a low surface coverage monolayer with the additional residual redox signal of the bridge unit (above) prepared with the disulfide of molecule **B** in tetrahydrofuran for three days and of a sufficient surface coverage monolayer without any redox signal of the bridge unit (below) prepared with the free thiol of molecule **B** after one day recorded with a scan rate of 1.00 V s^{-1} in tetrabutylammonium hexafluorophosphate in acetonitrile (0.5 M).

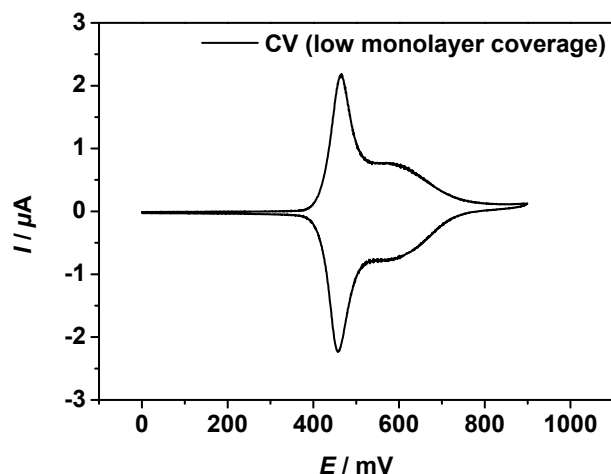


Figure 19. Cyclic voltammograms (CV) of a low surface coverage monolayer with the additional residual signal of the bridge unit prepared with diethylamine promoted deprotection of molecule **B** after three weeks recorded with a scan rate of 1.00 V s^{-1} in tetrabutylammonium hexafluorophosphate in dichloromethane (0.5 M).

Due to the various difficulties encountered with the employment of protected thiols for the preparation of the monolayers, free thiols were used, even though these had to be freshly prepared for each batch of monolayers to avoid the generation of disulfides.^[120, 121] The preceding deprotection of the acetyl capped thiols was carried out using a procedure developed by *Han et al.*^[142] utilizing potassium carbonate in a tetrahydrofuran-methanol mixture. This procedure was directly followed by purification with high performance liquid chromatography to separate any disulfides and due to the very small batches subsequent characterization by matrix-assisted laser desorption/ionization mass spectroscopy. Employing these free thiols in the preparation reproducibly yielded high quality monolayers of all target molecules within 24 h (see Tables 10–12 in Section 4.2.6). However, in case of molecule **B** preparation times longer than two days resulted in degradation of the monolayers. For example, a surface coverage of only $1.53 \times 10^{-10} \text{ mol} \times \text{cm}^{-2}$ (average of two monolayers) remained after three days and $0.628 \times 10^{-10} \text{ mol} \times \text{cm}^{-2}$ (average of two monolayers) after six days. Nevertheless, the monolayers of molecules **A** and **C** retained good surface coverages of $4.22 \times 10^{-10} \text{ mol} \times \text{cm}^{-2}$ (average of 4 monolayers) and $3.59 \times 10^{-10} \text{ mol} \times \text{cm}^{-2}$ (average of 4 monolayers) for at least one week.

The utility of the common technique^[111, 114, 115, 125, 136, 143-148] of employing alkylthiols of appropriate length to dilute ferrocene terminated alkyl thiols and isolate and therefore limit

intermolecular effects between the oxidized redox centers within the monolayer was tested with molecule **A**. Molecule **A** was chosen, since it was the only molecule whose monolayers showed a substantial broadening of the oxidation and to a lesser extent the reduction wave of the first oxidation which could be ascribed to intermolecular effects within the monolayer (see Section 4.2.6). The surface coverage of $0.557 \times 10^{-10} \text{ mol} \times \text{cm}^{-2}$ (average of 2 monolayers) of the redox active molecule was within the expected range considering the usage of 10% of molecule **A** and 90% alkylthiol ($\text{C}_{18}\text{H}_{37}\text{SH}$) for the preparation solutions and a maximum value of $4.5 \times 10^{-10} \text{ mol} \times \text{cm}^{-2}$ for the densest packing of ferrocene on an Au(111) surface.^[115] While this reduced the mentioned broadening in the cyclic voltammograms typical for the high density monolayers of **A**, the peak separation increased, which is a sign for decreased order of the monolayer.^{157,172} Furthermore, the fits in the data analysis of the impedance measurements were deviating strongly and, most importantly, the determined electron transfer rates were significantly higher than the average value determined for the non-diluted monolayers prepared from molecule **A** (see Table 9 in Section 4.2.6). Poorer data quality as a result of dilution has already been observed in other systems.^[112] The problem might lie in the different structure of the backbones of the diluting alkyl thiols and the target molecules which prevents the insulation of the redox centers of the target molecules during the formation of the monolayer and therefore the creation of uniform monolayers and instead creating islands of different compositions. Because of this, and due to the dilution of the redox active molecules, the overall surface coverage (a crucial factor for the assessment of the monolayer quality) could no longer be determined by cyclic voltammetry. This method was therefore not investigated further.

4.2.2 MEASUREMENT CONDITIONS

Within this study, an investigation of measurements employing an electrolyte solution consisting of tetrabutylammonium hexafluorophosphate in dichloromethane, in which the monolayers show a very high stability in their neutral as well as their oxidized state, was carried out. This investigation yielded a very strong dependence of the determined electron transfer rates on the distance between the working and the reference electrode (see Table 2). Furthermore, a significant dependence on the concentration of the supporting electrolyte in the electrolyte solution could be detected (see Table 2). These substantial deviations by slight changes of the measurement setup greatly reduce the comparability and reproducibility of measurement results acquired in this electrolyte solution.

Table 2. Molecules used for the monolayer preparation, measurement number, distances of working and reference electrode (d_{w-r}) and concentrations of tetrabutylammonium hexafluorophosphate in dichloromethane (c_{se}) used in the setup for the impedance measurements and electron transfer rates (k_{ET}) of the monolayers.

monolayer	molecule	measurement	d_{w-r} / mm	c_{se} / mol×l ⁻¹	k_{ET} / s ⁻¹
M_A1	A	1 st	1	0.5	290
		2 nd	3	0.5	1500
		3 rd	1	0.5	500
M_B1	B	2 nd	1	0.5	650
		3 rd	3	0.5	2200
		4 th	1	0.5	950
		5 th	1	0.05	90
M_B2	B	1 st	<1	0.5	350
		3 rd	3	0.5	3000
		4 th	1	0.5	750

The commercially available advanced potentiostat used in the present study (see Experimental Section) allowed gathering the required impedance data very quickly, in

contrast to many former studies,^[110-112, 134, 136-139, 143, 149, 150] effectively reducing the time the redox active monolayers remained in their oxidized state. This reduction of stress allowed consecutive electron transfer rate determinations on the same monolayer in an electrolyte solution consisting of tetrabutylammonium hexafluorophosphate in acetonitrile (0.5 M) while additionally extending the frequency range from 1 MHz down to 1 Hz. The possibility to conduct impedance measurements in this electrolyte solution was crucial to this study, because in this solvent the influence of the positioning of the reference to the working electrode and the concentration of the supporting electrolyte was negligible (see Table 3). This ensured good reproducibility of the results. Furthermore, the determined electron transfer rates of consecutive impedance measurements remained identical within the experimental error (see Tables 10, 11 and 12). This was the case even though in this electrolyte solution the monolayer surface coverage determined by cyclic voltammetry decreased slightly with each impedance scan, which involved oxidizing the redox centers in the monolayers (and Tables 10, 11 and 12). An example of such cyclic voltammograms showing the degradation of a surface coverage from $3.58 \times 10^{-10} \text{ mol} \times \text{cm}^{-2}$ before to $3.09 \times 10^{-10} \text{ mol} \times \text{cm}^{-2}$ after an impedance measurement is given (see Figure 20). The surface coverage stayed constant when the redox centers remained in their neutral state during reference scans (see Figure 21). The very slight deviations of the cyclic voltammograms before and after the reference scans can be explained by degeneration of the redox centers during the recording of the first cyclic voltammogram, as they do not exceed the aberrations between two immediately consecutive cyclic voltammograms (see Figure 22).

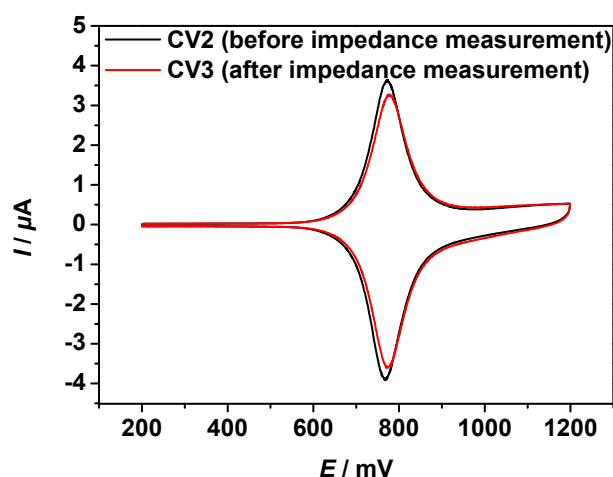


Figure 20. Cyclic voltammograms of a monolayer prepared with the thiol of molecule **B** recorded with a scan rate of 1.00 V s^{-1} in tetrabutylammonium hexafluorophosphate in acetonitrile (0.5 M) before (CV2) and after (CV3) an impedance scan followed by an reference scan.

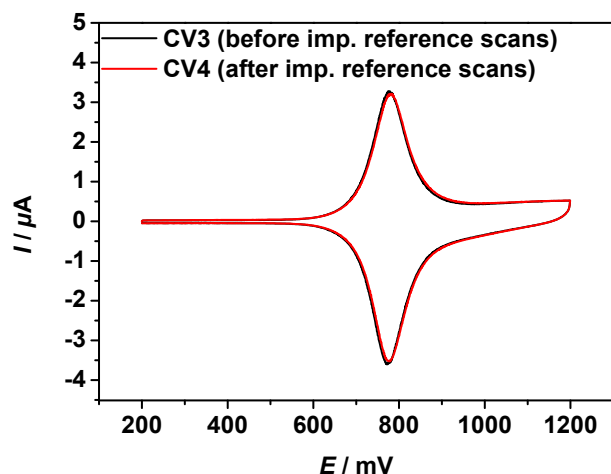


Figure 21. Cyclic voltammograms of a monolayer prepared with the thiol of molecule **B** recorded with a scan rate of 1.00 V s^{-1} in tetrabutylammonium hexafluorophosphate in acetonitrile (0.5 M) before (CV3) and after (CV4) two reference scans.

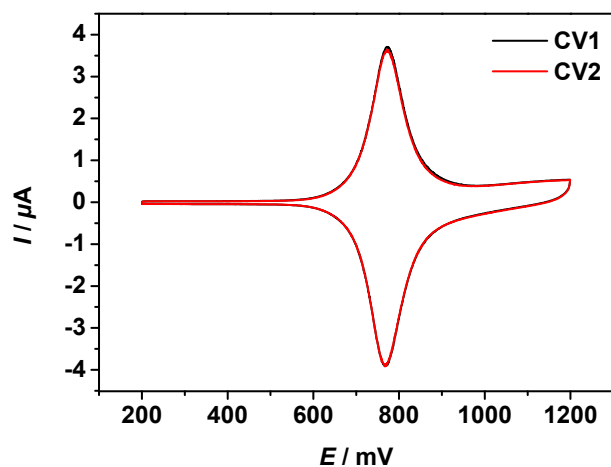


Figure 22. Immediately consecutive cyclic voltammograms (CV1 and CV2) of a monolayer prepared with the thiol of molecule **B** recorded with a scan rate of 1.00 V s^{-1} in tetrabutylammonium hexafluorophosphate in acetonitrile (0.5 M).

The above mentioned opportunity to extend the lower boundary of the frequency range of the impedance measurements allowed fitting especially low electron transfer rates accurately—such as those of the monolayer prepared with molecule **C**. Furthermore, it was a precondition to extract the values (CPE_{ct} and n_{ct}) of the electron transfer constant phase element of the electrochemical cell directly from the impedance scans in advance (see

Figures 41, 42 and 43 in Section 4.2.6). The predetermination of these values was necessary for the accurate acquisition of the electron transfer rates (see Section 4.2.3).

Tetrabutylammonium hexafluorophosphate in benzonitrile was also tested but was not suitable due to the still considerable dependence on the distance between the working and reference electrode (see Table 4). Employing perchloric acid in water yielded no assignable redox signals at all.

Table 3. Molecules used for the monolayer preparation, measurement number, distances of working and reference electrode (d_{w-r}) and concentrations of tetrabutylammonium hexafluorophosphate (c_{se}) in acetonitrile used in the setup for the impedance measurements and electron transfer rates (k_{ET}) of the monolayers.

monolayer	molecule	measurement	d_{w-r} / mm	c_{se} / mol×l ⁻¹	k_{ET} / s ⁻¹
M_B3	B	4 th	2	0.5	3400
	B	5 th	3	0.5	4500
M_B4	B	2 nd	1	0.5	2200
	B	3 rd	3	0.5	3200
	B	4 th	1	0.5	2600
M_C1	C	2 nd	1	0.5	480
	C	3 rd	3	0.5	470
M_R1	R	1 st	1	0.25	3800
	R	2 nd	1	0.5	3700
	R	3 rd	1	1.0	4100

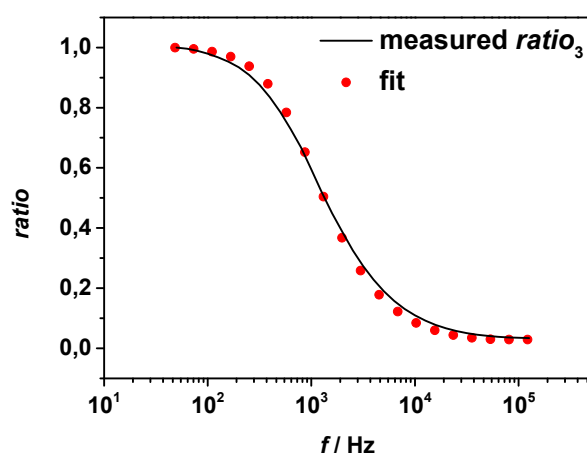
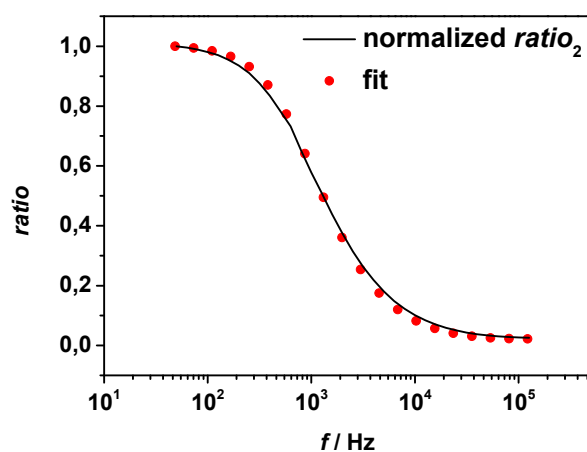
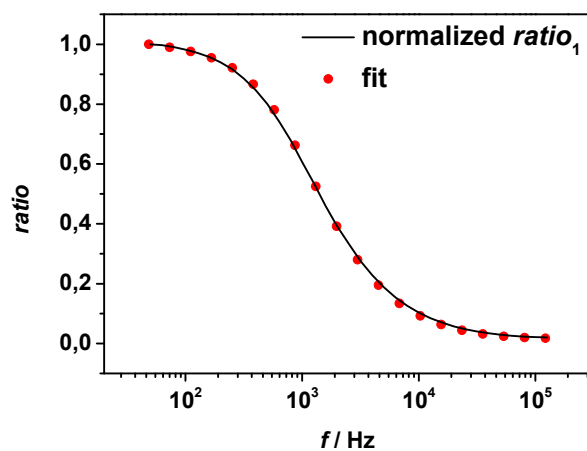


Figure 23. Fitted $ratio$ ($= |Z_{ref}|/|Z_{imp}|$) of three consecutive impedance measurements with similar electron transfer rates (5200 s^{-1} , 4900 s^{-1} and 5400 s^{-1}) on a monolayer prepared from **A** measured in 0.5 M tetrabutylammonium hexafluorophosphate in acetonitrile (10 frequency points per decade).

Table 4. Molecules used for the monolayer preparation, measurement number, distances of working and reference electrode (d_{w-r}) and concentrations of tetrabutylammonium hexafluorophosphate (c_{se}) in benzonitrile used in the setup for the impedance measurements and electron transfer rates (k_{ET}) of the monolayers.

monolayer	molecule	measurement	d_{w-r} / mm	c_{se} / mol·l ⁻¹	k_{ET} / s ⁻¹
M_B2	B	5 th	1	0.5	770
	B	6 th	3	0.5	2600

4.2.3 ADAPTED PROTOCOL FOR IMPEDANCE MEASUREMENT ANALYSIS

For the purposes of this study, the simplified protocol developed by *Creager et al.*^[111] for the extraction of electron transfer rates from impedance measurements proved to be insufficient (see below). Therefore, the method had to be extended slightly to fully describe the measured data.

First, the capacitors in the equivalent circuits were replaced by constant phase elements (see Figures 24 and 25), since the electrical response of the electrochemical cells could not be adequately fitted by ideal capacitors. In detail, in the regions of the maximum constant slope of the Bode Plots of the reference scan and the impedance scan, where the values of the capacitors should be determined, their slope deviated from the predefined slope of ideal capacitors. Thus, due to these deviating slopes, the capacitor values extracted from the fit were dependent on the frequency range in which the plot showed this constant slope. However, the higher boundary of this frequency range is determined by R_u or R_{ct} while the lower boundary is chosen to reduce measurement time and stress on the monolayer. Therefore, the values extracted from the fit are contaminated by factors which clearly physically should not affect them. To overcome this problem, as in the more complicated complex-plane impedance analysis,^[128] constant phase elements were employed, which is a common technique in impedance spectroscopy to account for non-ideal behavior of double layers even if the origin of this behavior is unknown.^[151] As possible reasons, electrode roughness,^[152] distribution of reaction rates,^[153] varying thickness or composition of a coating^[154] or non-uniform current distribution^[155, 156] have been discussed. As shown in the examples, the employment of constant phase elements substantially improves the fit quality (see Figures 26 and 27).

Second, the process of the data analysis was extended to fitting the simulated electrical response of the equivalent circuit corresponding to the Bode Plot of the impedance scan in addition to fitting the one of the reference scan (see Figure 27). This allowed the predetermination of the values of both constant phase elements. This is important since the procedure in the original protocol involves the determination of the maximum value of the *ratio* which is in the present measurements contaminated by non-ideal slopes of the underlying Bode Plots.

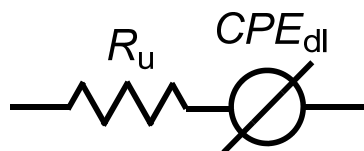


Figure 24. Adapted reference equivalent circuit.

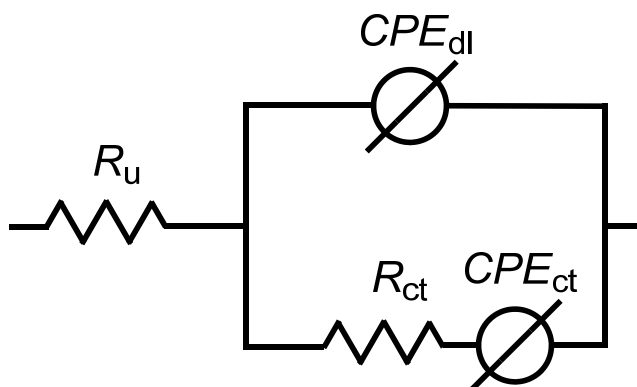


Figure 25. Adapted Randles equivalent circuit.

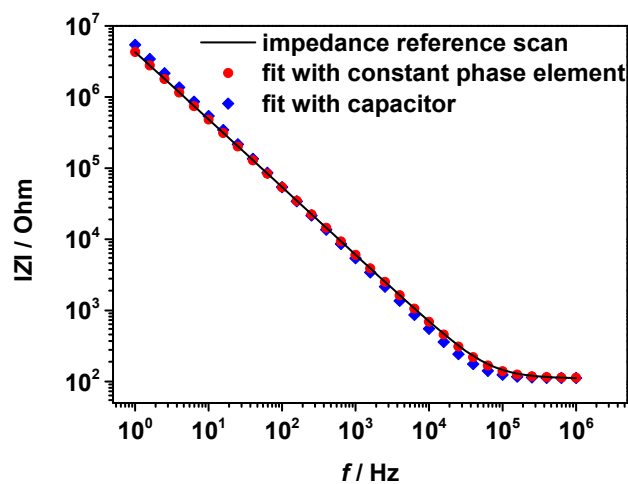


Figure 26. Fit of the Bode Plot of the first reference scan (10 frequency points per decade) of a monolayer on an electrode with the equivalent cell with a capacitor ($R_u = 112 \text{ Ohm}$, $C_{dl} = 29.4 \times 10^{-9} \text{ F}$) and the equivalent cell with a constant phase element ($R_u = 112 \text{ Ohm}$, $CPE_{dl} = 40.5 \times 10^{-9} \text{ F}$ with $n = 0.951$). For clarity, only every second data point of the fit is shown.

The full description of the adapted procedure to determine the electron transfer rate is as follows. First, the Bode Plot of the reference scan is fitted in the frequency region with the maximal negative slope to determine the values of the double layer constant phase element (CPE_{dl} and n_{dl}) of the reference equivalent circuit (see Figure 26). The value of the resistance (R_u), which stands for the uncompensated resistance of the reference equivalent cell can be determined at the highest frequency point of the plot, due to the Bode plot reaching the expected high-frequency plateau (see Section 3.3).

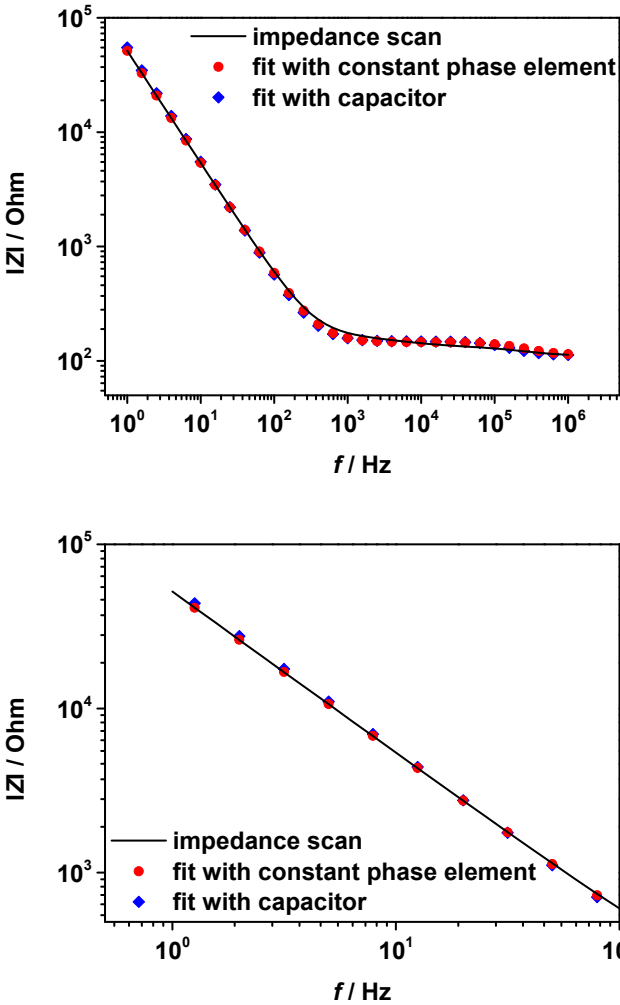


Figure 27. Fit of the Bode Plot of the first impedance scan (10 frequency points per decade) of a monolayer on an electrode with the equivalent cell with a capacitor ($R_u = 112 \text{ Ohm}$, $C_{dl} = 29.4 \times 10^{-9} \text{ F}$, $R_{ct} = 36.8 \text{ Ohm}$, $C_{ct} = 2.87 \times 10^{-9} \text{ F}$) and the equivalent cell with a constant phase element ($R_u = 112 \text{ Ohm}$, $CPE_{dl} = 40.5 \times 10^{-9} \text{ F}$, $n_{dl} = 0.951$, $R_{ct} = 34.5 \text{ Ohm}$, $CPE_{ct} = 3,17 \times 10^{-6} \text{ F}$, $n_{ct} = 0.980$). For clarity, only every second data point of the fits is shown.



This information is then used in the simulation of the low frequency region of the Bode Plot of the impedance scan where, aside from values predetermined from the reference scan, only the constant phase element governs the response of the Randels equivalent circuit and therefore yields its values (CPE_{ct} and n_{ct}). However, due to non-ideal behavior, no accurate fit of the mid to high-frequency region to determine an exact value of the charge transfer resistance is possible.

To circumvent this, following the protocol of *Creager et al.*,^[111] the *ratio* of the moduli of the impedances from the reference scan and the impedance scans are plotted vs. the logarithmic frequency, which results in a sinusoidal curve (see Figure 28). Next, a formula to simulate and fit this sinusoidal curve is derived. For this, similar to the protocol of *Creager et al.*, the mathematical expression to describe the ratio of the impedances of both cells is developed by combining the impedances R_u (Z_1), CPE_{dl} (Z_2), R_{ct} (Z_3) and CPE_{ct} (Z_4) according to common electrical rules regarding their arrangement in the circuits (see equation 8).

$$\frac{Z_{ref}}{Z_{imp}} = \frac{Z_1 + Z_2}{Z_1 + \frac{Z_2 Z_3 + Z_2 Z_4}{Z_2 + Z_3 + Z_4}} \quad (8)$$

However, when replacing the impedances by the corresponding impedance equations those of the constant phase elements were used (see Table 5).

Table 5. Circuit elements and their corresponding impedance equations.

circuit element	impedance equation	label
	$Z = R$	resistor
	$Z = \frac{j}{CPE(2\pi f)^n}$	constant phase element

Since, in the protocol used here, the values of both constant phase elements and the uncompensated resistance have already been determined, only the charge transfer resistance remains to be extracted by fitting the sinusoidal curve. Employing the given equations (9 and 10), it can be expressed in terms of the electron transfer rate k_{ET} (see

equation 11). Thus, k_{ET} , due primarily affecting the horizontal position of the inflection point of the plot, can be determined manually in a straightforward manner (see Figure 28). The advantage of this approach developed by *Creager et al.* is, that apparently certain non-ideal behavior appearing in the Bode plots cancels out when plotting the ratio and thus simplifies the fit of the charge transfer resistance and thereby the determination of the electron transfer rate.

$$R_{ct} = \frac{2RT}{F^2 G_a k_{et}} \quad (9)$$

$$CPE_{ad} = \frac{F^2 G_a}{4RT} \quad (10)$$

$$\left| \frac{Z_{ref}}{Z_{imp}} \right| = \frac{R_u + \frac{1}{CPE_{dl}(2\pi f)^{n_{dl}}}}{R_u + \frac{\frac{1}{CPE_{dl}(2\pi f)^{n_{dl}}} \frac{1}{2k_{et}CPE_{ct}} + \frac{1}{CPE_{dl}(2\pi f)^{n_{dl}}} \frac{1}{CPE_{ct}(2\pi f)^{n_{ct}}}}{\frac{1}{CPE_{dl}(2\pi f)^{n_{dl}}} + \frac{1}{2k_{et}CPE_{ct}} + \frac{1}{CPE_{ct}(2\pi f)^{n_{ct}}}}} \quad (11)$$

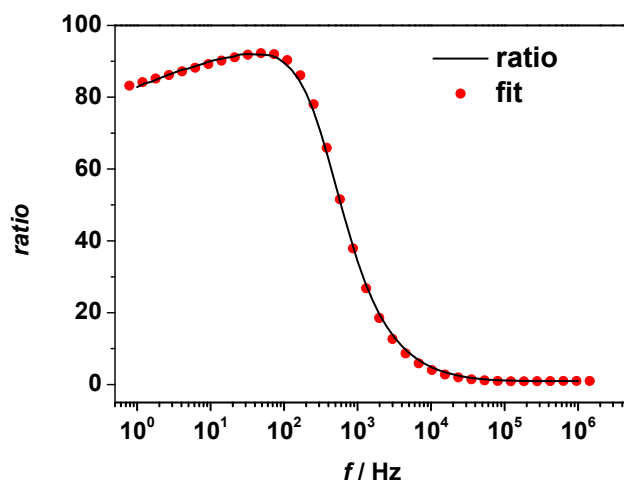


Figure 28. Fitted *ratio* ($= |Z_{ref}|/|Z_{imp}|$) of an exemplary redox-active monolayer (10 frequency points per decade).

4.2.4 IMPEDANCE MEASUREMENT PARAMETERS

If, during the impedance measurements, the reference scans were conducted at a potential of 300 mV below the halfway potential, deviations from the simulated response of the reference equivalent circuit were found (see Figure 29). The mentioned deviations probably originate from residual redox processes of the redox centers within the monolayer. This assumption is substantiated by the fact that, if the reference scans were recorded 500 mV (see Figure 29) below the halfway potential, these vanished and no further changes occurred when increasing the distance further to 700 mV (see Figure 29).

Table 6. Molecules used for the monolayer preparation, measurement number, root mean square of the voltage amplitude (**rms amplitude**) of the alternate current used in the impedance measurement and electron transfer rates (k_{ET}) of the monolayers.

monolayer	molecule	measurement	rms amplitude / mV	k_{ET} / s^{-1}
M_{A2}	A	3 rd	50	2500
	A	4 th	10	2400
	A	5 th	1	2100

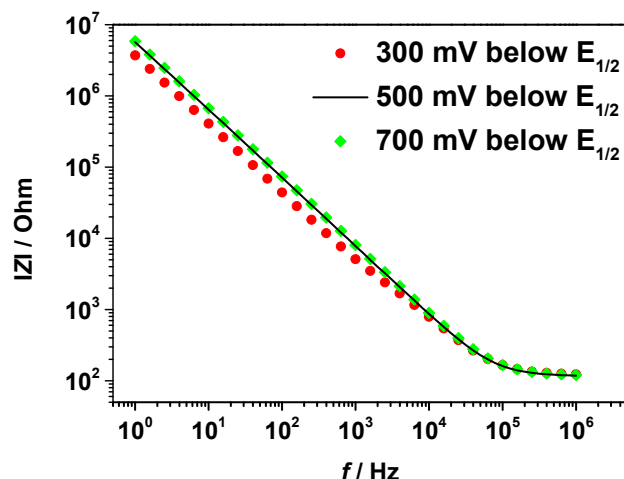


Figure 29. Bode Plots of impedance reference scans at 300 mV, 500 mV and 700 mV below the halfwave potential of the ferrocene redox centers of a monolayer prepared with molecule **A** recorded in (0.5 M) tetrabutylammonium hexafluorophosphate in acetonitrile (10 frequency points per decade). For clarity only every second data point of the impedance reference scans at 300 mV and 700 mV is shown.

The possible influence of changes of the voltage amplitude of the alternating current down to 1 mV and up to 50 mV used in the impedance measurements was investigated. The effect on the determined electron transfer rates was found to be negligible (see Table 6).

Furthermore, it was ruled out that potential drifts during the impedance scans of up to 20 mV are affecting the determined electron transfer rates significantly (see Table 7). In contrast, when greater potential drifts occur, this can contaminate the results since a change of, for example, 100 mV had a profound effect on the acquired electron transfer rates (see Table 7).

Table 7. Molecules used for the monolayer preparation, measurement number, potential offset from the halfway potential of the ferrocene redox centers in the monolayer during impedance scans and electron transfer rates (k_{ET}) of the monolayers.

monolayer	molecule	measurement	<i>potential offset</i>	k_{ET}
			/ mV	/ s ⁻¹
M_B5	B	4 th	0	3100
	B	5 th	+20	4000 ^b
	B	6 th	0	3500 ^b
	B	7 th	-20	3800 ^b
	B	8 th	0	3700 ^b
M_B6	B	3 rd	0	2400 ^b
	B	4 th	-20	2900 ^a
	B	5 th	+20	2700 ^a
M_C2	C	1 st	-100	1700 ^c
	C	2 nd	0	630

^a reference scan from measurement 3 was used. ^b reference scan from measurement 8 was used. ^c reference scan from measurement 2 was used.

4.2.5 ELECTROCHEMICAL CHARACTERIZATION TEST

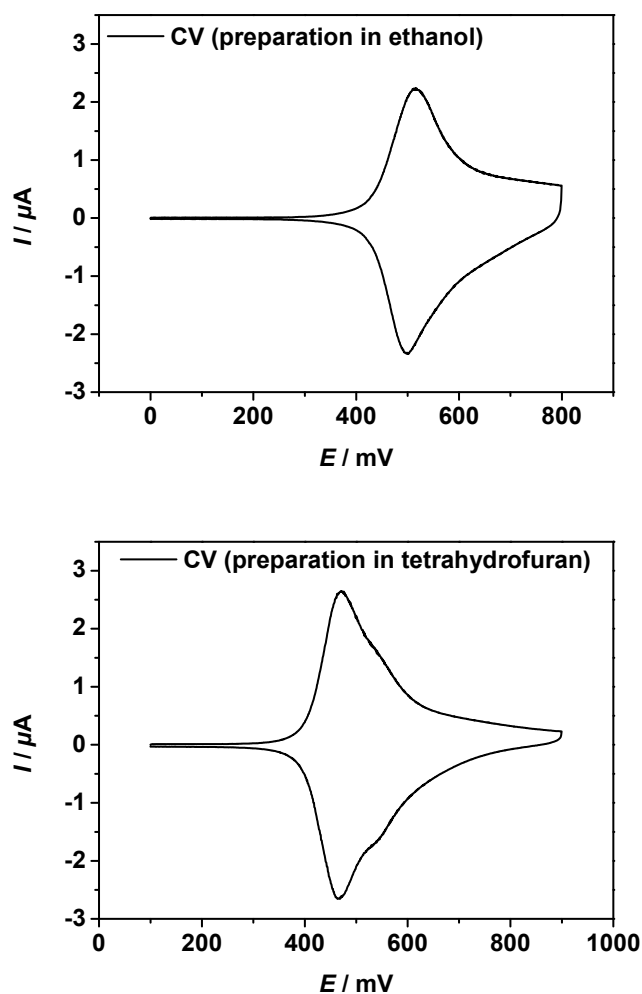


Figure 30. Examples of cyclic voltammograms of monolayers prepared with the reference molecule **R** in ethanol (above) and tetrahydrofuran (below) recorded with a scan rate of 1.00 V s^{-1} in tetrabutylammonium hexafluorophosphate in acetonitrile (0.5 M) before the first impedance measurement.

The functionality of the electrochemical characterization setup and procedure of data analysis employed throughout this work was tested by conducting measurements on monolayers prepared with reference molecule **R** (see Figure 17 in Section 4.2.1). The monolayers were prepared in ethanol as well as in tetrahydrofuran. The cyclic voltammograms of the monolayers (see Figure 30) show some distortion typical of ferrocene terminated alkyl thiols that are not diluted by redox center free alkyl thiols of appropriate

length.^[115, 125, 157] The origin of this behavior is believed to be a result of the close distance between the ferrocene redox centers and is discussed in detail with the cyclic voltammograms of monolayers prepared from **A** (see Section 4.2.6).

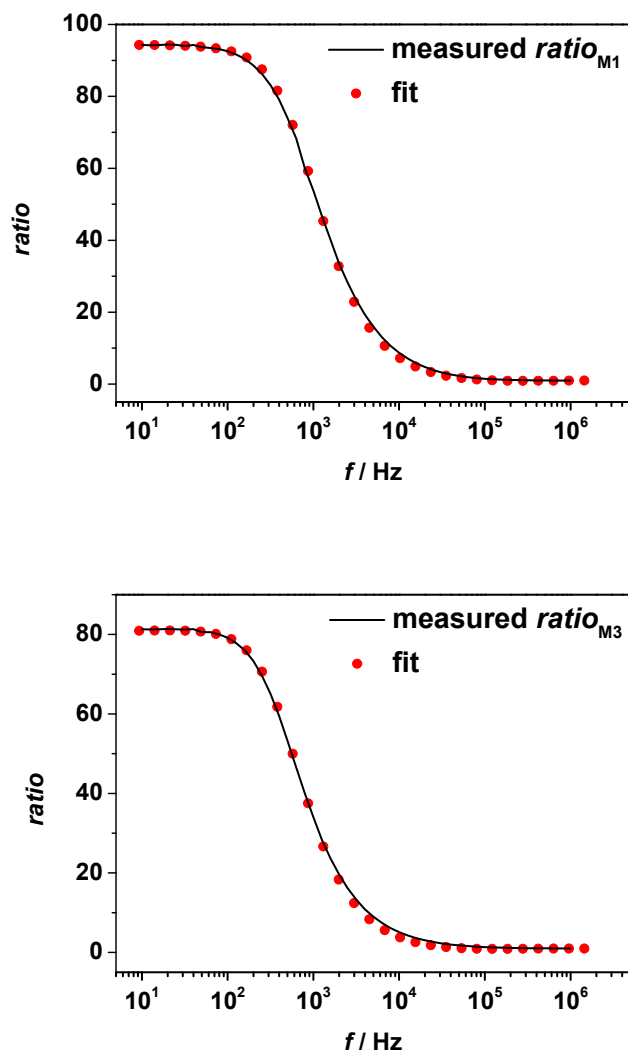


Figure 31. Examples of fits of the *ratio* ($= |Z_{\text{ref}}|/|Z_{\text{imp}}|$) of the first impedance measurements (10 frequency points per decade) of monolayers prepared from the reference molecule **R** in ethanol (above) and tetrahydrofuran (below) both determined in tetrabutylammonium hexafluorophosphate in acetonitrile (0.5 M).

Table 8. Measurement number, solvent, immersion times (t_{imm}) and real surfaces (A_{real}) of the electrodes used for the monolayer preparation, average transferred charges during oxidation and reduction during a voltammetric cycle (Q_{CV}), surface coverage (Γ) and electron transfer rates (k_{ET}) of the monolayers prepared with the reference molecule **R**.

monolayer	measurement	solvent	t_{imm} / days	A_{real} / $\times 10^{-3} \text{ cm}^2$	Q_{CV} / nC	Γ $\times 10^{-10}$ / $\text{mol} \times \text{cm}^{-2}$	k_{ET} / s^{-1}
M_{R2}	1 st	ethanol	1	10.7	391	3.79	7300
	2 nd	ethanol	1	10.7	362	3.51	6500
	3 rd	ethanol	1	10.7	347	3.36	5800
M_{R3}	1 st	ethanol	4	9.54	436	4.73	5500
	2 nd	ethanol	4	9.54	387	4.20	5700
	3 rd	ethanol	4	9.54	374	4.06	5800
M_{R4}	1 st	tetrahydrofuran	1	10.9	500	4.74	5000
	2 nd	tetrahydrofuran	1	10.9	403	3.82	4800
	3 rd	tetrahydrofuran	1	10.9	390	3.70	4800
M_{R5}	1 st	tetrahydrofuran	4	9.54	365	3.96	7100
	2 nd	tetrahydrofuran	4	9.54	326	3.54	6600
	3 rd	tetrahydrofuran	4	9.54	315	3.42	6200

It was found that the effect is very weak in the present study considering its extent in literature.⁸ The mean surface coverage for monolayers prepared in both solvents could be determined without problems and is nearly identical and close to the theoretical value of $4.5 \times 10^{-10} \text{ mol} \times \text{cm}^{-2}$ of the densest packing of ferrocene on an Au(111) surface.^[115] The mean surface coverage for monolayers prepared in ethanol amounts to $4.26 \times 10^{-10} \text{ mol} \times \text{cm}^{-2}$ (see Table 8 for data on the individual monolayers) and the mean surface coverage for monolayers prepared from tetrahydrofuran is $4.35 \times 10^{-10} \text{ mol} \times \text{cm}^{-2}$ (see Table 8 for data on the individual monolayers).

Furthermore, the *ratio* fits of the impedance measurements on the monolayers for both preparation solvents proved to be of high quality (see Figure 31).

In addition, the determined average electron transfer rates of 6250 s^{-1} (see Table 8 for data of individual measurements) for the monolayers prepared in ethanol and 5550 s^{-1} (see Table 8 for data of individual measurements) for the monolayers prepared in tetrahydrofuran are also identical within the experimental error and closely match the literature value ($4700 \pm 900 \text{ s}^{-1}$).^[137] This literature value can be considered very accurate because it was determined for a monolayer where the reference molecule had been diluted with alkyl thiols, and the measurements were conducted in aqueous media. Especially under such conditions, the acquisition of electron transfer rates by impedance measurements have been proven to give very reliable results for ferrocene terminated alkylthiols in numerous studies.^{[110-112, 134,}

136-139, 143, 149, 150]

4.2.6 ELECTROCHEMICAL CHARACTERIZATION

Within this section, the detailed characteristics of the electrochemical measurement data of the monolayers **M_A**, **M_B** and **M_C** prepared with the target molecules **A**, **B** and **C** are discussed on the basis of examples. Thereafter, the average electrochemical characterization data for each type of monolayer is given and interpreted. To ensure high quality data, in rare cases monolayers on electrodes showing surface inhomogeneities, with an insufficient surface coverage of less than $3.0 \times 10^{-10} \text{ mol} \times \text{cm}^{-2}$ or where a potential drift of more than 20 mV occurred during the impedance measurements were excluded to avoid contamination by possibly unreliable data (details in Sections 4.2.1-4.2.4).

Photos of the self-made electrodes used to prepare example monolayers **M_A**, **M_B** and **M_C** for which the characterization data is discussed are shown (see Figure 32). As depicted, the electrodes can be approximated as being spherical and their surfaces are free of macroscopic inhomogeneities.

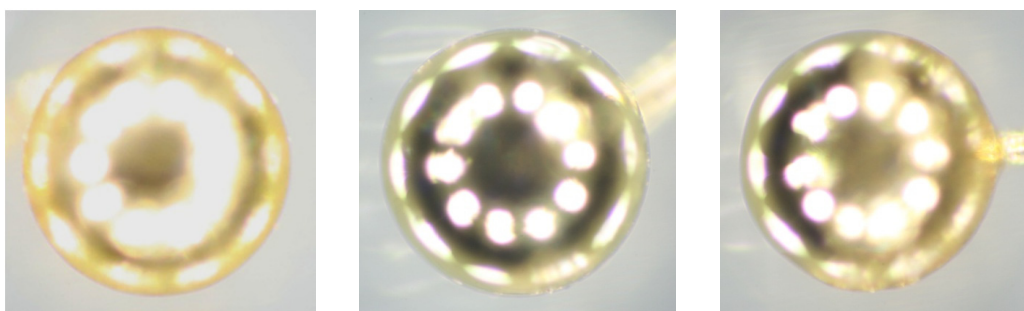


Figure 32. Photo of the self-made gold electrodes used to prepare the example **M_A** (left, $r = 252 \mu\text{m}$), **M_B** (middle, $r = 270 \mu\text{m}$) and **M_C** (right, $r = 270 \mu\text{m}$).

The shapes of the cyclic voltammograms (see Figures 33, 34 and 35) conducted on the example monolayers are characteristic for each type of monolayer. The detected peak separation of the redox waves in the first oxidation in the cyclic voltammograms of the example monolayers are 2 mV (**M_A**), 7 mV (**M_B**) and 5 mV (**M_C**), and are very close to the ideal value of 0 mV.^[143, 158] The bell shapes of redox waves in the cyclic voltammograms conducted on **M_B** and **M_C** are essentially those of ideal redox active monolayers.^[143, 158] The average full width at half-maximum (FWHM) of the cathodic and anodic peaks after correction for residual currents amount to 87 mV for **M_B** and 101 mV for **M_C** and are within the range of the ideal value of 90.6 mV ^[159]. These characteristics are a sign for a very high

degree of order of the monolayers.^[143, 158, 160, 161] However, it is pointless to determine FWHM in the cyclic voltammogram of **M_A** since the oxidation peak and, albeit to a lesser extent, the reduction peak is broadened towards higher potentials (see Figure 33). This broadening somewhat resembles the one observed in the monolayers prepared with the reference molecule (see Figure 20 in Section 4.2.2). Such unusual shapes of the cyclic voltammograms are typical of monolayers prepared from pure or only weakly diluted ferrocene terminated molecules.^[115, 125, 157] They are probably a result of the very dense packing of the ferrocene redox centers in the monolayer. Suggestions regarding the origin comprise steric crowding of the ferrocene,^[162] different solvent environments of the ferrocene units in different regions of the monolayer,^[163] double layer effects^[144, 164, 165] and electrostatic effects^{[166, 167], [125]}. In the present case of **M_A**, electrostatic effects are a very probable explanation for the broadening. During the oxidation in the cyclic voltammogram, more and more ferrocene centers become oxidized. This amassment of positive charges in an extremely dense packing affects the neighboring neutral ferrocene groups through electrostatic interaction, making it harder and harder to oxidize these remaining neutral ferrocene centers. This results in higher oxidation potentials of these ferrocene units, thus broadening the oxidation peak towards higher potentials.^[125] During the following reduction, the opposite effect can be observed, meaning that in the proximity of positive charges, it becomes easier to reduce the ferrocene units and as a result broadening the reduction peak towards higher potentials. However, this effect is not as strong as the one occurring in the oxidation wave, which might originate from spatial reorganization of the charged ferrocene groups due to the electrostatic forces within the monolayer. This rearrangement of the oxidized ferrocene units increases the distance of the positive charges thereby minimizing the electrostatic forces and thus weakening the broadening effect. Such an origin is supported by the fact that with each consecutive impedance measurement conducted on **M_A**, where redox centers are degenerating while the structural integrity is left mostly intact (see Section 4.2.2), this effect decreases more and more. This manifests itself in the shape of the cyclic voltammograms (see Figure 36), which show less broadening and thus more resemble those of **M_B** (see Figure 34) or **M_C** (see Figure 35). The reason for **M_B** and **M_C** not showing the same effect is probably their lower mean surface coverage (see Table 8), which is a sign for looser packing of the terminating ferrocene redox centers that weakens the electrostatic interaction between them. This lower mean surface coverage is most certainly a result of the substituents attached to the bridges of these molecules filling space in the monolayers.

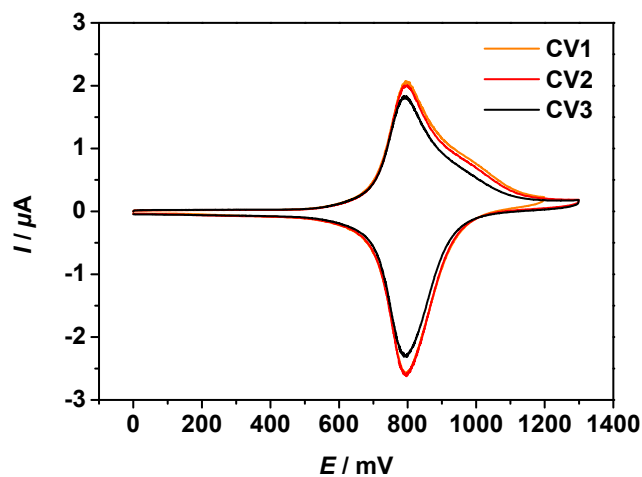


Figure 33. Cyclic voltammograms of the example M_A recorded with a scan rate of 1.00 V s^{-1} in tetrabutylammonium hexafluorophosphate in acetonitrile (0.5 M) before (CV1 and CV2) and after (CV3) the first impedance measurement.

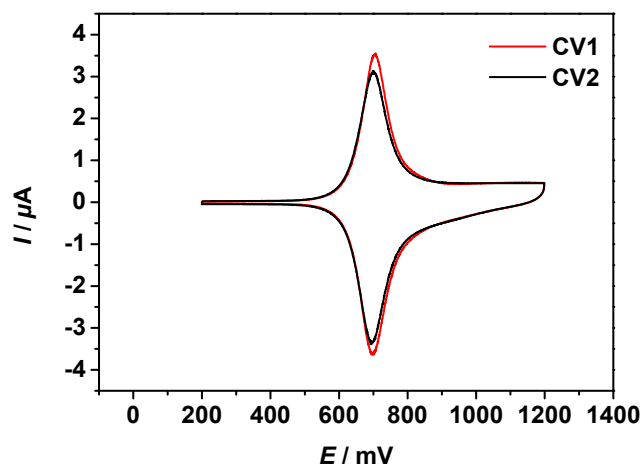


Figure 34. Cyclic voltammograms of the example M_B recorded with a scan rate of 1.00 V s^{-1} in tetrabutylammonium hexafluorophosphate in acetonitrile (0.5 M) before (CV1) and after (CV2) the first impedance measurement.

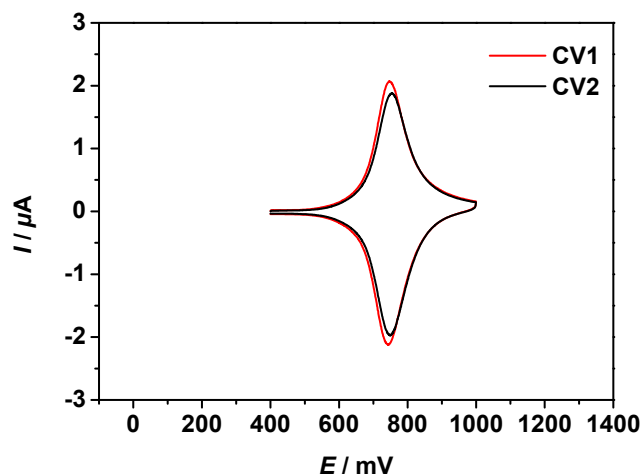


Figure 35. Cyclic voltammograms of the example M_C recorded with a scan rate of 1.00 V s^{-1} in tetrabutylammonium hexafluorophosphate in acetonitrile (0.5 M) before (CV1) and after (CV2) the first impedance measurement.

In the cyclic voltammograms of M_B (see CV1 in Figure 37) one would, due to the close proximity of the half-wave potential determined by cyclic voltammetry of the fully solvated subunits (see Section 4.1.5), expect to observe the redox process of the bridge unit. However, as stated before (see Section 4.2.1), the redox waves of the bridge unit could not be detected in monolayers of dense coverage. The alteration of redox waves in cyclic voltammograms of redox centers buried within monolayers has been investigated in several studies.^[143-146, 163, 168] These investigations show that, if the redox centers are surrounded by alkyl chains within monolayers, it leads to a shift of the half-wave potential to higher values, which is accompanied by an increase of the full width at half maximum of the redox waves. The shift can be explained by the non-polar environment surrounding the redox centers in monolayers of high density, which hampers stabilization of the oxidized redox centers by preventing the intrusion of polar solvents and counter ions from the electrolyte solution. The broadening is believed to be an effect of the varying microenvironments of each bridge redox center created by the different distances to the counter ions and solvent molecules of the electrolyte solution. Furthermore, within the monolayer of M_B additional broadening might arise from electrostatic effects from neighboring oxidized redox centers similar to those in M_A . Thus, the invisibility of the bridge redox processes in M_B , aside from a slightly increased current at higher potentials during the voltammetric scan, can be assigned to the mentioned effects. However, such near complete disappearance of the signals has, to the best knowledge of the investigator, never been observed in the literature before and is probably a result of the formation of an extremely highly ordered dense monolayer. Especially the first

effect is supported by the partial unveiling of the masked redox process after several impedance scans (see CV2 in Figure 37).^[143-146, 163, 168]

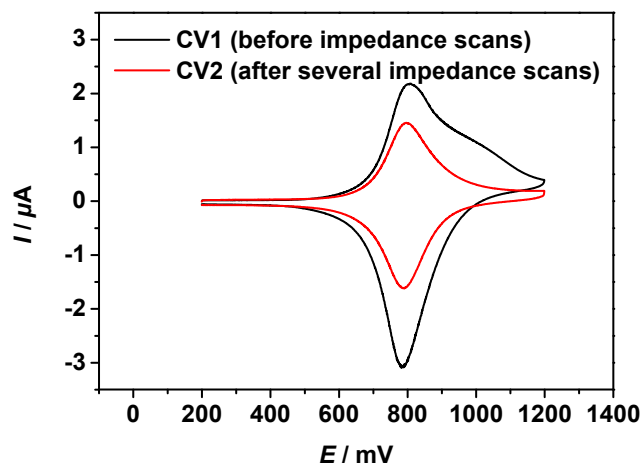


Figure 36. Cyclic voltammograms of the example M_A recorded with a scan rate of 1.00 V s^{-1} in tetrabutylammonium hexafluorophosphate in acetonitrile (0.5 M) before (CV1) and after (CV2) several impedance scans.

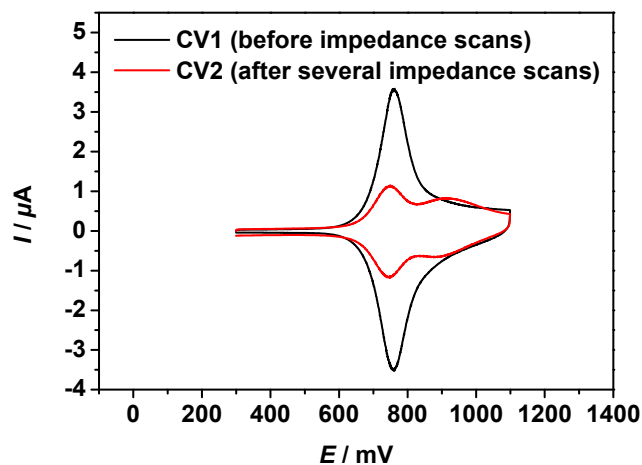


Figure 37. Cyclic voltammograms of M_B recorded with a scan rate of 1.00 V s^{-1} in tetrabutylammonium hexafluorophosphate in acetonitrile (0.5 M) before (CV1) and after (CV2) several impedance scans.

The data acquired during the impedance measurements of all the example monolayers prepared from the three target molecules was analyzed following the adapted protocol (see Section 4.2.3).

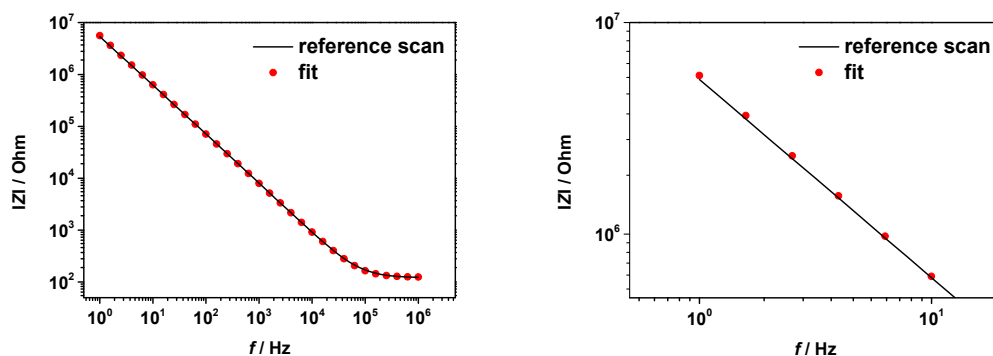


Figure 38. Fit of the Bode Plot of the first reference scan of example M_A recorded in tetrabutylammonium hexafluorophosphate in acetonitrile (0.5 M) (10 frequency points per decade). For clarity, only every second data point of the fit is shown.

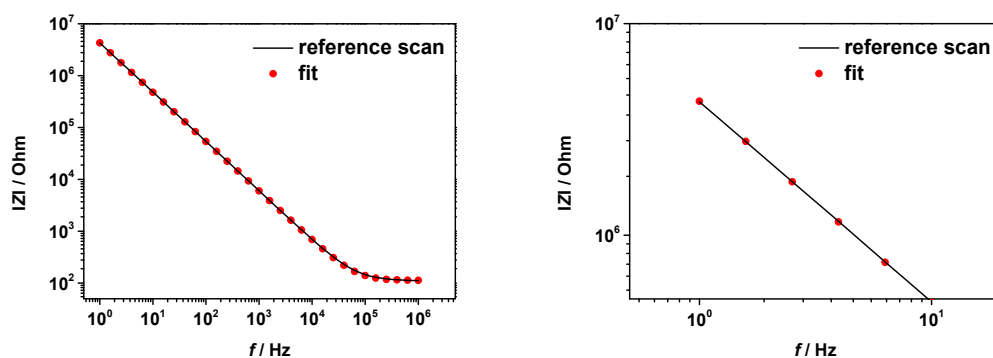


Figure 39. Fit of the Bode Plot of the first reference scan of the example M_B recorded in tetrabutylammonium hexafluorophosphate in acetonitrile (0.5 M) (10 frequency points per decade). For clarity, only every second data point of the fit is shown.

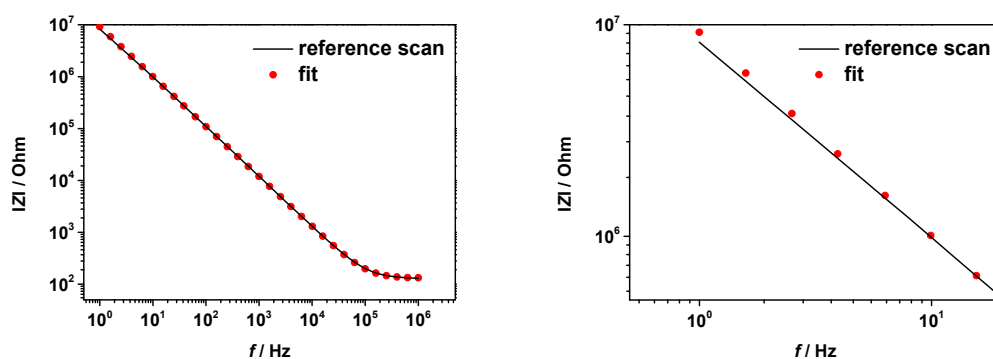


Figure 40. Fit of the Bode Plot of the first reference scan of the example M_C recorded in tetrabutylammonium hexafluorophosphate in acetonitrile (0.5 M) (10 frequency points per decade). For clarity, only every second data point of the fit is shown.

Regarding the Bode plots of the reference scans, all could be fitted with the electrical response of the reference equivalent circuit (see Figure 31 in Section 4.2.3) very well (see Figures 38, 39 and 40). In each Bode plot, the modulus of the impedance shows the expected constant slope in the mid-frequency region, and therefore, the values of the constant phase element could be readily determined. However, independent of the type of monolayer, in some cases, close inspection revealed very slight deviations from the fit in the low frequency region (see Figures 38, 39 and 40), which probably originates from residual redox processes (see Section 4.2.4). Therefore, in these cases, it was crucial to exclude the deviating frequency region when determining the values of the constant phase element. Furthermore, in all Bode plots, the modulus of the impedance approaches the expected plateau in the high frequency region (see Section 4.2.3). As a result, at the maximum frequency measured (1 MHz), the uncompensated resistance could be approximated as being equal to the modulus of the impedance.

However, as expected (see Section 4.2.3), all the Bode plots show a small deviation from the response of the equivalent circuit in the high- and mid-frequency region (see Figures 41, 42 and 43 which makes the determination of the charge transfer resistance highly inaccurate. Therefore, according to the protocol (see Section 4.2.3), the following technique developed by *Creager et al.* was employed.

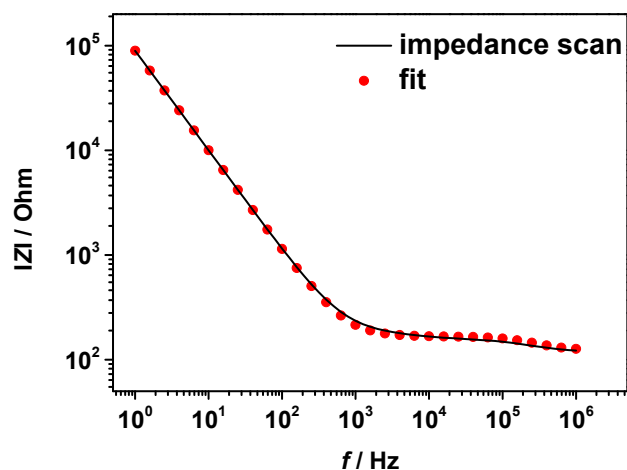


Figure 41. Fitted Bode Plot of the first impedance scan of the example **M_A** recorded in tetrabutylammonium hexafluorophosphate in acetonitrile (0.5 M) (10 frequency points per decade). For clarity, only every second data point of the fit is shown.

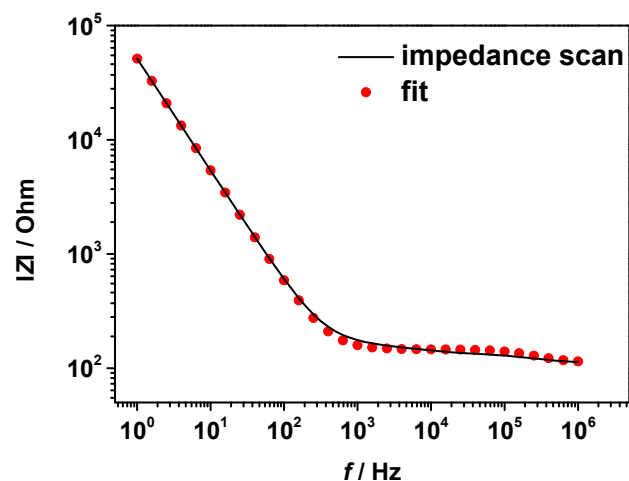


Figure 42. Fitted Bode Plot of the first impedance scan of the example M_B recorded in tetrabutylammonium hexafluorophosphate in acetonitrile (0.5 M) (10 frequency points per decade). For clarity, only every second data point of the fit is shown.

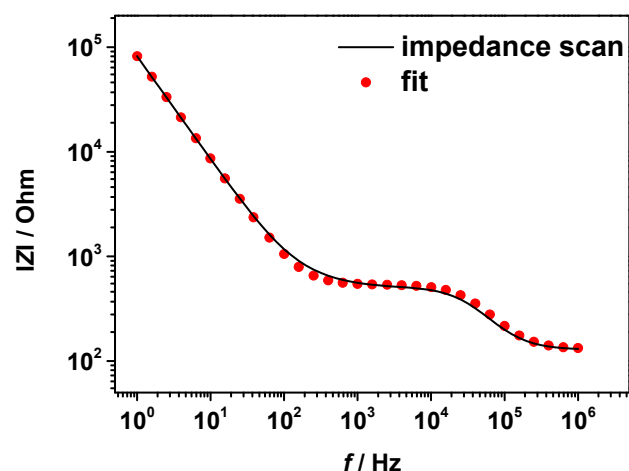


Figure 43. Fitted Bode Plot of the first impedance scan of the example M_C recorded in tetrabutylammonium hexafluorophosphate in acetonitrile (0.5 M) (10 frequency points per decade). For clarity, only every second data point of the fit is shown.

The frequency dependence of the *ratio* of the moduli of the impedances from the impedance and the reference scans conducted on all the example monolayers were plotted (see Figures 44, 45 and 46). As expected (see Section 4.2.3), the non-ideal effects in the Bode plots canceled out and the value of the charge transfer resistance and therefore the electron transfer rate, which is mainly dependent on the point of inflection of the slope in the mid-frequency region, could be determined with high accuracy.

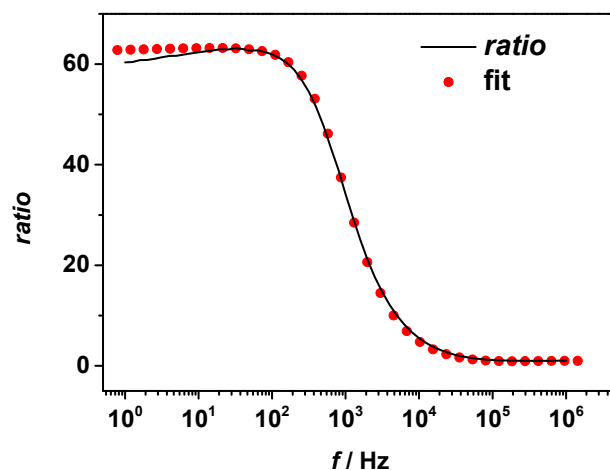


Figure 44. Fitted $ratio$ ($= |Z_{ref}|/|Z_{imp}|$) of the first impedance measurement on example M_A measured in tetrabutylammonium hexafluorophosphate in acetonitrile (0.5 M) (10 frequency points per decade).

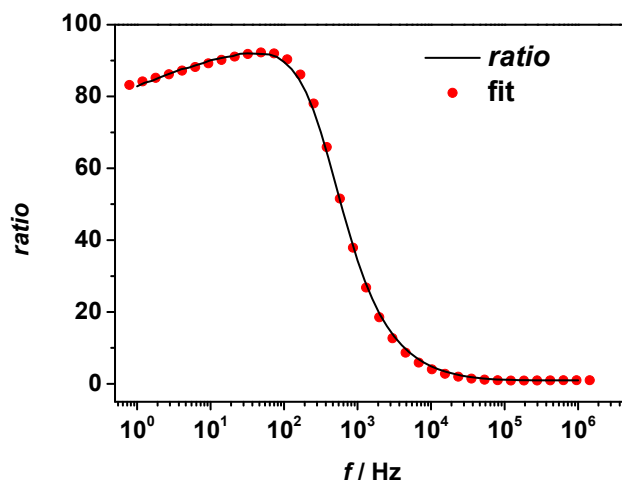


Figure 45. Fitted $ratio$ ($= |Z_{ref}|/|Z_{imp}|$) of the first impedance measurement on example M_B measured in tetrabutylammonium hexafluorophosphate in acetonitrile (0.5 M) (10 frequency points per decade).

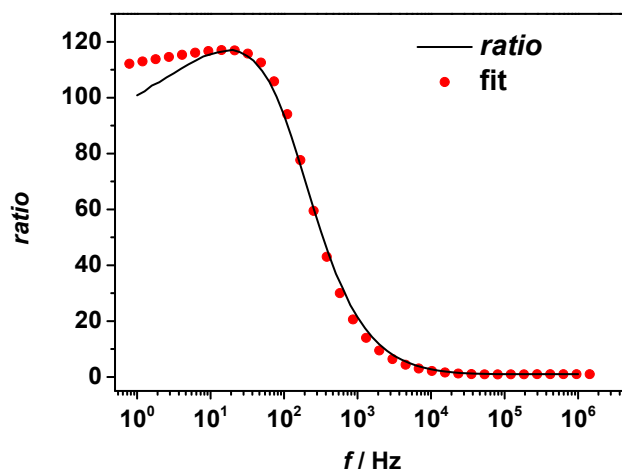


Figure 46. Fitted *ratio* ($= |Z_{\text{ref}}|/|Z_{\text{imp}}|$) of the first impedance measurement on example **M_C** measured in tetrabutylammonium hexafluorophosphate in acetonitrile (0.5 M) (10 frequency points per decade).

However, it should be noted that the plotted *ratio* shows a slightly smaller slope than those of the fit in the mid-frequency region. This slightly smaller slope can probably be traced back to the fact, that in an actual monolayer, one always deals with a distribution of different electron transfer rates due to the varying microenvironment of each molecule in the monolayer.^[169] Nevertheless, this effect is more pronounced in the literature,^[110-112, 134, 136-138, 143, 149, 170] and therefore, the data presented here can be considered to be of exceptional quality, especially if taking into account the tightly logarithmically spaced frequency points (10 per decade) with no apparent scattering of the moduli of the impedance measured.

Furthermore, in the fits of the examples **M_A** and **M_C**, a deviation occurred in the low frequency region. The magnitude of this deviation is not typical for the choice of molecule from which the monolayer was prepared. This non-ideal behavior has so far only been assigned to advancing degeneration of the redox centers leading to a stronger rising of the impedance while lowering the frequency during the impedance scans.^[112] In the present study, this effect, which might be enhanced by potential drift during impedance measurements, is accounted for by determining the exponential value of the constant phase element of the electron transfer capacitance in advance. This interpretation is, however, contradicted by the fact that these deviations during the measurement were sometimes smaller even if substantially more of the redox centers degraded or the potential drift was higher (see Figures 47 and 48).

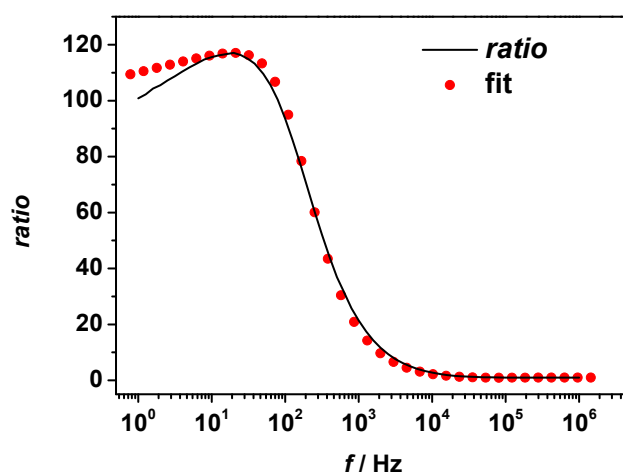


Figure 47. Fitted $ratio$ ($= |Z_{ref}|/|Z_{imp}|$) of an impedance measurement on a monolayer prepared with the thiol of **C** measured in tetrabutylammonium hexafluorophosphate in acetonitrile (0.5 M) (10 frequency points per decade) where only little of the redox centers degraded (7 %) and low potential drift (6 mV) occurred during the impedance measurement.

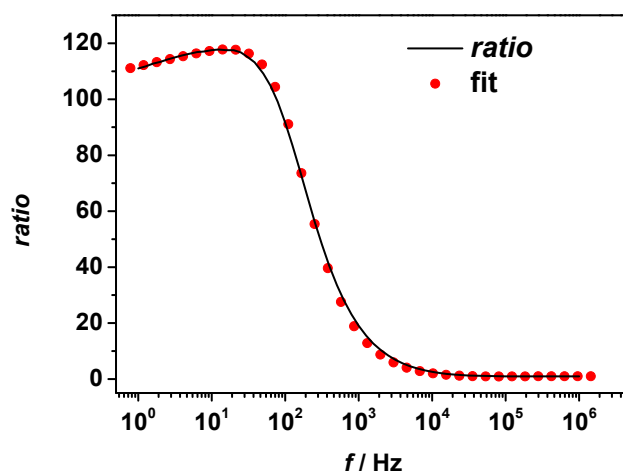


Figure 48. Fitted $ratio$ ($= |Z_{ref}|/|Z_{imp}|$) of an impedance measurement on a monolayer prepared with the thiol of molecule **C** measured in tetrabutylammonium hexafluorophosphate in acetonitrile (0.5 M) where more of the redox centers degraded (16 %) and a higher potential drift (11 mV) occurred during the impedance measurement.

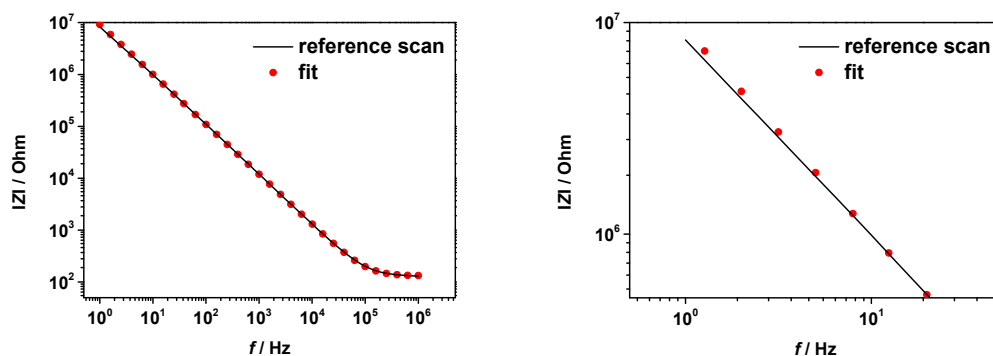


Figure 49. Fitted Bode Plot of the reference scan of a monolayer prepared with **C** recorded in (0.5 M) tetrabutylammonium hexafluorophosphate in acetonitrile (10 frequency points per decade) where only little of the redox centers degraded (7 %) and low potential drift (6 mV) occurred during the impedance measurement. For clarity, only every second data point of the fit is shown.

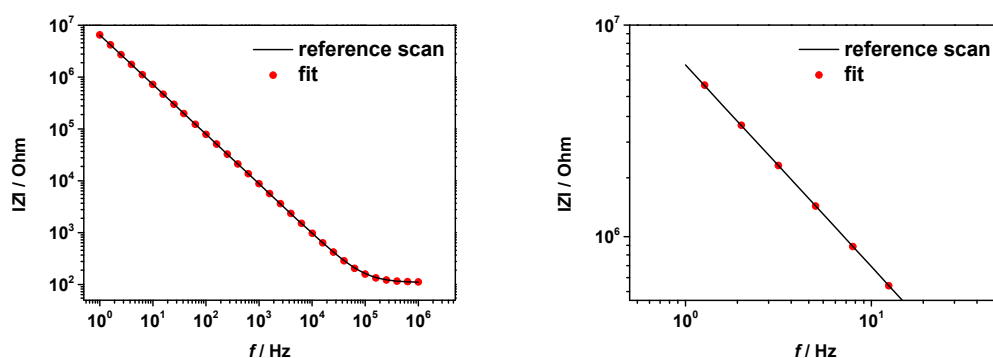


Figure 50. Fitted Bode Plot of the reference scan of a monolayer prepared with **C** recorded in (0.5 M) tetrabutylammonium hexafluorophosphate in acetonitrile (10 frequency points per decade) where more of the redox centers degraded (16 %) and a higher potential drift (11 mV) occurred during the impedance measurement. For clarity, only every second data point of the fit is shown.

Within this study, the deviation in the low frequency region could be traced back to the Bode Plots of the corresponding reference scans deviating in the low frequency region from the simulated response of the reference equivalent circuit (see Figures 49 and 50). Therefore, these deviations might be assigned to residual redox processes during the reference scans (see Section 4.2.4). However, it was ensured, by following the adapted protocol of data

analysis (see 4.2.3), that its occurrence did not contaminate the measurement results. As mentioned (see 4.2.3), this was realized by excluding these regions from the fit during the analysis of the Bode plot and making the fit of this region in the plot of the ratio obsolete due to the predetermination of all the values of the constant phase elements from the Bode plots.

Table 9. Mean surface coverage (Γ) and mean electron transfer rate (k_{ET}) of the monolayers prepared from the different molecules.

molecule	Γ $\times 10^{-10} / \text{mol} \times \text{cm}^{-2}$	k_{ET} $/ \text{s}^{-1}$
A	4.49 \pm 0.29	4160 \pm 650
B	3.57 \pm 0.11	2540 \pm 370
C	3.65 \pm 0.36	613 \pm 201

Finally, from the individual measurement results which show low dispersion (see Tables 10, 11 and 12) arithmetic means of the surface coverages and electron transfer rates of the monolayers prepared from the different target molecules were calculated (see Table 9). For the determination of the average surface coverage, the first cyclic voltammogram conducted on each monolayer was used. The average electron transfer rates were acquired from the first and, if determined, the second electron transfer rate of all the monolayers prepared with a certain target molecule. These average surface coverages are all close to the ideal value of $4.5 \times 10^{-10} \text{ mol} \times \text{cm}^{-2}$ of the densest packing of ferrocene on a gold surface.^[115] The values of M_B and M_C are slightly lower than the one for M_A , which can probably be assigned to the substituents on their bridge units requiring space within the monolayers.

The average electron transfer rate of M_A is slightly higher than the one of M_B , and both are higher than the one of M_C (see Table 9). Although no such monolayers have been studied in literature, some indications concerning the validity of the results can be found. In detail, since 5 of the 23 units which link the ferrocene head group to the thiol anchor group in M_A , M_B and M_C are saturated methylene units and the transfer rate always decreases if additional units are attached to the molecular backbones, the transfer rate should be significantly lower than through backbones with 5 saturated methylene units. For such monolayers, *Creager*^[114] determined an electron transfer rate of $1.6 \times 10^7 \text{ s}^{-1}$ and *Hsu*^[171] calculated an electron transfer rate of $1.6 \times 10^6 \text{ s}^{-1}$, which corresponds well to the rate of $1.6 \times 10^6 \text{ s}^{-1}$ found by *Smalley*.^[172]

Furthermore, if ignoring possible effects of the oxidized bridge state alignment, the electron transfer rates of monolayers **M_A**, **M_B** and **M_C** should be lower than $6 \times 10^4 \text{ s}^{-1}$ as has been determined by *Creager* for 24 unsaturated carbon units.^[173] However, when taking into account the anticipated energetic alignment of the bridge states, the charge transfer rate of **M_B** should be several orders of magnitude higher than those of **M_A**, which in turn should exceed the one of **M_C**.^[75-77, 105, 106] In detail, the half-wave potentials determined for the fully solvated subunits **A₁**, **B₃**, **C₁** and **F₂** predict the oxidized bridge state to be very close to the oxidized state of the donor in **M_B** and far above in **M_A** and even further beyond in **M_C**. Due to the close proximity in **M_B**, one would expect the more effective hopping mechanism to dominate in this monolayer, which should result in a very high charge transfer rate. Based on the larger energy gaps, the less effective superexchange mechanism should dominate in **M_A** and **M_C**. Furthermore, in **M_C** the larger energy gap should lead to a higher tunneling barrier and therefore an even slower charge transfer rate than in **M_A**. However, the charge transfer rate is clearly not several orders of magnitude higher in **M_B** than in **M_A** or **M_C**. In conclusion, in sharp contrast to the expected behavior, due to the similar charge transfer rates, the superexchange process is assumed to be dominating not only in **M_A** and **M_C** but also in **M_B**. This result can probably be explained by the oxidized bridge states being shifted towards higher potentials and broadened when being embedded within the very dense monolayers in contrast to those of the fully solvated subunits. These shifts probably originate from the microenvironments of the bridge units, including the presence of counter ions and polar solvent molecules as well as intermolecular electrostatic effects. This assumption is supported by the shape of the cyclic voltammograms conducted on **M_B** (see above). In summary, classic cyclic voltammetry of solvated redox centers is an inadequate tool to predict the energetics of redox centers embedded deep within dense monolayers. Nevertheless, even when shifted, the energetic order of the oxidized bridge states predicted by the half-wave potentials of the solvated subunits should lead to a moderately decreasing charge transfer rate due to the resulting decreased tunneling barrier from **M_B** over **M_A** to **M_C**. A reason for the charge transfer rate in **M_A** in fact being slightly higher than in **M_B** might be found in the electrostatic interference of the terminal redox centers in **M_A** as pointed out in the discussion of the cyclic voltammogram conducted on **M_A**(see above).

Table 10. Measurement number (N), immersion times (t_{imm}) and surface area (A) of the electrodes used for the monolayer preparation, average transferred charge during oxidation and reduction during a voltammetric cycle (Q_{CV}), uncompensated resistance (R_u) of the measurement cell, surface coverage (Γ) and charge transfer rates (k_{ET}) of the monolayers prepared with molecule **A**.

monolayer	N	t_{imm} / days	A / mm ²	Q_{CV} / nC	R_u	Γ $\times 10^{-10}$ / mol \times cm ⁻²	k_{ET} / s ⁻¹
M_{A2}	1 st	7	11.3	474	102	4.34	3300
	2 nd	7	11.3	369	104	3.38	3100
M_{A3}	2 nd	3	10.4	340	119	3.40	4800
M_{A4}	1 st	3	10.7	425	118	4.12	5200
	2 nd	3	10.7	340	128	3.30	4900
M_{A5}	1 st	3	9.18	421	123	4.75	4000
	2 nd	3	9.18	359	121	4.05	4900
M_{A6}	1 st	8	8.75	356	117	4.22	4900
	2 nd	8	8.75	320	119	3.79	5100
M_{A7}	1 st	8	10.6	416	114	4.06	4600
	2 nd	8	10.6	369	117	3.60	4500
M_{A8}	1 st	1	11.5	541	113	4.88	4100
	2 nd	1	11.5	456	115	4.11	4000
M_{A9}	1 st	1	11.7	549	102	4.88	3700
	2 nd	1	11.7	403	104	3.58	3100
M_{A10}	1 st	2	12.1	540	106	4.64	4100

monolayer	N	t_{imm} / days	A_{real} / mm^2	Q_{cv} / nC	R_{u}	Γ $\times 10^{-10}$ / $\text{mol} \times \text{cm}^{-2}$	k_{ET} / s^{-1}
M_A11	1 st	2	10.1	445	111	4.58	4000
	2 nd	2	10.1	393	114	4.04	3900
M_A12	1 st	3	10.9	472	100	4.48	4000
	2 nd	3	10.9	378	103	3.58	3600
M_A13	1 st	7	12.2	530	108	4.49	3500

Table 11. Measurement number (N), immersion times (t_{imm}) and surface area (A) of the electrodes used for the monolayer preparation, average transferred charge during oxidation and reduction during a voltammetric cycle (Q_{CV}), uncompensated resistance (R_u) of the measurement cell, surface coverage (Γ) and charge transfer rates (k_{ET}) of the monolayers prepared with molecule **B**.

monolayer	N	t_{imm} / days	A_{real} / mm^2	Q_{CV} / nC	R_u	Γ $\times 10^{-10}$ / $\text{mol} \times \text{cm}^{-2}$	k_{ET} / s^{-1}
M_B4	1 st	1	11.2	386	116	3.58	2000
	2 nd	1	11.2	333	116	3.09	2200
M_B5	1 st	2	10.5	358	112	3.52	2900
	2 nd	2	10.5	321	112	3.16	3100
M_B6	1 st	1	10.6	357	134	3.49	2300
	2 nd	1	10.6	322	136	3.14	2400
M_B7	1 st	2	11.2	404	112	3.75	2700
M_B8	1 st	2	10.7	361	108	3.50	2700

Table 12. Measurement number (N), immersion times (t_{imm}) and surface area (A) of the electrodes used for the monolayer preparation, average transferred charge during oxidation and reduction during a voltammetric cycle (Q_{CV}), uncompensated resistance (R_{u}) of the measurement cell, surface coverage (Γ) and charge transfer rates (k_{ET}) of the monolayers prepared with molecule **C**.

monolayer	Nr.	t_{imm} / days	A_{real} / mm ²	Q_{CV} / nC	R_{u}	Γ $\times 10^{-10}$ / mol \times cm ⁻²	k_{ET} / s ⁻¹
M_{C1}	1 st	1	7.58	267	131	3.65	490
	2 nd	1	7.58	248	131	3.39	480
M_{C3}	1 st	1	9.62	329	118	3.54	420
	2 nd	1	9.62	308	118	3.32	410
M_{C4}	1 st	1	8.60	273	139	3.29	840
	2 nd	1	8.60	244	139	2.94	830
M_{C5}	1 st	12	6.99	236	129	3.50	820
	2 nd	12	6.99	220	126	3.26	880
M_{C6}	1 st	12	9.84	404	111	4.25	430
	2 nd	12	9.84	338	106	3.56	530

5 SUMMARY AND CONCLUSION

Within this study, the influence of the energetics of the bridge unit on electron transfer (ET) in an electrode-bridge-donor system was investigated in a monolayer environment.

This was realized by specifically designing molecules containing ferrocene carboxylic ester donors and hydroquinone derivatives as bridge units and by using a gold electrode as acceptor. The energetics of the hydroquinone derivatives was adjusted by synthetically varying its substituents with the intention of changing the ET speed and mechanisms. Thereby the choice of the substituents was based on the literature known half-wave potentials of similar solvated hydroquinone derivatives and successively confirming them by conducting cyclic voltammetry on the actual bridge units synthesized. Then, a synthetic pathway, which accommodated the limited stability of the integrated terminal ferrocene carbon acid ester, was developed and successfully employed. This was followed by developing a procedure for preparing very dense and highly ordered monolayers from the target molecules on self-made gold microelectrodes. For the electrochemical investigations, several electrolyte solutions were tested until one, which ensured low susceptibility of the characterization setup towards slight changes of the electrode arrangement and measurement parameters while ensuring sufficient stability of the monolayers, was found. Furthermore, a new, commercially available potentiostat was established for the impedance measurements, which reduced the stress on the monolayers during the electrochemical characterizations in comparison to the equipment used in many former studies.^[110-112, 134, 136-139, 143, 149, 150] Regarding the determination of the ET rates, the data analysis protocol for the impedance measurements developed by *Creager et al.*^[111] was slightly adapted to allow analysis of the investigated monolayers despite their non-ideal behavior. In addition, the influence of changes to the electrical parameters of the impedance scans was investigated to minimize the error in the acquired data.

The electrochemical analysis of the monolayers by conducting cyclic voltammetry on **M_A**, **M_B** and **M_C** prepared from **A**, **B** and **C** confirmed the accomplishment of near ideal surface coverage and exceptionally high order. The surface coverages of **M_B** and **M_C** were, probably due to the space filled by the substituents on their bridge units, slightly lower than those of **M_A**. Furthermore, the shape of the redox waves of the ferrocene carboxylic acid redox center in the voltammogram of **M_A** showed a broadening and a shift towards higher potentials, which was assigned to electrostatic interference of oxidized terminal redox centers due to the especially dense packing. However, in the voltammogram of **M_B**, no sharp redox waves of the bridge units, as predicted by the analysis of preliminary monolayers of the same type with

low surface coverage, were present. This was attributed to the different and varying microenvironment of the bridge units deeply embedded within high-density monolayers. In detail, the different degree of shielding of each individual bridge unit from counter ions and solvent molecules probably resulted in the half wave potential being shifted to varying higher potentials, thus preventing the formation of sharp redox waves. In addition, electrostatic effects of oxidized bridge units could have enhanced this effect. This leads to the conclusion that the half-wave potentials of fully solvated bridge units determined by the cyclic voltammetry are not suited to predict the energetics of the oxidized bridge states embedded within the prepared high density monolayers.

Finally, the monolayers were successfully analyzed by impedance spectroscopy, which showed that the ET rate of \mathbf{M}_A is slightly higher than that of \mathbf{M}_B , and both are higher than that of \mathbf{M}_C . All of the values were, according to literature, in the expected region considering the length and degree of conjugation of the backbone. However, this picture is relativized when considering the targeted energetic alignment of the bridge units. According to the predicted very small energy gap between the oxidized states of the donor and the bridge unit in \mathbf{M}_B , a domination of the hopping mechanism should have led to a several orders of magnitude higher ET rate than in \mathbf{M}_A and \mathbf{M}_C . That this was not the case was attributed to the underestimation of the energy of the oxidized bridge states by utilizing cyclic voltammetry of the fully solvated bridge units (see above). According to the small differences of the ET rates the superexchange process was assumed to be the dominating mechanism not only in \mathbf{M}_A and \mathbf{M}_C but also in \mathbf{M}_B . However, even when shifted, the predicted energetic order of the oxidized bridge states should have led to a moderately decreasing ET rate from \mathbf{M}_B over \mathbf{M}_A to \mathbf{M}_C . The reason for the actual ET rate in \mathbf{M}_A being slightly higher than in \mathbf{M}_B might be found in the electrostatic interference of the terminal redox centers in \mathbf{M}_A (see above).

In conclusion, the targeted model systems were prepared and the ET rates were successfully determined. However, the problems concerning the relative energetic positioning of the involved states within the dense monolayers prevented the specific alteration of the speed and mechanism of the ET. The reason for this can be probably found in the high density and order of the monolayers prepared within this work, which hamper the intrusion of the components of the electrolyte solutions. This various degree of stabilization for the individual bridge units by counter ions and solvent molecules leads to the energy of the oxidized bridge states being splitted and shifted towards higher potentials with respect to fully solvated bridge units. This effect might be further enhanced by electrostatics of neighboring already oxidized bridge states. All this makes the predetermination of the energetics of the embedded bridge units extremely difficult. On one hand, this behavior can be considered an

obstacle and could probably be circumvented by designing molecules with bulky anchor groups and rigid molecular backbones, which would ensure perpendicular arrangement to the surface and full exposure of the bridge and terminal redox centers to the solvent molecules and counter ions. On the other hand, monolayers which completely embed integral redox centers might open up the opportunity to study the effects of microenvironments similar to those in solid state materials.

6 EXPERIMENTAL SECTION

6.1 PREPARATIVE AND ANALYTICAL METHODS

SYNTHESES

All reactions were carried out in standard glassware. All commercial compounds, including solvents, were purchased from Merck, Acros, Alfa Aesar, Avocado, Chempur, Sigma-Aldrich or ABCR and used without further purification. The reactions specified as being performed under nitrogen atmosphere were performed in air-free conditions (nitrogen, dried with Sicapent® from Merck, oxygen was removed by copper oxide catalyst PuriStar® R3-11 from BASF) using solvents freshly dried by standard procedures.^[174]

CHROMATOGRAPHY

Flash column chromatography was performed on standard silica gel, 40–63 μm (MERK or MACHEREY-NAGEL). High performance liquid chromatography was conducted on NUCLEOSIL® 120-5 (MACHEREY-NAGEL).

NMR SPECTRA

The ^1H and ^{13}C NMR spectra were recorded at the given temperature either on an AVANCE 400 FT-NMR spectrometer (^1H : 400 Mhz, ^{13}C : 101 MHz) or a BRUKER AVANCE DMX 600 FT-NMR Spectrometer (^1H : 600 Mhz, ^{13}C : 151 MHz). The residual signal of the respective solvent was used as the internal reference and the chemical shifts are given in ppm on a δ -scale. The coupling constants (J) are expressed in Hertz [Hz]. The apparent spin multiplicities are denoted as: s = singlet, d = doublet, dd = doublet of doublets, t = triplet, m = multiplet, AA' = $[\text{AB}]_2$ -spin-system ($>$ ppm), BB' = $[\text{AB}]_2$ -spin-system ($<$ ppm). NMR spectroscopic data are quoted as follows: chemical shift (multiplicity, coupling constants, number of protons, assignment). In case of not chemically equivalent carbons being isochronous the number of carbons, as indicated by the integrals of the carbons of the same type (primary secondary, tertiary and quaternary) is provided.

MASS SPECTROMETRY

The exact masses (ESI) were recorded on a Bruker Daltonik microTOF focus and a Bruker Daltonik autoflex II at the Institute of Organic Chemistry, University of Würzburg.

CYCLIC VOLTAMMETRY OF SOLUTES

All measurements were performed using a BAS CV-50 W electrochemical workstation or a GAMRY INSTRUMENTS potentiostat/galvanostat/ZRA model REFERENCE 600 workstation. All electrochemical experiments were performed using a platinum disk working electrode, an Ag/AgCl reference electrode and a helical platinum counter electrode. In all cases the ferrocene/ferrocenium (Fc/Fc⁺) redox couple was used as an internal reference. All experiments were performed in a sealed glass vessel under argon atmosphere (dried with Sicapent® from Merck and traces of oxygen removed with a copperoxide catalyst PuriStar® R3-11 from BASF). Acetonitrile or dichloromethane with tetrabutylammonium hexafluorophosphate as the supporting electrolyte were used. All solvents and supporting electrolytes used were purified, dried and/or degassed according to established procedures.^[174]

ELECTRODE AND MONOLAYER PREPARATION

Gold electrodes for monolayer coating were prepared by melting the end of a clean gold wire (0.05 mm, Premion®, 99.95%, Alfa Aesar) into a small spherical ball in a gas-air flame. After each gold ball was formed, it was held in the flame, brought to red heat and allowed to cool. This tempering process was repeated three times. The diameter of the spherical ball varied from one electrode to another, but was always within the range of 0.44 mm to 0.58 mm. The gold balls were always prepared directly before immersing them into the coating solution to form the monolayer.

In the general procedure, coating solutions for preparing monolayers with molecules possessing thiol anchor groups were always 0.5 mM in dry tetrahydrofuran. Monolayer formation was allowed to proceed for not less than 24 h, after which the electrodes were rinsed with the immersion solvent prior to mounting in the electrochemical cell. If *in situ* deprotection of acetyl protected thiols was employed, 2.5 to 3 equivalents of dried and degassed diethylamine were used. All monolayer preparations were conducted under inert gas conditions (nitrogen, dried with Sicapent® from Merck, traces of oxygen removed with

copper oxide catalyst PuriStar® R3-11 from BASF) and were carried out in flame-dried Schlenk vessels. All solvents used were purified, dried and/or degassed according to established procedures from the literature.^[174]

ELECTROCHEMICAL CHARACTERISATION OF MONOLAYERS

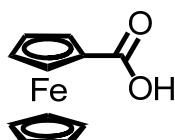
For the collection and analysis of impedance and cyclic voltammetry data on the monolayers, a GAMRY INSTRUMENTS potentiostat/galvanostat/ZRA model REFERENCE 600 including software GAMRY INSTRUMENTS FRAMEWORK and GAMRY Echem Analyst was employed.

The electrochemical experiments were conducted in a three-electrode configuration, unless stated otherwise, using 1 M tetrabutylammonium hexafluorophosphate supporting electrolyte in dry acetonitrile. A silver wire served as the pseudoreference electrode and a platinum coil as the counter electrode. The working electrode consisted of a gold ball covered by the monolayer to be investigated, which was immersed such that the gold ball was just below the surface of the electrolyte solution with as little of the gold wire as possible exposed to the solution. The pseudoreference electrode was positioned at a distance of 1 mm to the working electrode. Due to the volatility of the solvent and sensitivity of the set-up, the measurements could not be performed in an inert gas stream and were carried out under air. Even so, all solvents and supporting electrolytes used were purified, dried and/or degassed according to established procedures from the literature^[174] and the cell was flushed with argon (dried with Sicapent® from Merck and traces of oxygen removed with a copperoxide catalyst PuriStar® R3-11 from BASF) while setting it up. The redox current during the impedance scan was determined at the formal equilibrium redox potential of the monolayer, as determined in a cyclic voltammogram prior to each measurement. The background current was investigated at a value of 500 mV below the formal equilibrium redox potential.

6.2 SYNTHESIS

6.2.1 SYNTHESIS OF FERROCENE COMPOUND F3

Synthesis of F1



CAS:135364-39-2

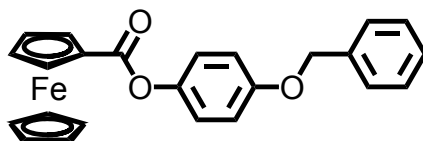
Synthesis similar to Lit.^[175]

Under nitrogen atmosphere, dry tetrahydrofuran (250 ml) was added to a mixture of ferrocene (6.75 g, 36.3 mmol) and potassium *tert*-butoxide (814 μ g, 7.26 mmol). A solution of *tert*-butyllithium (48.4 ml, 72.6 mmol, 1.50 M) in *n*-pentane was added slowly at -95°C during 30 min. The reaction mixture was stirred for 30 min at -95°C . A stream of carbon dioxide was bubbled through the reaction mixture for 15 min. Then the reaction mixture was allowed to warm to rt and hydrolyzed with water (5 ml). The solvents were evaporated *in vacuo*. Dichloromethane was added, the organic phase was washed with diluted acetic acid and water, dried over magnesium sulfate and the solvent was removed *in vacuo*. The product was dried in HV.

Yield: 7.68 g (33.4 mmol, 92 %) orange solid $\text{C}_{11}\text{H}_{10}\text{FeO}_2$ [230.0 g/mol].

$^1\text{H-NMR}$ (400 MHz, CDCl_3 , 300 K): δ / ppm = 4.88-4.84 (m, 2H, CH_{Fc}), 4.48-4.46 (m, 2H, CH_{Fc}), 4.26 (s, 5H, CH_{Fc}).

Synthesis of F2



CAS: /

Under nitrogen atmosphere dry dichloromethane (250 ml) was added to a mixture of compound **F1** (8.10 g, 35.2 mmol), 4-(benzyloxy)phenol (9.17 g, 45.8 mmol), triphenylphosphine (12.0 g, 45.8 mmol). Diisopropyl azodicarboxylate (8.99 ml, 45.8 mmol) was added slowly during 10 min. The reaction mixture was stirred for 5 d at rt. The reaction mixture was hydrolyzed with water and extracted with dichloromethane. The combined organic phases were dried over magnesium sulfate and the solvent was removed *in vacuo*. The residue was purified by flash column chromatography on silica gel (petroleum ether/dichloromethane 1:1) and by flash column chromatography on silica gel (petroleum ether/dichloromethane 2:1). The product was dried in HV.

Yield: 6.80 g (16.5 mmol, 47 %) orange solid C₂₄H₂₀FeO₃ [412.3 g/mol].

¹H-NMR (600 MHz, CDCl₃, 298.5 K): δ / ppm = 7.47-7.44 (m, 2H, CH_{phenyl}), 7.42-7.39 (m, 2H, CH_{phenyl}), 7.36-7.33 (m, 1H, CH_{phenyl}), 7.10 (AA', 2H, CH_{arom.}), 7.01 (BB', 2H, CH_{arom.}), 5.08 (s, 2H, CH₂), 4.97-4.95 (m, 2H, CH_{Fc}), 4.51-4.48 (m, 2H, CH_{Fc}), 4.30 (s, 5H, CH_{Fc}).

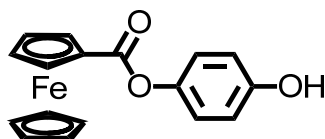
¹³C-NMR (151 MHz, CDCl₃, 298.5 K): δ / ppm = 170.8 (quart.), 156.4 (quart.), 144.7 (quart.), 137.0 (quart.), 128.8 (tert.), 128.2 (tert.), 127.6 (tert.), 122.6 (tert.), 115.6 (tert.), 72.0 (tert.), 70.7 (tert.), 70.6 (sec.), 70.3 (quart.), 70.1 (tert.).

High Resolution Mass (ESI): calc.: 410.08031 M⁺

found: 410.07910 M⁺

Δ : 2.95 ppm

Synthesis of F3



CAS: /

Under a nitrogen atmosphere, ethyl acetate (250 ml) was added to a mixture of **F2** (4.65 g, 11.3 mmol) and palladium on activated charcoal (1.20 g, 1.13 mmol, 10 %) suspended in acetic acid (2.50 ml). The reaction mixture was stirred for 3 d at rt under an atmosphere of 3 bar of hydrogen. The reaction mixture was filtered over celite and the solvents, including the side product, were removed *in vacuo*. The product was dried in HV.

Yield: 3.20 g (9.93 mmol, 88 %) orange solid C₁₇H₁₄FeO₃ [322.1 g/mol].

¹H-NMR (600 MHz, CDCl₃, 298.5 K): δ / ppm = 7.02 (AA', 2H, CH_{arom.}), 6.83 (BB', 2H, CH_{arom.}), 5.03–4.92 (—, 3H, CH_{Fc} and OH), 4.53–4.47 (m, 2H, CH_{Fc}), 4.30 (s, 5H, CH_{Fc}).

¹³C-NMR (151 MHz, CDCl₃, 298.5 K): δ / ppm = 171.2 (quart.), 153.3 (quart.), 144.5 (quart.), 122.8 (tert.), 116.2 (tert.), 72.1 (tert.), 70.8 (tert.), 70.15 (quart.), 70.10 (tert.).

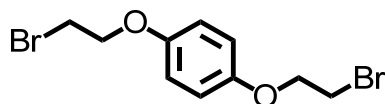
High Resolution Mass (ESI): calc.: 355.00276 (M+Cl)⁻

found: 355.00262 (M+Cl)⁻

Δ : 1.94 ppm

6.2.2 SYNTHESIS OF DIBROMIDE PRECURSOR OF A

Synthesis of A1



CAS: 5471-84-1.

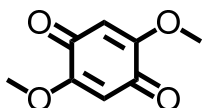
Under a nitrogen atmosphere, tetrahydrofuran (200 ml) was added to a mixture of 2,2'-(1,4-phenylenebis(oxy))diethanol^[131] (10.0 g, 50.5 mmol) and carbon tetrabromide (41.8 g, 126 mmol). Then triphenylphosphine (33.1 g, 126 mmol) was added slowly. The reaction mixture was stirred for 2 d at rt. The residue was purified by flash chromatography on silica gel (petroleum ether/dichloromethane 3:1). The product was dried in HV.

Yield: 7.00 g (21.5 mmol, 43 %) colorless solid C₁₀H₁₂Br₂O₂ [324.0 g/mol].

¹H-NMR (400 MHz, CDCl₃, 300 K): 6.86 (s, 4H, CH_{arom.}), 4.25 (t, ³J_H = 6.32, CH₂), 3.61 (t, ³J_H = 6.32, CH₂).

6.2.3 SYNTHESIS OF DIBROMIDE PRECURSOR OF B

Synthesis of B1

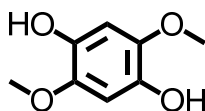


CAS: 53796-97-7.

Dry methanol (400 ml) and sulfuric acid (10.0 ml, 1.96 mol, 98% in water) were added to 2,5-dihydroxycyclohexa-2,5-diene-1,4-dione (26.6 g, 190 mmol). The suspension was heated under reflux conditions for 30 min. The reaction mixture was allowed to cool to rt and filtered. The residue was washed with cold methanol. The crude product (25.3 g, colorless solid) was dried in HV.

¹H-NMR (400 MHz, CDCl₃, 300.0 K): δ / ppm = 5.87 (s, 2H, CH_{arom.}), 3.85 (s, 6H, OCH₃).

Synthesis of B2

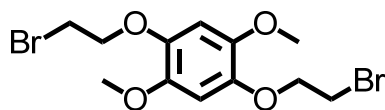


CAS: 13239-13-9.

Dichloromethane (200 ml) was added to crude 2,5-dimethoxycyclohexa-2,5-diene-1,4-dione (**B1**) (24.8 g, ca. 142 mmol). A solution of sodium hydrosulfite in water (300 ml, 638 mmol, 2.13 M) was added to the reaction mixture. The suspension was stirred for 30 min at rt. The organic phase was dried over magnesium sulfate. The solvent was removed *in vacuo*. The crude product (11.0 g, colorless solid) was dried in HV.

¹H-NMR (400 MHz, CDCl₃, 300.0 K): δ / ppm = 6.58 (s, 2H, CH_{arom.}), 5.20 (s, 2H, OH), 3.82 (s, 6H, OCH₃).

Synthesis of B3



CAS: /

Under a nitrogen atmosphere, dry acetonitrile (300 ml) was added to a mixture of crude 2,5-dimethoxybenzene-1,4-diol (**B2**) (11.0 g, ca. 54.9 mmol), potassium carbonate (38.0 g, 275 mmol), 12-crown-4 (1.45 g, 5.49 mmol) and 1,2-dibromoethane (243 g, 1.29 mol). The reaction mixture was stirred for 3 d under reflux conditions. The solvent was removed *in vacuo*. The residue was hydrolyzed with water and extracted with dichloromethane. The combined organic phases were dried over magnesium sulfate and the solvent was removed *in vacuo*. The residue was purified by flash chromatography on silica gel (dichloromethane/petroleum ether 2:1). The product was dried in HV.

Yield: 7.00 g (18.2 mmol, (ca. 33%) 10% over the last 3 steps) colorless solid C₁₂H₁₆Br₂O₄ [384.1 g/mol].

¹H-NMR (400 MHz, CDCl₃, 300 K): 6.67–6.63 (—, 2H, CH_{arom.}), 4.30 (t, ³J_H = 6.48, 4H, CH₂), 3.82 (s, 6H, CH₃), 3.62 (t, ³J_H = 6.52, 4H, CH₂).

¹³C-NMR (101 MHz, CDCl₃, 299.9 K): δ / ppm = 144.7 (quart.), 142.9 (quart.), 105.1 (tert.), 71.1 (sec.), 57.2 (prim.), 29.6 (sec.).

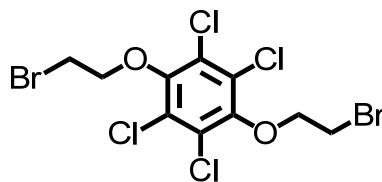
High Resolution Mass (ESI): calc.: 381.94099 M⁺

found: 381.94019 M⁺

Δ: 2.09 ppm

6.2.4 SYNTHESIS OF DIBROMIDE PRECURSOR OF C

Synthesis of C1



CAS: /

Under a nitrogen atmosphere, dry acetonitrile (300 ml) was added to a mixture of 2,3,5,6-tetrachlorobenzene-1,4-diol (12.5 g, 50.5 mmol) and potassium carbonate (35.1 g, 254 mmol). The reaction mixture was stirred for 2 d under reflux conditions. The solvent was removed *in vacuo*. The residue was hydrolyzed with water and extracted with dichloromethane. The combined organic phases were dried over magnesium sulfate and the solvent was removed *in vacuo*. The residue was purified by flash chromatography on silica gel (petroleum ether/dichloromethane 3:1). The product was dried in HV.

Yield: 12.3 g (26.6 mmol, 53 %) colorless solid C₁₀H₈Br₂Cl₄O₂ [461.8 g/mol].

¹H-NMR (400 MHz, CDCl₃, 300 K): 4.32 (t, ³J_H = 6.70, 4H, CH₂), 3.70 (t, ³J_H = 6.63, 4H, CH₂).

¹³C-NMR (101 MHz, CDCl₃, 300 K): δ / ppm = 149.3 (quart.), 127.9 (quart.), 73.0 (sec.), 28.7 (sec.).

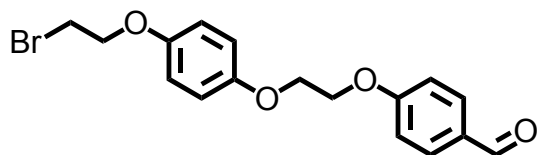
High Resolution Mass (EI): calc.: 457.76397 M⁺

found: 457.76368 M⁺

Δ : 0.63 ppm

6.2.5 SYNTHESIS OF A

Synthesis of A2



CAS: /

Under a nitrogen atmosphere, dry acetonitrile (150 ml) was added to a mixture of **A1** (8.00 g, 24.6 mmol), 4-hydroxybenzaldehyde (3.47 g, 28.4 mmol) and potassium carbonate (3.92 g, 28.4 mmol). The reaction mixture was stirred for 16 h under reflux conditions. The reaction mixture was hydrolyzed with water and extracted with dichloromethane. The combined organic phases were dried over magnesium sulfate and the solvent was removed *in vacuo*. The residue was purified by flash column chromatography on silica gel (gradient: dichloromethane/ethyl acetate 25:1 → 4:1). The product was dried in HV.

Yield: 3.35 g (9.17 mmol, 37 %) colorless solid C₁₇H₁₇BrO₄ [365.2 g/mol].

¹H-NMR (400 MHz, CDCl₃, 300 K): δ / ppm = 9.90 (s, 1H, C(O)H), 7.85 (AA', 2H, CH_{arom.}), 7.06 (BB', 2H, CH_{arom.}), 6.92–6.84 (—, 4H, CH_{arom.}), 4.42–4.36 (m, 2H, CH₂), 4.34–4.29 (m, 2H, CH₂), 4.25 (t, ³J_H = 6.32, 2H, CH₂), 3.61 (t, ³J_H = 6.32, 2H, CH₂).

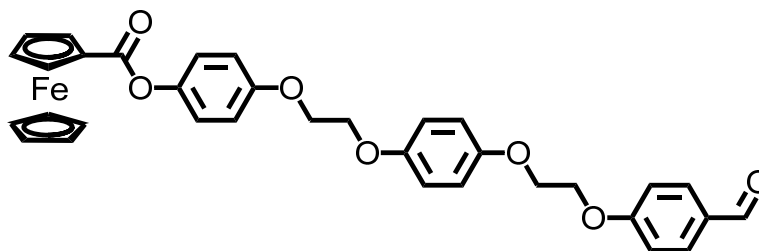
¹³C-NMR (101 MHz, CDCl₃, 300 K): δ / ppm = 190.9 (tert.), 163.8 (quart.), 153.4 (quart.), 152.9 (quart.), 132.1 (tert.), 130.4 (quart.), 116.3 (ter.), 116.0 (tert.), 115.1 (tert.), 68.9 (sec.), 67.2 (sec.), 67.1 (sec.), 29.4 (sec.).

High Resolution Mass (ESI): calc.: 365.03885 (M+H)⁺

found: 365,03813 (M+H)⁺

Δ : 1.96 ppm

Synthesis of A3



CAS: /

Under a nitrogen atmosphere, acetonitrile (500 ml) was added to a mixture of **F3** (3.03 g, 9.41 mmol), **A2** (3.44 g, 9.41 mmol) and potassium carbonate (1.95 g, 14.1 mmol). The reaction mixture was stirred for 2 d under reflux conditions. The solvent was removed *in vacuo*. The residue was purified by flash column chromatography on silica gel (gradient: dichloromethane → dichloromethane/ethyl acetate 20:1) and by flash column chromatography on silica gel (dichloromethane/ethyl acetate 40:1). The product was dried in HV.

Yield: 2.21 g (3.49 mmol, 39 %) orange solid C₃₄H₃₀FeO₇ [606.4 g/mol].

¹H-NMR (400 MHz, CDCl₃, 300 K): δ / ppm = 9.91 (s, 1H, C(O)H), 7.85 (AA', 2H, CH_{arom.}), 7.10 (AA', 2H, CH_{arom.}), 7.07 (AA', 2H, CH_{arom.}), 6.99 (BB', 2H, CH_{arom.}), 6.94-6.87 (m, 4H, CH_{arom.}), 4.97-4.94 (m, 2H, CH_{Fc}), 4.51-4.48 (m, 2H, CH_{Fc}), 4.42-4.37 (m, 2H, CH₂), 4.35-4.27 (—, 11H, CH₂ and CH_{Fc}).

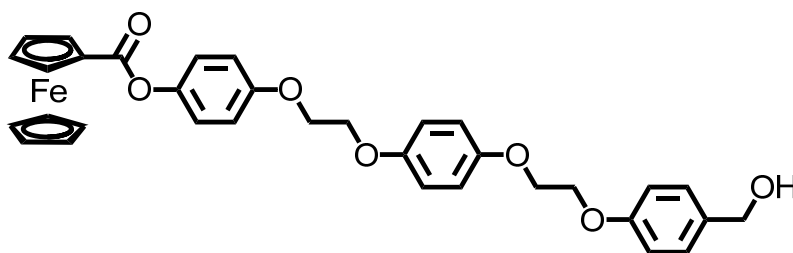
¹³C-NMR (101 MHz, CDCl₃, 300 K): δ / ppm = 190.9 (tert.), 170.8 (quart.), 163.8 (quart.), 156.4 (quart.), 153.5 (quart.), 153.1 (quart.), 144.9 (quart.), 132.1 (tert.), 130.4 (quart.), 122.7 (tert.), 116.05 (tert.), 115.99 (tert.), 115.6 (tert.), 115.1 (tert.), 72.0 (tert.), 70.8 (tert.), 70.3 (quart.), 70.1 (tert.) 67.4 (sec.) 67.3 (sec.) 67.2 (sec.) 67.1 (sec.).

High Resolution Mass (ESI): calc.: 604.13822 M⁺

found: 604.13877 M⁺

Δ : 0.81 ppm

Synthesis of A4



CAS: /

Under a nitrogen atmosphere, dry dichloromethane (10 ml) was added to a mixture of **A3** (1.00 g, 1.65 mmol) and sodium borohydride (47.0 mg, 1.24 mmol). Methanol (10ml) was added slowly within 15 min. The reaction mixture was stirred for 15 min at rt. The reaction mixture was quenched with acetic acid (10% in water). The organic phase was dried over magnesium sulfate, filtered over celite and the solvent was removed *in vacuo*. The product was dried in HV.

Yield: 824 mg (1.35 mmol, 82 %) orange solid C₃₄H₃₂FeO₇ [608.5 g/mol].

¹H-NMR (400 MHz, CDCl₃, 298.5 K): δ / ppm = 7.31 (AA', 2H, CH_{arom.}), 7.10 (AA', 2H, CH_{arom.}), 6.99 (BB', 2H, CH_{arom.}), 6.95 (BB', 2H, CH_{arom.}), 6.93-6.88 (—, 4H, CH_{arom.}), 4.98-4.93 (m, 2H, CH_{Fc}), 4.66-4.60 (m, 2H, CH₂), 4.52-4.48 (m, 2H, CH_{Fc}), 4.35-4.25 (—, 13 H, CH_{Fc} and CH₂).

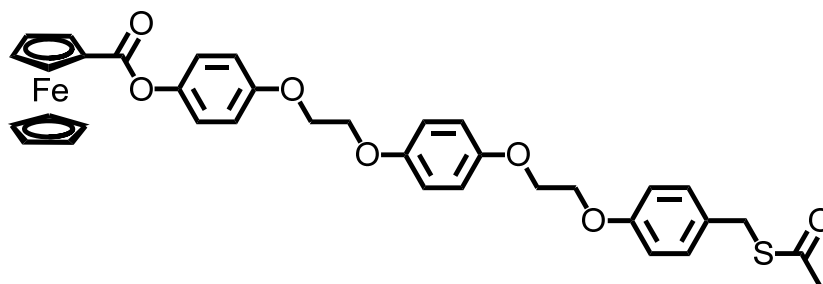
¹³C-NMR (101 MHz, CDCl₃, 298.5 K): δ / ppm = 170.8 (1C, quart.), 158.4 (1C, quart.), 156.3 (1C, quart.), 153.2 (2C, quart.), 144.8 (1C, quart.), 133.6 (1C, quart.), 128.8 (2C, tert.), 122.7 (2C, tert.), 115.9 (4C, tert.), 115.5 (2C, tert.), 114.9 (2C, tert.), 72.0 (2C, tert.), 70.8 (2C, tert.), 70.3 (1C, quart.), 70.1 (5C, tert.), 67.3 (2C, sec.), 67.2 (1C, sec.), 66.8 (1C, sec.), 65.2 (1C, sec.).

High Resolution Mass (ESI): calc.: 629.14364 [M+Na]⁺

found: 629.14364 [M+Na]⁺

Δ : 0.00 ppm

Synthesis of A



CAS: /

Under a nitrogen atmosphere, dry dichloromethane (100 ml) was added to a mixture of **A4** (300 mg, 493 μmol), triphenylphosphine (259 mg, 986 μmol) and thioacetic acid (280 μl , 3.94 mmol). Diisopropyl azodicarboxylate (194 μl , 986 μmol) was added slowly during 5 min. The reaction mixture was stirred for 6 d at rt. The solvents were removed *in vacuo*. The residue was purified by flash column chromatography on silica gel (dichloromethane). The product was dried in HV.

Yield: 42.0 mg (63.0 μmol , 13 %) orange solid $\text{C}_{36}\text{H}_{34}\text{FeO}_7\text{S}$ [666.6 g/mol].

$^1\text{H-NMR}$ (600 MHz, CDCl_3 , 298.6 K): δ / ppm = 7.21 (AA', 2H, $\text{CH}_{\text{arom.}}$), 7.10 (AA', 2H, $\text{CH}_{\text{arom.}}$), 6.99 (BB', 2H, $\text{CH}_{\text{arom.}}$), 6.93-6.89 (—, 4H, $\text{CH}_{\text{arom.}}$), 6.88 (BB', 2H, $\text{CH}_{\text{arom.}}$), 4.96-4.95 (m, 2H, CH_{Fc}), 4.50-4.48 (m, 2H, CH_{Fc}), 4.34-4.25 (—, 13H, CH_{Fc} and CH_2), 4.08 (s, 2H, CH_2), 2.34 (s, 3H, CH_3).

$^{13}\text{C-NMR}$: (151 MHz, CDCl_3 , 298.6 K): δ / ppm = 195.5 (quart.), 170.8 (quart.), 158.0 (quart.), 156.3 (quart.), 153.23 (quart.), 153.22 (quart.), 144.8 (quart.), 130.17 (quart.), 130.13 (tert.), 122.7 (tert.), 115.90 (tert.), 115.89 (tert.), 115.5 (tert.), 114.9 (tert.), 72.0 (tert.), 70.8 (tert.), 70.3 (quart.), 70.1 (tert.), 67.34 (sec.), 67.30 (sec.), 67.2 (sec.), 66.8 (sec.), 33.1 (sec.), 30.5 (prim.)

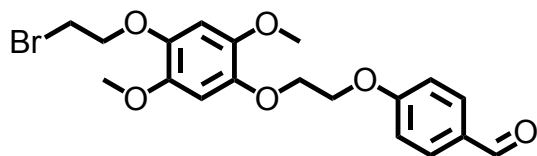
High Resolution Mass (ESI): calc.: 664.14149 M^+

found: 664,14113 M^+

Δ : 0.54 ppm

6.2.6 SYNTHESIS OF B

Synthesis of B4



CAS: /

Under a nitrogen atmosphere, dry acetonitrile (500 ml) was added to a mixture of 1,4-bis(2-bromoethoxy)-2,5-dimethoxybenzene (**B3**) (9.60 g, 25.0 mmol), 4-hydroxybenzaldehyde (3.36 g, 27.5 mmol) and potassium carbonate (4.84 g, 35.0 mmol). The reaction mixture was stirred for 16 h under reflux conditions. The solvent was removed *in vacuo*. The reaction mixture was hydrolyzed with water and extracted with dichloromethane. The combined organic phases were dried over magnesium sulfate and the solvent was removed *in vacuo*. The residue was purified by flash column chromatography on silica gel (gradient: dichloromethane/petroleum ether 3:1 → dichloromethane). The product was dried in HV.

Yield: 3.76 g (8.84 mmol, 35 %) colorless solid C₁₉H₂₁BrO₆ [425.3 g/mol].

¹H-NMR (400 MHz, CDCl₃, 300.0 K): δ / ppm = 9.90 (s, 1H, C(O)H), 7.85 (AA', 2H, CH_{arom.}), 7.05 (BB', 2H, CH_{arom.}), 6.69–6.64 (—, 2H, CH_{arom.}), 4.40–4.37 (—, 4H, CH₂), 4.30 (t, ³J_H = 6.51, 2H, CH₂), 3.80 (s, 6H, OCH₃), 3.62 (t, ³J_H = 6.51, 2H, CH₂).

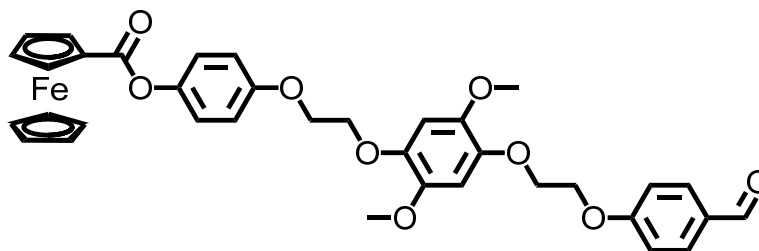
¹³C-NMR (101 MHz, CDCl₃, 300.0 K): δ / ppm = 190.9 (tert.), 163.8 (quart.), 144.62 (quart.), 144.59 (quart.), 143.4 (quart.), 142.7 (quart.), 132.1 (tert.), 130.4 (quart.), 115.1 (tert.), 105.1 (tert.), 104.8 (tert.), 71.1 (sec.), 69.4 (sec.), 67.3 (sec.), 57.2 (prim.), 57.1 (prim.), 29.6 (sec.).

High Resolution Mass (ESI): calc.: 447.04137 [M+Na]⁺

found: 447.04138 [M+Na]⁺

Δ : 0.02 ppm

Synthesis of B5



CAS: /

Under a nitrogen atmosphere, dry acetonitrile (300 ml) was added to a mixture of **B4** (2.30 g, 5.40 mmol), **F3** (1.74 g, 5.40 mmol) and potassium carbonate (1.12 g, 8.10 mmol). The reaction mixture was stirred for 2 d under reflux conditions. The solvent was removed *in vacuo*. The residue was purified by flash column chromatography on silica gel (dichloromethane/ethyl acetate 40:1). The product was dried in HV.

Yield: 2.39 g (3.59 mmol, 66 %) orange solid C₃₆H₃₄FeO₉ [666.5 g/mol].

¹H-NMR (600 MHz, CDCl₃, 298.5 K): δ / ppm = 9.91 (s, 1H, C(O)H), 7.85 (AA', 2H, CH_{arom.}), 7.09 (AA', 2H, CH_{arom.}), 7.06 (BB', 2H, CH_{arom.}), 6.98 (BB', 2H, CH_{arom.}), 6.72–6.67 (—, 2H, CH_{arom.}), 4.97–4.94 (m, 2H, CH_{Fc}), 4.51–4.48 (m, 2H, CH_{Fc}), 4.41–4.39 (m, 4H, CH₂), 4.38–4.29 (—, 4H, CH₂), 4.30 (s, 5H, CH_{Fc}), 3.800 (s, 3H, OCH₃), 3.796 (s, 3H, OCH₃).

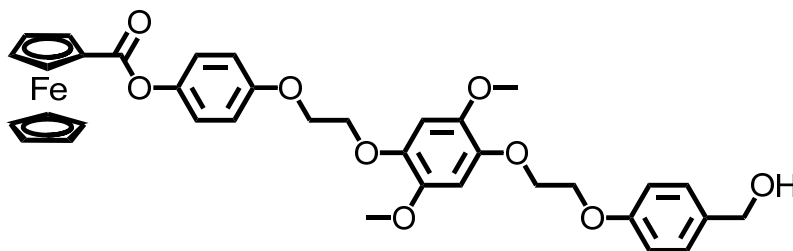
¹³C-NMR (151 MHz, CDCl₃, 298.5 K): δ / ppm = 190.9 (tert.), 170.8 (quart.), 163.8 (quart.), 156.3 (quart.), 144.8 (quart.), 144.5 (quart.), 144.3 (quart.), 143.3 (quart.), 142.7 (quart.), 132.1 (tert.), 130.3 (quart.), 122.7 (tert.), 115.4 (tert.), 115.1 (tert.), 104.6 (tert.), 104.2 (tert.), 72.0 (tert.), 70.8 (tert.), 70.2 (quart.), 70.1 (tert.), 69.5 (sec.), 69.4 (sec.), 67.3 (sec.), 67.2 (sec.), 57.1 (prim.), 57.0 (prim.).

High Resolution Mass (ESI): calc.: 689.14912 [M+Na]⁺

found: 689.14916 [M+Na]⁺

Δ : 0.06 ppm

Synthesis of B6



CAS: /

Under a nitrogen atmosphere, dry dichloromethane (60 ml) was added to a mixture of **B5** (760 mg, 1.14 mmol) and sodium borohydride (32.3 mg, 855 μmol). Methanol (6 ml) was added slowly within 15 min. The reaction mixture was stirred for 15 min at rt. The reaction mixture was quenched with acetic acid (10% in water). The organic phase was dried over magnesium sulfate, filtered over celite and the solvent was removed *in vacuo*. The residue was purified by recrystallization (acetone). The product was dried in HV.

Yield: 180 mg (269 μmol , 24 %) orange solid $\text{C}_{36}\text{H}_{36}\text{FeO}_9$ [668.5 g/mol].

$^1\text{H-NMR}$ (600 MHz, CDCl_3 , 298.5 K): δ / ppm = 7.29 (AA', 2H, $\text{CH}_{\text{arom.}}$), 7.09 (AA', 2H, $\text{CH}_{\text{arom.}}$), 6.98 (BB', 2H, $\text{CH}_{\text{arom.}}$), 6.94 (BB', 2H, $\text{CH}_{\text{arom.}}$), 6.71–6.69 (—, 2H, $\text{CH}_{\text{arom.}}$), 4.96–4.94 (m, 2H, CH_{Fc}), 4.64–4.61 (m, 2H, CH_2), 4.51–4.48 (m, 2H, CH_{Fc}), 4.38–4.34 (—, 4H, CH_2), 4.33–4.28 (s, 9 H, CH_{Fc} and CH_2), 3.81–3.78 (—, 6H, OCH_3).

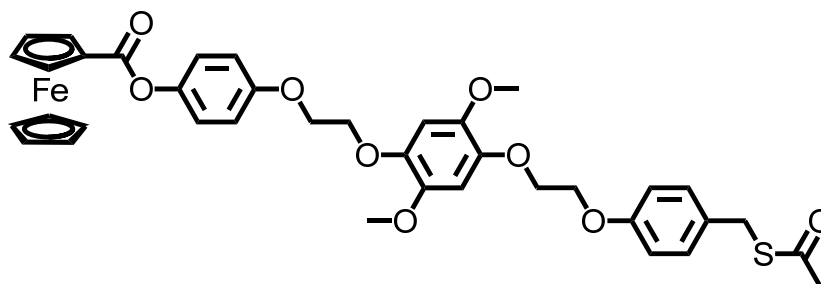
$^{13}\text{C-NMR}$ (151 MHz, CDCl_3 , 298.5 K): δ / ppm = 170.8 (quart.), 158.4 (quart.), 156.34 (quart.), 144.8 (quart.), 144.34 (quart.), 144.33 (quart.), 143.01 (quart.), 143.00 (quart.), 133.6 (quart.), 128.8 (tert.), 122.7 (tert.), 115.4 (tert.), 114.8 (tert.), 104.4 (tert.), 104.3 (tert.), 72.0 (tert.), 70.7 (tert.), 70.2 (quart.), 70.1 (tert.), 69.53 (sec.), 69.51 (sec.), 67.3 (sec.), 66.9 (sec.), 65.2 (sec.), 57.08 (prim.), 57.07 (prim.).

High Resolution Mass (ESI): calc.: 689.16477 $[\text{M}+\text{Na}]^+$

found: 629.16477 $[\text{M}+\text{Na}]^+$

Δ : 0.00 ppm

Synthesis of B



CAS: /

Under a nitrogen atmosphere, dry dichloromethane (30 ml) was added to a mixture of **B6** (1.12 g, 1.68 mmol), triphenylphosphine (659 mg, 2.51 mmol) and thioacetic acid (237 μ l, 3.35 mmol). Diisopropyl azodicarboxylate (493 μ l, 2.51 mmol) was added slowly during 5 min. The reaction mixture was stirred for 3 d at rt. The solvents were removed *in vacuo*. The residue was purified by flash column chromatography on silica gel (dichloromethane) followed by column chromatography on aluminium oxide (dichloromethane). The product was dried in HV.

Yield: 210 mg (289 μ mol, 17 %) orange solid C₃₈H₃₈FeO₉S [726.6 g/mol].

¹H-NMR (600 MHz, CDCl₃, 303.4 K): δ / ppm = 7.20 (AA', 2H, CH_{arom.}), 7.09 (AA', 2H, CH_{arom.}), 6.98 (BB', 2H, CH_{arom.}), 6.87 (BB', 2H, CH_{arom.}), 6.71–6.67 (—, 2H, CH_{arom.}), 4.96–4.94 (m, 2H, CH_{Fc}), 4.50–4.48 (m, 2H, CH_{Fc}), 4.38–4.26 (—, 13H, CH₂ and CH_{Fc}), 4.07 (s, 2H, CH₂), 3.80 (s, 3H, OCH₃), 3.79 (s, 3H, OCH₃), 2.34 (s, 3H, CH₃).

¹³C-NMR: (151 MHz, CDCl₃, 303.4 K): δ / ppm = 195.5 (quart.), 170.8 (quart.), 158.1 (quart.), 156.4 (quart.), 144.8 (quart.), 144.41 (quart.), 144.39 (quart.), 143.09 (quart.), 143.06 (quart.), 130.122 (tert.), 130.118 (quart.), 122.7 (tert.), 115.5 (tert.), 114.9 (tert.), 104.5 (tert.), 104.4 (tert.), 72.0 (tert.), 70.76 (tert.), 70.3 (quart.), 70.1 (tert.), 69.6 (sec.), 69.5 (sec.), 67.4 (sec.), 66.9 (sec.), 57.13 (prim.), 57.12 (prim.), 33.1 (sec.), 30.5 (prim.).

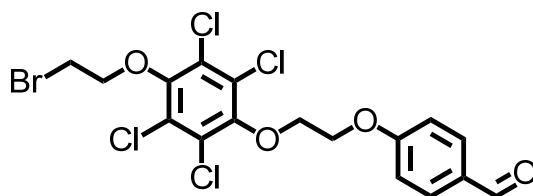
High Resolution Mass (ESI): calc.: 724.16272 M⁺

found: 724.16399 M⁺

Δ : 1.75 ppm

6.2.7 SYNTHESIS OF C

Synthesis of C2



CAS: /

Under a nitrogen atmosphere, dry acetonitrile (300 ml) was added to a mixture of **C1** (9.24 g, 20.0 mmol), 4-hydroxybenzaldehyde (2.44 g, 20.0 mmol) and potassium carbonate (3.87 g, 28.0 mmol). The reaction mixture was stirred for 2 d under reflux conditions. The solvent was removed *in vacuo*. The reaction mixture was hydrolyzed with water and extracted with dichloromethane. The combined organic phases were dried over magnesium sulfate and the solvent was removed *in vacuo*. The residue was purified by flash column chromatography on silica gel (gradient: dichloromethane → dichloromethane/ethyl acetate 20:1). The product was dried in HV.

Yield: 3.02 g (6.00 mmol, 30 %) colorless solid C₁₇H₁₃BrCl₄O₄ [503.0 g/mol].

¹H-NMR (400 MHz, CDCl₃, 300 K): δ / ppm = 9.91 (s, 1H, C(O)H), 7.86 (AA', 2H, CH_{arom.}), 7.04 (BB', 2H, CH_{arom.}), 4.49-4.41 (—, 4H, CH₂), 4.32 (t, ³J_H = 6.63, 2H, CH₂), 3.70 (t, ³J_H = 6.70, 2H, CH₂).

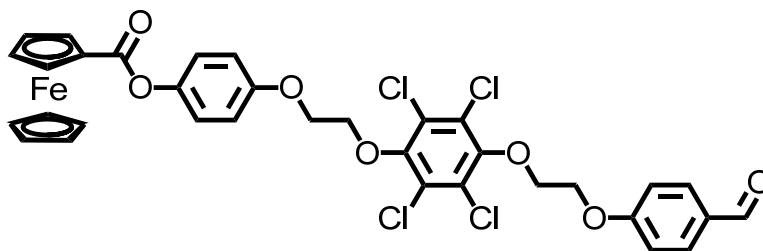
¹³C-NMR (101 MHz, CDCl₃, 300 K): δ / ppm = 190.9 (tert.), 163.5 (quart.), 149.8 (quart.), 149.3 (quart.), 132.2 (tert.), 130.6 (quart.), 127.9 (quart.), 127.8 (quart.), 115.0 (tert.), 73.0 (sec.), 71.8 (sec.), 67.2 (sec.), 28.7 (sec.).

High Resolution Mass (ESI): calc.: 500.88241 [M+H]⁺

found: 500.88213 [M+H]⁺

Δ : 0.56 ppm

Synthesis of C3



CAS: /

Under a nitrogen atmosphere, dry acetonitrile (350 ml) was added to a mixture of **C2** (2.72 g, 5.40 mmol), **F3** (1.74 g, 5.40 mmol) and potassium carbonate (1.12 g, 8.10 mmol). The reaction mixture was stirred for 12 h under reflux conditions. The solvent was removed *in vacuo*. The residue was purified by flash column chromatography on silica gel (dichloromethane). The product was dried in HV.

Yield: 2.00 g (2.69 mmol, 50 %) orange solid C₃₄H₂₆Cl₄FeO₇ [744.2 g/mol].

¹H-NMR (400 MHz, CDCl₃, 300 K): δ / ppm = 9.91 (s, 1H, C(O)H), 7.86 (AA', 2H, CH_{arom.}), 7.09 (AA', 2H, CH_{arom.}), 7.05 (BB', 2H, CH_{arom.}), 6.96 (BB', 2H, CH_{arom.}), 5.03–4.97 (m, 2H, CH_{Fc}), 4.57–4.49 (m, 2H, CH_{Fc}), 4.27 (—, 13H, CH₂ and CH_{Fc}).

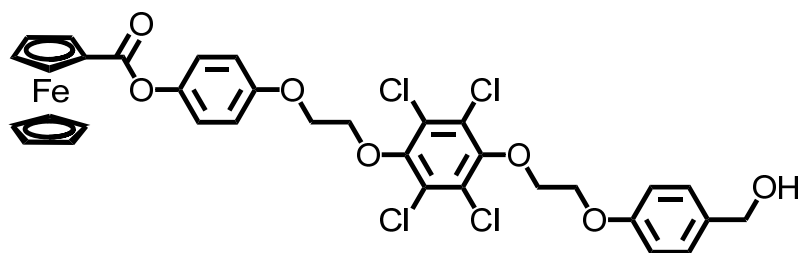
¹³C-NMR (101 MHz, CDCl₃, 300 K): δ / ppm = 190.9 (tert.), 170.8 (quart.), 163.6 (quart.), 156.1 (quart.), 149.9 (quart.), 149.5 (quart.), 145.0 (quart.), 132.2 (tert.), 130.5 (quart.), 127.9 (quart.), 127.8 (quart.), 122.8 (tert.), 115.5 (tert.), 115.0 (tert.), 72.3 (tert.), 72.2 (sec.), 71.8 (sec.), 70.9 (tert.), 70.4 (quart.), 70.3 (tert.), 67.5 (sec.), 67.3 (sec.).

High Resolution Mass (ESI): calc.: 741.97766 M⁺ (⁵⁶Fe)

found: 741.97705 M⁺ (⁵⁶Fe)

Δ : 0.82 ppm

Synthesis of C4



CAS: /

Under a nitrogen atmosphere, dry dichloromethane (50 ml) was added to a mixture of **C3** (1.75 g, 2.35 mmol) and sodium borohydride (91.5 mg, 2.42 mmol). Methanol (8ml) was added slowly within 15 min. The reaction mixture was stirred for 2 h at rt. The reaction mixture was quenched with acetic acid (10% in water). The organic phase was dried over magnesium sulfate, filtered over celite and the solvent was removed *in vacuo*. The residue was purified by flash column chromatography on silica gel (ethyl acetate/dichloromethane 1:1). The product was dried in HV.

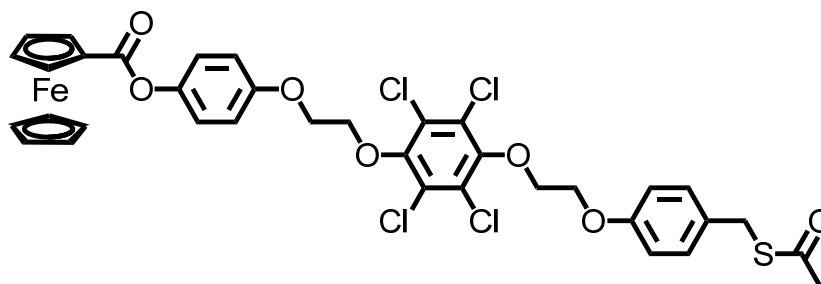
Yield: 1.16 g (1.55 mmol, 66 %) orange solid C₃₄H₂₈Cl₄FeO₇ [746.2 g/mol].

¹H-NMR (400 MHz, CDCl₃, 300 K): δ / ppm = 7.30 (AA', 2H, CH_{arom.}), 7.10 (AA', 2H, CH_{arom.}), 6.96 (BB', 2H, CH_{arom.}), 6.91 (BB', 2H, CH_{arom.}), 5.02-4.92 (m, 2H, CH_{Fc}), 4.71-4.60 (m, 2H, CH₂), 4.55-4.47 (m, 2H, CH_{Fc}), 4.45-4.34 (—, 8 H, CH₂), 4.31 (s, 5 H, CH_{Fc}).

¹³C-NMR (101 MHz, CDCl₃, 300 K): δ / ppm = 170.8 (1C, quart.), 158.2 (1C, quart.), 156.1 (1C, quart.), 149.76 (1C, quart.), 149.74 (1C, quart.), 145.0 (1C, quart.), 133.9 (1C, quart.), 128.8 (2C, tert.), 127.8 (4C, quart.), 122.7 (2C, tert.), 115.5 (2C, tert.), 114.8 (2C, tert.), 72.2 (2C, tert.), 72.1 (2C, sec.), 70.9 (2C, tert.), 70.4 (1C, quart.), 70.2 (5C, tert.), 67.5 (1C, sec.), 67.1 (1C, sec.), 65.2 (1C, sec.).

MS (MALDI): m/z (%) = M⁺ : 744 (77 %), 745 (29 %), 746 (100 %), 747 (36 %), 748 (52 %), 749 (15 %), 750 (11 %).

Synthesis of C



CAS: /

Under a nitrogen atmosphere, dry dichloromethane (100 ml) was added to a mixture of **C4** (500 mg, 670 μmol), triphenylphosphine (228 mg, 871 μmol) and thioacetic acid (61.7 μl , 871 μmol). Diisopropyl azodicarboxylate (171 μl , 871 μmol) was added slowly during 5 min. The reaction mixture was stirred for 16 h at rt. The solvents were removed *in vacuo*. The residue was purified by flash column chromatography on silica gel (gradient: dichloromethane \rightarrow dichloromethane/ethyl acetate 100:1). The product was dried in HV.

Yield: 120 mg (149 μmol , 22 %) orange solid $\text{C}_{36}\text{H}_{30}\text{Cl}_4\text{FeO}_7\text{S}$ [804.3 g/mol].

$^1\text{H-NMR}$ (600 MHz, CDCl_3 , 298.5 K): δ / ppm = 7.21 (AA', 2H, $\text{CH}_{\text{arom.}}$), 7.10 (AA', 2H, $\text{CH}_{\text{arom.}}$), 6.97 (BB', 2H, $\text{CH}_{\text{arom.}}$), 6.85 (BB', 2H, $\text{CH}_{\text{arom.}}$), 4.98-4.95 (m, 2H, CH_{Fc}), 4.51-4.48 (m, 2H, CH_{Fc}), 4.43-4.32 (—, 8H, CH_2), 4.30 (—, 5H, CH_{Fc}), 4.08 (s, 2H, CH_2), 2.34 (s, 3H, CH_3).

$^{13}\text{C-NMR}$: (151 MHz, CDCl_3 , 298.6 K): δ / ppm = 195.5 (1C, quart.), 170.8 (1C, quart.), 157.8 (1C, quart.), 156.1 (1C, quart.), 149.73 (1C, quart.), 149.71 (1C, quart.), 144.9 (1C, quart.), 130.3 (1C, quart.), 130.2 (2C, tert.), 127.8 (4C, quart.), 122.7 (2C, tert.), 115.4 (2C, tert.), 114.9 (2C, tert.), 72.11 (1C, sec.), 72.10 (1C, sec), 72.0 (2C, tert.), 70.8 (2C, tert.), 70.2 (1C, quart.), 70.1 (5C, tert.), 67.4 (1C, sec.), 67.0 (1C, sec.), 33.1 (1C, sec.), 30.5 (1C, prim.).

High Resolution Mass (ESI): calc.: 799.98570 M^+

found: 799.98383 M^+

Δ : 2.34 ppm

7 LITERATURE

- [1] E. Sabatani, I. Rubinstein, R. Maoz, J. Sagiv *J. Electroanal. Chem.* **1987**, 219, 365–371.
- [2] E. Sabatani, I. Rubinstein *J. Phys. Chem.* **1987**, 91, 6663–6669.
- [3] E. B. Troughton, C. D. Bain, G. M. Whitesides, R. G. Nuzzo, D. L. Allara, M. D. Porter *Langmuir* **1988**, 4, 365–385.
- [4] V. Kriegisch, C. Lambert *Top. Curr. Chem.* **2005**, 258, 257–313.
- [5] A. Ulman *Chem. Rev.* **1996**, 96, 1533–1554.
- [6] F. Schreiber *Prog. Surf. Sci.* **2000**, 65, 151–256.
- [7] E. Pensa, E. Cortés, G. Corthey, P. Carro, C. Vericat, M. H. Fonticelli, G. Benítez, A. A. Rubert, R. C. Salvarezza *Acc. Chem. Res.* **2012**, 45, 1183–1192.
- [8] L. Ferrighi, Y. Pan, H. Grönbeck, B. Hammer *J. Phys. Chem. C* **2012**, 116, 7374–7379.
- [9] H. Häkkinen *Nat. Chem.* **2012**, 4, 443–455.
- [10] Z. W. Wang, R. E. Palmer *Nano Lett.* **2012**, 12, 91–95.
- [11] P. Maksymovych, O. Voznyy, D. B. Dougherty, D. C. Sorescu, J. T. Yates Jr. *Prog. Surf. Sci.* **2010**, 85, 206–240.
- [12] F. Li, L. Tang, W. Zhou, Q. Guo *J. Am. Chem. Soc.* **2010**, 132, 13059–13063.
- [13] D. Natali, M. Caironi *Adv. Mater.* **2012**, 24, 1357–1387.
- [14] H. Ma, H.-L. Yip, F. Huang, A. K.-Y. Jen *Adv. Funct. Mater.* **2010**, 20, 1371–1388.
- [15] F. D. Fleischli, S. Suárez, M. Schaer, L. Zuppiroli *Langmuir* **2010**, 26, 15044–15049.
- [16] S. K. Hau, Y.-J. Cheng, H.-L. Yip, Y. Zhang, H. Ma, A. K.-Y. Jen *ACS Appl. Mater. Interfaces* **2010**, 2, 1892–1902.
- [17] F. Rissner, G. M. Rangger, O. T. Hofmann, A. M. Track, G. Heimel, E. Zojer *ACS Nano* **2009**, 3, 3513–3520.
- [18] X. Y. Cheng, Y.-Y. Noh, J. P. Wang, M. Tello, J. Frisch, R.-P. Blum, A. Vollmer, J. P. Rabe, N. Koch, H. Sirringhaus *Adv. Funct. Mater.* **2009**, 19, 2407–2415.
- [19] A. von Mühlengen, M. Castellani, M. Schaer, L. Zuppiroli *Phys. Status Solidi B* **2008**, 245, 1170–1174.
- [20] G. Heimel, L. Romaner, E. Zojer, J.-L. Bredas *Acc. Chem. Res.* **2008**, 41, 721–729.
- [21] T. C. Monson, M. T. Lloyd, D. C. Olson, Y.-J. Lee, J. W. P. Hsu *Adv. Mater.* **2008**, 20, 4755–4751.
- [22] S. K. Hau, H.-L. Yip, O. Acton, N. S. Baek, H. Ma, A. K.-Y. Jen *J. Mater. Chem.* **2008**, 18, 5113–5119.
- [23] C. Ganzorig, K.-J. Kwak, K. Yagi, M. Fujihira *Appl. Phys. Lett.* **2001**, 79, 272–274.

- [24] M. Kondratenko, A. G. Moiseev, D. F. Perepichka *J. Mater. Chem.* **2011**, 21, 1470–1478.
- [25] C. A. Nijhuis, W. F. Reus, J. R. Barber, M. D. Dickey, G. M. Whitesides *Nano Lett.* **2010**, 10, 3611–3619.
- [26] G. J. Ashwell, B. Urasinska-Wojcik, L. J. Phillips *Angew. Chem., Int. Ed.* **2010**, 49, 3508–3512.
- [27] R. M. Metzger *Anal. Chim. Acta* **2006**, 568, 146–155.
- [28] G. J. Ashwell, W. D. Tyrrell, A. J. Whittam *J. Mater. Chem.* **2003**, 13, 2855–2857.
- [29] A. Coskun, J. M. Spruell, G. Barin, W. R. Dichtel, A. H. Flood, Y. Y. Botros, J. F. Stoddart *Chem. Soc. Rev.* **2012**, 41, 4827–4859.
- [30] K. Terada, K. Kanaizuka, V. M. Iyer, M. Sannodo, S. Saito, K. Kobayashi, M. A. Haga *Angew. Chem., Int. Ed.* **2011**, 50, 6287–6291.
- [31] M. Mannini, F. Pineider, P. Sainctavit, C. Danieli, E. Otero, C. Sciancalepore, A. M. Talarico, M.-A. Arrio, A. Cornia, D. Gatteschi, R. Sessoli *Nat. Mater.* **2009**, 8, 194–197.
- [32] W. R. Dichtel, J. R. Heath, J. F. Stoddart *Phil. Trans. R. Soc., A* **2007**, 365, 1607–1625.
- [33] C. Simão, M. Mas-Torrent, J. Casado-Montenegro, F. Otón, J. Veciana, C. Rovira *J. Am. Chem. Soc.* **2011**, 133, 13256–13259.
- [34] N. Katsonis, M. Lubomska, M. M. Pollard, B. L. Feringa, P. Rudolf *Prog. Surf. Sci.* **2007**, 82, 407–434.
- [35] W. R. Browne, B. L. Feringa *Annu. Rev. Phys. Chem.* **2009**, 60, 407–428.
- [36] M. Han, T. Honda, D. Ishikawa, E. Ito, M. Hara, Y. Norikane *J. Mater. Chem.* **2011**, 21, 4696–4702.
- [37] J. M. Mativetsky, G. Pace, M. Elbing, M. A. Rampi, M. Mayor, P. Samorì *J. Am. Chem. Soc.* **2008**, 130, 9192–9193.
- [38] K. Smaali, S. Lenfant, S. Karpe, M. Oçafrain, P. Blanchard, D. Deresmes, S. Godey, A. Rochefort, J. Roncali, D. Vuillaume *ACS Nano* **2010**, 4, 2411–2421.
- [39] D. Liu, Y. Xie, H. Shao, X. Jiang *Angew. Chem., Int. Ed.* **2009**, 48, 4406–4408.
- [40] C. Li, B. Ren, Y. Zhang, Z. Cheng, X. Liu, Z. Tong *Langmuir* **2008**, 24, 12911–12918.
- [41] C. Y. Lee, J. K. Jang, C. H. Kim, J. Jung, B. K. Park, J. Park, W. Choi, Y.-K. Han, T. Joo, J. T. Park *Chem. Eur. J.* **2010**, 16, 5586–5599.
- [42] N. Terasaki, N. Yamamoto, T. Hiraga, Y. Yamanoi, T. Yonezawa, H. Nishihara, T. Ohmori, M. Sakai, M. Fujii, A. Tohri, M. Iwai, Y. Inoue, S. Yoneyama, M. Minakata, I. Enami *Angew. Chem., Int. Ed.* **2009**, 48, 1585–1587.
- [43] Y. Matsuo, K. Kanaizuka, K. Matsuo, Y.-W. Zhong, T. Nakae, E. Nakamura *J. Am. Chem. Soc.* **2008**, 130, 5016–5017.

- [44] A. Llanes-Pallas, M. Matena, T. Jung, M. Prato, M. Stöhr, D. Bonifazi *Angew. Chem., Int. Ed.* **2008**, 47, 7726–7730.
- [45] G. T. Carroll, M. M. Pollard, R. van Delden, B. L. Feringa *Chem. Sci.* **2010**, 1, 97–101.
- [46] H. Jian, J. M. Tour *J. Org. Chem.* **2003**, 68, 5091–5103.
- [47] G. T. Carroll, G. London, T. F. Landaluce, P. Rudolf, B. L. Feringa *ACS Nano* **2011**, 5, 622–630.
- [48] G. London, G. T. Carroll, T. F. Landaluce, M. M. Pollard, P. Rudolf, B. L. Feringa *Chem. Commun.* **2009**, 1712–1714.
- [49] M. M. Pollard, M. Lubomska, P. Rudolf, B. L. Feringa *Angew. Chem., Int. Ed.* **2007**, 46, 1278–1280.
- [50] Z. Matharu, A. J. Bhandodkar, V. Gupta, B. D. Malhotra *Chem. Soc. Rev.* **2012**, 41, 1363–1402.
- [51] M. A. Mohsin, F.-G. Banica, T. Oshima, T. Hianik *Electroanalysis* **2011**, 23, 1229–1235.
- [52] D. Samanta, A. Sarkar *Chem. Soc. Rev.* **2011**, 40, 2567–2592.
- [53] S. K. Arya, P. R. Solanki, M. Datta, B. D. Malhotra *Biosens. Bioelectron.* **2009**, 24, 2810–2817.
- [54] M. Gebala, L. Stoica, S. Neugebauer, W. Schuhmann *Electroanalysis* **2009**, 21, 325–331.
- [55] J. Y. Park, S. M. Park *Sensors* **2009**, 9, 9513–9532.
- [56] P. Jonkheijm, D. Weinrich, H. Schröder, C. M. Niemeyer, H. Waldmann *Angew. Chem., Int. Ed.* **2008**, 47, 9618–9647.
- [57] J. Fritz *Analyst* **2008**, 133, 855–863.
- [58] S. Campuzano, F. Kuralay, J. Wang *Electroanalysis* **2012**, 24, 483–493.
- [59] S. Campuzano, F. Kuralay, M. J. Lobo-Castañón, M. Bartošík, K. Vyavahare, E. Paleček, D. A. Haake, J. Wang *Biosens. Bioelectron.* **2011**, 26, 3577–3583.
- [60] Y. Egawa, T. Seki, S. Takahashi, J. Anzai *Mater. Sci. Eng., C* **2011**, 31, 1257–1264.
- [61] N. Phares, R. J. White, K. W. Plaxco *Anal. Chem.* **2009**, 81, 1095–1100.
- [62] F. Ricci, N. Zari, F. Caprio, S. Recine, A. Amine, D. Moscone, G. Palleschi, K. W. Plaxco *Bioelectrochemistry* **2009**, 76, 208–213.
- [63] J.-Y. Park, S.-M. Park *Sensors* **2009**, 9, 9513–9532.
- [64] S. D. Keighley, P. Li, P. Estrela, P. Migliorato *Biosens. Bioelectron.* **2008**, 23, 1291–1297.
- [65] J. Zhang, R. Lao, S. Song, Z. Yan, C. Fan *Anal. Chem.* **2008**, 80, 9029–9033.
- [66] L. P. Ding, Y. Fang *Chem. Soc. Rev.* **2010**, 39, 4258–4273.
- [67] M. Mazloum-Ardakani, H. Beitollahi, M. K. Amini, B.-F. Mirjalili, F. Mirkhalaf *J. Electroanal. Chem.* **2011**, 651, 243–249.

- [68] J. P. Collman, N. K. Devaraj, R. A. Decréau, Y. Yang, Y.-L. Yan, W. Ebina, T. A. Eberspacher, C. E. D. Chidsey *Science* **2007**, 315, 1565–1568.
- [69] A. Ciaccafava, P. Infossi, M. Ilbert, M. Guiral, S. Lecomte, M. T. Giudici-Ortoni, E. Lojou *Angew. Chem., Int. Ed.* **2012**, 51, 953–956.
- [70] M. Pita, C. Gutierrez-Sanchez, D. Olea, M. Velez, C. Garcia-Diego, S. Shleev, V. M. Fernandez, A. L. De Lacey *J. Phys. Chem. C* **2011**, 115, 13420–13428.
- [71] T. de F. Paulo, I. C. N. Diógenes, H. D. Abruña *Langmuir* **2011**, 27, 2052–2057.
- [72] R. A. Decréau, J. P. Collman, A. Hosseini *Chem. Soc. Rev.* **2010**, 39, 1291–1301.
- [73] S. Ciampi, J. J. Gooding *Chem. Eur. J.* **2010**, 16, 5961–5968.
- [74] Y. Chen, X.-J. Yang, L.-R. Guo, B. Jin, X.-H. Xia, L.-M. Zheng *Talanta* **2009**, 78, 248–252.
- [75] E. A. Weiss, M. R. Wasielewski, M. A. Ratner *Molecular Wires: From Design to Properties, Vol. 257* (Ed. L. DeCola), Springer-Verlag Berlin, Berlin, **2005**, 103–133.
- [76] E. A. Weiss, J. K. Kriebel, M.-A. Rampi, G. M. Whitesides *Phil. Trans. R. Soc., A* **2007**, 365, 1509–1537.
- [77] M. D. Newton, J. F. Smalley *Phys. Chem. Chem. Phys.* **2007**, 9, 555–572.
- [78] Y. Selzer, M. A. Cabassi, T. S. Mayer, D. L. Allara *Nanotechnology* **2004**, 15, S483–S488.
- [79] Y. Selzer, M. A. Cabassi, T. S. Mayer, D. L. Allara *J. Am. Chem. Soc.* **2004**, 126, 4052–4053.
- [80] P. A. Brooksby, K. H. Anderson, A. J. Downard, A. D. Abell *Langmuir* **2010**, 26, 1334–1339.
- [81] R. Venkatramani, K. L. Davis, E. Wierzbinski, S. Bezer, A. Balaeff, S. Keinan, A. Paul, L. Kocsis, D. N. Beratan, C. Achim, D. H. Waldeck *J. Am. Chem. Soc.* **2011**, 133, 62–72.
- [82] A. Paul, R. M. Watson, E. Wierzbinski, K. L. Davis, A. Sha, C. Achim, D. H. Waldeck *J. Phys. Chem. B* **2010**, 114, 14140–14148.
- [83] Y. Arikuma, H. Nakayama, T. Morita, S. Kimura *Langmuir* **2011**, 27, 1530–1535.
- [84] Y. Arikuma, H. Nakayama, T. Morita, S. Kimura *Angew. Chem., Int. Ed.* **2010**, 49, 1800–1804.
- [85] Y. Arikuma, K. Takeda, T. Morita, M. Ohmae, S. Kimura *J. Phys. Chem. B* **2009**, 113, 6256–6266.
- [86] K. Takeda, T. Morita, S. Kimura *J. Phys. Chem. B* **2008**, 112, 12840–12850.
- [87] Y. Arikuma, K. Takeda, T. Morita, M. Ohmae, S. Kimura *J. Phys. Chem. B* **2009**, 113, 15900.
- [88] N. Darwish, I. Díez-Pérez, S. Guo, N. Tao, J. J. Gooding, M. N. Paddon-Row *J. Phys. Chem. C* **2012**, 116, 21093–21097.

- [89] F. Blobner, P. B. Coto, F. Allegretti, M. Bockstedte, O. Rubio-Pons, H. Wang, D. L. Allara, M. Zharnikov, M. Thoss, P. Feulner *J. Phys. Chem. Lett.* **2012**, 3, 436–440.
- [90] Y. Qi, O. Yaffe, E. Tirosh, A. Vilan, D. Cahen, A. Kahn *Chem. Phys. Lett.* **2011**, 511, 344–347.
- [91] H. Song, H. Lee, T. Lee *J. Am. Chem. Soc.* **2007**, 129, 3806–3807.
- [92] Z. Xie, T. Z. Markus, S. R. Cohen, Z. Vager, R. Gutierrez, R. Naaman *Nano Lett.* **2011**, 11, 4652–4655.
- [93] P. Kao, S. Neppl, P. Feulner, D. L. Allara, M. Zharnikov *J. Phys. Chem. C* **2010**, 114, 13766–13773.
- [94] L. Wang, W. Chen, C. Huang, Z.-K. Chen, A. T. S. Wee *J. Phys. Chem. B* **2006**, 110, 674–676.
- [95] N. Darwish, P. K. Eggers, S. Ciampi, Y. Tong, S. Ye, M. N. Paddon-Row, J. J. Gooding *J. Am. Chem. Soc.* **2012**, 134, 18401–18409.
- [96] P. K. Eggers, H. M. Zareie, M. N. Paddon-Row, J. J. Gooding *Langmuir* **2009**, 25, 11090–11096.
- [97] W. R. Yang, M. W. Jones, X. Li, P. K. Eggers, N. Tao, J. J. Gooding, M. N. Paddon-Row *J. Phys. Chem. C* **2008**, 112, 9072–9080.
- [98] F. Goujon, C. Bonal, B. Limoges, P. Malfreyt *J. Phys. Chem. B* **2010**, 114, 6447–6454.
- [99] W. F. Reus, C. A. Nijhuis, J. R. Barber, M. M. Thuo, S. Tricard, G. M. Whitesides *J. Phys. Chem. C* **2012**, 116, 6714–6733.
- [100] V. Kaliginedi, P. Moreno-García, H. Valkenier, W. Hong, V. M. García-Suarez, P. Buitter, J. L. H. Otten, J. C. Hummelen, C. J. Lambert, T. Wandlowski *J. Am. Chem. Soc.* **2012**, 134, 5262–5275.
- [101] H. Hamoudi, S. Neppl, P. Kao, B. Schüpbach, P. Feulner, A. Terfort, D. Allara, M. Zharnikov *Phys. Rev. Lett.* **2011**, 107, 1–4.
- [102] L. Sepunaru, I. Pecht, M. Sheves, D. Cahen *J. Am. Chem. Soc.* **2011**, 133, 2421–2423.
- [103] T. Kurita, Y. Nishimori, F. Toshimitsu, S. Muratsugu, S. Kume, H. Nishihara *J. Am. Chem. Soc.* **2010**, 132, 4524–4525.
- [104] I. V. Pobelov, Z. Li, T. Wandlowski *J. Am. Chem. Soc.* **2008**, 130, 16045–16054.
- [105] B. P. Paulson, J. R. Miller, W.-X. Gan, G. Closs *J. Am. Chem. Soc.* **2005**, 127, 4860–4868.
- [106] E. A. Weiss, M. J. Ahrens, L. E. Sinks, A. V. Gusev, M. A. Ratner, M. R. Wasielewski *J. Am. Chem. Soc.* **2004**, 126, 5577–5584.
- [107] K. Weber, S. E. Creager *Anal. Chem.* **1994**, 66, 3164–3172.
- [108] M. Malagoli, J. L. Brédas *Chem. Phys. Lett.* **2000**, 327, 13–17.
- [109] A. Heckmann, C. Lambert *Angew. Chem., Int. Ed.* **2012**, 51, 326–392.

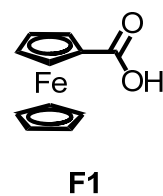
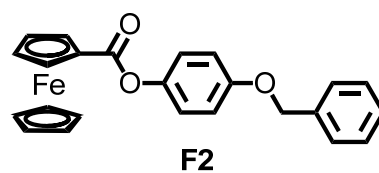
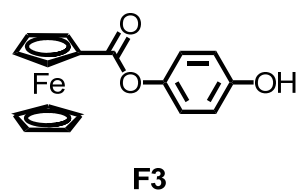
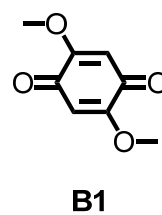
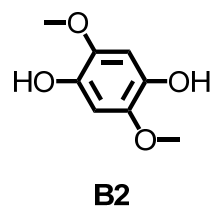
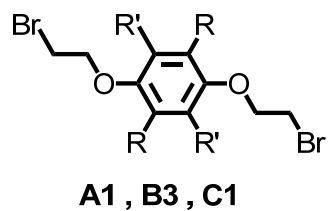
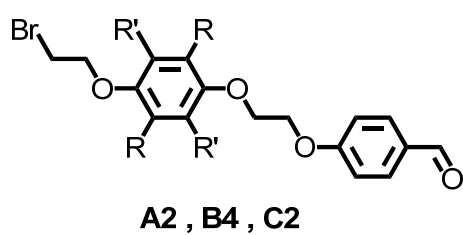
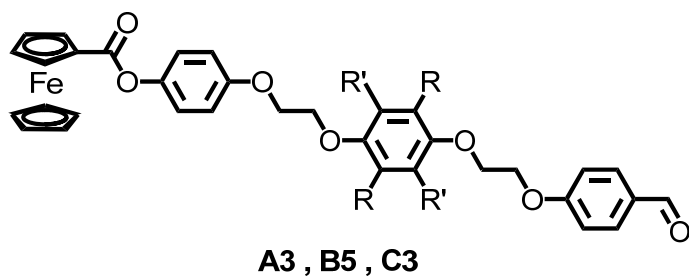
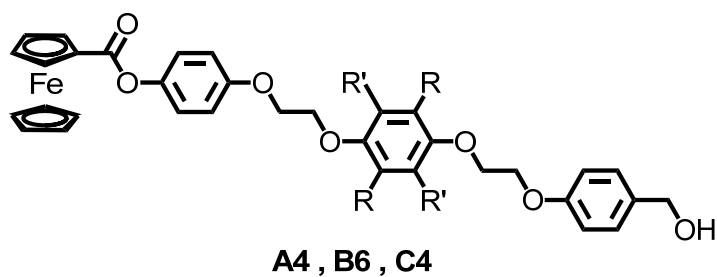
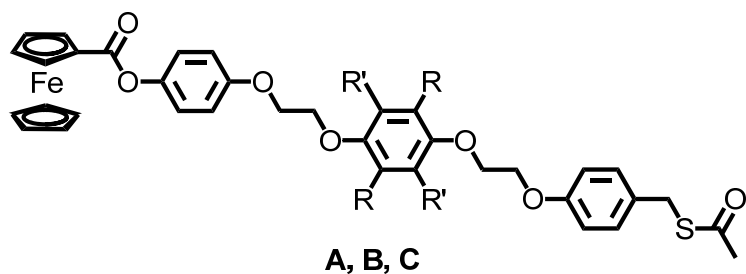
- [110] C. Lambert, V. Kriegisch, A. Terfort, B. Zeysing *J. Electroanal. Chem.* **2006**, 590, 32–36.
- [111] S. E. Creager, T. T. Wooster *Anal. Chem.* **1998**, 70, 4257–4263.
- [112] C. Lambert, V. Kriegisch *Langmuir* **2006**, 22, 8807–8812.
- [113] C. E. D. Chidsey *Science* **1991**, 251, 919–922.
- [114] J. F. Smalley, H. O. Finklea, C. E. D. Chidsey, M. R. Linford, S. E. Creager, J. P. Ferraris, K. Chalfant, T. Zawodzinsk, S. W. Feldberg, M. D. Newton *J. Am. Chem. Soc.* **2003**, 125, 2004–2013.
- [115] C. E. D. Chidsey, C. R. Bertozzi, T. M. Putvinski, A. M. Majsce *J. Am. Chem. Soc.* **1990**, 112, 4301–4306.
- [116] T. Matsumura-Inoue, K. Kuroda, Y. Umezawa, Y. Achiba *J. Chem. Soc., Faraday Trans.* **1989**, 85, 857–866.
- [117] A. Zweig, W. G. Hodgson, W. H. Jura *J. Am. Chem. Soc.* **1964**, 86, 4124–4129.
- [118] F. Buckel, F. Effenberger, C. Yan, A. Götzhäuser, M. Grunze *Adv. Mater.* **2000**, 12, 901–905.
- [119] Y.-T. Tao, C.-C. Wu, J.-Y. Eu, W.-L. Lin, K.-C. Wu, C. Chen *Langmuir* **1997**, 13, 4018–4023.
- [120] J. M. Tour, L. Jones II, D. L. Pearson, J. J. S. Lamba, T. P. Burgin, G. M. Whitesides, D. L. Allara, A. N. Parikh, S. V. Atre *J. Am. Chem. Soc.* **1995**, 117, 9529–9534.
- [121] L. Cai, Y. Yao, J. Yang, D. W. Price, J. M. Tour *Chem. Mater.* **2002**, 14, 2905–2909.
- [122] D. K. Schwartz *Annu. Rev. Phys. Chem.* **2001**, 52, 107–137.
- [123] J. C. Love, L. A. Estroff, J. K. Kriebel, R. G. Nuzzo, G. M. Whitesides *Chem. Rev.* **2005**, 105, 1103–1169.
- [124] H.-G. Hong, W. Park *Electrochim Acta* **2005**, 51, 579–587.
- [125] L. Y. S. Lee, T. C. Sutherland, S. Rucareanu, R. B. Lennox *Langmuir* **2006**, 22, 4438–4444.
- [126] B.-Y. Chang, S.-M. Park *Annu. Rev. Anal. Chem.* **2010**, 3, 207–229.
- [127] B. Pejčić, R. De Marco *Electrochim Acta* **2006**, 51, 6217–6229.
- [128] J. R. Macdonald, L. D. Potter Jr. *Solid State Ionics* **1987**, 24, 61–79.
- [129] E. Laviron *J. Electroanal. Chem.* **1979**, 97, 135–149.
- [130] E. Laviron *J. Electroanal. Chem.* **1979**, 105, 35–42.
- [131] B. Li, H. Xi, X. Sun *Huaxue Shiji* **2003**, 25, 29–30.
- [132] V. V. Pavlishchuk, A. W. Addison *Inorg. Chim. Acta* **2000**, 298, 97–102.
- [133] H. O. Finklea, *Electroanalytical Chemistry: A Series of Advances*, Marcel Dekker, New York, **1996**.

- [134] S. Sek, A. Sepiol, A. Tolak, A. Misicka, R. Bilewicz *J. Phys. Chem. B* **2004**, 108, 8102–8105.
- [135] S. Sek, B. Palys, R. Bilewicz *J. Phys. Chem. B* **2002**, 106, 5907–5914.
- [136] J. J. Sumner, S. E. Creager *J. Am. Chem. Soc.* **2000**, 122, 11914–11920.
- [137] J. J. Sumner, K. S. Weber, L. A. Hockett, S. E. Creager *J. Phys. Chem. B* **2000**, 104, 7449–7454.
- [138] C. Hortholary, F. Minc, C. Coudret, J. Bonvoisin, J. P. Launay *Chem. Commun.* **2002**, 1932–1933.
- [139] L. V. Protsailo, W. R. Fawcett *Electrochim Acta* **2000**, 45, 3497–3505.
- [140] Y. Kang, D.-J. Won, S. R. Kim, K. Seo, H.-S. Choi, G. Lee, Z. Noh, T. S. Lee, C. Lee *Mater. Sci. Eng., C* **2004**, 24, 43–46.
- [141] H. A. Biebuyck, C. D. Bain, G. M. Whitesides *Langmuir* **1994**, 10, 1825–1831.
- [142] C.-C. Han, R. Balakumar *Tetrahedron Lett.* **2006**, 47, 8255–8258.
- [143] J. J. Sumner, S. E. Creager *J. Phys. Chem. B* **2001**, 105, 8739–8745.
- [144] G. K. Rowe, S. E. Creager *J. Phys. Chem.* **1994**, 98, 5500–5507.
- [145] S. E. Creager, G. K. Rowe *Anal. Chim. Acta* **1991**, 246, 233–239.
- [146] G. K. Rowe, S. E. Creager *Langmuir* **1991**, 7, 2307–2312.
- [147] H. Ju, D. Leech *Langmuir* **1998**, 14, 300–306.
- [148] L. Zhang, L. A. Godinez, T. Lu, G. W. Gokel, A. E. Kaifer *Angew. Chem., Int. Ed.* **1995**, 34, 235–237.
- [149] R. P. Janek, W. R. Fawcett, A. Ulman *J. Phys. Chem. B* **1997**, 101, 8550–8558.
- [150] H. O. Finklea, M. S. Ravenscroft, D. A. Snider *Langmuir* **1993**, 9, 223–227.
- [151] *Impedance Spectroscopy: Emphasizing Solid Materials and Systems*, (Ed. J. R. Macdonald), John Wiley & Sons, New York, **1987**, 121–132.
- [152] W. H. Mulder, J. H. Sluyters, T. Pajkossy, L. Nyikos *J. Electroanal. Chem.* **1990**, 285, 103–115.
- [153] C.-H. Kim, S.-I. Pyun, J.-H. Kim *Electrochim Acta* **2003**, 48, 3455–3463.
- [154] C. A. Schiller, W. Strunz *Electrochim Acta* **2001**, 46, 3619–3625.
- [155] J.-B. Jorcin, M. E. Orazem, N. Pébère, B. Tribollet *Electrochim. Acta* **2006**, 51, 1473–1479.
- [156] K. B. Oldham *Electrochem. Commun.* **2004**, 6, 210–214.
- [157] K. Seo, I. C. Jeon, D. J. Yoo *Langmuir* **2004**, 20, 4147–4154.
- [158] E. Laviron *J. Electroanal. Chem.* **1979**, 101, 19–28.
- [159] A. J. Bard, L. R. Faulkner, *Electrochemical Methods*, John Wiley & Sons, New York, **2001**.

- [160] C. Amatore, Y. Bouret, E. Maisonhaute, J. I. Goldsmith, H. D. Abruña *Chem. Eur. J.* **2001**, 7, 2206–2226.
- [161] C. Amatore, Y. Bouret, E. Maisonhaute, J. I. Goldsmith, H. D. Abruña *ChemPhysChem* **2001**, 2, 130–134.
- [162] G. K. Rowe, M. T. Carter, J. N. Richardson, R. W. Murray *Langmuir* **1995**, 11, 1797–1806.
- [163] S. E. Creager, G. K. Rowe *J. Electroanal. Chem.* **1997**, 420, 291–299.
- [164] C. P. Smith, H. S. White *Anal. Chem.* **1992**, 64, 2398–2405.
- [165] W. R. Fawcett *J. Electroanal. Chem.* **1994**, 378, 117–124.
- [166] K. Uosaki, Y. Sato, H. Kita *Langmuir* **1991**, 7, 1510–1514.
- [167] T. Auletta, F. C. J. M. van Veggel, D. N. Reinhoudt *Langmuir* **2002**, 18, 1288–1293.
- [168] C. Amatore, E. Maisonhaute, B. Schöllhorn, J. Wadhawan *ChemPhysChem* **2007**, 8, 1321–1329.
- [169] J. H. Li, K. Schuler, S. E. Creager *J. Electrochem. Soc.* **2000**, 147, 4584–4588.
- [170] K. M. Roth, D. T. Gryko, C. Clausen, J. Li, J. S. Lindsey, W. G. Kuhr, D. F. Bocian *J. Phys. Chem. B* **2002**, 106, 8639–8648.
- [171] C.-P. Hsu *J. Electroanal. Chem.* **1997**, 438, 27–35.
- [172] J. F. Smalley, S. W. Feldberg, C. E. D. Chidsey, M. R. Linford, M. D. Newton, Y.-P. Liu *J. Phys. Chem.* **1995**, 99, 13141–13149.
- [173] S. Creager, C. J. Yu, C. Bamdad, S. O'Connor, T. MacLean, E. Lam, Y. Chong, G. T. Olsen, J. Luo, M. Gozin, J. F. Kayyem *J. Am. Chem. Soc.* **1999**, 121, 1059–1064.
- [174] J. Salbeck, PhD thesis, Universität Regensburg, **1988**.
- [175] B. Breit, D. Breuninger *Synthesis* **2005**, 2782–2786.

8 STRUCTURAL FORMULA TABLE

A: R = R' = H
 B: R = H; R' = OMe
 C: R = R' = Cl



II) PREPARATION AND INVESTIGATION OF MODEL SYSTEMS FOR INTERMOLECULAR ELECTRON TRANSFER*

1 INTRODUCTION	110
2 PROJECT AIM	116
3 RESULTS AND DISCUSSION	121
3.1 SYNTHESIS	121
3.1.1 BUILDING BLOCKS	121
3.1.2 RETROSYNTHETIC SCHEME OF PARACYCLOPHANE 10	122
3.1.3 SYNTHESIS OF PARACYCLOPHANE PRECURSOR 2	123
3.1.4 SYNTHESIS OF PARACYCLOPHANE PRECURSOR 7	124
3.1.5 SYNTHESIS OF PARACYCLOPHANE 10	125
3.1.6 SYNTHESIS OF NAPHTALENE BISIMIDE ACCEPTOR 11.....	126
3.1.7 SYNTHESIS OF NAPHTALENE BISIMIDE CYCLOPHANES 13 AND E	127
3.1.8 SYNTHESIS OF DONOR-ACCEPTOR DYADS A AND B	128
3.1.9 SYNTHESIS OF DONOR-ACCEPTOR DYAD C.....	129
3.1.10 SYNTHESIS OF MIXED-VALENCE PRECURSOR F	130
3.1.11 SYNTHESIS OF MIXED-VALENCE PRECURSOR J.....	131
3.1.12 SYNTHESIS OF LITERATURE KNOWN MIXED-VALENCE PRECURSOR K.....	132
3.2 CRYSTAL STRUCTURES	133
3.3 CYCLIC VOLTAMMETRY.....	137
3.3.1 CYCLIC VOLTAMMETRY OF MIXED-VALENCE PRECURSOR F ...	137
3.3.2 CYCLIC VOLTAMMETRY OF DONOR-ACCEPTOR DYADS A–C ...	140

* Parts of this chapter have already been published in C. Kaiser, A. Schmiedel, M. Holzapfel, C. Lambert *J. Phys. Chem. C* **2012**, 116, 15265-15280 and D. R. Kattinig, B. Mladenova, G. Grampp, C. Kaiser, A. Heckmann, C. Lambert *J. Phys. Chem. C* **2009**, 113, 2983-2995.

3.4	STEADY STATE SPECTROSCOPY	144
3.4.1	VIS/NIR SPECTROSCOPY DURING CHEMICAL OXIDATION OF F AND J	144
3.4.2	UV/VIS SPECTROSCOPY OF DONOR-ACCEPTOR DYADS A-C...	153
3.4.3	UV/VIS SPECTROELECTROCHEMISTRY OF A, B AND C.....	156
3.4.4	FLUORESCENCE SPECTROSCOPY OF D AND E	158
3.5	TRANSIENT ABSORPTION SPECTROSCOPY	160
3.5.1	FEMTOSECOND TRANSIENT ABSORPTION SPECTROSCOPY ...	160
3.5.2	NANOSECOND TRANSIENT ABSORPTION SPECTROSCOPY	173
4	DISCUSSION	181
4.1	DISCUSSION OF MIXED VALENCE COMPOUND F ⁺	181
4.2	DISCUSSION OF DYADS A-C	184
5	SUMMARY AND CONCLUSION	195
6	EXPERIMENTAL SECTION.....	197
6.1	PREPARATIVE AND ANALYTICAL METHODS	197
6.2	SYNTHESIS	203
6.2.1	SYNTHESIS OF PARACYCLOPHANE PRECURSOR 2	203
6.2.2	SYNTHESIS OF PARACYCLOPHANE PRECURSOR 7	205
6.2.3	SYNTHESIS OF DIBROMO-PARACYCLOPHANE 10	210
6.2.4	SYNTHESIS OF NAPHTALENE BISIMIDE ACCEPTOR 11.....	213
6.2.5	SYNTHESIS OF NAPHTALENE BISIMIDE CYCLOPHANES 13 AND E	215
6.2.6	SYNTHESIS OF DONOR-ACCEPTOR DYADS A AND B	219
6.2.7	SYNTHESIS OF DONOR-ACCEPTOR DYAD C.....	223
6.2.8	SYNTHESIS OF MIXED-VALENCE PRECURSOR F	225
6.2.9	SYNTHESIS OF MIXED-VALENCE PRECURSOR J.....	227
6.2.10	SYNTHESIS OF MIXED-VALENCE PRECURSOR K	229
6.3	CALCULATIONS	230

7 LITERATURE	231
8 STRUCTURAL FORMULA TABLE	238

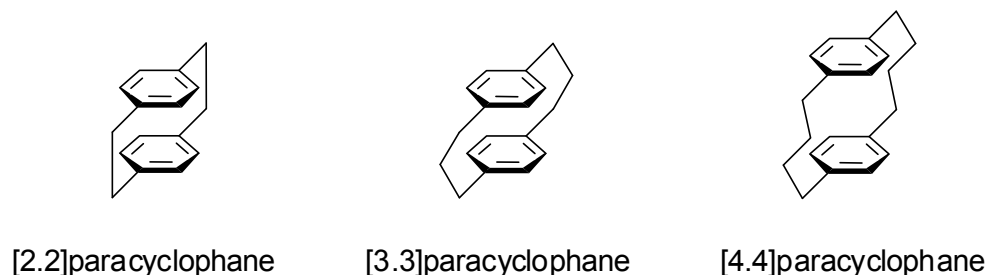
1 INTRODUCTION

In this part of the thesis, electron transfer (ET) was investigated in donor-bridge-acceptor (triarylamine - paracyclophane - triarylamine cation/naphthalene diimide) systems with differently sized paracyclophane bridge units mimicking intermolecular pathways.

A unique aspect of the present study is the integration of [3.3]paracyclophane (see Chart 1) bridges and [2.2]paracyclophane (see Chart 1) bridges into the donor-bridge-acceptor model systems. Paracyclophanes are well known for being one of the simplest rigid structures, which allow for strong through space interactions. The potential for these interactions, which is a result of their closely stacked integral π -systems, make them ideal candidates for studying intermolecular ET.^[1-7]

In the following, a short overview of the most recent advances, regarding unsubstituted [n.n]paracyclophanes (see Chart 1) and systems in which redox active chromophores are linked by such simple cyclophanes, will be provided.

Chart 1

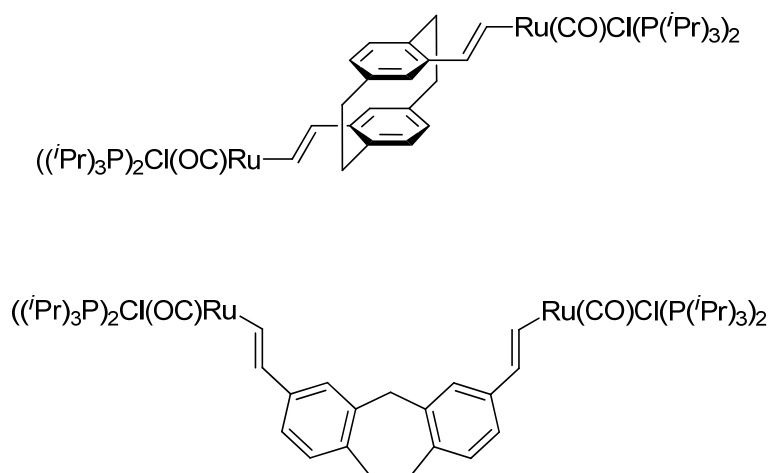


Concerning studies of simple paracyclophanes, basic aspects like rotational barriers, ring strain and structure have been assessed for [2.2]-, [3.3]- and [4.4]paracyclophanes (see Chart 1) in a theoretical study^[8]. Especially the structure and dynamics of [3.3]paracyclophane has been investigated in detail by nuclear magnetic resonance spectroscopy complemented with density functional theory calculations.^[9] In addition, strong charge delocalization for monocations and monoanions between the rings of [3.3]paracyclophanes was detected by employing transient absorption spectroscopy consecutive to pulse radiolysis

and γ -ray irradiation, respectively^[10, 11]. A particularly notable approach utilizing a monolayer environment is the core-hole clock implementation of resonant photoemission spectroscopy which allowed direct measurement of charge transfer rates between aromatic rings in [2.2]- and [4.4]paracyclophanes.^[12]

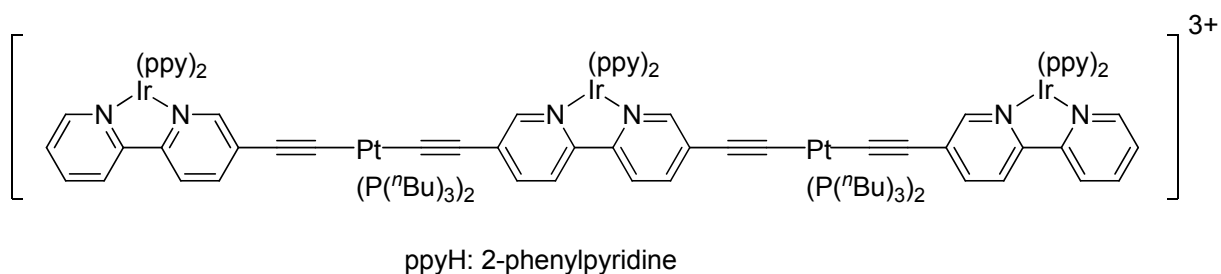
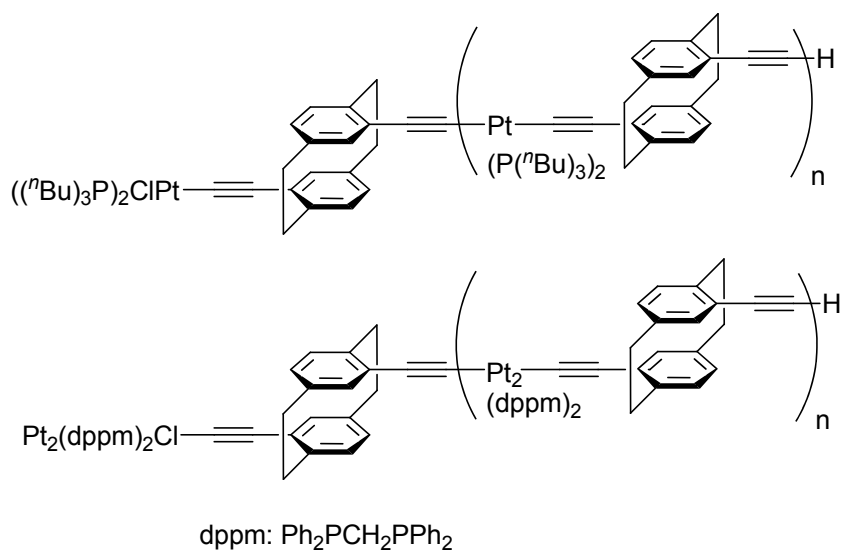
Regarding chromophores interlinked by paracyclophanes, investigations are mostly limited to pseudo-*para* substituted [2.2]paracyclophane bridged systems.

Chart 2



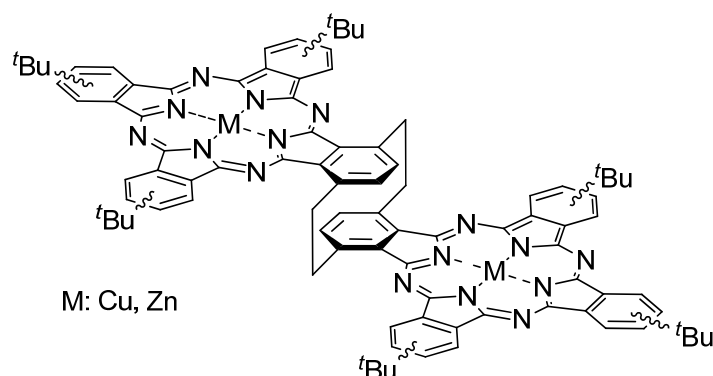
A valuable investigation in this context involved evaluating the effect of the through-space fraction of the ground state electronic interactions provided by the [2.2]paracyclophane. This was realized by bridging Ru-complexes with a [2.2]paracyclophane and with a [2.1]orthocyclophane unit respectively (see Chart 2). The strength of the interactions was estimated by employment of cyclic voltammetry thus determining the half-wave potential difference between both redox centers. Furthermore, shifts of carbon monoxide absorption bands and the intensity of charge transfer bands in the absorption spectra of the monocations, which are mixed-valence compounds, were examined. The results suggest a domination of the through-space interaction in the ground state.^[13]

Chart 3



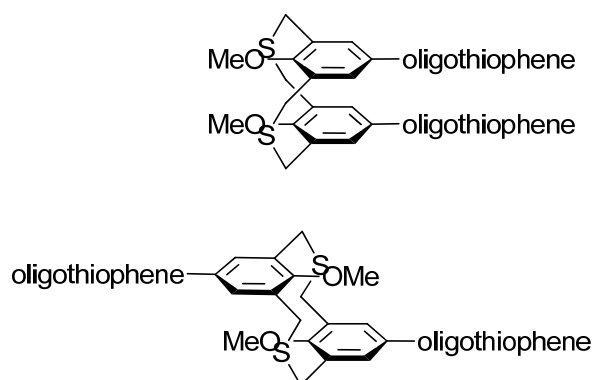
Another study focuses on the strength of the excited state electronic communications mediated by the [2.2]paracyclophane units. The triplet energy transfer between terminal and internal metal-complexes connected by a paracyclophane-bridge was found to be as fast as when they were connected by a Pt-complex (see Chart 3). However, the study has the disadvantage that, aside from the different nature of the bridge units, interactions between different metal complexes (Pt-complexes vs. Ir-complexes) and in different environments (polymer vs. a trimer) were compared. The triplet energy transfer rates used for the assessment were acquired through time dependent fluorescence measurements. ^[14, 15]

Chart 4



An examination proving considerable excited state interactions mediated by a cyclophane involved the inspection of phthalocyanine units forced into a slipped formation by a [2.2]paracyclophane linker (see Chart 4). For this system the strength of the interactions was derived from the analysis of absorption and fluorescence spectra. It was found to be halfway between a phthalocyanine dimer stack^[16] and a dimer where the phthalocyanine rings are directly connected by sharing a terminal phenyl ring^{[17],[18]}.

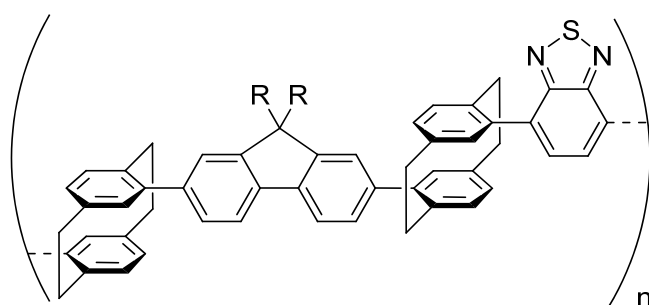
Chart 5



Strong excited state interactions were also observed in systems where thiocyclophane-bridges forced two oligothiophenes into a cofacial in contrast to an “unfolded” arrangement

(see Chart 5). The interactions were detected by analyzing the corresponding fluorescence spectra where the cofacial species showed exciplex bands. However, in these systems the interactions allowing the exciplex formation could progress through both the thiocyclophane units, as well as, due to the close stacking of the thiophenes, directly between the chromophores.^[19, 20]

Chart 6



A study encompassing ground and excited state interactions via paracyclophane units investigated a donor-[2.2]paracyclophane-acceptor-[2.2]paracyclophane-polymer (see Chart 6). The interactions were spotted by comparing the UV/Vis/NIR absorption and emission spectra with those of corresponding monomers. Shifts in the absorption and photoluminescence maxima and the detection of considerable *Förster* resonance energy transfer hinted at strong electronic coupling in the ground and excited state via the paracyclophane-units.^[21, 22]

While assessing the interactions mediated by cyclophanes it has been found to be crucial to carefully account for the nature of the linkage of the redox centers to the cyclophane unit.^[23] This is especially true when steric effects can have considerable influence on the electronic interactions.^[14] Thus, an observed weak overall electronic interaction might lead to an underestimation of the targeted electronic through-space communication potential of the chosen cyclophane unit.

Regarding recent publications, a review concerning bichromophores interlinked by [2.2]paracyclophanes should be mentioned. This review comprises studies on paracyclophanes substituted by various styrene-, amine- and nitro derivatives. These studies treat the photophysical effects of variations to the cyclophane substitution patterns, solvation and the

two photon-absorption behavior of certain of these systems which would go beyond the scope of this introduction.^[24]

In conclusion, while much progress has been made considering through-space interactions, even those in small stacked systems, like paracyclophanes, are still far from being fully understood. The present study will try to provide further insights on interactions mediated by paracyclophanes. Furthermore, while most studies only address the overall interactions (through-bond and through-space) provided via the [2.2]paracyclophane, the present study extends to [3.3]paracyclophane bridges in which through-bond interactions are negligible due to the three consecutive saturated carbons in the linkers.

2 PROJECT AIM

The main goal of this study was to gain insight into intermolecular electron transfer (ET) processes through synthesis and inspection of donor-bridge-acceptor-model systems (see Figure 1), whereby the bridge unit provides a through-space pathway mimicking intermolecular ET.

Nanosecond- and femtosecond-transient absorption spectroscopy, steady state UV/Vis/NIR absorption and fluorescence spectroscopy as well as electrochemistry were employed. Furthermore, electron paramagnetic resonance spectroscopy^[25] and x-ray crystallography data were acquired with the help of cooperation partners. Some results are complemented by kinetic simulations and quantum chemical calculations.



Figure 1. Donor-bridge-acceptor model system.

The specifically designed donor-bridge-acceptor model systems (see Figure 1) utilized in this study consist of the following elements.

Bridging units [2.2]- and [3.3]paracyclophanes were selected (see Section 1 Chart 1). These units are known to be simple rigid structures which allow for strong electronic through-space interactions via their π -stacked aromatic rings.^[3] Thus, they are ideal model systems for studying intermolecular ET via well-defined pathways. The considerable through space π - π -interactions can be attributed to the distances between the unsubstituted carbons of the aromatic rings of 3.1 Å ^[2, 26] in [2.2]paracyclophane and 3.3 Å ^[27] in [3.3]paracyclophane within the double *van der Waals* radii ($2 \times 1.7 \text{ \AA} = 3.4 \text{ \AA}$) of the carbon atoms for both units. The emphasis on [3.3]paracyclophanes is explained by the fact that in [2.2]paracyclophanes the magnitude of the through-bond-interactions is an issue of ongoing discussion.^[1-7] In [3.3]paracyclophanes these through-bond interactions can be neglected due to the three consecutive saturated carbons in the linkers. In [4.4]paracyclophanes the distance of the

unsubstituted carbon atoms of the aromatic rings of 4 Å^[28] is no longer within the double *van-der-Waals* radii of the carbon atoms and, thus, the electronic interactions are expected to be much weaker.^[12] Furthermore, the rigidity is lost as it allows for flipping of the rings.^[8, 29] These considerations led to the abandonment of this possible bridging unit in the present study.

Para-substituted triarylamine (TAA) was employed as a strong donor. TAAs are well-known for their application in the XEROX[®] process and for their use as hole transport materials in other (opto-)electronic devices, like organic light-emitting diodes, field-effect transistors or solar cells.^[30-35] Furthermore, *para*-position substituted triarylaminines can be converted into very stable radical cations, which generally show a characteristic strong and sharp absorption band in the 13 000–15 000 cm⁻¹ region.^[7, 36] In addition their redox potential can be tuned by altering the substituents in *para*-position.^[36, 37]

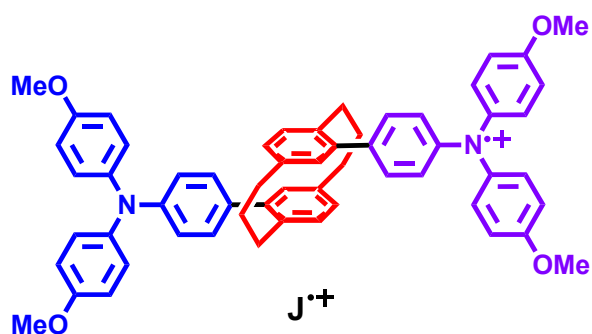
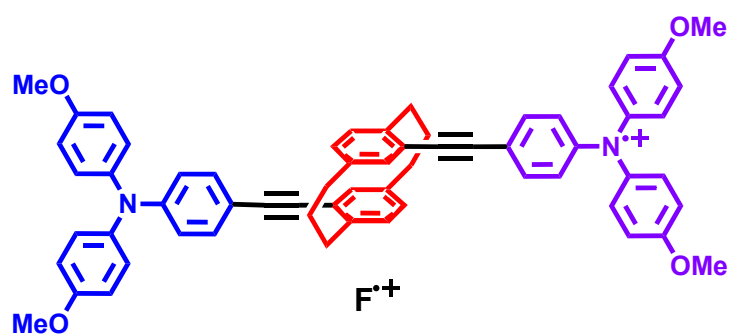
Two different acceptors were chosen to meet the preconditions of the available measurement techniques and the aims of the studies. The stable *para*-substituted triarylamine radical cation (see above) was utilized to yield symmetric organic mixed-valence^[38] model compounds I (see Figure 2) to study optically and thermally induced ET. For studies on charge separation (CS) and charge recombination (CR), naphthalene-1,8:4,5-bis(dicarboximide) (NDI) was used to create donor-acceptor model compounds II (see Figure 3). Some NDI derivatives are promising candidates as air stable semiconductors with high electron mobility for the application in organic field effect transistors.^[39-44] A particular property of NDI is to undergo fast intersystem crossing (ca. 10 ps in chloroform)^[45] without the use of heavy metals.^[46-48] However, this is only true for N-alkyl substituted NDI while in N-aryl substituted NDI the formation of CT states is faster (0.5 ps in chloroform). However, these CT states can still yield locally excited triplet states.^[45] Another property of NDI is that it may form a stable radical anion which shows a sharp and intense absorption band at 21 000 cm⁻¹ and a low intensity band at about 16 500 cm⁻¹. In particular, its steady state absorption can be electronically tuned by core substituents.^[42, 47, 49-64] Furthermore, the the lowest unoccupied molecular orbital (LUMO) comprises the oxygen lone pairs in the σ -plane in unsubstituted NDI.^[40, 58] This changes if conjugated substituents are attached to the NDI-nitrogen, which makes the LUMO to be π -type.^[40, 58] Due to the nodes in the LUMO and the π -highest occupied molecular orbital (HOMO) along the molecular long axis, the substituents connected via the nitrogen atoms are electronically decoupled from the central π -system, therefore delaying possible CS and CR processes.^[40, 58] Another favorable side effect of this weak electronic interaction is that local electronic transitions and the reduction potentials of

N-attached NDI are left unchanged when altering bridging molecules or the donor strength in dyads that contain NDIs.^[40, 41, 46, 49, 56, 57, 65-71]

The resulting model systems I (see Figure 2) are symmetric organic mixed valence compounds. This class of compounds can be defined as systems in which structurally identical redox centers in different formal redox states are connected (via organic bridges). Furthermore they possess, in contrast to other organic donor-acceptor systems (see below), an open-shell ground state. These compounds have proven to be ideally suited for electron transfer investigations on numerous occasions.^[38] A special virtue of these compounds is that electron transfer can be induced optically as well as thermally. The specific choice of bistriarylamine systems for the present investigation is due to the fact that the absorption charge transfer bands of these compounds are usually in the near infrared and can therefore be investigated by conventional UV/Vis/NIR absorption spectroscopy.^[7, 38, 72-81] Another reason was the experience within our workgroup regarding the photophysical properties of bistriarylamine mixed valence compounds.^[7, 72-81] In particular, the characteristics of bistriarylaminines **G**⁺ and **N**⁺ and monotriarylamine fragments **L**⁺ and **D**⁺ serve as a basis for the discussion of the target compounds of this work (see Figure 2).^[7]

Model systems II are organic donor-acceptor compounds (see Figure 3). Such compounds are organic molecules in which a donor, a redox center which provides electrons is connected (via a bridge) to an acceptor, a redox center which accepts electrons. An important advantage resulting from the specific selection of the redox chromophores is that the spectra of the main absorption bands of the TAA radical cation and NDI radical anion do not overlap with the ground state absorption of the dyads, which ensures unequivocal characterization of the charge separated states. This makes them well-suited to be studied by transient absorption spectroscopy. Furthermore, the cyclophane bridge as well as its attachment to the nitrogen of the NDI (see above) should lead to a weakly coupled system, which promotes the longevity of the charge separated states upon photoexcitation. In addition, the unique properties of the NDI are expected to enhance the probability of intersystem crossing (see above) and therefore to provide the opportunity to study the effects of triplet generation on the speed of charge recombination.

TARGET COMPOUNDS



LITERATURE KNOWN MAIN REFERENCE COMPOUNDS

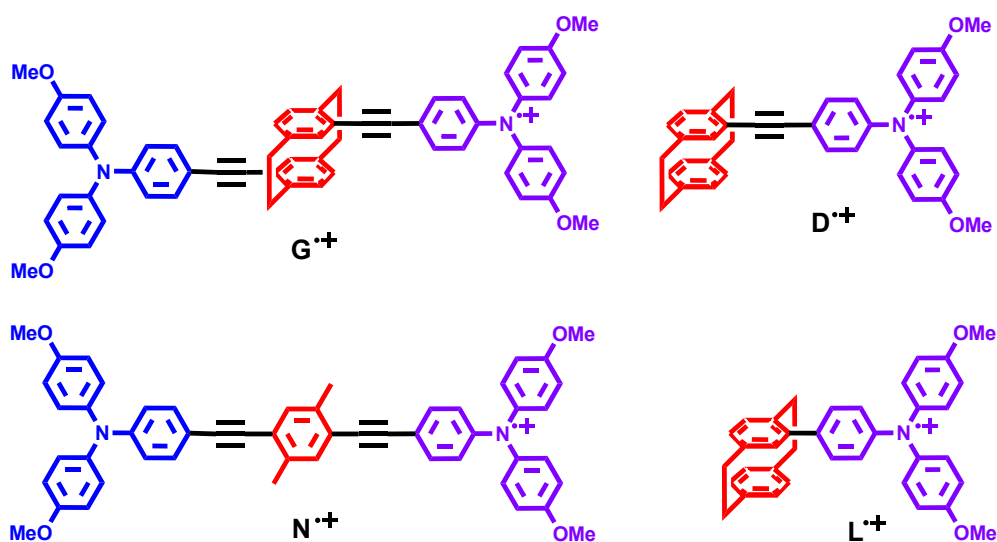


Figure 2. Structural formulas of target model systems and main reference compounds including functional assignment of their segments: donor (blue), bridge unit (red) and acceptor (purple).

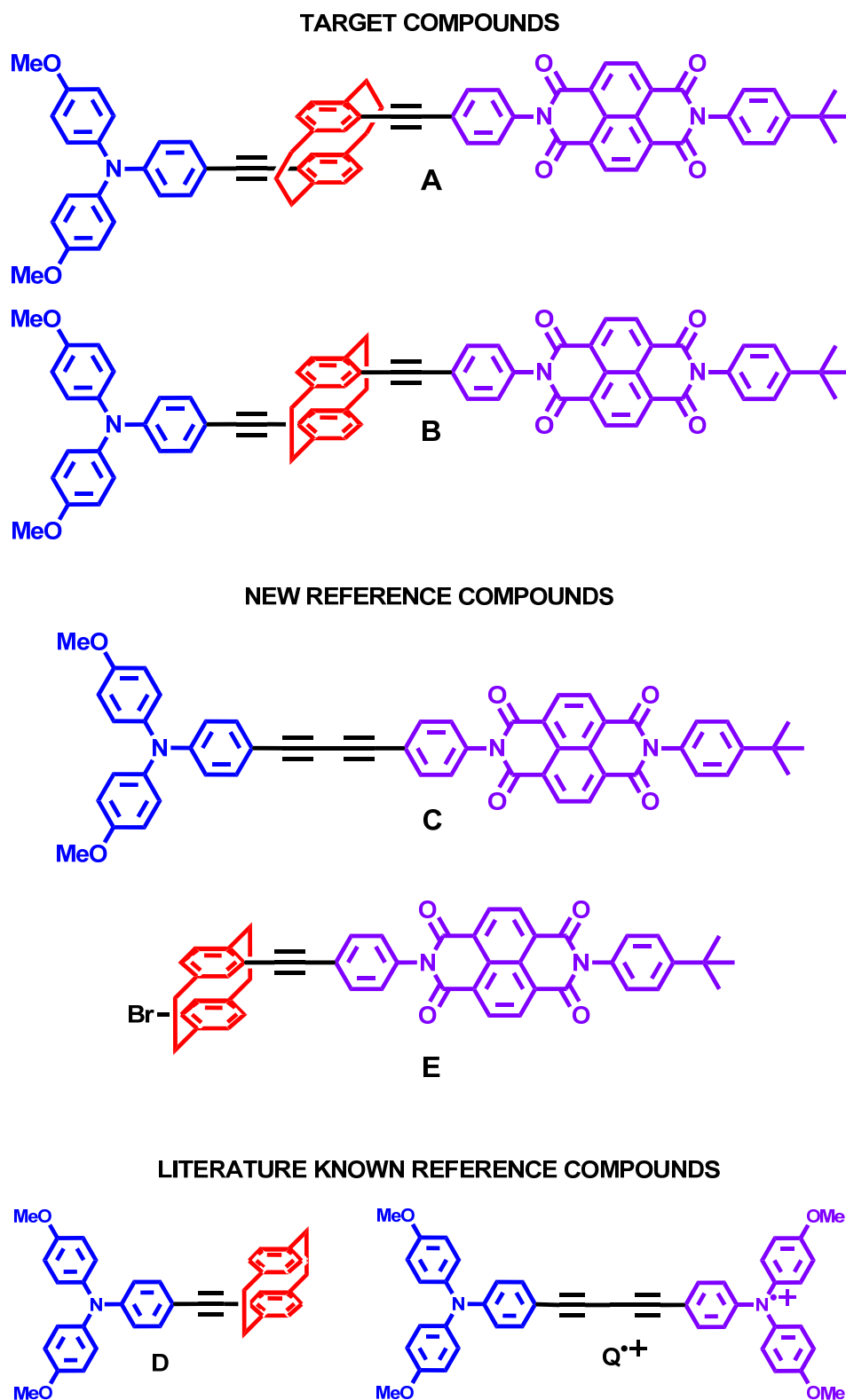


Figure 3. Structural formulas of target model systems and main reference compounds including functional assignment of their segments: donor (blue), bridge unit (red) and acceptor (purple).

3 RESULTS AND DISCUSSION

3.1 SYNTHESIS

3.1.1 BUILDING BLOCKS

All target compounds were synthesized via the building blocks shown (see Figure 4).

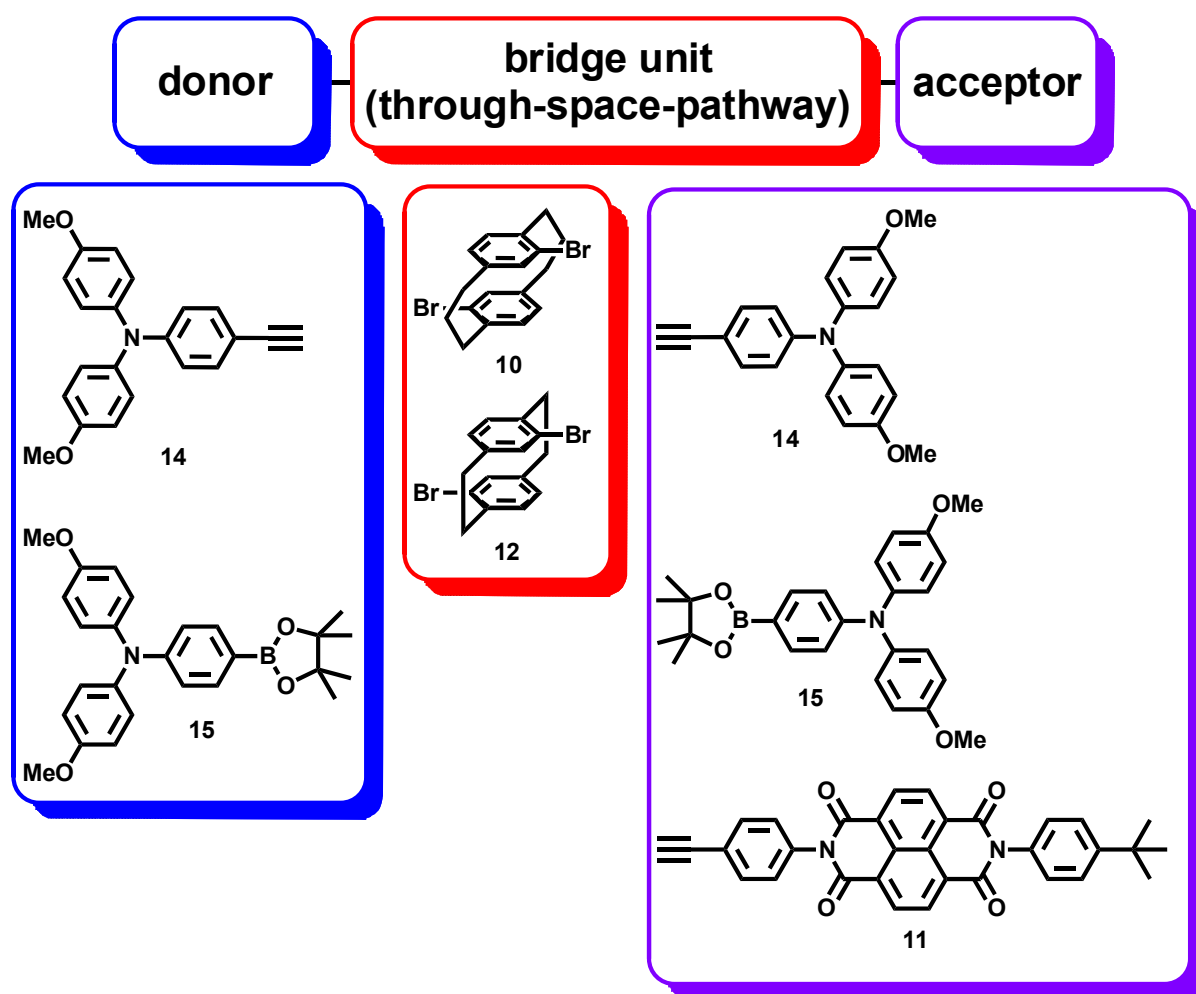
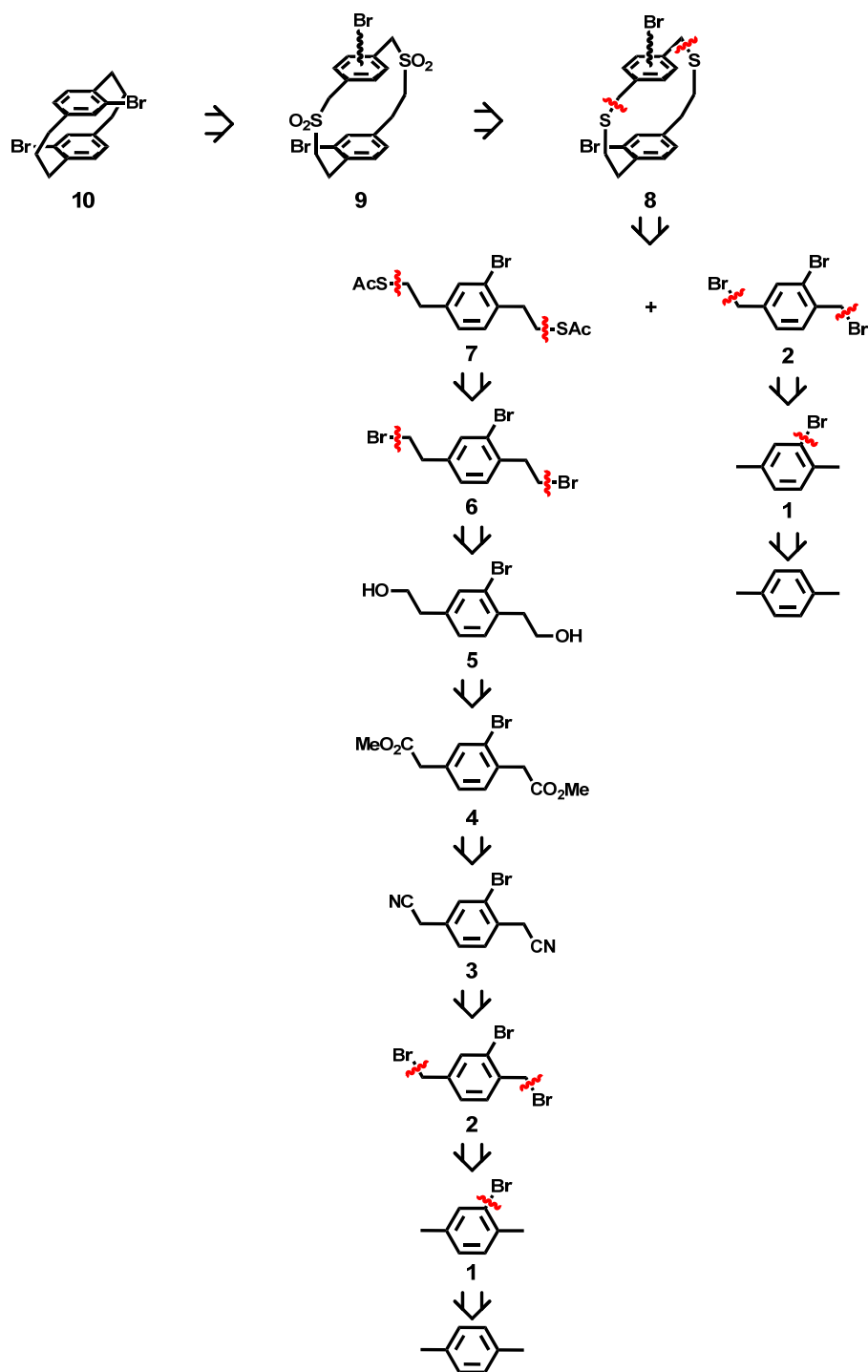


Figure 4. Structural formulas of building blocks including targeted functional assignment: donor (blue), bridge unit (red) and acceptor (purple).

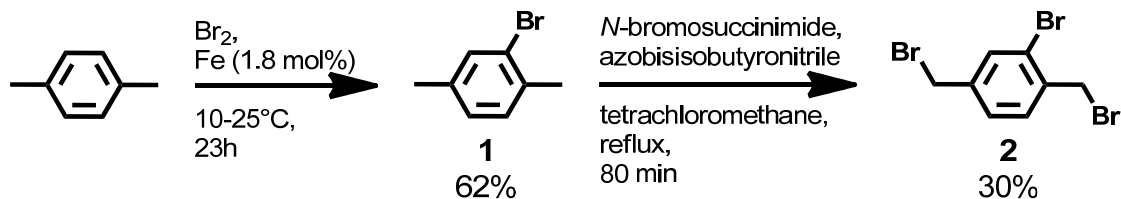
3.1.2 RETROSYNTHETIC SCHEME OF PARACYCLOPHANE 10

Paracyclophane **10** was synthesized according to the retrosynthetic scheme shown (see Scheme 1)



Scheme 1. Retrosynthetic scheme of Paracyclophane **10**.

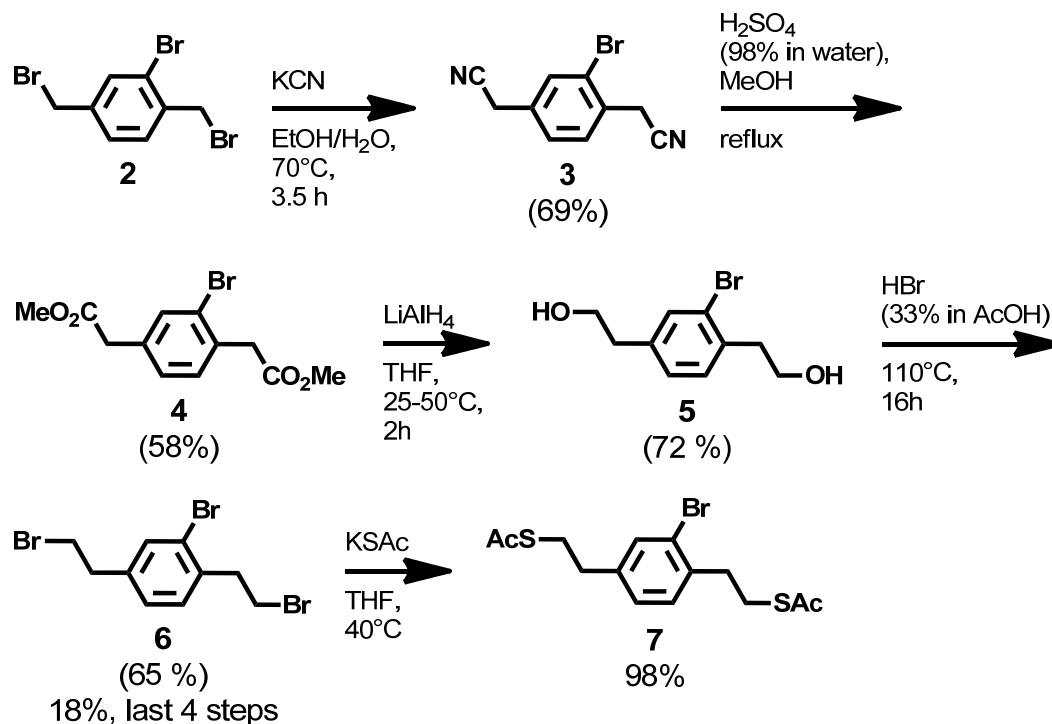
3.1.3 SYNTHESIS OF PARACYCLOPHANE PRECURSOR 2



Scheme 1. Synthesis of Precursor 2.

p-Xylene was monobrominated with bromine by iron catalysis (see Scheme 1). Due to the batch size, great care had to be taken to avoid escape of the considerable amounts hydrobromide generated. Purification was easily accomplished via fractional distillation under reduced pressure. Intermediate **1** was brominated at its two methyl groups by radical reaction with *N*-bromosuccinimide (see Scheme 1). Tetrachloromethane under reflux conditions was chosen as a solvent to ensure the immediate reaction of the successively added *N*-bromosuccinimide/azobisisobutyronitrile portions and thus avoid postponed high-energy exothermic reactions.

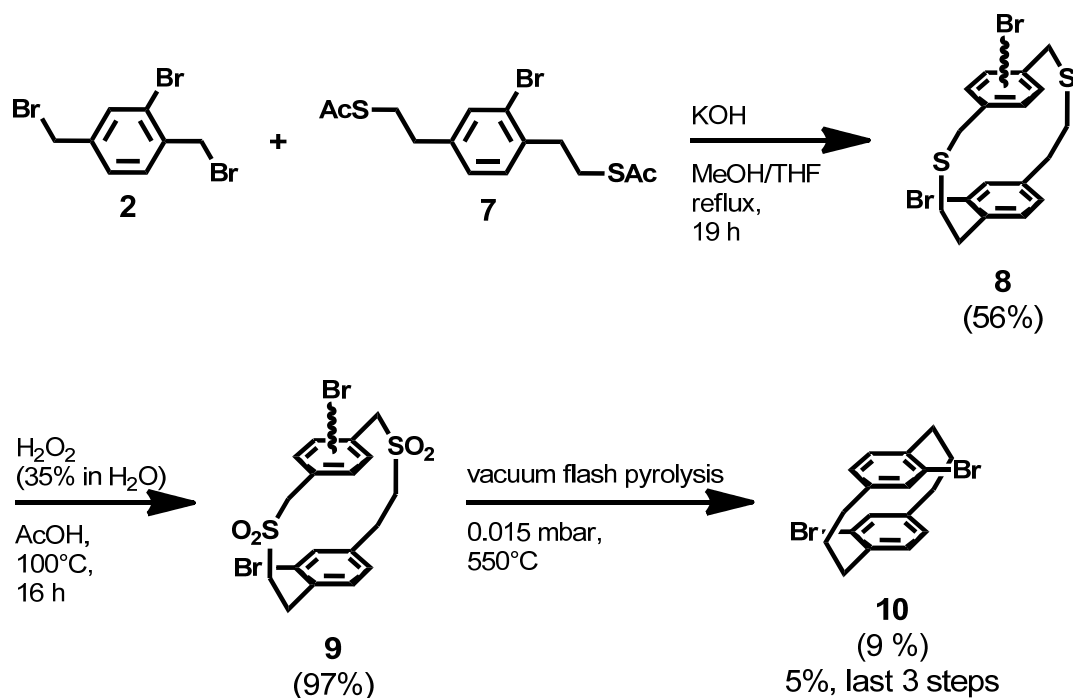
3.1.4 SYNTHESIS OF PARACYCLOPHANE PRECURSOR 7



Scheme 2. Synthesis of Precursor 7. (Yields in brackets are estimated by nuclear magnetic resonance spectra of the crude product.)

Alkyl chain elongation was achieved by nucleophilic substitution of the two benzylic bromine atoms of **2** with potassium cyanide to give the dinitrile **3**, followed by nitrile hydrolysis combined with *in situ* esterification in a single step with sulfuric acid in dry methanol (see Scheme 2). The resulting diester **4** was then reduced with lithium aluminum hydride to yield the diol **5** (see Scheme 2). Subsequent bromination of this intermediate diol was carried out with hydrogen bromide solution in acetic acid as described by Hopf *et. al.*^[82] for paracyclophane synthesis and gave **6** (see Scheme 2). While **6** was purified by flash column chromatography, only analytic samples of **3**, **4** and **5** were purified to save resources and the yields were estimated by nuclear magnetic resonance spectroscopy. Thereafter an acetyl protected thiol group was introduced into compound **6** via a nearly quantitative nucleophilic substitution of bromine with potassium thioacetate. Due to the analytic purity upon workup, no purification technique had to be employed (see Scheme 2).

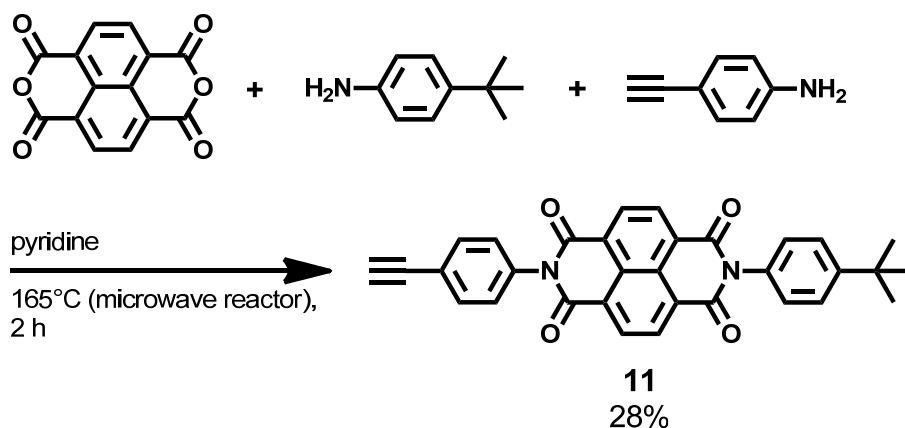
3.1.5 SYNTHESIS OF PARACYCLOPHANE 10



Scheme 3. Synthesis of Paracyclophane **10**. (Yields in brackets are estimated by nuclear resonance spectra of the crude product.)

In a high dilution reaction, the *in situ* deprotected sulfides of compound **7** reacted with compound **2** in a one-step cyclisation thereby yielding the dithia-paracyclophane **8** as a mixture of isomers with regard to the relative position of the bromine substituents (see Scheme 3). Subsequently, the sulfur atoms were oxidized by hydrogen peroxide to give the bis-sulfone-paracyclophane **9**. The isomeric mixtures **8** and highly insoluble **9** were not fully characterized and the yield of **9** was only estimated by the mass of the crude product. Paracyclophane **9** was treated in a vacuum flash pyrolysis, which induces a ring contraction by SO_2 extrusion (see Scheme 3). Separation of 5,18-dibromo-[3.3]paracyclophane **10** from the other regioisomers of the product mixture was achieved by repetitive recrystallization, thus limiting the yield of this final step.

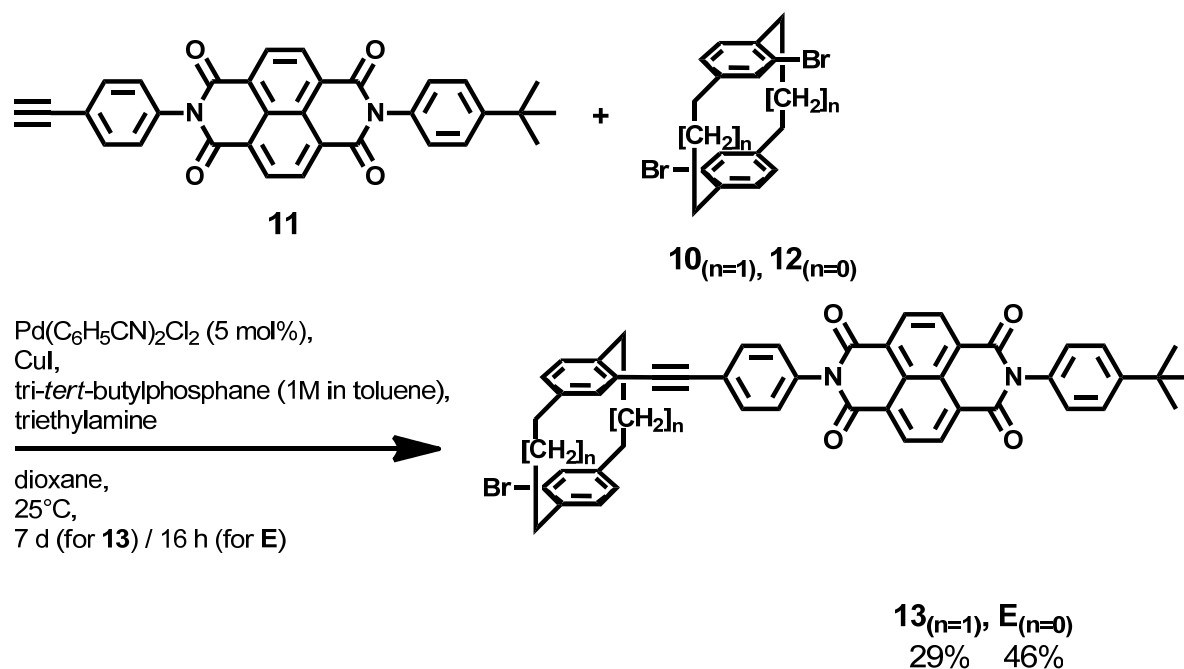
3.1.6 SYNTHESIS OF NAPHTHALENE BISIMIDE ACCEPTOR 11



Scheme 4. Synthesis of naphthalene diimide acceptor **11**.

The naphthalene diimide acceptor **11** was synthesized by a one pot double imide formation in a microwave reactor from readily available compounds: namely, the naphthalene dianhydride and the two different aniline derivatives, 4-*tert*-butylaniline and 4-ethynylaniline (see Scheme 4). The bisalkyne side product could, due to its insolubility, be separated easily, and the bis-*tert*-butyl side product was removed by flash column chromatography.

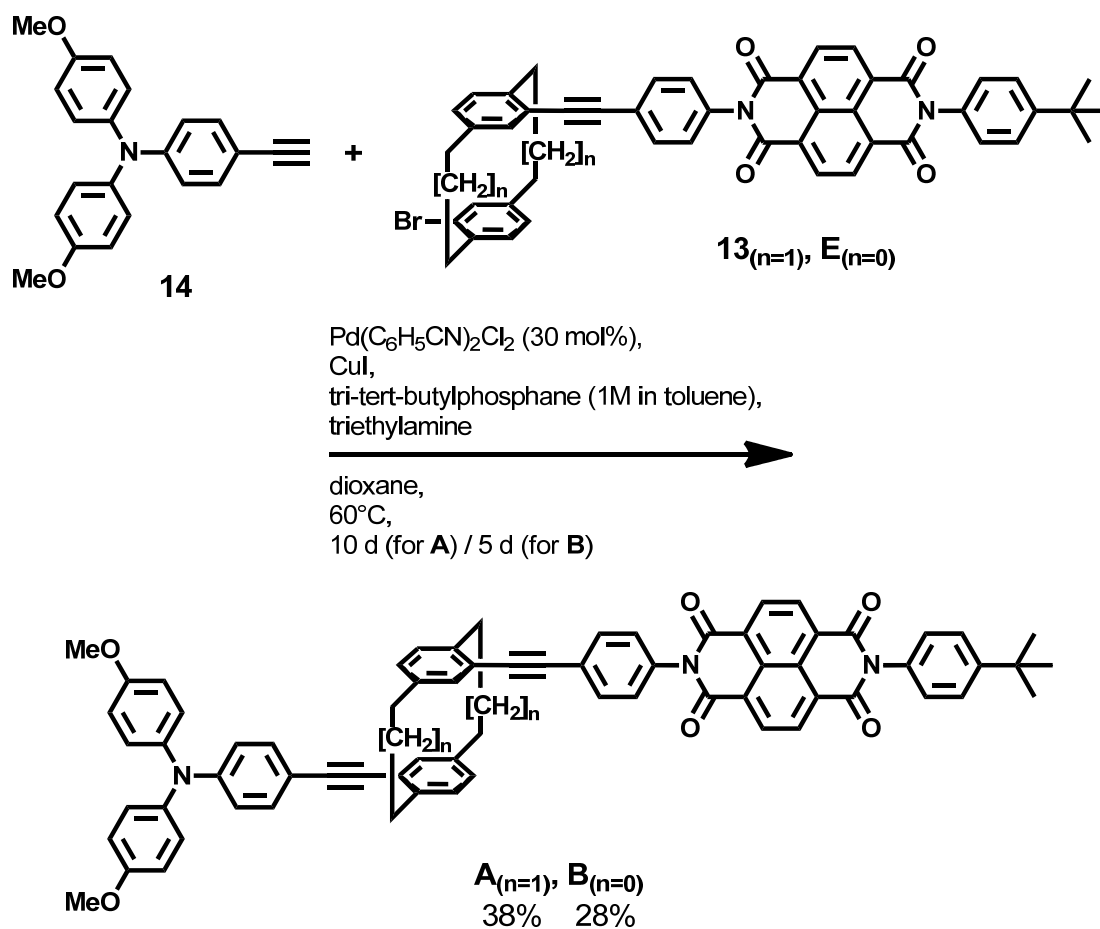
3.1.7 SYNTHESIS OF NAPHTHALENE BISIMIDE CYCLOPHANES **13** AND **E**



Scheme 5. Synthesis of naphthalene diimide cyclophanes **13** and **E**.

The cyclophanes compound **13** and **E** were synthesized by coupling of the naphthalene diimide acceptor **11** via a Sonogashira reaction to the dibrominated paracyclophanes **10** and **12**, respectively (see Scheme 5). The product was purified by flash column chromatography and solvent extraction (of remaining traces of impurities). Especially during this coupling reaction, regulating the temperature was crucial for obtaining the best—though still quite moderate—yields.

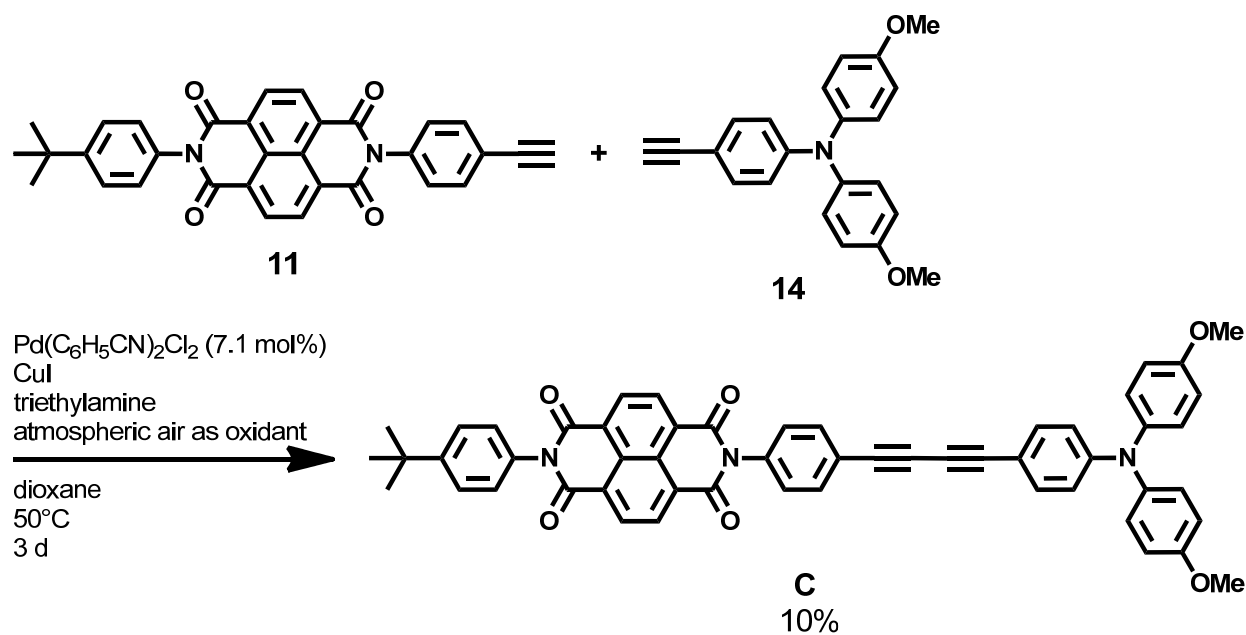
3.1.8 SYNTHESIS OF DONOR-ACCEPTOR DYADS A AND B



Scheme 6. Synthesis of donor-acceptor dyads **A** and **B**.

Compound **14** was coupled via Sonogashira coupling with the acceptor substituted cyclophanes **13** and **E** to obtain **A** and **B** (see Scheme 6).

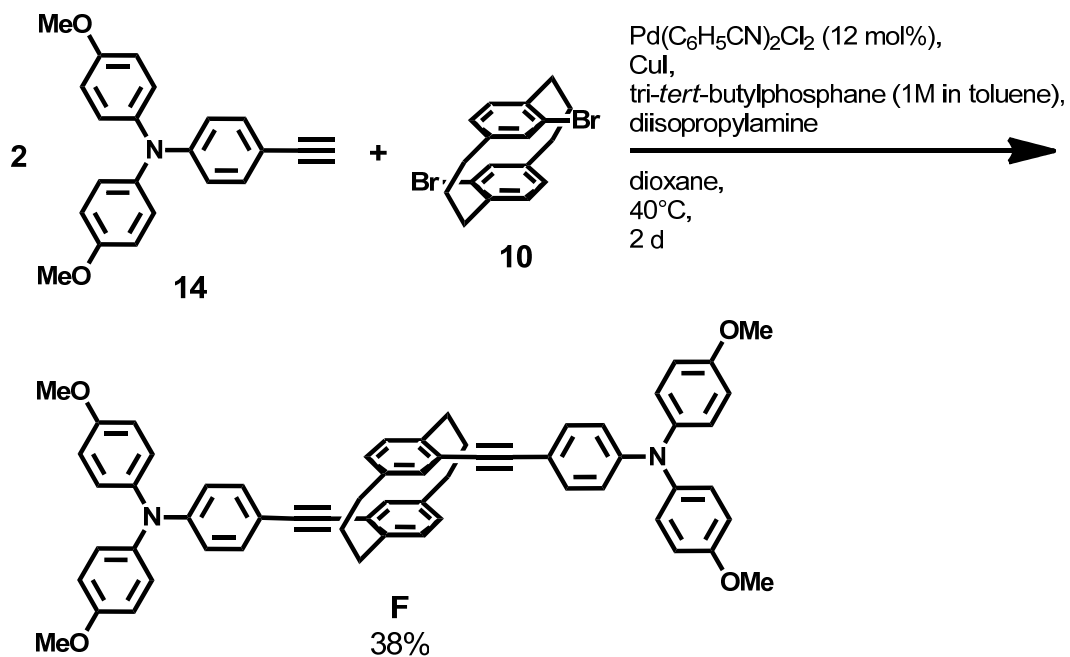
3.1.9 SYNTHESIS OF DONOR-ACCEPTOR DYAD C



Scheme 7. Synthesis of donor-acceptor dyad **C**.

Reference dyad **C** was prepared by oxidative Pd-catalyzed coupling of the donor and acceptor compounds **14** and **11** (see Scheme 7). For purification, flash column chromatography followed by gel permeation chromatography was employed.

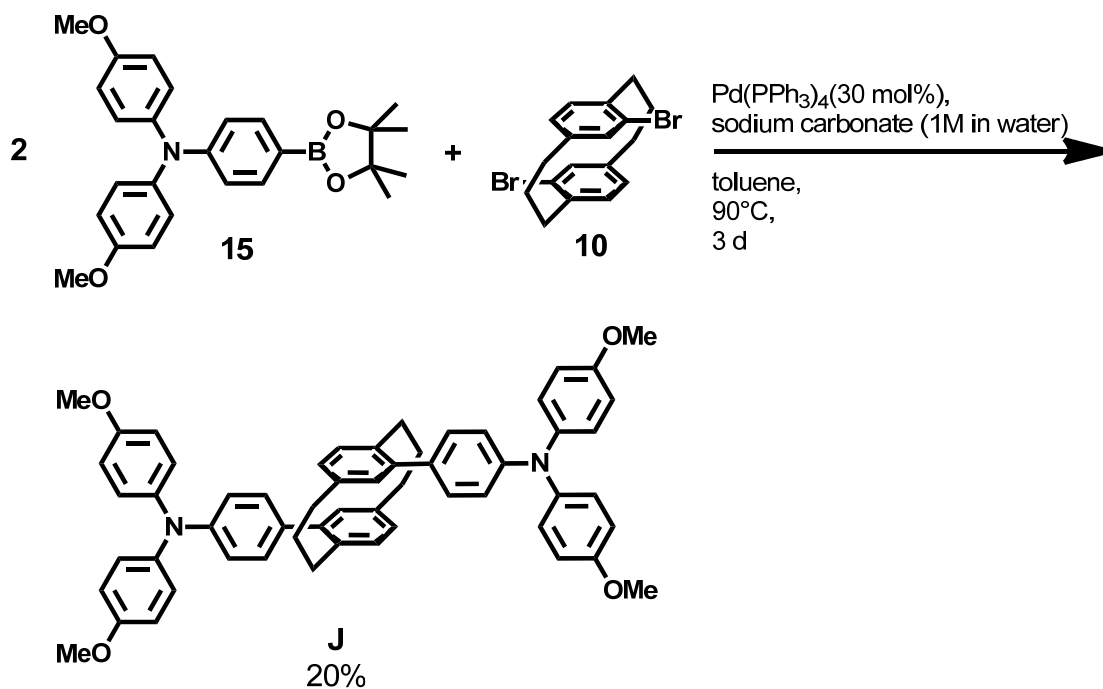
3.1.10 SYNTHESIS OF MIXED-VALENCE PRECURSOR F



Scheme 8. Synthesis of mixed-valence precursor **F**.

14 was coupled via Sonogashira coupling to the dibromocyclophane **10**. For purification, column chromatography followed by recrystallization was employed (see Scheme 8).

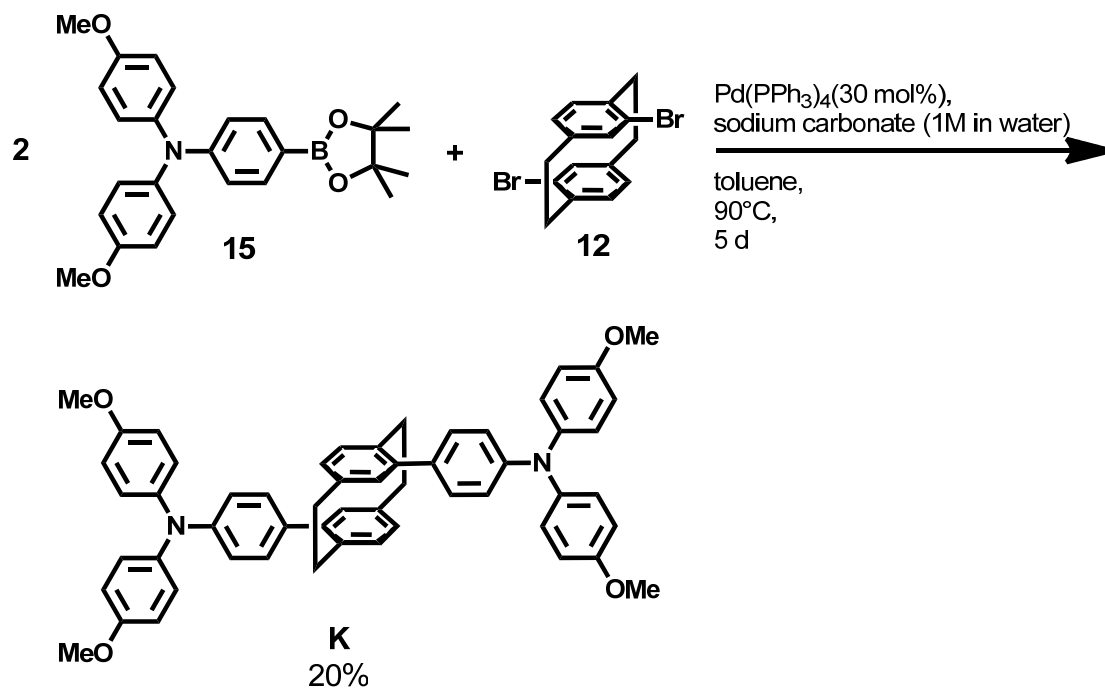
3.1.11 SYNTHESIS OF MIXED-VALENCE PRECURSOR J



Scheme 9. Synthesis of mixed-valence precursor **J**.

The TAA compound **J** was synthesized by coupling of the TAA **15** via a Suzuki-reaction with the dibrominated paracyclophane **12** (see Scheme 9).

3.1.12 SYNTHESIS OF LITERATURE KNOWN MIXED-VALENCE PRECURSOR K



Scheme 10. Synthesis of mixed-valence precursor **K**.

For the synthesis of precursor **K** a modified version of the literature known Suzuki-reaction^[7] was used to couple the triaryl amines **15** to the paracyclophane **12** (see Scheme 10).

3.2 CRYSTAL STRUCTURES

Single crystals of compounds **10**, **J** and **K**, which allowed for X-ray crystal structure analysis, were prepared. The crystallographic data confirms unequivocal identification of the compounds. In particular, it ensures in the targeted *pseudo*-para substitution pattern of the paracyclophanes (see Figures 5-7). In addition, close inspection of the molecular structures reveals the three-dimensional arrangement of the stacked aromatic rings within the target compounds. As expected from literature, unsubstituted [3.3]paracyclophanes in contrast to [2.2]paracyclophanes showed a shift between the stacked aromatic rings (see Figure 8 and Table 1). The magnitude of this shift d_{shift} is dependent on the substituents and is substantially more pronounced in the dibromo-substituted compound **10** than the very similar values of compound **J** and unsubstituted [3.3]paracyclophane. Furthermore, depending on the extent of this shift, the distance between the planes of the aromatic rings d_{planes} is smaller than one would expect from the distance of the unsubstituted carbons d_{unsubst} of the aromatic rings (see Figure 8 and Table 1).

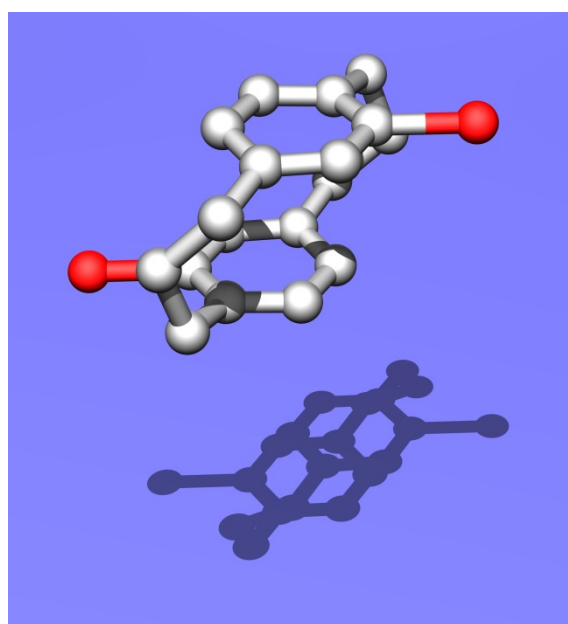


Figure 5. Crystal structure of **10**: $\text{C}_{18}\text{H}_{18}\text{Br}_2$, $M_r = 394.14$, colorless plate, $0.20 \times 0.10 \times 0.08$, Triclinic space group $P-1$, $a = 8.5921(9)\text{\AA}$, $b = 10.0413(10)\text{\AA}$, $c = 10.2789(10)\text{\AA}$, $\alpha = 109.600(2)^\circ$, $\beta = 92.007(2)^\circ$, $\gamma = 112.712(2)^\circ$, $V = 756.71(13)\text{\AA}^3$, $Z = 2$, $\rho_{\text{calcd}} = 1.730 \text{ g}\cdot\text{cm}^{-3}$, $\mu = 5.344 \text{ mm}^{-1}$, $F(000) = 392$, $T = 173(2) \text{ K}$, $R_1 = 0.0517$, $\omega R^2 = 0.1098$, 4737 independent reflections [$2\theta \leq 63.5^\circ$] and 181 parameters.

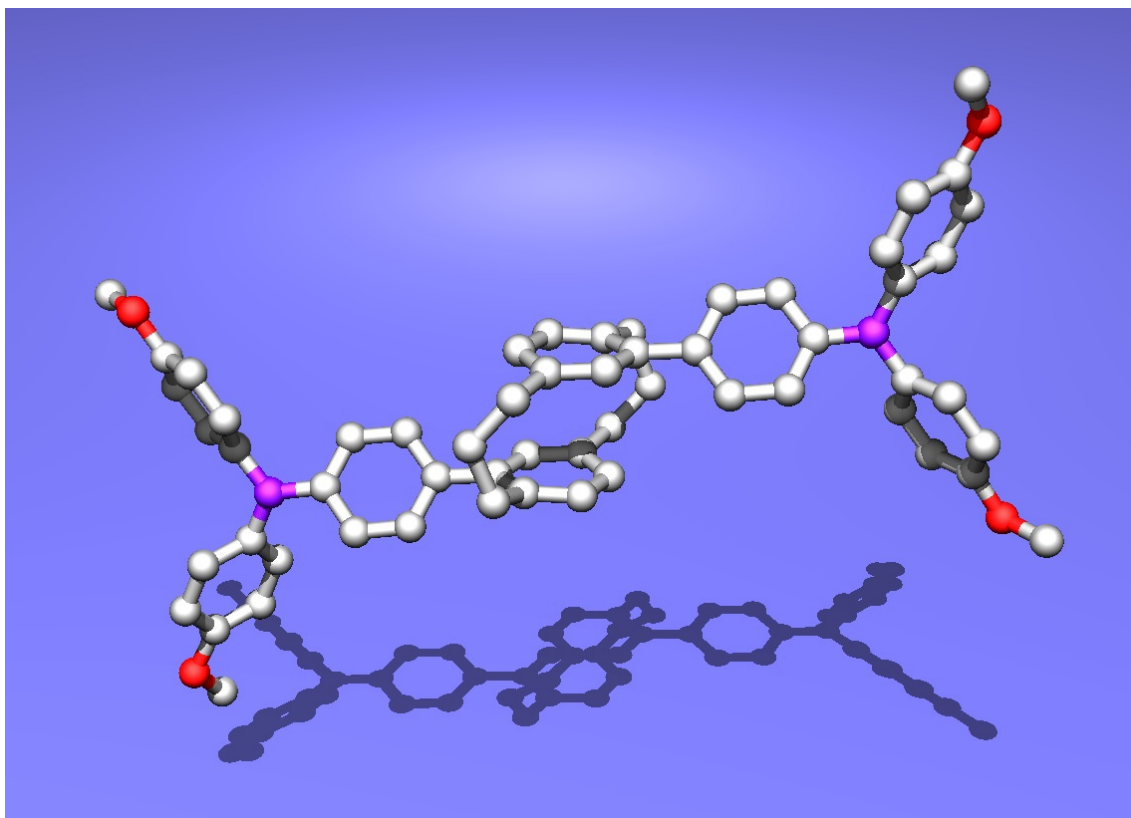


Figure 6. Crystal structure of **J** (cocrystallized benzol molecules not shown): $C_{82}H_{78}N_2O_4$, $M_r = 1155.46$, colourless plate, $0.30 \times 0.21 \times 0.07 \text{ mm}^3$, Triclinic space group $P-1$, $a = 7.7868(5) \text{ \AA}$, $b = 9.9920(7) \text{ \AA}$, $c = 21.3840(14) \text{ \AA}$, $\alpha = 87.677(2)^\circ$, $\beta = 89.502(2)^\circ$, $\gamma = 73.517(2)^\circ$, $V = 1594.10(18) \text{ \AA}^3$, $Z = 1$, $\rho_{\text{calcd}} = 1.204 \text{ g}\cdot\text{cm}^{-3}$, $\mu = 0.073 \text{ mm}^{-1}$, $F(000) = 616$, $T = 100(2) \text{ K}$, $R_1 = 0.0570$, $\omega R^2 = 0.1284$, 6464 independent reflections [$2\theta \leq 52.8^\circ$] and 375 parameters.

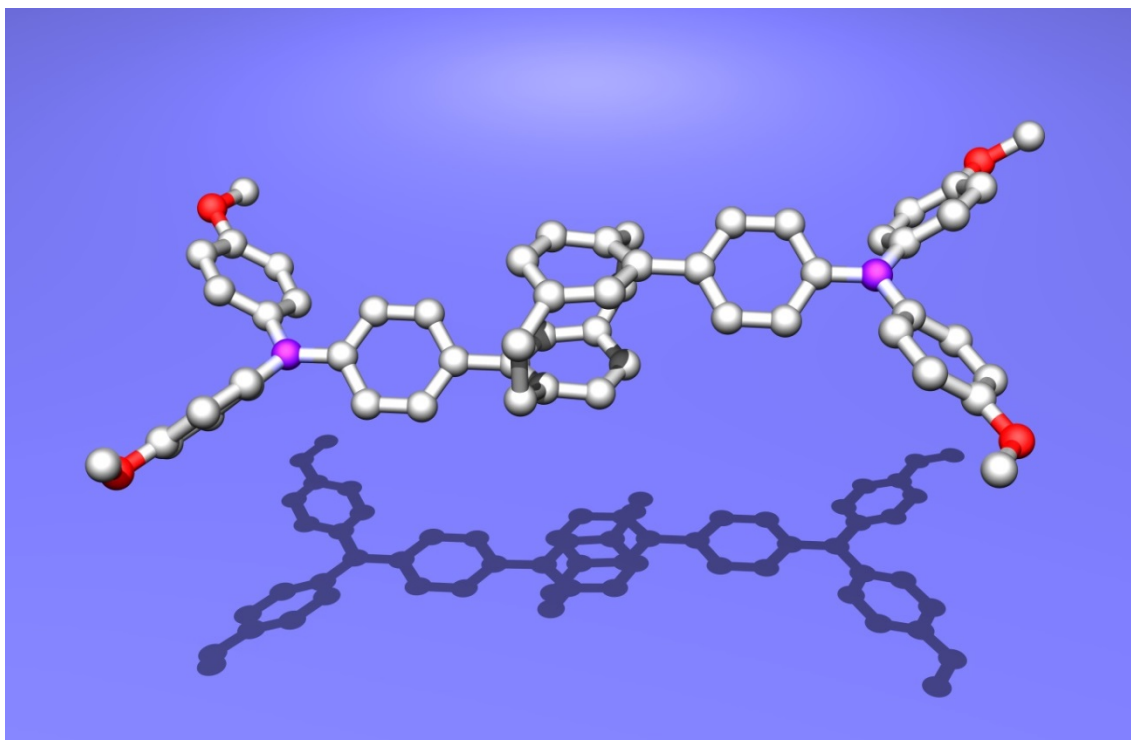


Figure 7. Crystal structure of **K**: C₅₆H₅₀N₂O₄, $M_r = 814.98$, colourless plate, 0.35×0.25×0.05 mm³, Orthorhombic space group *Pna*2₁, $a = 12.1294(12)$ Å, $b = 7.6822(7)$ Å, $c = 45.398(5)$ Å, $V = 4230.2(7)$ Å³, $Z = 4$, $\rho_{\text{calcd}} = 1.280$ g·cm⁻³, $\mu = 0.080$ mm⁻¹, $F(000) = 1728$, $T = 100(2)$ K, $R_1 = 0.0731$, $wR^2 = 0.1294$, 8174 independent reflections [$2\theta \leq 52.82^\circ$] and 564 parameters.

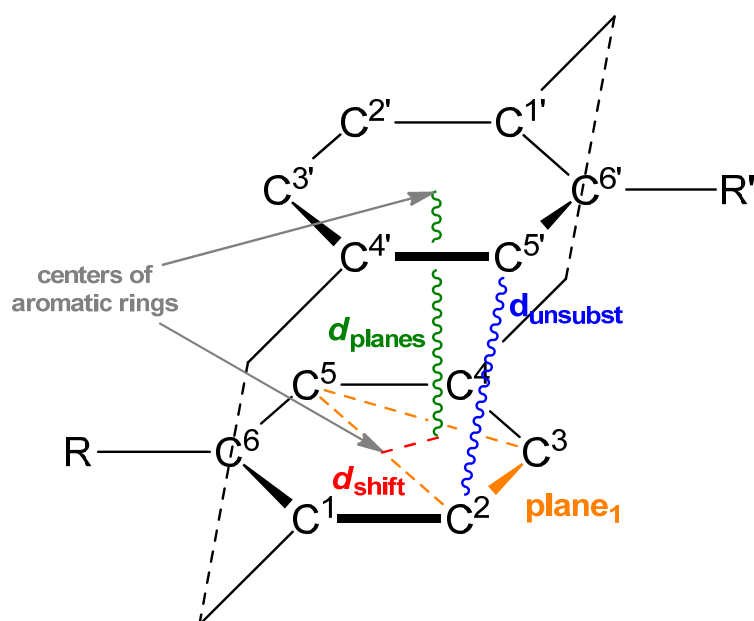


Figure 8. Cyclophane model defining key distances and plane₁.

Table 1. Key distances d (see Figure 5): d_{unsubst} between C² and C^{5'}, d_{planes} between the stacked aromatic rings (approximated by the averaged distance between plane₁ and carbons C^{2'}, C^{3'} and C^{5'}) and d_{shift} of parallel shift of the stacked aromatic rings (approximated by the distance from C² to the projection of C^{5'} onto plane₁) of the compounds **10**, **J**, **K** in comparison to [2.2]paracyclophane^[2, 26] and [3.3]paracyclophane^[27].

compound	d_{unsubst}	d_{planes}	d_{shift}
10	3.24 Å	3.18 Å	0.62 Å
J	3.29 Å	3.25 Å	0.51 Å
[3.3]paracyclophane	3.30 Å ^[27]	3.26 Å ^[27]	0.48 Å ^[27]
K	3.07 Å		0
[2.2]paracyclophane	3.09 Å ^[2, 26]		0

3.3 CYCLIC VOLTAMMETRY

3.3.1 CYCLIC VOLTAMMETRY OF MIXED-VALENCE PRECURSOR F

The cyclic voltammogram of dyad **F** was recorded and analyzed to roughly estimate the strength of interactions between [3.3]paracyclophane bridged triarylamine redox centers. Furthermore, the gathered data were used to assess the fraction of biradical cations $\mathbf{F}^{\bullet\bullet+}$ present during the recording of the UV/Vis/NIR spectra and electron paramagnetic resonance spectra of the monoradical cation $\mathbf{F}^{\bullet+}$.

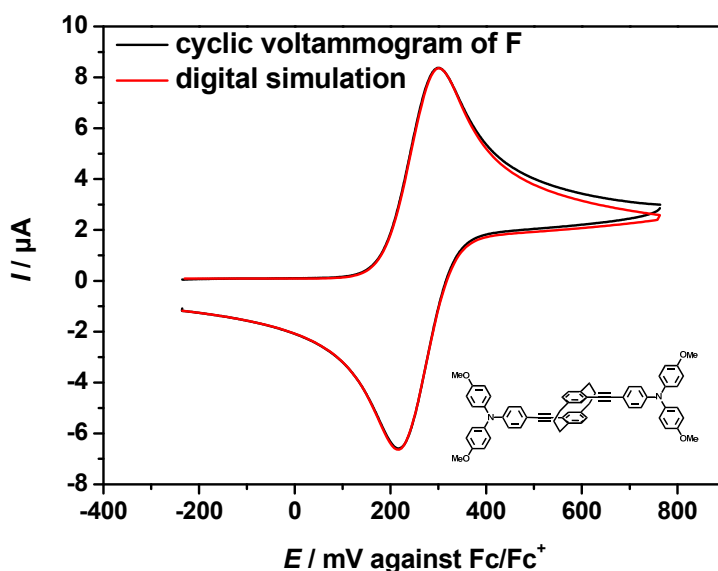


Figure 9. Cyclic voltammogram (CV) of **F** recorded with a scan rate of 250 mV s^{-1} in dichloromethane (0.15 M tetrabutylammonium hexafluorophosphate) versus ferrocene/ferrocenium.

In the cyclic voltammogram of **F** (see Figure 9), one apparent redox wave with a half-wave potential $E_{1/2}$ of about 260 mV could be detected. However, since the underlying redox processes of the two triarylamine redox centers could not be resolved, digital simulation with DigiSim^[83] was employed in the analysis. Thus, a simultaneous 2-electron process was excluded for both compounds. Furthermore, two half-wave potentials of 235 mV and 280 mV with a potential difference $\Delta E(\text{Ox1}, \text{Ox2})$ of 45 mV were determined for **F**. These potential differences are larger than the statistic value of 35.6 mV at 298 K ^[84] for two non-interacting

redox centers and, therefore, suggests electronic coupling between the redox centers within both compounds. For other paracyclophane bridged systems higher values like 215 mV^[13] for Ru-complexes attached via their ethylene ligands, 100 mV^[85] for Fe-complexes attached via ethynyl-ligands and 80 mV^[23] for Re-complexes attached via the terminal nitrogen of their picolinaldimin-ligands were observed. Even larger values were determined for systems where the paracyclophane rings are part of the redox centers, like 200 mV for 1,4-naphthoquinone, 420 mV for 1,4-benzoquinone or 290 mV for 1,4-dimethoxybenzol.^[86-88] These values indicate that the interactions in **F** are weak. However, one has to bear in mind that contributions from solvation energy changes and ion pairing are not accounted for and thus the values cannot serve as a basis for a more elaborate interpretation.^[89-92] The comparability between the following values is more reliable since they at least possess the same triarylamine redox centers and are acquired in the same electrolyte solutions. Considering the absolute positioning of the redox potential of **F**, it is similar to the one of the literature-known monotriarylamine **D**^[7] (see Chart 7 and Table 2) and, hence, suggests confinement of the hole in the corresponding mixed-valence compounds **F**⁺ to one redox center and possibly the bridge. Furthermore, the half-wave potential is congruent with the one of the literature-known reference dyads **G**^[7] (see Chart 7 and Table 2). This indicates that the electronic coupling in **F**⁺ should be around the same order of magnitude as for **G**⁺ ($V_{\text{two-level}} = 320 \text{ cm}^{-1}$ ^[7, 25]).

Chart 7

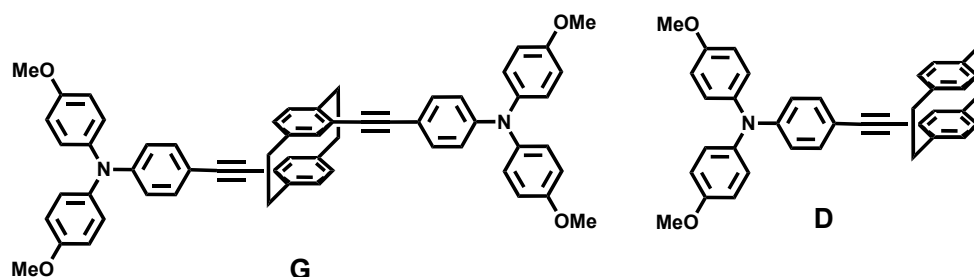


Table 2. Half-wave potentials $E_{1/2}$ and potential differences ΔE of the reference compounds **G** and **D**.^a

compound	$E_{1/2}(\text{Ox1})$ / mV	$E_{1/2}(\text{Ox2})$ / mV	$\Delta E (\text{Ox1/Ox2})$ / mV
F	235	280	45
G	240 ^[7]	290 ^[7]	50 ^[7]
D	265 ^[7]		

^a The half-wave potentials are measured by cyclic voltammetry in dichloromethane vs. ferrocene/ferrocenium (0.15–0.20 M tetrabutylammonium hexafluorophosphate)

Aside from these findings, the knowledge of the potential difference allowed an estimation of the equilibrium constant K_D of the disproportionation reaction of the monoradical $F^{\bullet+}$ (see Scheme 11 and equation 1).^[93] By employing the potential difference $\Delta E = -45$ mV, the Faraday constant F_c and the universal gas constant R , K_D amounts to a value of 0.173 at a temperature $T = 298$ K. During the recording of the steady-state absorption spectra used for the extrapolation “pure” monocation $F^{\bullet+}$ (see Section 3.4.1), a ratio of $[F]/[F^{\bullet+}] = 4/1$ was employed; therefore, the ratio of the concentrations in the sample solutions amounted to $[F^{\bullet+}]/[F^{\bullet2+}] = 23/1$. This makes significant contamination of the spectra by the bication highly improbable. For electron paramagnetic spectroscopy studies (see Section 4.1), an even higher excess of $[F]/[F^{\bullet+}] = 9/1$ was used, which resulted in an even higher ratio of $[F^{\bullet+}]/[F^{\bullet2+}] = 46/1$.



Scheme 11. Disproportionation reaction of the monoradical cation of **F**.^[92]

$$K_D = \frac{[F] \times [F^{\bullet2+}]}{[F^{\bullet+}]^2} = e^{\frac{\Delta E \times F_c}{R \times T}} \quad (1)$$

3.3.2 CYCLIC VOLTAMMETRY OF DONOR-ACCEPTOR DYADS A–C

In the case of compounds **A–C**, cyclic voltammetry was employed to gain a rough impression of the electronic coupling between the integrated redox centers and to determine the energies of the charge separated states in which the naphthalene diimide acceptor is reduced and the triarylamine donor is oxidized.

The half-wave potentials (see Table 2) of these fully reversible processes were extracted from the cyclic voltammograms (see Figures 10-12) of compounds **A–C**.

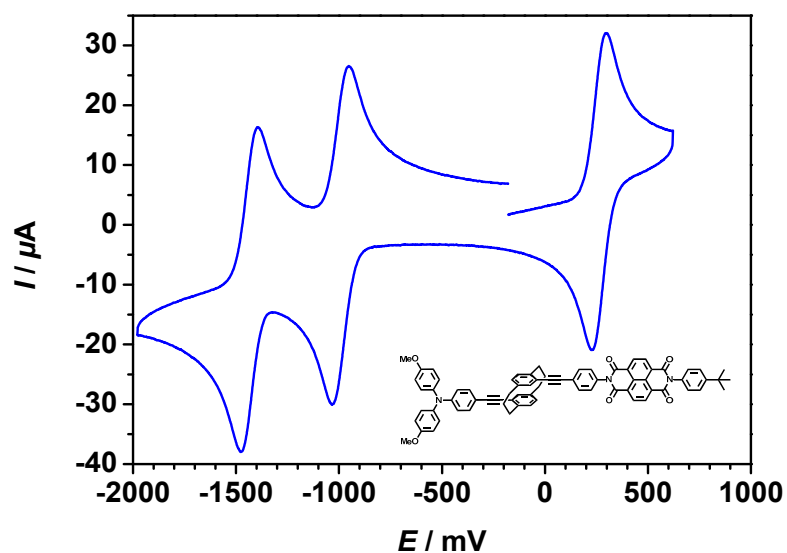


Figure 10. Cyclic voltammogram (glassy carbon working electrode) of **A** recorded with a scan rate of 500 mV s^{-1} in dichloromethane (0.2 M tetrabutylammonium hexafluorophosphate) versus ferrocene/ferrocenium.

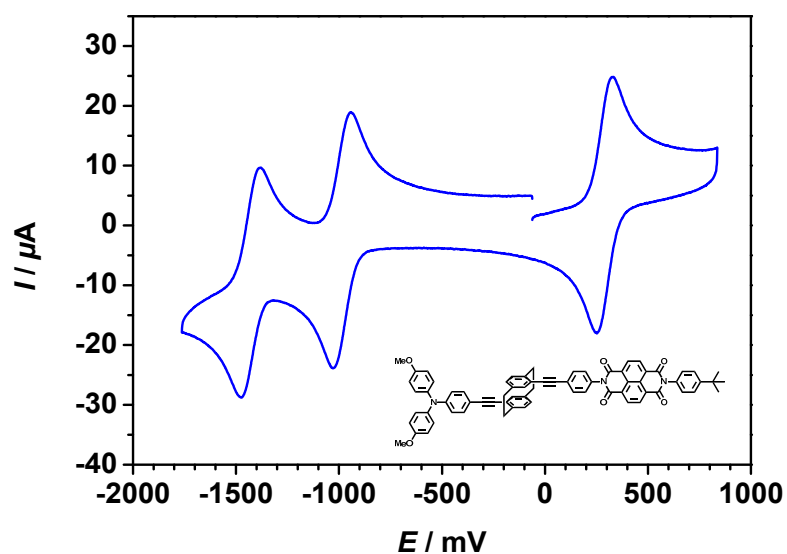


Figure 11. Cyclic voltammogram (glassy carbon working electrode) of **B** recorded with a scan rate of 500 mV s^{-1} in dichloromethane (0.2 M tetrabutylammonium hexafluorophosphate) versus ferrocene/ferrocenium.

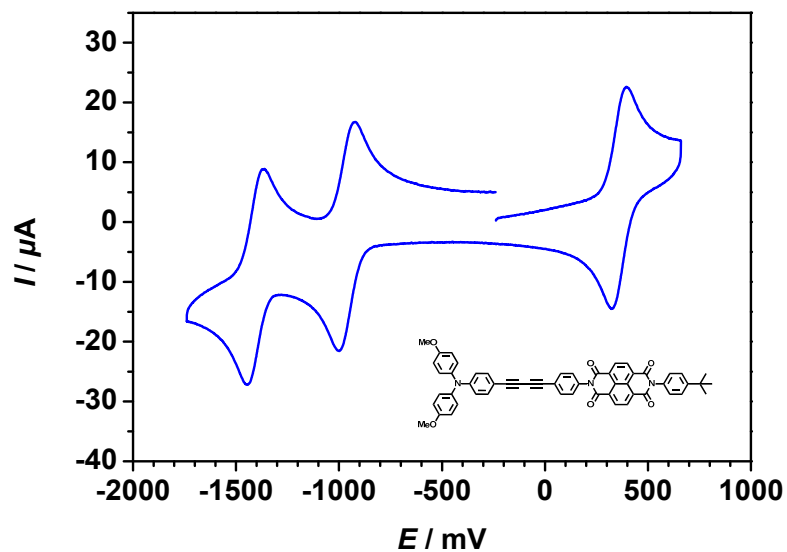


Figure 12. Cyclic voltammogram (glassy carbon working electrode) of **C** recorded with a scan rate of 500 mV s^{-1} in dichloromethane (0.2 M tetrabutylammonium hexafluorophosphate) versus ferrocene/ferrocenium.

Table 3. Half-wave potentials $E_{1/2}$ of the dyads **A**, **B**, and **C**^a

dyad	$E_{1/2}(\text{Ox1})$ / mV	$E_{1/2}(\text{Red1})$ / mV	$E_{1/2}(\text{Red2})$ / mV
A	265	-995	-1435
B	290	-985	-1430
C	360	-960	-1405

^aThe half-wave potentials are measured by cyclic voltammetry (glassy carbon working electrode) in dichloromethane vs. ferrocene/ferrocenium (0.2 M tetrabutylammonium hexafluorophosphate) at 500 mV s⁻¹ scan rate.

The half-wave potentials of the first reduction of NDI in dyads **A** and **B** match those of NDI molecules which are not substituted by donors.^[40, 41] In addition, the half-wave potentials of the first oxidation of **A** and **B** (see Table 3) agree with those of donor fragment **D**^[7] (see Table 2 Section 3.3.1). These findings indicate weak electronic coupling between donor and acceptor moieties in **A** and **B** and suggest localization of the charge on the redox centers and possibly the bridge in their charge separated states. In contrast, dyad **C** shows distinctly different values, which indicates stronger electronic coupling. However, it has to be kept in mind that possible contributions from solvation energy changes and ion pairing are not accounted for.^[89-92]

Furthermore, the determined half-wave potentials (see Table 3) were used to calculate the free energy of the charge separated state $\Delta G_{1\text{CS}}^0$ for **A–C** using the Weller approach (eq. 2), which equaled 2.00 eV for **A**, 2.01 eV for **B** and 2.00 eV for **C**.^[94]

$$\Delta G_{1\text{CS}}^0 = \frac{N_A}{1000} \cdot z \cdot e \cdot (E_{\text{ox}}(\text{D/D}^+) - E_{\text{red}}(\text{A/A}^-)) - \frac{N_A \cdot e^2}{1000 \cdot 4\pi\epsilon_0} \left[\left(\frac{1}{2r_D} + \frac{1}{2r_A} \right) \left(\frac{1}{\epsilon_r} - \frac{1}{\epsilon_s} \right) + \frac{1}{\epsilon_s \cdot d_{\text{DA}}} \right] \quad (2)$$

with (r_D (= 4.96 Å), r_A (= 3.97 Å) and d_{DA} (=23.1 Å for **A**, 23.0 Å for **B**, and 18.6 Å for **C**) are the radii of the donor and acceptor and the center to center distance between them, respectively. The radii r_D and r_A were calculated from the corresponding Connolly Molecular Surfaces of the subunits optimization with ChemBio3D Ultra^[95] and the distances d_{DA} were determined at a CAM-B3LYP/6-31G* level of theory using Gaussian09,^[96] respectively. N_A is

Avogadro's constant, e the elementary charge, z the number of transferred charges. The redox potentials of D and A correspond to $E_{1/2}(\text{Ox1})$ and $E_{1/2}(\text{Red1})$ (see above), ϵ_0 is the vacuum permittivity, ϵ_r is the permittivity of the solvent used for cyclic voltammetry and ϵ_s is that for the solvent used in the photophysical experiment.

3.4 STEADY STATE SPECTROSCOPY

3.4.1 VIS/NIR SPECTROSCOPY DURING CHEMICAL OXIDATION OF F AND J

Visible/near infrared (Vis/NIR) steady state absorption spectra were recorded during stepwise chemical oxidation of **F** and **J** with SbCl_5 in dichloromethane (see Figures 13, 14, 18 and 19) to extract and to deconvolute the spectra of the corresponding mono cations (see Figures 15, 16 and 20). This was performed to determine the most fundamental electron transfer parameters, the reorganization energy λ , the electronic coupling matrix element V and the thermal barrier ΔG^* of the *in situ* generated symmetric mixed-valence compounds F^+ and J^+ .

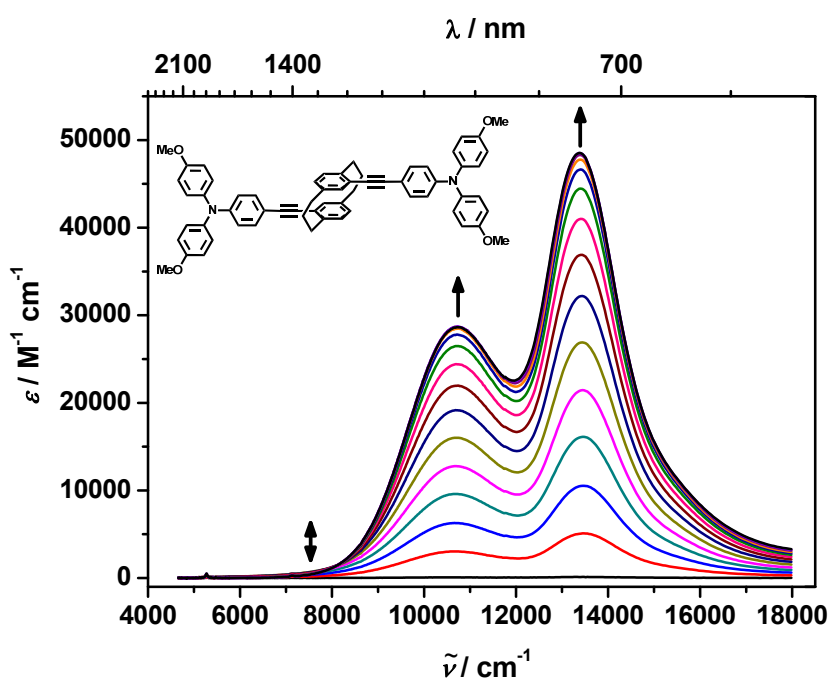


Figure 13. Vis/NIR absorption spectra during stepwise chemical oxidation of **F** with SbCl_5 in dichloromethane.

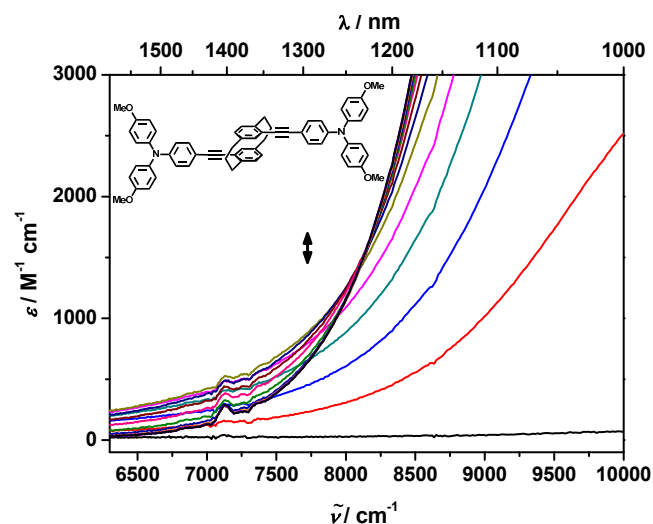


Figure 14. Enlarged section of Vis/NIR absorption spectra during stepwise chemical oxidation of **F** with SbCl_5 in dichloromethane.

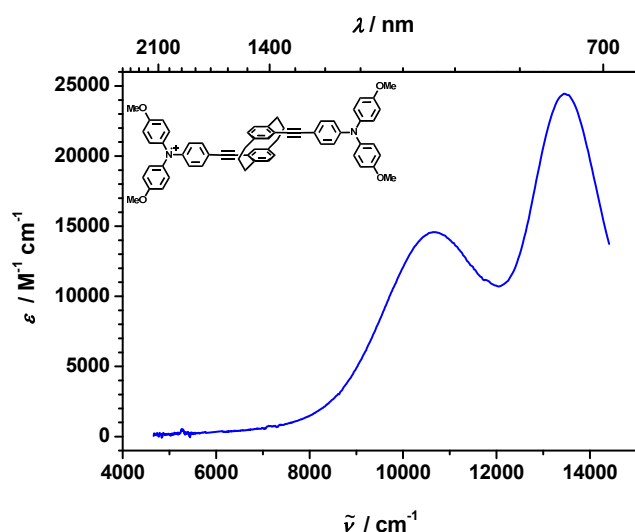
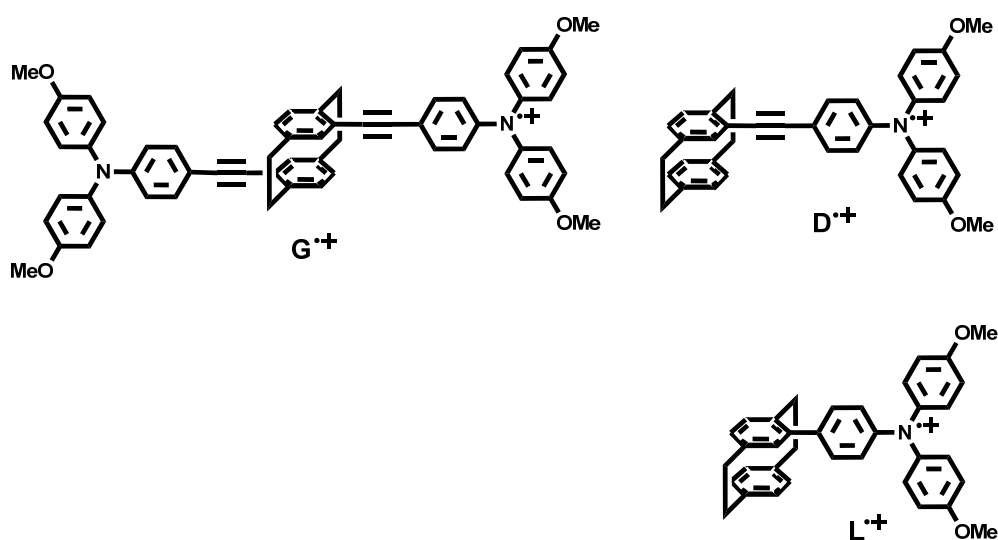


Figure 15. Extracted Vis/NIR absorption spectrum of F^+ in dichloromethane.

To extract the spectrum of F^+ from the measurement data, the intensity of the spectrum of the first addition of SbCl_5 was amplified, so that the extinction coefficient of its most intense band corresponding to a local π - π^* -transition (see below) equaled half of the one of the spectrum recorded after the last addition of SbCl_5 (see Figure 13). The ratio of the concentrations $[\text{F}^{2+}]/[\text{F}^+] = 1/23$ (see Section 3.3.1) and therefore the contamination by F^{2+} was minimized in this way.

Regarding the extracted Vis/NIR absorption spectrum of \mathbf{F}^+ (see Figure 15), the strongest absorption band with its maximum $\tilde{\nu}_a = 13\,440\text{ cm}^{-1}$ and extinction coefficient maximum $\varepsilon_a = 24\,450\text{ M}^{-1}\text{cm}^{-1}$ corresponds to a localized π - π^* -transition within the triarylamine radical cation moiety. The positioning of the maximum between $13\,000\text{ cm}^{-1}$ and $13\,500\text{ cm}^{-1}$ is characteristic for cationic triarylamine moieties with two para-methoxy substituents.^[7, 36] In particular the band occurs at the same position and has a very similar extinction coefficient to those of the literature known monotriarylamine reference compound \mathbf{D}^+ ($\tilde{\nu}_a = 13\,440\text{ cm}^{-1}$, $\varepsilon_a = 23\,900\text{ M}^{-1}\text{cm}^{-1}$) (see Chart 8 and Table 4),^[7] which indicates no significant influence by the additional triarylamine or by the enlargement of the cyclophane.

Chart 8



The second strongest absorption band with its maximum $\tilde{\nu}_b = 10\,710\text{ cm}^{-1}$ and an extinction coefficient $\varepsilon_b = 14\,580\text{ M}^{-1}\text{cm}^{-1}$ can be assigned to a hole-transfer from the triarylamine cation to the bridge unit. The occurrence of such so-called bridge bands is typical for triarylamines in conjugation with phenylcompounds.^[7] The present bridge band is positioned at practically the same wavenumber and has virtually the same extinction coefficient as the one of the literature known reference compound \mathbf{D}^+ (see Chart 8, $\tilde{\nu}_b = 10\,680\text{ cm}^{-1}$, $\varepsilon_b = 15\,400\text{ M}^{-1}\text{cm}^{-1}$)^[7] thus again supporting no significant influence from the second triarylamine or the extension of the cyclophane.

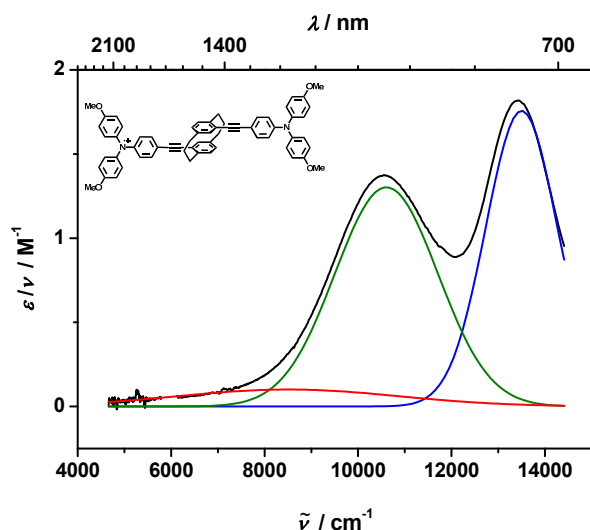


Figure 16. Deconvolution of reduced^[97] extracted(see text) absorption spectrum of \mathbf{F}^{2+} by three Gaussians.

The most important band, especially regarding the extraction of the electron transfer parameters, is the intervalence charge transfer band related to the optically induced hole-transfer within monocationic bistriarylamine from the oxidized triarylamine moiety to the neutral one. Such bands, characteristic for electronically coupled triarylamine, are usually situated in the NIR-region between $6\,000\text{ cm}^{-1}$ and $12\,000\text{ cm}^{-1}$.^[7, 72, 76] The main characteristic of these bands is their first rising and then declining absorption during the stepwise oxidation of the investigated compounds. This is explained by the gradual generation of the monocation, which is, upon further oxidation, transformed into the dication, where both redox centers are oxidized and thus no neutral triarylamine donor is present. In case of \mathbf{F}^{2+} the band is positioned at the low energy foot of the bridge band (see Figure 14). Due to its low intensity and strong overlap with this bridge band, a direct deconvolution of the reduced^[97] extrapolated spectrum of \mathbf{F}^{2+} by using Gaussians proved difficult. Therefore, the position of the intervalence charge transfer band was narrowed down by subtracting the absorption spectrum with half intensity of \mathbf{F}^{2+} from the absorption spectrum of \mathbf{F}^{2+} . This yielded an intervalence charge transfer band with a maximum around $9\,000\text{ cm}^{-1}$. By using this energy and the apparent maxima of the two other bands as starting values for three Gaussians in the fit of the reduced absorption spectrum (see Figure 16), it yielded $\tilde{\nu}_c = 8\,500\text{ cm}^{-1}$ as a lower bound of the energy of the maximum of the intervalence charge transfer band. Thus, the intervalence charge transfer band of \mathbf{F}^{2+} has a much higher transition energy than the $\tilde{\nu}_c = 5\,870\text{ cm}^{-1}$ ^[25] of the bistriarylamine reference compound \mathbf{G}^{2+} (see Chart 8 and Table 4). This trend is supported by AM1-CISD calculations which include the solvent

shifts by the COSMO method and yielded $\tilde{\nu}_c = 10\,030\text{ cm}^{-1}$ for \mathbf{F}^+ and $\tilde{\nu}_c = 12\,660\text{ cm}^{-1}$ for \mathbf{G}^+ .^[25]

The data acquired via the deconvolution of the intervalence-charge transfer band was analyzed by means of a traditional two-level *Mulliken-Hush* approach (see Figure 17).^[98, 99] While the reorganization energy within this model equals $\tilde{\nu}_c$, a value of 320 cm^{-1} was determined for the electronic coupling $V_{\text{two-level}}$ between the two diabatic states. The strength of the electronic coupling is thus essentially equivalent to the $V_{\text{two-level}} = 310\text{ cm}^{-1}$ ^[25] (see Table 4) of reference compound \mathbf{G}^+ (see Chart 8). Furthermore, the values for the reorganization energy and coupling of \mathbf{F}^+ were used to roughly estimate the thermal barrier via the two-state Mulliken-Hush approach to be $1\,820\text{ cm}^{-1}$ in comparison to $1\,170\text{ cm}^{-1}$ ^[25] for \mathbf{G}^+ . These values were determined by employing the following equations (3, 4, 5 and 6):

$$V_{\text{two-level}} = \frac{\mu_{ga}\tilde{\nu}_c}{\Delta\mu_{12}} \quad (3)$$

$$\mu_{ga}^2 = \frac{3hc\varepsilon_0 \ln 10}{2000\pi^2 N} \int \frac{\varepsilon}{\tilde{\nu}} d\tilde{\nu} \quad (4)$$

$$\Delta\mu_{12} = \sqrt{(\mu_{aa} - \mu_{gg}) + 4\mu_{ga}^2} \quad (5)$$

$$\Delta G^* = \frac{\tilde{\nu}_c}{4} - V_{\text{two-level}} + \frac{V_{\text{two-level}}^2}{\tilde{\nu}_c} \quad (6)$$

where μ_{ga} is the transition moment of the intervalence charge-transfer band (evaluated neglecting the refractive index corrections of the solvent), $\tilde{\nu}_c$ is the intervalence charge transfer band maximum, $\Delta\mu_{12}$ is the diabatic dipole moment difference between the two states, h is the Planck constant, c the speed of light *in vacuo*, ε_0 is the electric field constant, N is Avogadro's constant, ε and $\tilde{\nu}$ are the extinction coefficients and corresponding wavenumbers of the intervalence charge transfer absorption band and $\mu_{aa} - \mu_{gg} = 61.0\text{ D}$ is the adiabatic dipole moment difference (determined via AM1-CISD computations with the COSMO solvent model).

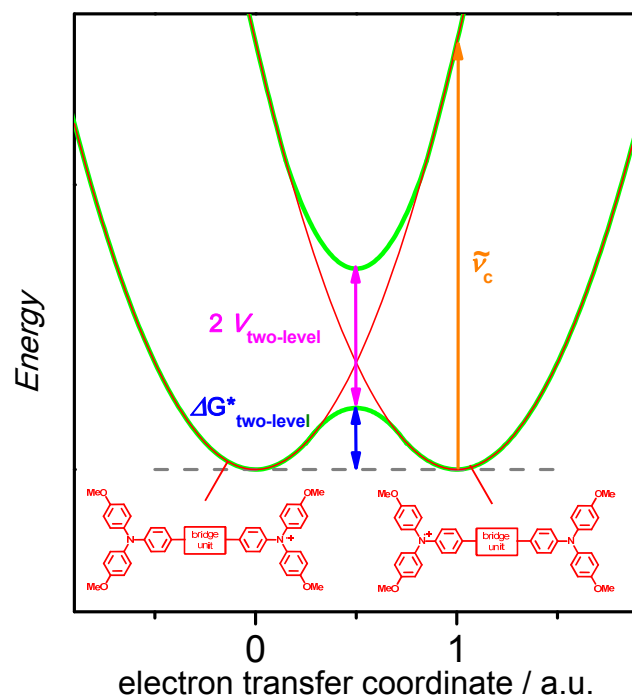


Figure 17. Adiabatic (green) and diabatic (red) states within a two-level model projected on one dimension including fundamental electron transfer parameters.

Table 4. Absorption maxima of local π - π^* -band $\tilde{\nu}_a$, bridge band band $\tilde{\nu}_b$ and intervalence charge transfer band $\tilde{\nu}_c$, the electronic coupling $V_{two-level}$ and the thermal barrier $\Delta G^*_{two-level}$ of compounds F^+ , J^+ and literature known reference compounds D^+ and G^+ and L^+ .

	F^+	D^+	G^+	J^+	L^+
$\tilde{\nu}_a$ / cm^{-1}	13 440	13 440 [7]	13 370 [25]	13 370	13 400 cm^{-1} [7]
$\tilde{\nu}_b$ / cm^{-1}	10 610	10 680 [7]	10 730 [25]	10 000-12 000	
$\tilde{\nu}_c$ / cm^{-1}	8 500		5 870 [25]		
$V_{two-level}$ / cm^{-1}	320		310 [25]		
$\Delta G^*_{two-level}$ / cm^{-1}	1 820		1 170 [25]		

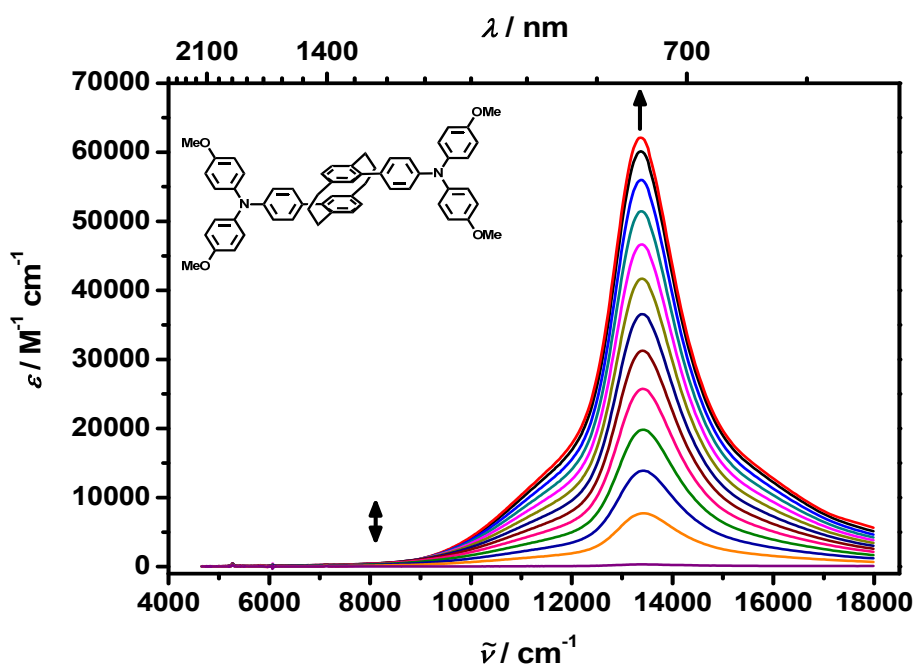


Figure 18. Vis/NIR absorption spectra during stepwise chemical oxidation of **J** with SbCl_5 in dichloromethane.

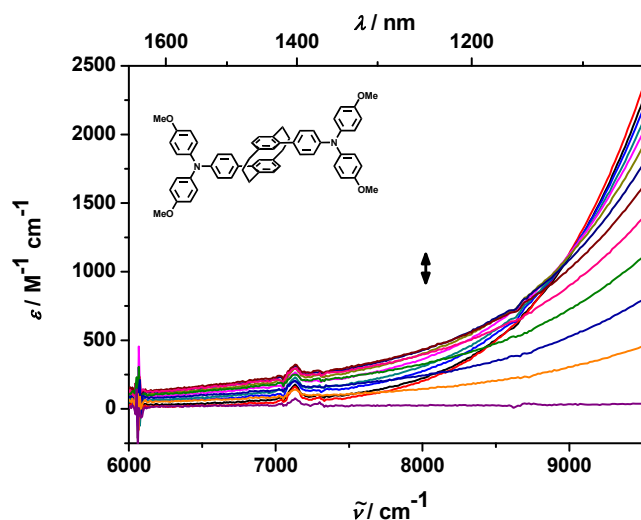


Figure 19. Enlarged section of Vis/NIR absorption spectra during stepwise chemical oxidation of **J** with SbCl_5 in dichloromethane.

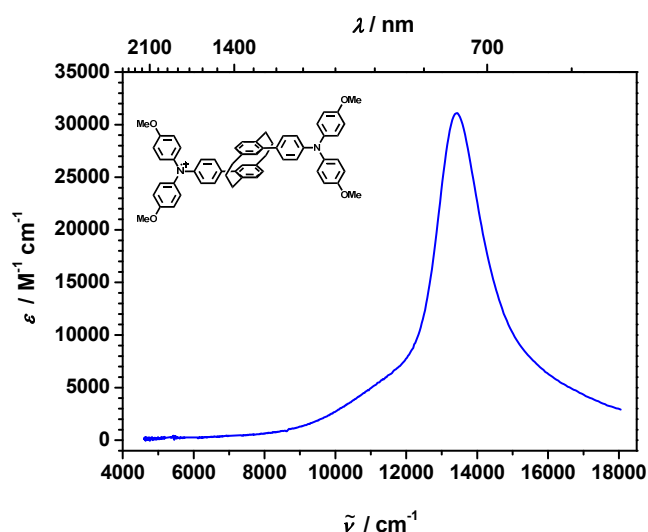


Figure 20. Extracted (see text) Vis/NIR absorption spectrum of \mathbf{J}^+ in dichloromethane.

As with compound **F**, to extract the spectrum of monoradical cation, the spectrum of the first addition of SbCl_5 to **J** was amplified to minimize contamination by the biradical dication \mathbf{J}^{2+} (see Section 3.3.1 and above).

When inspecting the extracted Vis/NIR absorption spectrum of \mathbf{J}^+ , a very intense band with its maximum $\tilde{\nu}_a = 13440 \text{ cm}^{-1}$ and extinction coefficient $\varepsilon_a = 31\,100 \text{ M}^{-1}\text{cm}^{-1}$ is visible (see

Figure 20). As for \mathbf{F}^+ (see above), it corresponds, with its typical position between $13\,000\text{ cm}^{-1}$ and $13\,500\text{ cm}^{-1}$,^[7, 36] to a localized π - π^* -transition within the triarylamine radical cation moiety. However, its extinction coefficient is higher than in the spectrum of the literature known monotriarylamine reference compound \mathbf{L}^+ (see Chart 8) ($\tilde{\nu}_a = 13\,400\text{ cm}^{-1}$, $\varepsilon_a = 24\,700\text{ M}^{-1}\text{cm}^{-1}$) (see Table 4).^[7] This finding can probably be assigned to the stronger overlap with the bridge band, which can only be detected by a distinct broadening at the bottom of the π - π^* -band, in contrast to \mathbf{L}^+ where it appears as a accentuated shoulder.^[7] Since electronic effects in between the two triarylamine units through the bridge unit in \mathbf{J}^+ are even smaller than in \mathbf{F}^+ , as indicated by the very weak intervalence charge transfer band (see below), this finding might be a result of the minimal steric influences of the directly linked phenyl-ring of the second triarylamine onto the structure of the [3.3]paracyclophane unit (see Table 1 in Section 3.2).

The presence of the intervalence charge transfer band assigned to the hole transfer within the monocationic bistriarylamine \mathbf{J}^+ from the oxidized triarylamine moiety to the neutral one is indicated in the original Vis/NIR spectra of the stepwise oxidation of \mathbf{J} (see Figures 18 and 19). It manifests itself by a first rising and then declining absorption at the low energy foot of the localized π - π^* -band merged with the bridge band (see Figure 19). As for \mathbf{F}^+ , the subtraction of the spectrum with half intensity of \mathbf{J}^{2+} from that of \mathbf{J}^+ yielded an intervalence charge transfer band at around $9\,000\text{ cm}^{-1}$ with even lower intensity than for \mathbf{F}^+ . However, due to the strong overlap of the three bands combined with the indicated very low intensity of the intervalence charge transfer band, unequivocal deconvolution of the extracted spectrum of \mathbf{J}^+ (see Figure 20) with Gaussians proved impossible.

3.4.2 UV/VIS SPECTROSCOPY OF DONOR-ACCEPTOR DYADS A–C

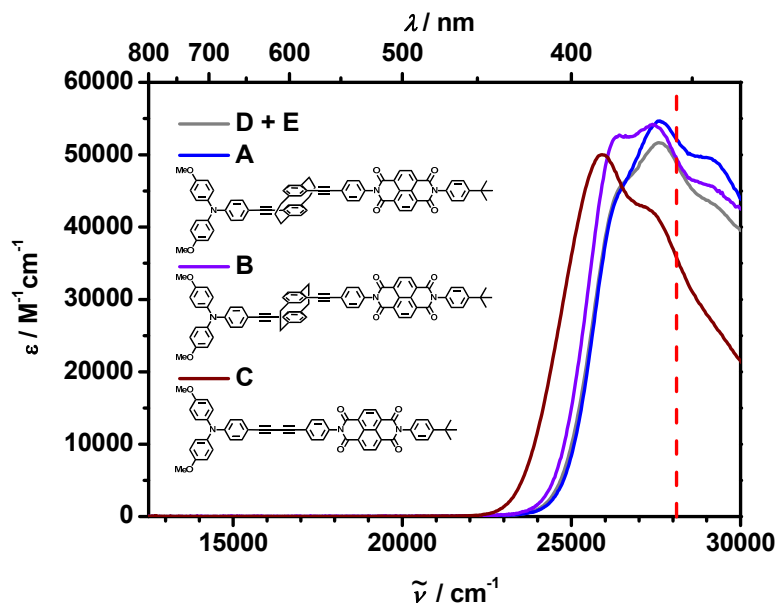


Figure 21. UV/Vis absorption spectra of dyads **A**, **B**, **C** and the sum of the fragments **D** and **E** in toluene. The excitation energy of the time resolved measurements at $28\,200\text{ cm}^{-1}$ is indicated by the dashed vertical line (red).

In order to assess possible ground state interactions between the triarylamine (TAA) donor and naphthalene diimide (NDI) acceptor in the dyads **A–C**, the ultraviolet/visible (UV/Vis) steady state absorption spectra of these compounds (see Figure 21) as well as of the reference compounds **D** and **E** (see Figure 22) were measured and compared. The UV/Vis absorption spectra of the cyclophane-containing dyads **A** and **B** are quite similar (see Figure 21) with the [2.2]cyclophane dyad showing a slightly more red-shifted onset of absorption ($24\,650\text{ cm}^{-1}$) than the [3.3]cyclophane dyad ($24\,830\text{ cm}^{-1}$). The strong and overlapping absorption features of the TAA and the NDI with molar extinction coefficients in the $10^4\text{ M}^{-1}\text{cm}^{-1}$ region are mainly due to $\pi\text{-}\pi^*$ transitions in addition to contributions which probably have charge transfer character.^[45, 67] The absorption spectrum of dyad **C** shows distinct differences compared to either **A** or **B**. The deviations above ca. $26\,000\text{ cm}^{-1}$ are certainly caused by the missing cyclophane bridging unit. The somewhat lower energy onset of absorption ($23\,590\text{ cm}^{-1}$) is probably due to a weak charge transfer interaction between the TAA and the NDI caused by the shorter and conjugated butadiyne bridge. As can be seen in Figures 21 and 22, the absorption spectra of dyad **B** can be approximated by the sum of the spectra of the fragments **D** and **E**, which suggests weak electronic interaction in

the ground state between the TAA and the central NDI core.^[40, 41, 46, 56, 65, 66, 68, 69, 71] The little deviations of the spectra probably arise, in addition to the weak electronic interactions, from the fact that the cyclophane unit is present in both fragments. The agreement with the spectrum of **A** is even better, although the latter has a [3.3]cyclophane bridge instead of the [2.2]cyclophane bridge of **B**. Nevertheless the electronic interactions between the donor and acceptor in both **A** and **B** can be considered to be very weak in contrast to the unsaturated system **C** with a similar donor acceptor distance. The weak interaction can partly be ascribed to the electronic properties of the NDI, which shows reduced electronic interaction with substituents attached to its nitrogen imide atoms in the dyads **A–C** because of the LUMO having a nodal plane along the molecular axis.^[40, 58] The electronic coupling in dyads **A** and **B** is expected to be even smaller than in similar dyads containing NDI and conjugated bridges of comparable size, like dyad **C**, due to the weak electronic through-space interaction of the cyclophane bridge.^[25] Thus, both effects contribute to a weak coupling in dyads **A** and **B**.

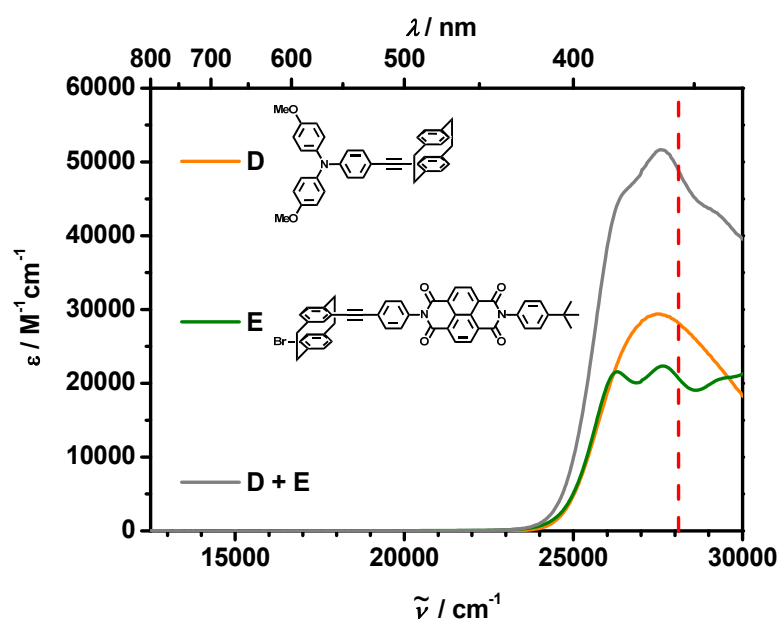


Figure 22. UV/Vis absorption spectra of the fragments **D** and **E** and the sum of the fragments **D** and **E** in toluene. The excitation energy of the time resolved measurements at 28 200 cm^{-1} is indicated by the dashed vertical line (red).

From the steady state absorption spectra (see Figures 21 and 22), it is obvious that due to the strong spectral overlap of the donor and acceptor moieties in dyad **B** (and possibly **A** and **C** as well), laser pulses at $28\,200\text{ cm}^{-1}$ will excite both the TAA and NDI part of the dyads at almost equal amounts.

3.4.3 UV/VIS SPECTROELECTROCHEMISTRY OF A, B AND C

To predict the absorption spectra and thereby facilitate the identification of the charge separated species of **A**, **B** and **C** in the transient absorption measurements (see below) UV/Vis-spectroelectrochemistry was employed. This was realized by summation of the thereby determined anion and cation spectra of each compound (see Figures 23, 24 and 25).

The molar extinction coefficients of the maxima of the anions and cations of the investigated compounds were $\epsilon_{20\,800\text{ cm}^{-1}}(\mathbf{A}^-) = 34\,300\text{ M}^{-1}\text{cm}^{-1}$, $\epsilon_{13\,400\text{ cm}^{-1}}(\mathbf{A}^+) = 25\,500\text{ M}^{-1}\text{cm}^{-1}$, $\epsilon_{20\,800\text{ cm}^{-1}}(\mathbf{B}^-) = 31\,600\text{ M}^{-1}\text{cm}^{-1}$, $\epsilon_{13\,300\text{ cm}^{-1}}(\mathbf{B}^+) = 24\,000\text{ M}^{-1}\text{cm}^{-1}$, $\epsilon_{20\,900\text{ cm}^{-1}}(\mathbf{C}^-) = 31\,400\text{ M}^{-1}\text{cm}^{-1}$ and $\epsilon_{12\,800\text{ cm}^{-1}}(\mathbf{C}^+) = 26\,300\text{ M}^{-1}\text{cm}^{-1}$. The high intensity band of NDI anion at around $21\,000\text{ cm}^{-1}$ and the low intensity band at about $16\,500\text{ cm}^{-1}$ are characteristic for this species.^[47] Furthermore, the TAA radical cation band with its main absorption between $13\,000$ and $15\,000\text{ cm}^{-1}$, even if it is slightly shifted in \mathbf{C}^+ , can be clearly identified.^[7, 36]

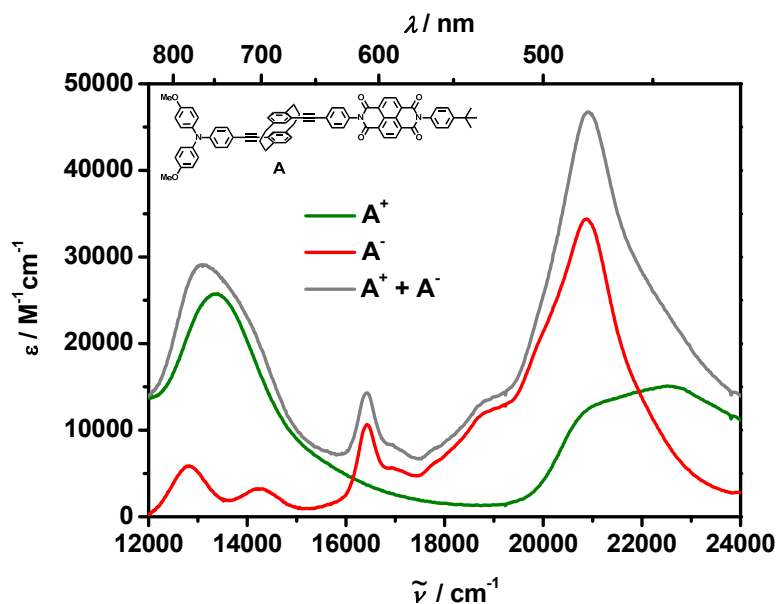


Figure 23. CS state absorption spectrum of **A** predicted by the sum of the monocation (\mathbf{A}^+) and monoanion (\mathbf{A}^-) UV/Vis steady state absorption spectra acquired via spectroelectrochemistry in dichloromethane (0.2 M tetrabutylammonium hexafluorophosphate).

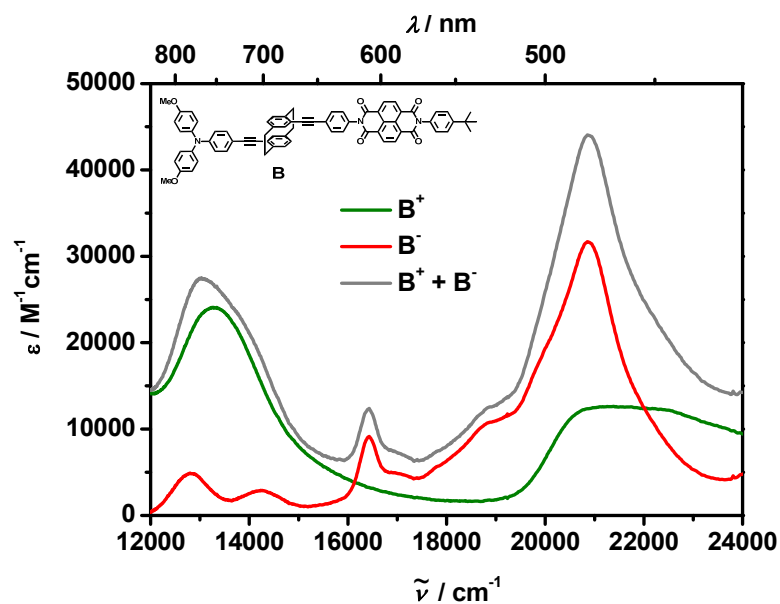


Figure 24. CS state absorption spectrum of **B** predicted by the sum of the monocation (B^+) and monoanion (B^-) UV/Vis steady state absorption spectra acquired via spectroelectrochemistry in dichloromethane (0.2 M tetrabutylammonium hexafluorophosphate).

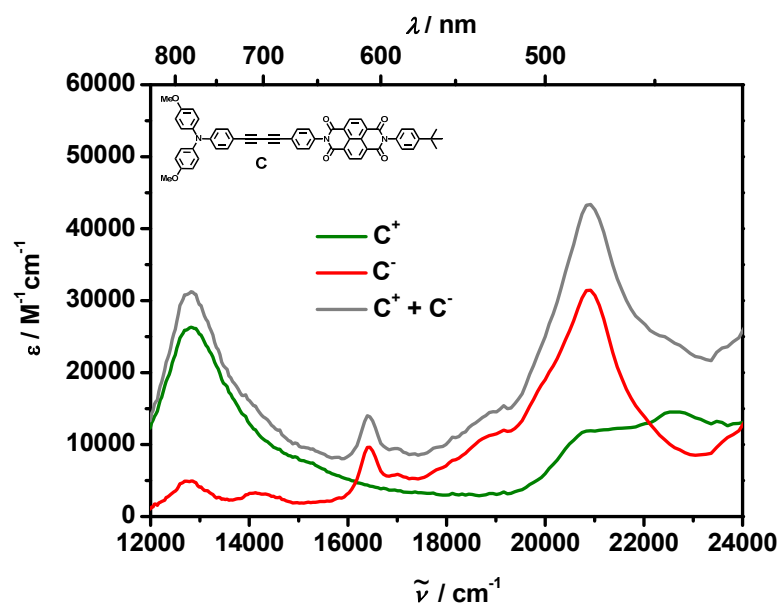


Figure 25. CS state absorption spectrum of **C** predicted by the sum of the monocation (C^+) and monoanion (C^-) UV/Vis steady state absorption spectra acquired via spectroelectrochemistry in dichloromethane (0.2 M tetrabutylammonium hexafluorophosphate).

3.4.4 FLUORESCENCE SPECTROSCOPY OF D AND E

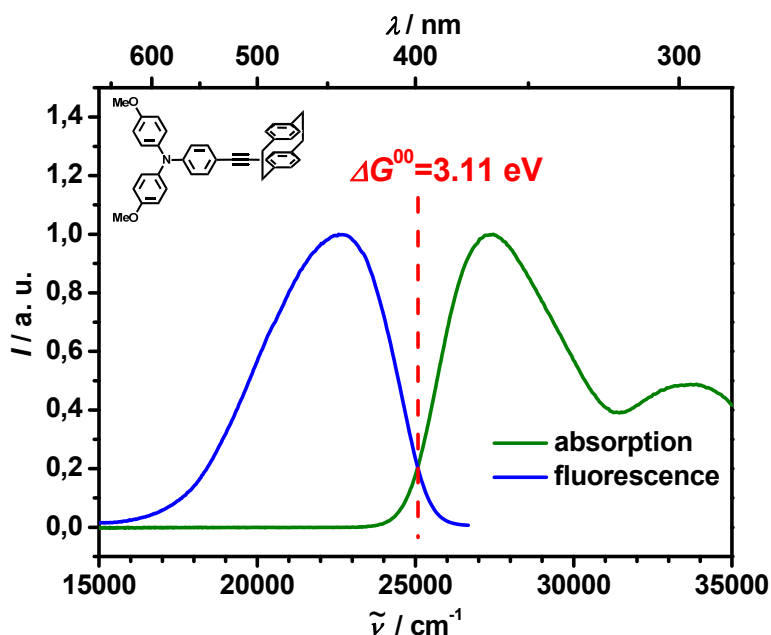


Figure 26. Reduced^[100] and normalized UV/Vis steady state absorption and reduced^[100] and normalized UV/Vis steady state fluorescence spectra (excitation at 28 200 cm^{-1}) of fragment **D** in toluene.

The steady state fluorescence spectra of reference compounds **D** and **E** were recorded to determine their excited state energies and therefore estimate those of the dyads **A–C**. While the dyads **A–C** are practically nonfluorescent ($\phi < 1\%$) in toluene because of efficient charge transfer quenching the fluorescence spectra of the reference compounds **D** and **E** could be measured (see Figures 26 and 27). For both compounds the diffuse shape of the fluorescence band probably indicates some CT character of the fluorescent state, even more for **D** than for **E**.^[45, 58, 66] While in case of *N*-alkyl substituted naphthalene diimides (NDIs) the fluorescence normally appears as a mirror image to the absorption spectrum,^[47] in **E** local NDI fluorescence is mostly quenched by the formation of charge transfer states from which fluorescence takes place as has been observed before in NDIs substituted by phenyl or stronger donors.^[45, 58, 66, 100] From the fluorescence spectra and the steady state absorption spectra, the ΔE^{00} free energy, of the excited states of fragments **D** and **E** were determined by two different methods: the crossing points of reduced^[97, 100] and normalized fluorescence and absorption spectra as well as by the midpoint of the respective maxima. Both methods yielded nearly identical values, 3.11 eV and 3.10 eV for **D** and 3.21 eV for **E**. Those values

are equal to those of ΔG^{00} , since the molecules dealt with are small. From these measurements it can be concluded that the locally excited state of **D** and **E** only differ by ca. 0.1 eV which would allow excitation transfer from the NDI fragment to the triarylamine moiety in the dyads **A**, **B** and probably **C**. The fluorescence of **D** was strong enough in order to measure the lifetime, which is 2.3 ns.

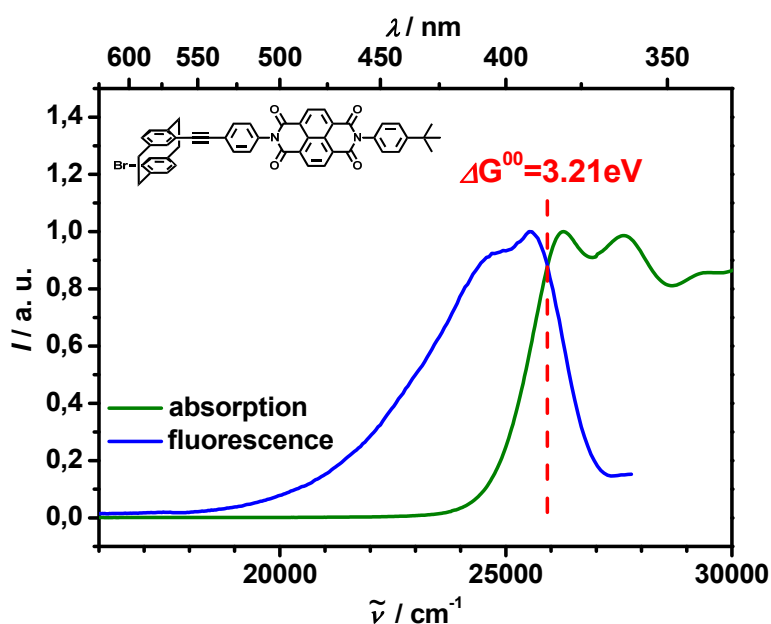


Figure 27. Reduced^[100] and normalized UV/Vis steady state absorption (green) and reduced^[100] and normalized UV/Vis steady state fluorescence spectra (excitation at 28 200 cm^{-1}) of fragment **E** in toluene.

3.5 TRANSIENT ABSORPTION SPECTROSCOPY

3.5.1 FEMTOSECOND TRANSIENT ABSORPTION SPECTROSCOPY

For the investigation of the charge separation processes of compounds **A-C** upon photoexcitation fs-transient absorption spectroscopy with a pump-probe set-up covering the dynamics from 100 fs to 8 ns was applied to these compounds as well as reference compounds **D** and **E**.

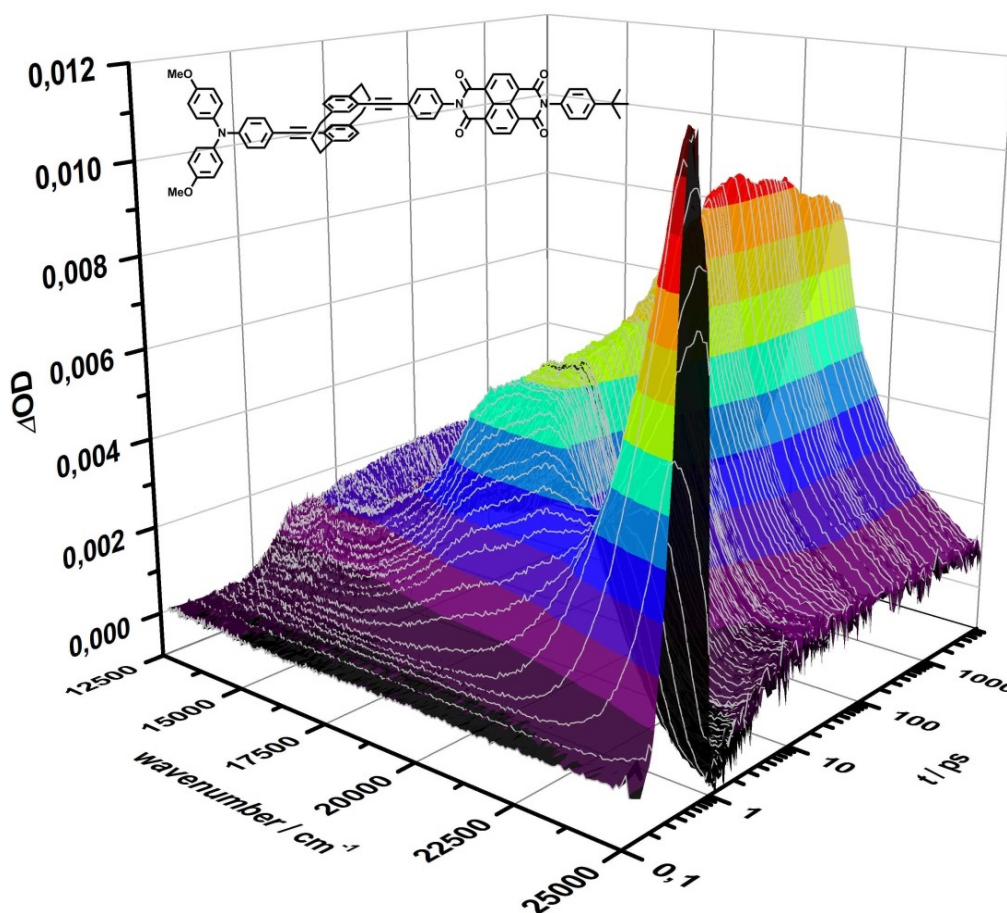


Figure 28. Example of raw data of femtosecond transient absorption of **A** in toluene (excitation at $28\,200\text{ cm}^{-1}$) including the coherent artifact and only corrected for scattered light.

All the compounds were excited at $28\,200\text{ cm}^{-1}$ with a 140 fs pulse in toluene and probed by a white light continuum between $12\,500\text{ cm}^{-1}$ (in case of **E** $14\,500\text{ cm}^{-1}$) and $24\,000\text{ cm}^{-1}$. The transient maps (see Figure 28) were deconvoluted by a widely used global fitting routine employing GLOTARAN^[101] (see Experimental Part) which yields evolution associated spectra (EAS) along with the corresponding time constants for their formation and decay. These EAS are shown in Figures 29–33. Generally, the first EAS rise with the instrument response time (ca. 200 fs) and decay with the time constants as given in the Figures 29–33. The following EAS rise with the time constant for the decay of their predecessor and decay with the time indicated. Lifetimes greater than 3 ns could not be determined with the fs-transient absorption setup and were marked as “final”. Before the pump-probe spectra of dyads **A–C** are discussed in detail, the photophysics of the fragments **D** and **E** are described, which will be helpful for the understanding of the dynamics of the dyads.

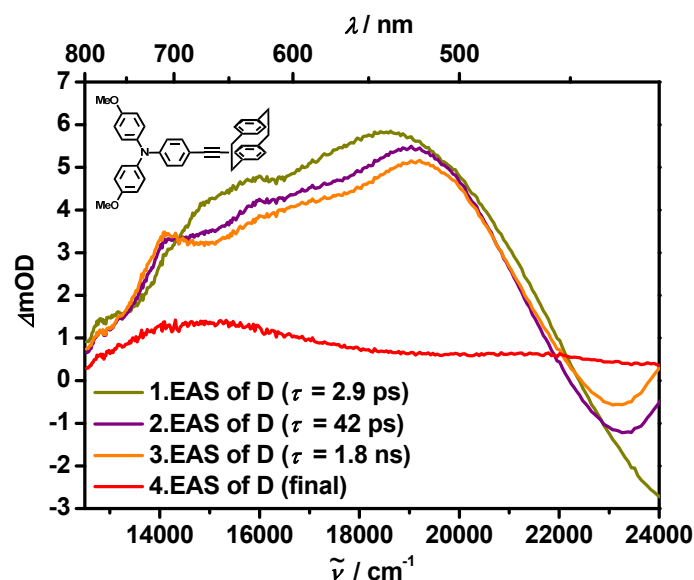


Figure 29. Evolution associated fs-transient absorption spectra (excitation at $28\,200\text{ cm}^{-1}$) of **D** in toluene.

The donor fragment **D** shows the formation of a broad transient absorption between $13\,000\text{ cm}^{-1}$ and $22\,000\text{ cm}^{-1}$ and a ground state bleach above $22\,000\text{ cm}^{-1}$ (see Figure 29). The broad absorption might be ascribed to a singlet excited species which decays with $\tau = 2.9\text{ ps}$ into a species which shows a somewhat more pronounced signal at $14\,000\text{ cm}^{-1}$, which could indicate the formation of a charge transfer (CT) state with positive charge at the

triarylamine (TAA) moiety (generally, TAA radical cations show strong and sharp absorption bands in the 13 000–15 000 cm^{-1} region).^[7, 36] This potential CT state could then transform with $\tau = 42$ ps into a spectrally very similar CT state. The spectral difference between these two states is minor and could be due to conformational issues. A decay with $\tau = 1.8$ ns follows, which agrees very well with the fluorescence lifetime of 2.3 ns (see Section 3.4.4), and finally a long-lived state (possibly a triplet state) is populated with a broad spectral feature at 15 000 cm^{-1} , which decays with $\tau = 47$ μs as determined by the ns-transient absorption setup.

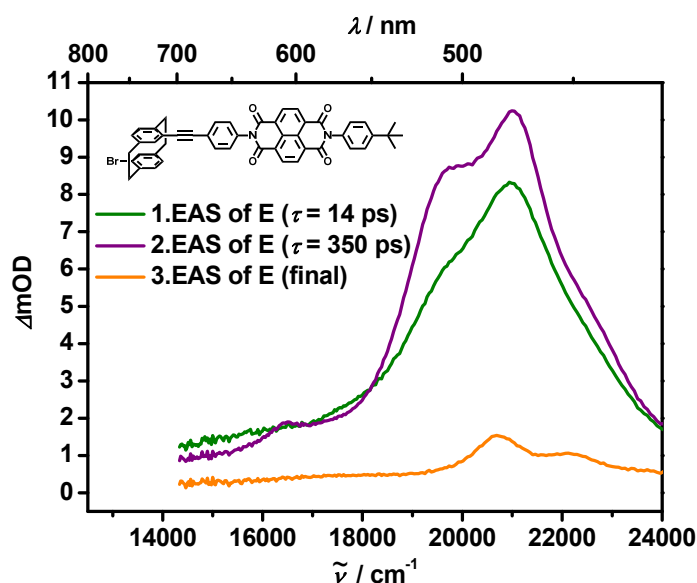


Figure 30. Evolution associated fs-transient absorption spectra (excitation at 28 200 cm^{-1}) of **E** in toluene.

The acceptor fragment **E** displays a transient signal at 21 000 cm^{-1} with a shoulder at 19 500 cm^{-1} (see Figure 30). Comparison with the transient spectra of a *N,N'*-dialkyl-substituted naphthalene diimide (NDI), whose local singlet excited state shows its main sharp absorption signal at 16 500 cm^{-1} , shows that this species cannot be a local singlet excited state of NDI but probably can be ascribed to a more delocalized state which also involves the cyclophane (CP) moiety.^[45] This interpretation is supported by previous studies, which have shown that even the attachment of a weak donor such as a phenyl group to NDI can actually lead to the formation of charge transfer (CT) states within less than 0.5 ps.^[45, 54, 58, 66] In **E** this delocalized state transforms with $\tau = 14$ ps into a species with possible charge transfer character as could be derived from the small peak at 16 500 cm^{-1}

which is typical of NDI radical anion formation.^[49, 53, 54] With $\tau = 350$ ps, this possible CT state leads to the NDI triplet state with $\tau = 13$ μ s as determined with ns-transient absorption setup and its typical transient features at 20 500 cm^{-1} and 22 000 cm^{-1} .^[45, 46, 102] The quantum yield of this process is unknown, but it appears that – as in phenyl substituted NDI – intersystem crossing (ISC) in **E** is slow compared to *N*-alkyl substituted NDIs which show ISC within ca. 10 ps.^[45] The rate of the formation of the local triplet state of the NDI in **E** allows to estimate the rate of the analogous process in the dyads **A** and **B**. In these dyads ISC however cannot compete with other faster processes like charge separation (see below) and, thus, is disfavored.

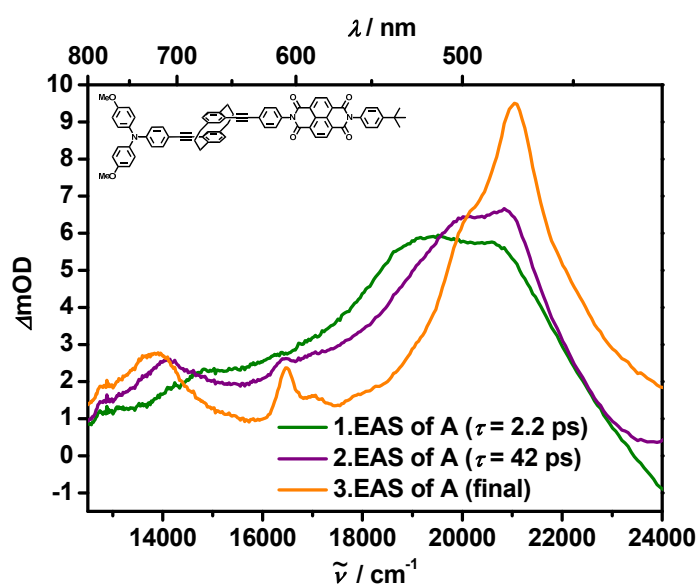


Figure 31. Evolution associated fs-transient absorption spectra (excitation at 28 200 cm^{-1}) of **A** in toluene.

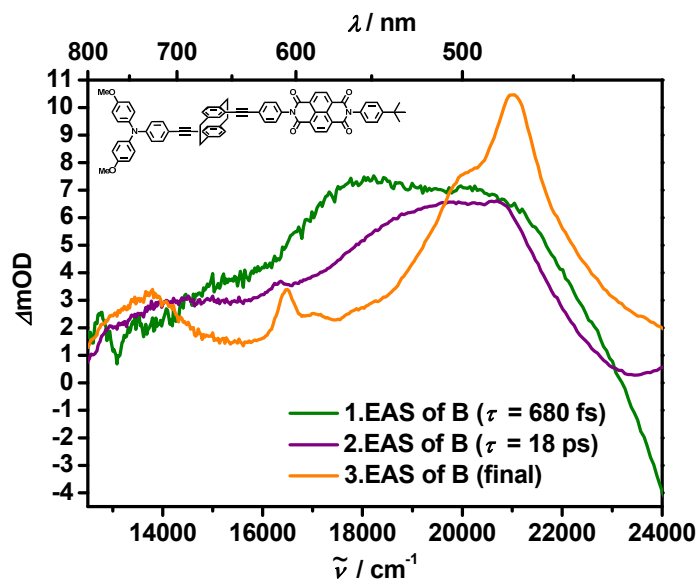


Figure 32. Evolution associated fs-transient absorption spectra (excitation at $28\,200 \text{ cm}^{-1}$) of **B** in toluene.

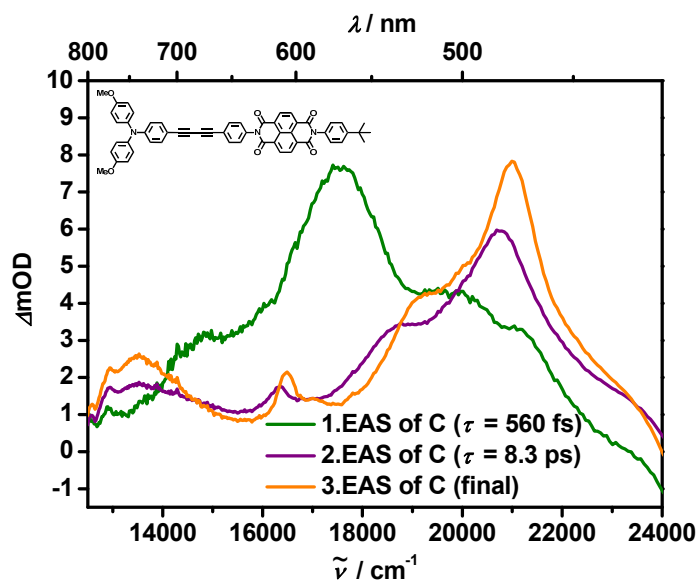


Figure 33. Evolution associated fs-transient absorption spectra (excitation at $28\,200 \text{ cm}^{-1}$) of **C** in toluene.

Since both chromophores of the dyads **A–C** are concomitantly excited by a fs-laser pulse at $28\,200\text{ cm}^{-1}$ (see Section 3.4.2), it is possible to approximate the first EAS of the CP containing dyads **A** and **B** by a linear combination of the first EAS of the fragments **D** and **E** (see Figures 34 and 35). While the assumption of these spectral contributions being the locally excited singlet states is probably correct for the TAA fragment, like in the spectra of fragment **E**, in the spectra of the dyads **A** and **B** no contribution of the locally excited NDI singlet state with its dominating sharp absorption band at $16\,500\text{ cm}^{-1}$ can be detected within the time resolution of the experimental set-up.^[45] This leads to the conclusion, that, like for **E**, the first EAS of the dyads **A** and **B** include a more delocalized NDI state, which involves the CP moiety (see above). This transient species decays with $\tau = 2.2\text{ ps}$ for **A** and $\tau = 680\text{ fs}$ for **B** to form a second transient species whose transient spectra again can be approximated by a superposition of the two probably CT-like states which are formed as the second detectable transient species in either the donor fragment **D** or acceptor fragment **E** (see Figures 36 and 37). A strong indication for the admixture of a NDI associated CT state in this second transient species of **A** and **B** is the slightly increased absorption around the characteristic small NDI anion band at $16\,500\text{ cm}^{-1}$.^[47] The dynamics of dyad **C** differ somewhat from those of **A** and **B** by the initial formation of a transient species with a very prominent transient signal at $17\,500\text{ cm}^{-1}$, which transforms with $\tau = 560\text{ fs}$ to the second transient species which is now spectrally more similar to the respective ones found in **A** and **B**. These second transient species of the dyads decay with $\tau = 42\text{ ps}$ for **A**, $\tau = 18\text{ ps}$ for **B** and $\tau = 8.3\text{ ps}$ for **C** to the last species that could be detected in the fs-set-up, which corresponds to the charge separated state (see Section 3.4.3). Therefore, these decay times of the second transient species dominate the charge separation step.

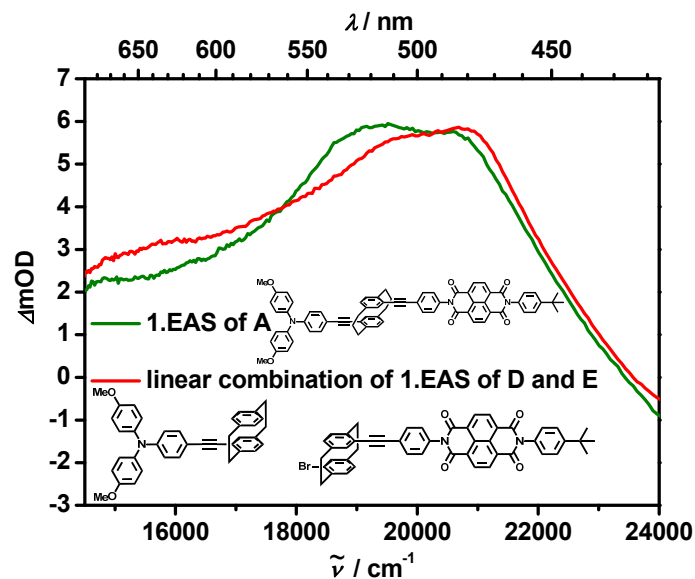


Figure 34. Approximation of the first evolution associated fs-transient absorption spectra of the dyad **A** in toluene by a linear combination of the first evolution associated fs-transient absorption spectra of the fragments **D** and **E** in toluene (excitation at 28 200 cm^{-1}).

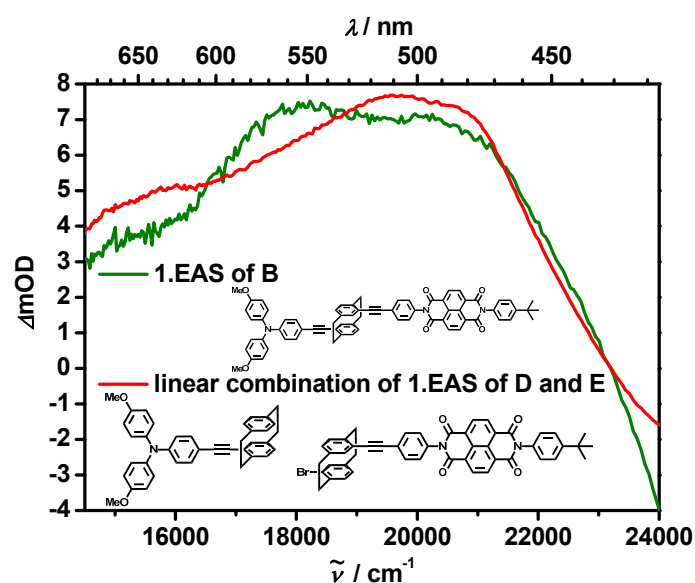


Figure 35. Approximation of the first evolution associated fs-transient absorption spectra of the dyad **B** in toluene by a linear combination of the first evolution associated fs-transient absorption spectra of the fragments **D** and **E** in toluene (excitation at 28 200 cm^{-1}).

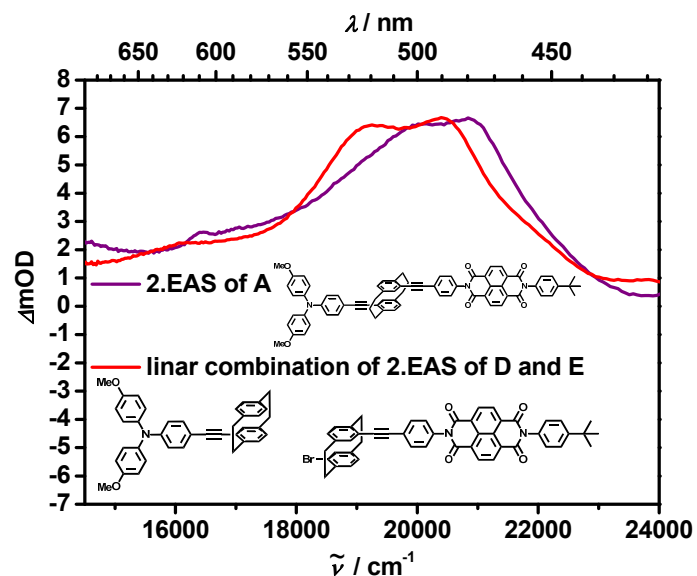


Figure 36. Approximation of the second evolution associated fs-transient absorption spectra of the dyad **A** in toluene by a linear combination of the second evolution associated fs-transient absorption spectra of the fragments **D** and **E** in toluene (excitation at $28\,200\text{ cm}^{-1}$).

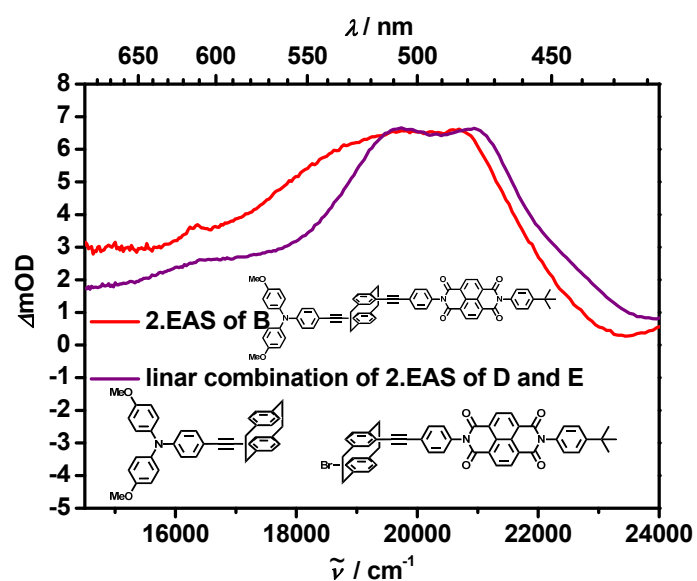


Figure 37. Approximation of the second evolution associated fs-transient absorption spectra of the dyad **B** in toluene by a linear combination of the second evolution associated fs-transient absorption spectra of the fragments **D** and **E** in toluene (excitation at $28\,200\text{ cm}^{-1}$).

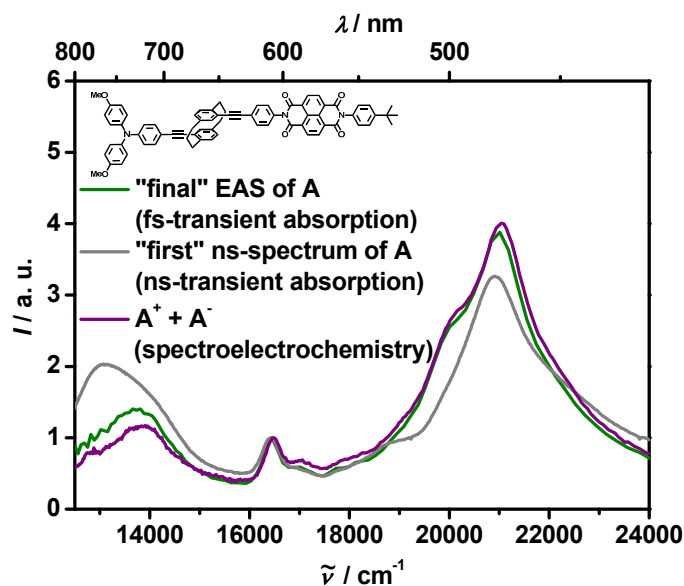


Figure 38. CS state spectra of **A**: superposition of the normalized “final” EAS ($\tau > 3$ ns) obtained by fs-transient absorption spectroscopy in toluene (excitation at 28200 cm^{-1}), the “first” spectra (at maximum instrument response) acquired via ns-transient transient absorption spectroscopy in toluene (excitation at $28\ 200\text{ cm}^{-1}$, averaged over 8 ns) and the sum of the monoanion and monocation spectra from spectroelectrochemistry in dichloromethane (0.2 M tetrabutylammonium hexafluorophosphate).

The “final” EAS with time constants $\tau > 3$ ns (time too long to be measured accurately with the fs-set-up) of the fs-measurements of the dyads **A–C** (see Figures 38-40) represent charge separated (CS) states in which the NDI is reduced and the TAA oxidized. This can easily be seen, since these transient spectra can be reproduced by the sum of the TAA cation and NDI anion spectra (see Figures 38-40) extracted from spectroelectrochemistry measurements (see Section 3.4.3). As in the spectra of the anions **A⁻–C⁻** (see Figures 23, 24 and 25 in Section 3.4.3) a high intensity band at around $21\ 000\text{ cm}^{-1}$ and a low intensity band at about $16\ 500\text{ cm}^{-1}$, which are characteristic for the NDI anion species can be detected.^[47] Furthermore, like in the spectra of the cations **A⁺–C⁺** the band with its main absorption between $13\ 000$ and $15\ 000\text{ cm}^{-1}$ can be clearly assigned to the TAA cation species,^[7, 36] even if it is somewhat shifted and weaker. Aside from solvent and supporting electrolyte effects (note that the spectroelectrochemistry was performed in dichloromethane and 0.2 M tetrabutylammonium hexafluorophosphate), the difference in shape and intensity in the TAA part of the fs-spectra of dyads, especially **B** and **C**, from the spectra determined via spectroelectrochemistry, can be partly attributed to a second order diffraction effect in the

experimental set-up. The ground state bleach at ca. $28\,600\text{ cm}^{-1}$ leads to a negative second order signal at ca. $14\,300\text{ cm}^{-1}$ (twice the wavelength) and therefore weakens the transient absorption signal right at the typical TAA band. In the present experiments this artifact was successfully reduced in the fs-transient absorption spectra of dyad **A** as well as all the ns-transient absorption spectra (see Section 3.5.2) by using an additional filter blocking the white light continuum in the region of the ground state bleach. Furthermore, a similar decrease in intensity and a broadening of the TAA radical cation band has been observed in transient absorption spectra while investigating CS states of small dyads involving naphthalene-monoimide as an acceptor.^[70] Finally, the “final” EAS of **A**, **B**, **C**, **D** and **E** (see Figures 38–42) match those recorded with the ns-set-up (see Section 3.5.2), especially if the deviations due to the second order effect are taken into account.

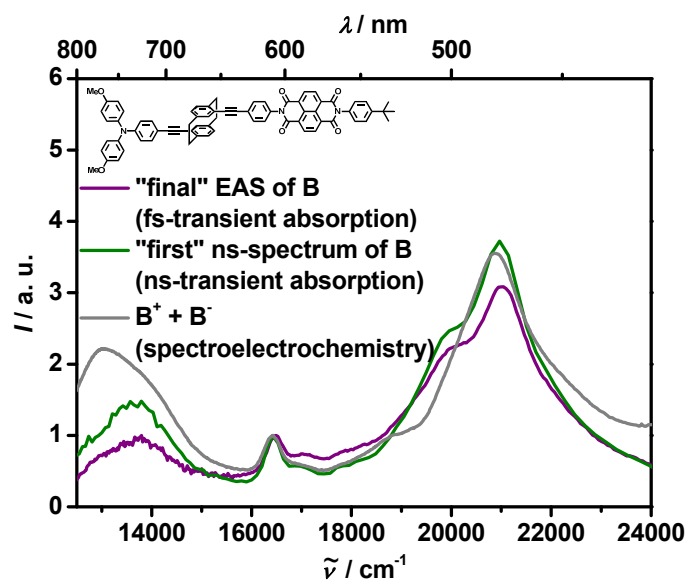


Figure 39. CS state spectra of **B**: superposition of the normalized “final” EAS ($\tau > 3\text{ ns}$) of **B**, obtained by fs-transient absorption spectroscopy in toluene (excitation at $28\,200\text{ cm}^{-1}$), the “first” spectra (at maximum instrument response) acquired via ns-transient transient absorption spectroscopy in toluene (excitation at $28\,200\text{ cm}^{-1}$, averaged over 8 ns) and the sum of the monoanion and monocation spectra from spectroelectrochemistry in dichloromethane (0.2 M tetrabutylammonium hexafluorophosphate).

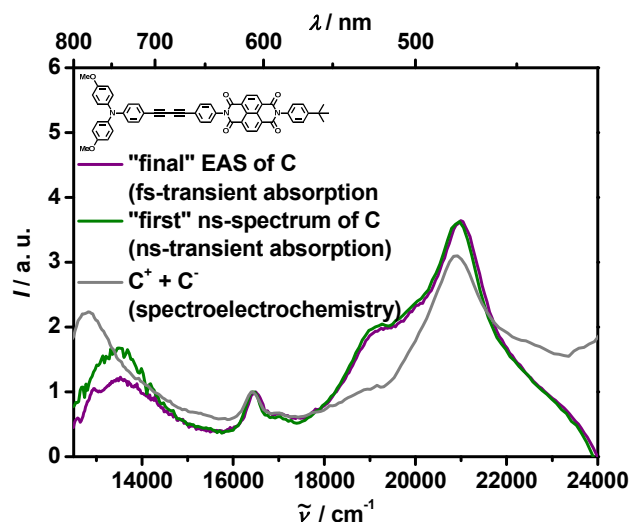


Figure 40. CS state spectra of **C**: superposition of the normalized “final” EAS ($\tau > 3$ ns) of **C** obtained by fs-transient absorption spectroscopy in toluene (excitation at 28200 cm^{-1}), the “first” spectra (at maximum instrument response) acquired via ns-transient transient absorption spectroscopy in toluene (excitation at $28\ 200\text{ cm}^{-1}$, averaged over 2 ns) and the sum of the monoanion and monocation spectra from spectroelectrochemistry in dichloromethane (0.2 M tetrabutylammonium hexafluorophosphate).

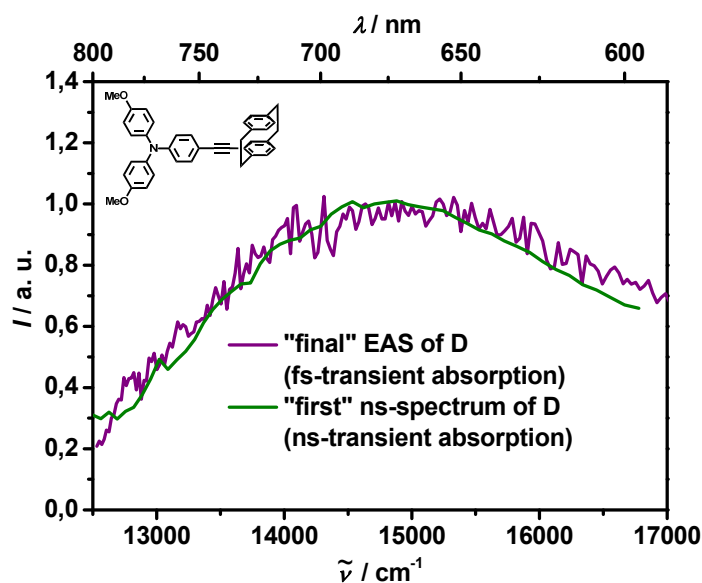


Figure 41. Triplet spectra of **D** in toluene (excitation at $28\ 200\text{ cm}^{-1}$): superposition of the normalized “final” EAS ($\tau > 3$ ns) of **D** obtained by fs-transient absorption spectroscopy and “first” spectrum acquired via ns-transient transient absorption spectroscopy (averaged over $0.5\ \mu\text{s}$).

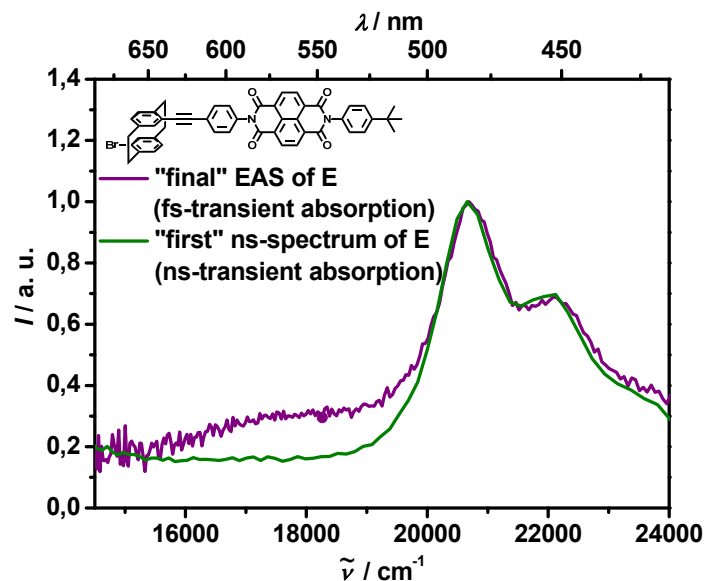


Figure 42. Triplet spectra of **E** in toluene (excitation at $28\,200\text{ cm}^{-1}$): superposition of the normalized “final” EAS ($\tau > 3\text{ ns}$) of **E** obtained by fs-transient absorption spectroscopy and “first” spectrum acquired via ns-transient transient absorption spectroscopy (averaged over $0.5\ \mu\text{s}$).

For dyad **A** additional fs-pump-probe measurements in acetonitrile (MeCN) in which both **B** and **C** proved to be not soluble enough were performed. Again two time constants until the CS state is reached were identified: 840 fs and 24 ps and two for the charge recombination 21 ns and 140 ns). The latter values have been measured with the ns-set-up, as described below (see Section 3.5.2). Compared to toluene, charge separation is enhanced by a factor of two in MeCN.

An overview of the EAS lifetimes from global deconvolution with GLOTARAN^[101] is given in Table 5.

Table 5. Lifetimes of the EASs from global fit.^a

	$\tau(1. \text{ EAS})$ / ps	$\tau(2. \text{ EAS})$ / ps	$\tau(3. \text{ EAS})$ / ps
A	2.2	42	
A(MeCN)	0.84	24	550
B	0.68	18	
C	0.56	8.3	
D	2.9	42	1800
E	14	350	

^aLifetimes are from the deconvolution of fs-transient absorption measurements in toluene (excitation at 28 200 cm⁻¹). Lifetimes which are too long for accurate measurement with the fs-set-up are not given.

3.5.2 NANOSECOND TRANSIENT ABSORPTION SPECTROSCOPY

To assess the quantum yield of charge separation and to monitor the dynamics of the longer lived states of **A–E**, like the charge recombination and intersystem crossing processes, a ns-pump-probe set-up was used. This allowed monitoring transient species from ca. 2 ns up to the ms time regime. Thus the ns-set-up has a temporal overlap with the fs-set-up in the 2–8 ns time window and therefore both together allow covering dynamics from ca. 100 fs to the ms time regime.

The quantum yield for the charge separation in the dyads was determined exemplarily by actinometry of **B** in toluene versus benzophenone in benzene with a laser pulse at $28\,200\text{ cm}^{-1}$ and laser pulse energies low enough to ensure direct proportionality to the transient absorption signals.^[103-105] A value of $\phi_{\text{CS}} = 0.80\text{--}0.85$ indicates almost quantitative charge separation.

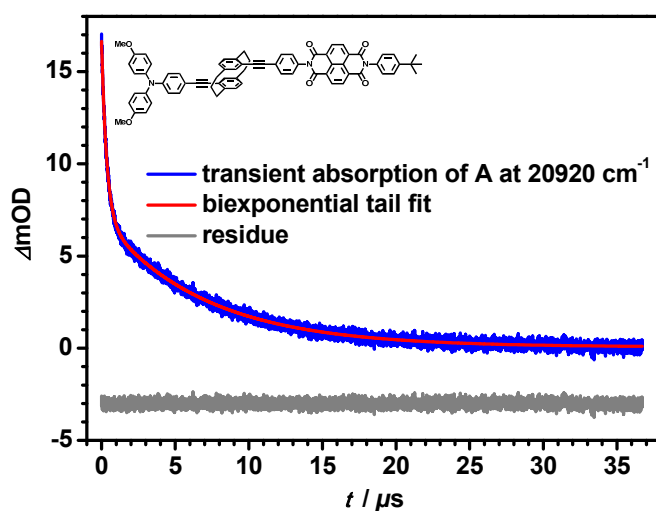


Figure 43. Biexponential tail fit of ns-transient absorption kinetics of **A** in toluene (excitation at $28\,200\text{ cm}^{-1}$).

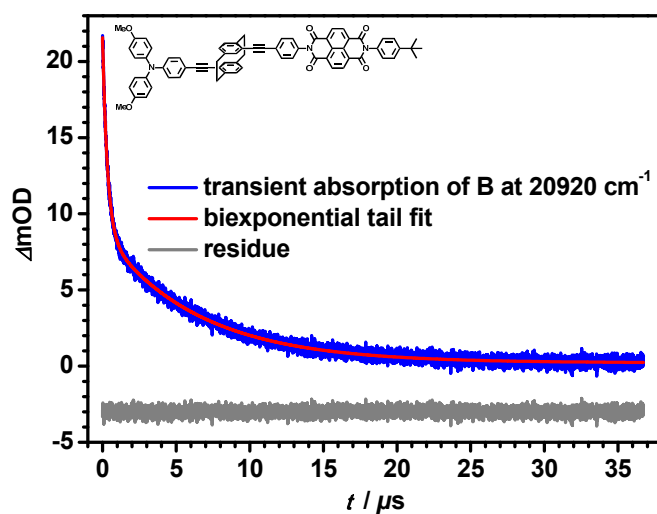


Figure 44. Biexponential tail fit of ns-transient absorption kinetics of **B** in toluene (excitation at $28\,200\text{ cm}^{-1}$).

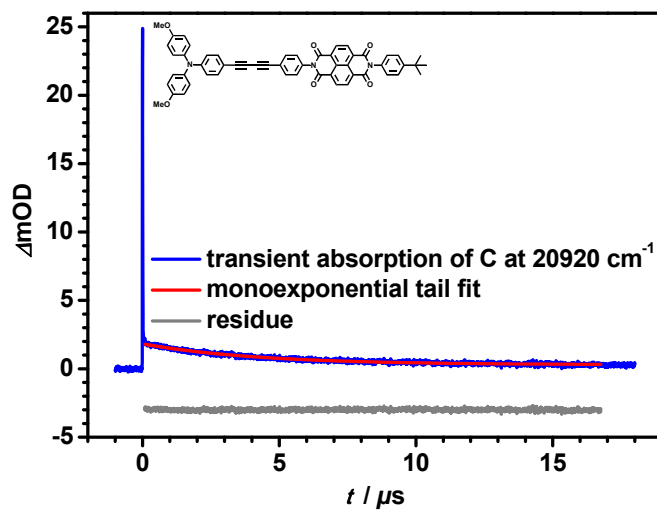


Figure 45. Monoexponential fit of ns-transient absorption kinetics of **C** at $20\,900\text{ cm}^{-1}$ in toluene (excitation at $28\,200\text{ cm}^{-1}$).

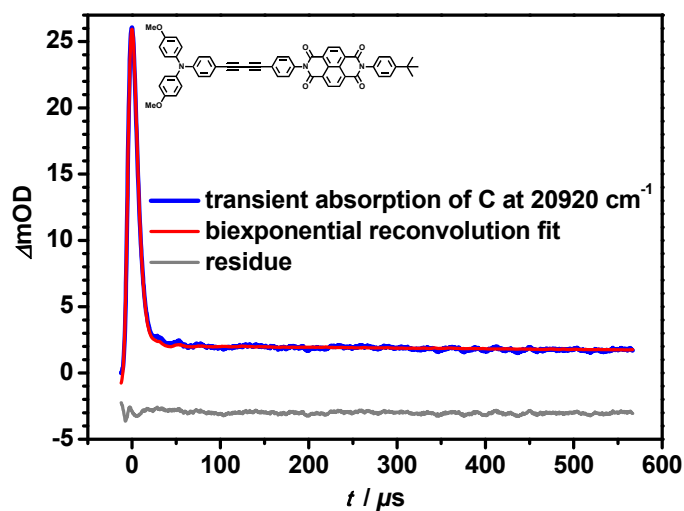


Figure 46. Biexponential reconvolution fit (with instrument response function) of ns-transient absorption kinetics of **C** at $20\,900\text{ cm}^{-1}$ in toluene (excitation at $28\,200\text{ cm}^{-1}$).

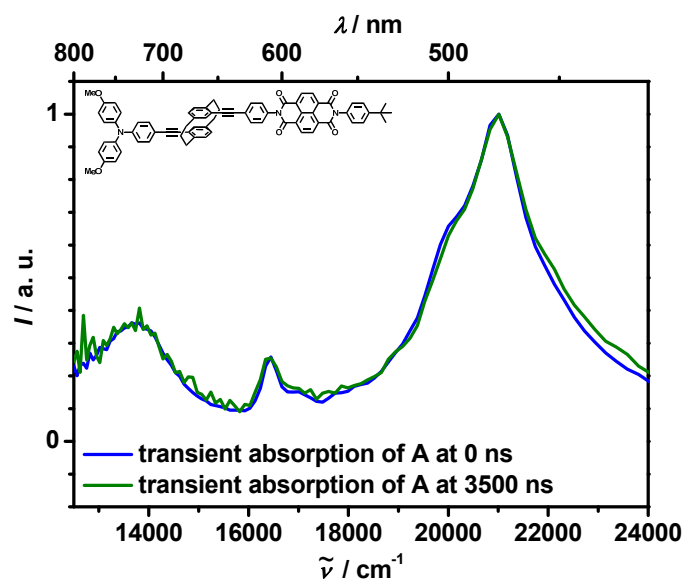


Figure 47. Superposition of ns-transient absorption spectra in toluene (excitation at $28\,200\text{ cm}^{-1}$) at the indicated time delays after $t = 0$ (maximum of instrument response) of **A** (spectrum at 0 ns averaged over 8 ns and at 3500 ns averaged over 20 ns).

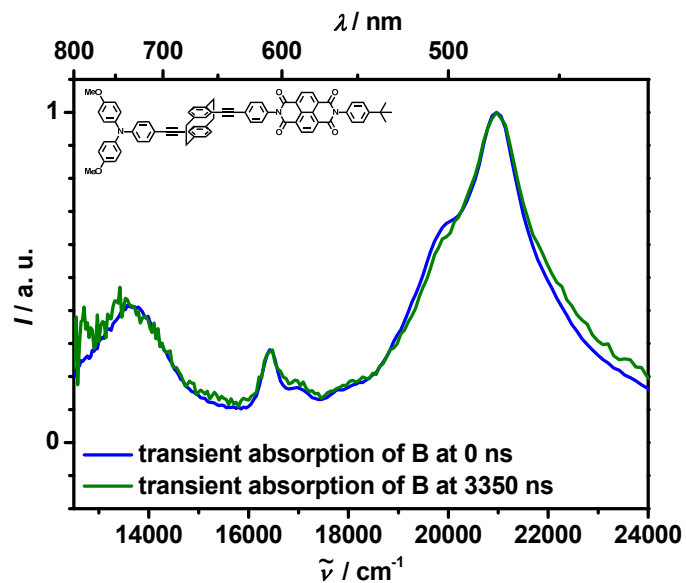


Figure 48. Superposition of ns-transient absorption spectra in toluene (excitation at $28\,200\text{ cm}^{-1}$) at the indicated time delays after $t = 0$ (maximum of instrument response) of **B** (spectrum at 0 ns averaged over 8 ns and at 3350 ns averaged over 20 ns).

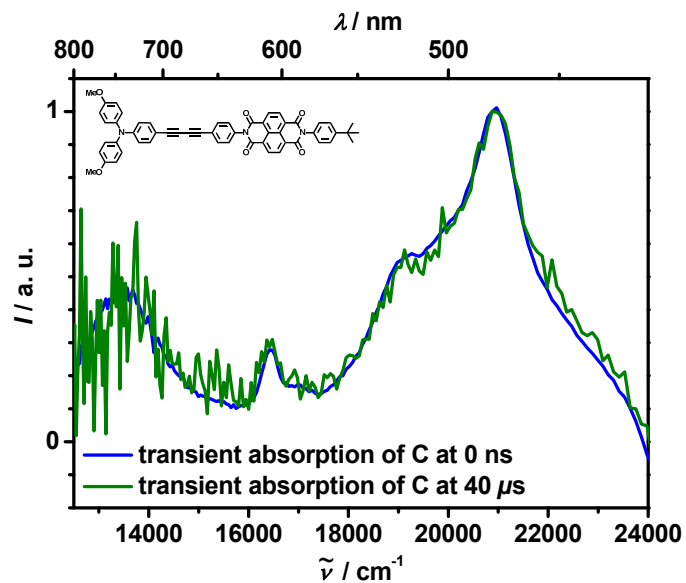


Figure 49. Superposition of ns-transient absorption spectra in toluene (excitation at $28\,200\text{ cm}^{-1}$) at the indicated time delays after $t = 0$ (maximum of instrument response) of **C** (spectrum at 0 ns averaged over 2 ns and at $40\ \mu\text{s}$ averaged over $2\ \mu\text{s}$).

Excitation of the dyads **A–C** with a ns-laser pulse at $28\,200\text{ cm}^{-1}$ yields a biexponential decay with a short component in the ns time regime and a long one in the μs time regime (see Figures 43–46). The spectral properties of both decay associated species are practically the same between $12\,500\text{ cm}^{-1}$ and $24\,000\text{ cm}^{-1}$ (see Figures 47–49). Especially if the deviations due to the second order effect are taken into account (see Section 3.5.1), they are identical to those of the last species detected with the fs-set-up as well as the sum of the anion and cation spectra determined by electrochemistry (see Sections 3.4.3 and 3.5.1). It is assumed that these two species are the charge separated states of singlet and triplet multiplicity (see below and Section 4.2), ^1CS and ^3CS .

Upon increasing the concentration (between $1\times 10^{-6}\text{ M}$ and $2\times 10^{-5}\text{ M}$) of the dyads **A** and **B** the short lifetimes decrease by 10–20% and the long lifetime by ca. 35% (the relative amplitudes remain almost constant though), which is likely to be due to bimolecular deactivation processes (see Table 6). A plot of τ_{long}^{-1} vs. the concentration of **A** or **B** indeed gives a linear correlation as expected for a bimolecular mechanism (see Figure 50). The rate constant $k_2 = 5\times 10^9$ extracted from the slope of the fit is also in agreement with a diffusion controlled bimolecular process. Thus, the underlined values in Table 6 present decay times/amplitudes that are measured at dilute concentrations at a reasonable signal to noise ratio which may be considered to be essentially free of bimolecular contributions, which can be seen from the plateau in the plot of τ_{long} vs. $1/[\text{M}]$ (see Figure 51). Excitation of dyads **A** and **B** with different laser pulse energy (between 0.8 mJ and 5.2 mJ led to excitation saturation of part of the probed volume which means that the possible bimolecular processes cannot be investigated by variation of the laser pulse energy in this range) and at different excitation wavenumbers ($28\,200\text{ cm}^{-1}$ and $24\,000\text{ cm}^{-1}$) neither change the decay dynamics nor the transient spectra within experimental error (see Table 6). Thus, any two-photon induced processes^[47] can be ruled out.

Table 6. Lifetimes (τ_{long} and τ_{short}) and ratio of the amplitudes ($A_{\text{long}}/A_{\text{short}}$) at 20 900 cm^{-1} of ns-transient absorption experiments at the given molarity and given laser pulse energy in toluene (excitation at 28 200 cm^{-1}) assuming biexponential decay.

	c /M	E_{laser} / mJ	τ_{long} / μs	τ_{short} / ns	$A_{\text{long}} / A_{\text{short}}$
A	1.3×10^{-6}	5.2	6.9	340	0.72
	<u>1.3×10^{-6}</u> ^a	<u>1.6</u> ^a	<u>7.0</u> ^a	<u>350</u> ^a	<u>0.72</u> ^a
	1.3×10^{-6}	0.80	7.1	360	0.61
	1.8×10^{-5}	1.6	4.5	320	0.70
	1.4×10^{-5} ^b	0.90 ^b	5.4 ^b	330 ^b	0.62 ^b
	5.8×10^{-6} ^{a, c}	1.6 ^{a, c}	0.14 ^{a, c}	21 ^{a, c}	0.20 ^{a, c}
B	9.8×10^{-7}	5.2	6.8	330	0.63
	<u>9.8×10^{-7}</u> ^a	<u>1.6</u> ^a	<u>6.9</u> ^a	<u>360</u> ^a	<u>0.62</u> ^a
	9.8×10^{-7}	0.80	6.9	340	0.63
	1.8×10^{-5}	1.6	4.3	300	0.664
	9.4×10^{-6} ^b	10 ^b	5.7 ^b	320 ^b	0.57 ^b
C	1.0×10^{-5}	5.2	3.2	4.2	0.025
	<u>1.0×10^{-5}</u> ^a	<u>1.6</u> ^a	<u>4.2</u> ^a	<u>4.0</u> ^a	<u>0.022</u> ^a
	2.4×10^{-5}	1.6	3.3	3.8	0.025
	2.3×10^{-5} ^b	0.90 ^b	3.2 ^b	3.8 ^b	0.013 ^b
	5.8×10^{-5} ^{b, d}	0.75 ^{b, d}	0.034 ^{b, d}	2.2 ^{b, d}	1.0 ^{b, d}

^a used for fits of rate constants and triplet CS state population maxima with TENUA^[106]

^b excitation at 24 000 cm^{-1} (416 nm). ^c in MeCN. ^d in oxygen saturated toluene.

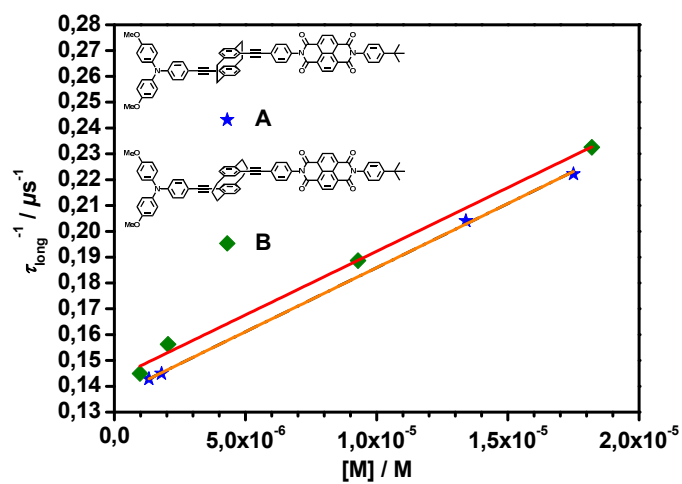


Figure 51. Inverse of time constant τ_{long} plotted vs. concentration of **A** and **B** from linearization of $\tau_{\text{long}} = 1/(k_1+k_2[M])$ for a bimolecular deactivation process.

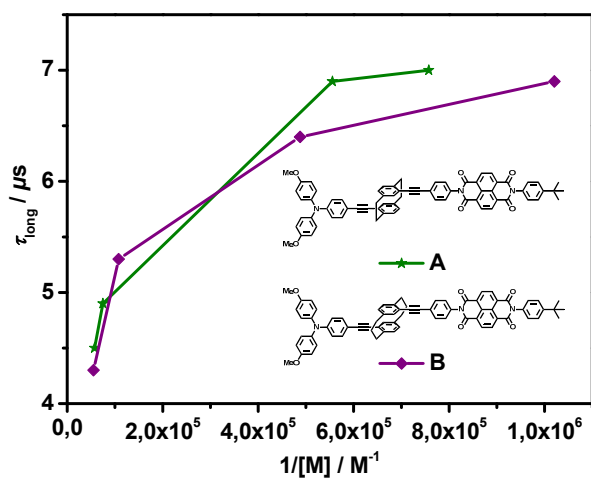


Figure 52. Plot of the long lifetime τ_{long} (from Table 6) vs. $1/\text{concentration}$ of the dyads **A** or **B**.

In contrast to **A** and **B**, for **C**, no reliable measurements at lower concentrations (only between 1×10^{-5} M and 2×10^{-5} M) could be performed because of otherwise low signal to noise ratio (see Table 6). Thus, the determined lifetimes of the longer lived species of **C** are probably afflicted by bimolecular contributions and are too short by ca. 2–3 μ s, as was estimated by comparison with the concentration dependent data for **A** and **B**. In addition, unlike for **A** and **B**, for **C** excitation at different wavenumbers ($28\,200\text{ cm}^{-1}$ and $24\,000\text{ cm}^{-1}$) changes the ratio of the amplitudes of the exponential decay fit functions indicating a change in the ratio of the two primarily generated species (TAA vs. NDI excitation) (see Table 6).

Furthermore, example measurements of **C** in oxygen-saturated toluene were conducted and gave a time constant for the slower component (see Table 6), which was reduced by two orders of magnitude probably through oxygen catalyzed intersystem crossing. This finding supports the conclusion that the long-lived species of the dyads are triplet CS states.^[107-109]

4 DISCUSSION

4.1 DISCUSSION OF MIXED VALENCE COMPOUND F^+

The results of the investigation of mixed-valence compound F^+ (see Figure 53) complemented by electron paramagnetic resonance (EPR) spectroscopy data acquired via a cooperation project with *Grampp et al.*^[25] will be discussed. There focus will be on comparison to the data of the literature known [2.2]-paracyclophane containing reference compounds G^+ and the fully conjugated reference compound N^+ (see Figure 53).^[7]

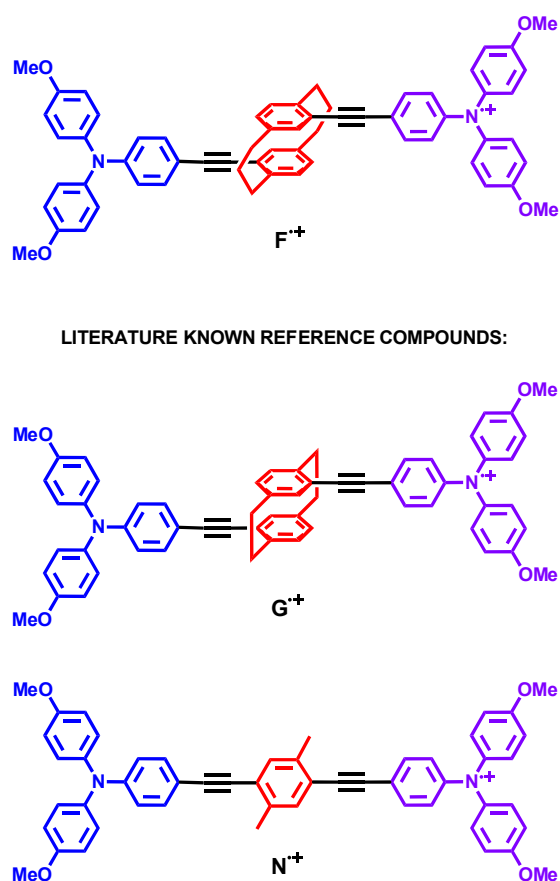


Figure 53. Structural formulas of target model systems and literature known reference compounds including functional assignment of their segments: donor (blue), bridge unit (red) and acceptor (purple).

First, the positioning of the maxima of the intervalence charge transfer absorption band of \mathbf{F}^+ with at least $8\,500\text{ cm}^{-1}$ in dichloromethane is addressed (see Section 3.4.1). It is significantly higher than the value of $5\,870\text{ cm}^{-1}$ in dichloromethane for \mathbf{G}^+ (see Table 7).^[7] Within the two-level Mulliken-Hush approach^[98, 99] (see Section 3.4.1), this value represents the reorganization energy associated with the charge transfer, which consists of an inner and an outer sphere contribution. The outer sphere contribution is caused by the readjustment of the solvent molecules after the charge transfer has taken place and thus is mainly dependent on the distance of the redox centers.^[38] The inner sphere energy contribution is caused by the rearrangement of the atoms i.e. bond length and angle alterations within the compound, usually concentrated at the redox centers upon changing their oxidation states.^[38] Since the distance between is nearly the same and the structure of the redox centers is identical in both compounds, one would assume these contributions to be similar. However, this is clearly not the case and therefore the slight structural difference of the bridging unit remains the only reasonable explanation for a substantial change of the internal reorganization energy. This deduction is supported by a similar conclusion regarding compounds where triarylamine redox centers are linked by similar bridging units to perchlorotriphenylmethyl radicals.^[110]

Table 7. $\tilde{\nu}_c$ maximum of intervalence charge transfer band determined with Vis-NIR spectroscopy in dichloromethane, $V_{\text{two-state}}$ electronic coupling and $\Delta G^*_{\text{two-state}}$ thermal barrier height acquired via application of two-state Mulliken-Hush theory on the spectroscopy data, ΔG^*_{EPR} thermal barrier and k_{EPR} electron transfer rate obtained by electron paramagnetic resonance spectroscopy (EPR) in dichloromethane.

	$\tilde{\nu}_c$ / cm^{-1}	$V_{\text{two-state}}$ / cm^{-1}	$\Delta G^*_{\text{two-state}}$ / cm^{-1}	ΔG^*_{EPR} / cm^{-1}	k_{EPR} / s^{-1}
\mathbf{F}^+	8 500	320	1 820	1 420	0.90×10^8
\mathbf{G}^+	5 870 ^[7]	310 ^[7]	1 170 ^[7]	1 250	0.69×10^8
\mathbf{N}^+	7 500 ^[7]	1 030 ^[7]	990 ^[7]	900 ^[25]	$13 \times 10^8\text{ s}^{-1}$ ^[25]

Regarding the electronic coupling in \mathbf{F}^+ , the application of the two-state Mulliken-Hush theory^[98, 99] yielded a value of 320 cm^{-1} (see Section 3.4.1), which is near identical to 310 cm^{-1} of \mathbf{G}^+ (see Table 7).^[7] This conformity is unexpected since the distance 3.3 \AA ^[27]

between the aromatic rings in [3.3]paracyclophane as incorporated within **F** is on the edge of the double Van der Waals radii, while the distance $3.1 \text{ \AA}^{[2, 26]}$ in [2.2]paracyclophane as integrated in **G**⁺ is well within. These findings weaken the common assumption of substantial electronic coupling via the ethylene orbitals of the linkers in [2.2]paracyclophane,^[1, 3, 4, 7] since such a contribution can be excluded in [3.3]paracyclophane due to the three consecutive saturated carbon atoms in the alkyl linkers.

Concerning the thermal barriers, they were roughly estimated via the two-state Mulliken-Hush approach yielding $1\,820 \text{ cm}^{-1}$ for **F**⁺ (see Section 3.4.1) in comparison to $1\,170 \text{ cm}^{-1}$ ^[25] for **G**⁺ (see Table 7). However, the more precise values provided by *Grampp et al.* via direct acquisition by temperature dependent electron paramagnetic resonance (EPR) spectroscopy are rather similar with $1\,420 \text{ cm}^{-1}$ for **F**⁺ and $1\,250 \text{ cm}^{-1}$ for **G**⁺ (see Table 7).^[25] Furthermore, the thermal electron transfer rates determined by EPR spectroscopy at 300 K in dichloromethane with $0.90 \times 10^8 \text{ s}^{-1}$ for **F**⁺ and $0.69 \times 10^8 \text{ s}^{-1}$ for **G**⁺ are nearly identical (see Table 7). These results clearly indicate “through space” charge transport of comparable efficiency via the [3.3]paracyclophane in **F**⁺ and the smaller [2.2]paracyclophane in **G**⁺. As with the electronic couplings (see above), the similarity of these results is quite exceptional because of the difference of the through-space distance and the missing pathway via ethylene orbitals in the [3.3]paracyclophane bridging unit.

Furthermore, when comparing these results to the charge transfer in the fully conjugated compound **N**⁺ of similar size, which has, as to be expected, a higher electronic coupling and lower thermal barrier, its charge transfer rate at 300 K in methylene chloride of $13 \times 10^8 \text{ s}^{-1}$ ^[25] proves to be just one order of magnitude higher (see Table 7). This leads to the assumption that intermolecular charge transfer can remain efficient as long as the through-space distance between stacked π -systems remains within the double Van der Waals radii of the integral carbons.

4.2 DISCUSSION OF DYADS A-C

In this section, from the results given, a hypothesis about the photophysical processes taking place upon laser excitation of the dyads **A–C** (see Figure 54) was set up.

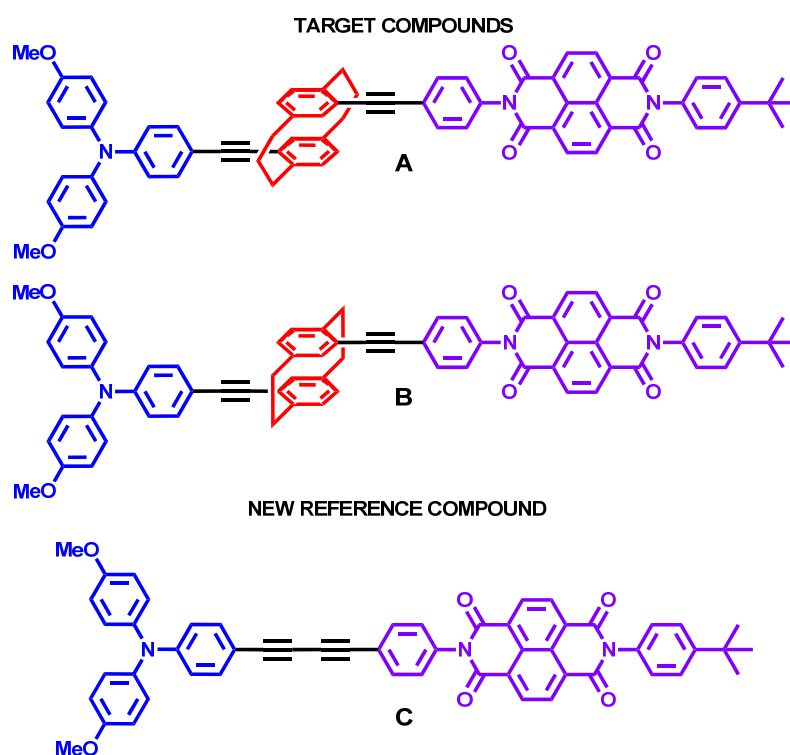


Figure 54. Structural formulas of target model systems and reference compound including functional assignment of their segments: donor (blue), bridge unit (red) and acceptor (purple).

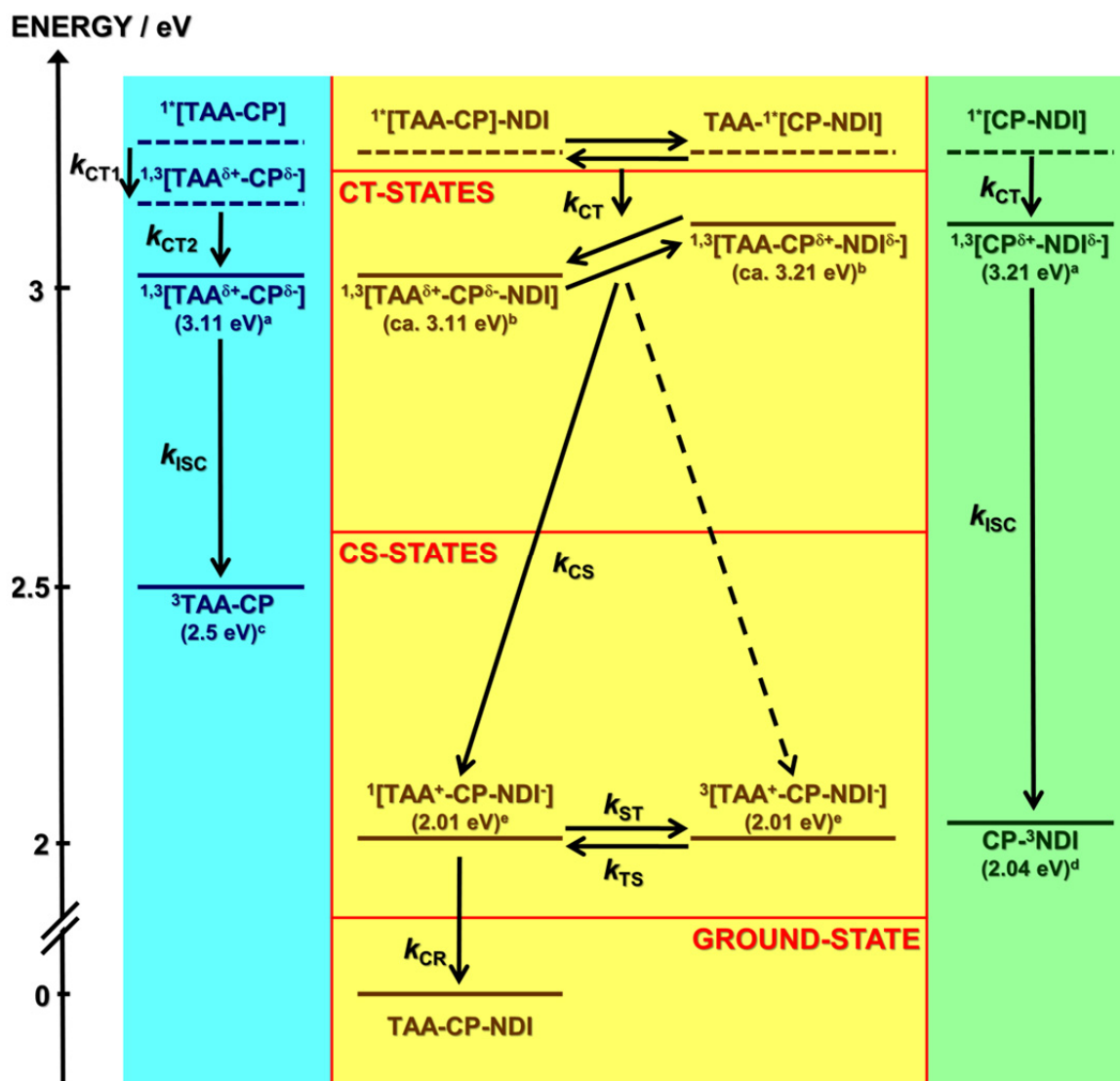


Figure 55. Energy scheme and dynamics of the photophysical processes in **A** and **B** (middle panel) upon excitation at 3.49 eV ($28\,200\text{ cm}^{-1}$). The left panel refers to data for **D**, the right panel for **E**. ^a From steady state absorption and fluorescence measurements. ^b Estimated from the charge transfer (CT) state energies of **D** and **E**. ^c Taken from the triplet energy of dianisylaminobiphenyl in toluene at 77 K^[70]. ^d Taken from the triplet energy of naphthalene diimide in ethanol at 77 K (2.03 eV)^[47] and in 2-methyltetrahydrofuran at 77 K (2.05 eV)^[46]. ^e Estimated by Rehm-Weller approximation (see Section 3.3.2). “1,3” indicates that the spin multiplicity and a dashed line that the state energy is unknown.

Table 8. Rate constants for charge transfer (k_{CT}), charge separation (k_{CS}), intersystem crossing to local triplet states (k_{ISC}), charge recombination (k_{CR}), singlet-triplet intersystem crossing (k_{ST}), triplet-singlet intersystem crossing (k_{TS}), starting value and population maximum of fraction of triplet charge separated states ($\rho_{start3CS}$ and ρ_{max3CS}) and electronic coupling for the charge separation (V_{CS}) and charge recombination process (V_{CR}).

	A	A (MeCN)	B	C	D	E
k_{CT} / $\times 10^{10} \text{ s}^{-1}$	45 ^b		150 ^b	180 ^b	34 / 2.4 ^b	7.1 ^b
k_{CS} / $\times 10^{10} \text{ s}^{-1}$	2.4 ^b	4.2 ^b	5.6 ^b	12 ^b		
k_{ISC} / $\times 10^6 \text{ s}^{-1}$					560 ^b	2900 ^b
k_{CR} / $\times 10^{10} \text{ s}^{-1}$	2.3 ^{a,c}	41 ^a	2.5 ^{a,c}	230 ^a		
k_{ST} / $\times 10^6 \text{ s}^{-1}$	0.54 ^{a,c}	5.8 ^a	0.56 ^{a,c}	0.28 ^a		
k_{TS} / $\times 10^6 \text{ s}^{-1}$	0.18 ^{a,c}	8.2 ^a	0.19 ^{a,c}	0.24 ^a		
$\rho_{start3CS}$	25%	0%	20%	1.9%		
ρ_{max3CS}	34% ^{a,c}	8.7% ^a	33% ^{a,c}	2.2% ^a		
V_{CS} / cm^{-1}	80 ^d		120 ^d			
V_{CR} / cm^{-1}	60 ^d		60 ^d			

^a Fits of nanosecond transient absorption data with TENUA^[106] (target analysis/time-invariant compartmental model). ^b Reciprocal values of EAS lifetime fits of femtosecond transient absorption data with GLOTARAN^[101] (sequential model). ^c The ratio $k_{ST}/k_{TS} = 3/1$ was fixed. ^d Estimated by using the Bixon-Jortner equation (eq. 7).

A detailed picture of these processes in particular for **A** and **B** is given in the energy level diagram in Figure 55 with the corresponding rate constants in Table 8. Because of spectral overlap of the TAA and the NDI moiety laser excitation populates both the singlet triarylamine

(TAA) (which also involves the cyclophane moiety) and the singlet naphthalene diimide (NDI) states (which also involves the cyclophane moiety) of **A–C** (in case of **A** and **B** one may also discuss the formation of “phane-states” but these are typically higher in energy^[24, 111-118]). In both **A** and **B** starting from the locally excited state of TAA, the singlet charge separated (CS) state $^1[\text{TAA}^+-\text{CP}-\text{NDI}^-]$ becomes populated via the intermediate charge transfer (CT) state $^1[\text{TAA}^{\delta+}-\text{CP}^{\delta-}-\text{NDI}]$ involving the TAA and the bridging cyclophane (CP). In a parallel process, the locally excited NDI-CP state relaxes into a CT state $^1[\text{TAA}-\text{CP}^{\delta+}-\text{NDI}^{\delta-}]$, which also undergoes charge separation into the singlet CS state $^1[\text{TAA}^+-\text{CP}-\text{NDI}^-]$. A possible side reaction from the CT state into the locally excited NDI triplet state $[\text{TAA}-\text{CP}-^3\text{NDI}]$ can be neglected (i.e. < 15%), as this is a relatively slow process compared to charge separation (see below for the rates of the processes). The formation of a locally excited TAA triplet state is even slower (see above) and can thus be ruled out. The postulation of intermediate CT states rests on the analysis of the transient spectra of **D** and **E** and the similarity of their spectra to those found in **A–C** (see Section 3.5.1).

As shown in Table 8, from the conducted fs-measurements two different rate constants for the charge separation process in **A–C**, a fast ($45 \times 10^{10} \text{ s}^{-1}$ – $180 \times 10^{10} \text{ s}^{-1}$) and a slow one ($2.4 \times 10^{10} \text{ s}^{-1}$ – $12 \times 10^{10} \text{ s}^{-1}$) could be extracted. The fast rate constant is interpreted as the one that leads to the hypothetical CT states and the slow constant as the one which leads to the CS states via a charge separation process. Clearly, these rate constants should be regarded as average values, since they involve a mixture of states and possibly also multiplicities. In this respect, it is surprising that especially for dyad **B** (and for **A**) the fast CT rate constant $150 \times 10^{10} \text{ s}^{-1}$ ($45 \times 10^{10} \text{ s}^{-1}$) is faster than the equivalent CT forming process in either model compound **D** ($34 \times 10^{10} \text{ s}^{-1}$) or **E** ($7.1 \times 10^{10} \text{ s}^{-1}$). This indicates that both hypothetical CT states of **B** (and of **A**) are not exactly equivalent to the analogous CT states of **D** and **E**.

Charge separation then occurs with a rate constant of $5.6 \times 10^{10} \text{ s}^{-1}$ for **B** (and $2.4 \times 10^{10} \text{ s}^{-1}$ for **A**), which is much faster than ISC into local triplet states in **D** ($5.6 \times 10^8 \text{ s}^{-1}$) and **E** ($2.9 \times 10^9 \text{ s}^{-1}$). This charge separation rate constant rises with increasing electronic donor-acceptor coupling in the series **A** ($2.4 \times 10^{10} \text{ s}^{-1}$), **B** ($5.6 \times 10^{10} \text{ s}^{-1}$) and **C** ($12 \times 10^{10} \text{ s}^{-1}$), as does the rate constant for formation of the CT state: **A** ($45 \times 10^{10} \text{ s}^{-1}$), **B** ($150 \times 10^{10} \text{ s}^{-1}$) and **C** ($180 \times 10^{10} \text{ s}^{-1}$).

Especially when interpreting the dynamics of charge recombination of **A–C**, it must be considered that the CS states may adopt a triplet configuration, which is in equilibrium with the singlet CS state having practically the same energy. Because of spin conservation rules, only the singlet CS state can recombine to yield the singlet ground state. If the primarily

populated state is the singlet CS state, which can include parallel population of the triplet CS state (but not primarily population of the triplet CS), e.g. via a triplet CT state or a locally excited triplet NDI state, then the proposed kinetic scheme (see Figure 55) leads to a biexponential decay (so called “relaxation mechanism”),^[108, 119-122] as indeed has been observed in the present ns-experiments. That the spectra of the two decaying components are identical supports the assumption of degenerate singlet and triplet CS states, as these should indeed be spectrally identical because of the large distance of the two radical ion centers. Furthermore, the exemplary induced oxygen catalyzed intersystem crossing of **C** substantiates the assumption of the long lived states of the dyads being triplet states.^[107-109] The significance of triplet states in NDI containing systems was recently mentioned by Langford *et al.*, who also observed long-lived CS states in Zn-porphyrin-NDI dyads and also suggested singlet-triplet (S-T) interconversion to be the reason for their longevity.^[123]

From the two time constants and the relative amplitude of the biexponential decay in deaerated toluene, one can evaluate the rate constants for S-T equilibrium of CS states (k_{ST} and k_{TS}) as well as that of the deactivation into the ground state (k_{CR}) by using analytical expressions.^[124] However, in the work here, these values were extracted by numerical fitting of the decay curves by the TENUA^[106] program (target analysis/time-invariant compartmental model, see Section 6.1). For the CS states equilibrium it was assumed that $k_{ST} = 3 \times k_{TS}$ ^[125] according to the spin statistics of degenerate states (if this constraint is released one nevertheless obtains similar rate constants). All of these rate constants are given in Table 8. Since an initially partially populated triplet CS state is possible (see above) the initial population percentage of the singlet and the triplet CS state of **A–C** were also fitted. In fact, an initial 1.9%–25% triplet population gives the best fit to the experimental data. Surprisingly, the rate constants for charge recombination k_{CR} and for the S-T equilibrium are very similar for **A** and **B**. This also holds true for the S-T equilibrium of **C**, but not for the charge recombination rate, which is three orders of magnitude larger for **C** than for **A** and **B**. This shows that charge recombination is strongly influenced by the type of the bridge (and the donor acceptor distance), while spin interconversion is not in the present case. In contrast, charge separation rises only moderately with relative rate constants k_{CS} 1/2.3/5 in the series **A–C**.

In toluene, the ratio k_{CS}/k_{CR} between charge separation and charge recombination from the singlet CS state is 1.0×10^4 for **A** and 2.3×10^4 for **B** but only 520 for **C**. Thus, the CS state of **A** and **B** may clearly be considered as “unusually long-lived” according to the definition of Verhoeven and Harriman *et al.*^[126] This is even more appropriate if the charge recombination from the triplet CS state with a maximal population of 34% and 33% for **A** and **B**, but only

2.2% for **C**, for which ratios of 1.3×10^5 for **A**, 2.9×10^5 for **B** and 5.0×10^5 for **C** are obtained, is considered.

Taking the evaluated energy data of the lowest CT state ${}^{1,3}[\text{TAA}^{\delta+}\text{-CP}^{\delta-}\text{-NDI}]$ (see Figure 55) and the CS states ${}^{1,3}[\text{TAA}^+\text{-CP-NDI}^-]$ (see Figure 55 and Section 3.3.2) gives a free energy of charge separation ΔG_{CS} of -1.10 eV for **B** and -1.11 eV for **A**. The reorganization energy for this process can be estimated by the arithmetic mean of the internal reorganization energy^[127] λ_v of triphenylamine (0.12 eV)^[128] and of naphthalene diimide (0.39 eV)^[129, 130], which yields 0.26 eV and the solvent reorganization energy λ_o for e.g. **B**, which was estimated by the Marcus equation^[38] to be 0.08 eV. Thus, because of $(\lambda_v + \lambda_o) < |\Delta G_{\text{CS}}|$ charge separation is in the Marcus inverted region. For the free energy of charge recombination (ΔG_{CR}), which corresponds to the energies of the CS states ${}^{1,3}[\text{TAA}^+\text{-CP-NDI}^-]$ with -2.01 eV for **B** and -2.00 eV for **A** (see Section 3.3.2) is even larger, charge recombination was concluded to be in the Marcus inverted region also. Furthermore, because of its higher exergonicity ($\Delta G_{\text{CS}} = -2.0$ eV *versus* $\Delta G_{\text{CS}} = -1.1$ eV), charge recombination compared to charge separation is expected to be much slower. These causal relations are supported by measurements of **A** in acetonitrile ($\lambda_v + \lambda_o = 1.65$ eV), which show an only slightly faster charge separation ($k_{\text{CS}} = 4.2 \times 10^{10} \text{ s}^{-1}$ compared to $2.4 \times 10^{10} \text{ s}^{-1}$ in toluene) but a much faster charge recombination ($k_{\text{CR}} = 4.1 \times 10^7 \text{ s}^{-1}$ compared to $2.3 \times 10^6 \text{ s}^{-1}$ in toluene) than in toluene. In fact, due to stabilization of the CS state in acetonitrile ($\Delta G_{\text{CR}} = -0.97$ eV), back electron transfer is now in the Marcus normal region while charge separation remains in the inverted region with $\Delta G_{\text{CS}} = -2.14$ eV.

If identical reorganization parameters for all species (which is a good approximation for **A** and **B** but might not be for **C**) are assumed, the ratio of ET rates as given by the Bixon-Jortner equation (7)^[131-135] reflects the square of the electronic donor-acceptor interaction integral V^2 .

$$k_{\text{-ET}} = 4\pi^2 \text{hc}^2 V^2 \sum_{j=0}^{\infty} \frac{e^{-S} S^j}{j!} \sqrt{\frac{1}{4\pi \text{hc} \lambda_o kT}} \exp\left[-\frac{\text{hc}(j\tilde{\nu}_v + \lambda_o + \Delta G^{00})^2}{4\lambda_o kT}\right] \quad (7)$$

with $S = \frac{\lambda_v}{\tilde{\nu}_v}$

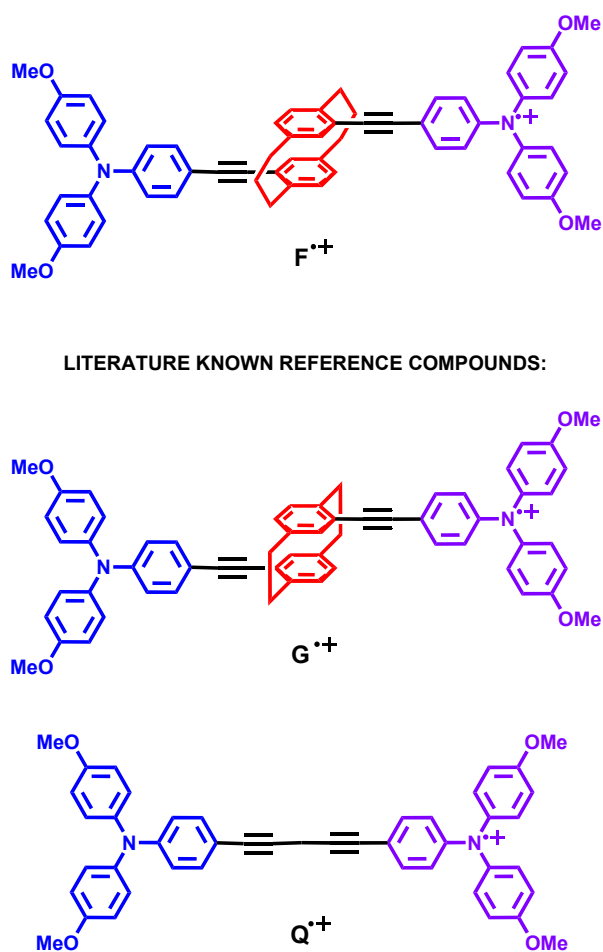


Figure 56. Structural formulas of target model systems and main reference compounds including functional assignment of their segments: donor (blue), bridge unit (red) and acceptor (purple).

A rough estimate for the electronic coupling in **A–C** can be obtained from the degenerate ET processes in the mixed valence bis(triarylamine) monoradical cation $\mathbf{F}^{\bullet+}$ investigated within this work (see Section 3.4.1) and the literature known monoradical cations $\mathbf{G}^{\bullet+}$ [25] and $\mathbf{Q}^{\bullet+}$ [25, 38] with analogous bridge moieties between the triarylamine redox centers (see Figure 56). While the only marginal difference between $V = 310 \text{ cm}^{-1}$ for $\mathbf{F}^{\bullet+}$ and $V_{\text{two-level}} = 320 \text{ cm}^{-1}$ for $\mathbf{G}^{\bullet+}$ (which agrees with the charge recombination behavior of **A** and **B**) with $V_{\text{two-level}} = 1790 \text{ cm}^{-1}$ the coupling of $\mathbf{Q}^{\bullet+}$ is a factor 5.8 higher than $\mathbf{F}^{\bullet+}$, which would lead to a rate constant factor $5.8^2 = 34$ higher for **C** than **A**. Experimentally a factor of 92 for k_{CR} of **C** vs. **A** was observed, which thus must be due to additional effects beyond that of electronic coupling issues of the bridging units. However, it should be noted that the nodal planes of the lowest unoccupied and highest occupied molecular orbitals^[40] in the NDI moiety reduce the

electronic coupling. Thus, the couplings in **A–C** are probably significantly smaller than those in the mixed valence species mentioned here.

The rate constants determined for charge separation and charge recombination of **A** and **B** allow a more accurate estimation of the electronic coupling for the ET process by using the Golden rule formula by Bixon and Jortner (eq. 7) mentioned above. Here for k_{-ET} the values for k_{CS} or k_{CR} as given in Table 8 and furthermore $\lambda_v = 0.26$ eV (2016 cm^{-1}) and $\lambda_o = 0.08$ eV (645 cm^{-1}) (see above) were used. (Bixon-Jortner theory rests on the assumption that low energy vibrations can be treated classically and are mainly associated with solvent modes whereas molecular modes are associated with high-energy vibrations which are treated quantum mechanically. While this assumption may work well for polar solvents, in apolar solvents where the solvent reorganization energy approaches zero, there should still be a sizable classical barrier from low frequency intramolecular modes left. This would in effect increase the classical barrier with $\lambda_o = 0.08$ eV. Because there is no information about these low frequency modes, the electronic coupling for $\lambda_o = 0.08$ eV as the pure solvent contribution is given to the low energy modes. A twofold reorganization energy would lead to the decrease of the electronic coupling by ca. 40%.) For the average vibrational mode, $\tilde{\nu}_v = 1500$ cm^{-1} was used as a typical value.^[131, 136-138] Application of the Rehm-Weller equation (see Section 3.3.2) gives $\Delta G_{CS} = -8\,872$ cm^{-1} (–1.10 eV) and $\Delta G_{CR} = -16\,211$ cm^{-1} (–2.01 eV) for ΔG^{00} in eq 7. With all these input values, $V_{CS}(\mathbf{A}) = 80$ cm^{-1} , $V_{CS}(\mathbf{B}) = 120$ cm^{-1} , $V_{CR}(\mathbf{A}) = 60$ cm^{-1} and $V_{CR}(\mathbf{B}) = 60$ cm^{-1} are obtained. These values are about one third to one sixth of those of bis(triarylamine) radical cations **F**⁺ and **G**⁺ which is reasonable if one takes the decoupling character of NDI into account when it is attached via its nitrogen atom. The difference between charge recombination and charge separation is also reasonable, because in the former it is dealt with the electronic coupling between the CS state and the ground state, but in the latter with the locally excited CT state and the CS state. Charge recombination is a ground state process for which the electronic coupling, similar to the electronic coupling in **F**⁺ and **G**⁺, does not depend on the two different cyclophanes. This is because in these cases the CPs merely act via virtual states as bridges in a superexchange mechanism^[38, 139] Charge separation, however, is an excited state process and depends on the cyclophane moiety because intermediate CT states probably play a role in which the cyclophane states are actually populated. Taking advantage of different electronic couplings in the ground and excited state of e.g. *para*- vs. *meta*-substituted benzene bridges has recently gained much attention in photoinduced ET processes^[54, 140-142] and might be a way to tailor ET dynamics in small dyads or triads.

At present one can only speculate about the mechanism of S-T interconversion of the CS species because there is a lack of e.g. magnetic field experiments which would give exact information about the size of the exchange interaction $2J$. S-T interconversion of organic radical (ion) pairs is often promoted by the hyperfine coupling (hfc) interaction, particularly in cases in which the triplet-singlet state are practically degenerate—that is at long separation of spin centers.^[94, 109, 143] In this case, the spin-spin exchange interaction is small and lies within the hfc interaction (e.g. for $2J = E(\text{singlet}) - E(\text{triplet}) = 50 \text{ G} = 4.67 \times 10^{-3} \text{ cm}^{-1} \rightarrow 1.4 \times 10^8 \text{ s}^{-1}$ interconversion rate).^[143] However, for radical centers in closer contact $2J$ may be substantial (several cm^{-1}).^[144] In that case, S-T interconversion is governed by the spin-lattice relaxation and thus falls in the $10^{-4} - 10^{-6} \text{ s}$ time regime.^[119, 145] From the observation of k_{ST} and k_{TS} being on the order of $10^{-5} - 10^{-6} \text{ s}^{-1}$ in **A-C** it is concluded that the mechanism is probably spin-lattice relaxation. In fact, charge separation and recombination rates are fast which implies a sizable electronic coupling and thus also a large exchange interaction $2J$. The fact that the rate constants k_{ST} and k_{TS} are significantly larger in acetonitrile may be explained by the solvent dependence of state energies with which the radical pair CS states mix in a perturbational approximation originally given by Anderson but recently often used by others^[107, 136, 144, 146-152] This approximation (eq. 8) develops the S-T splitting as a sum over states. In this series the electronic ET couplings $V_{1,3\text{CS}-N_n}$ between the given $^{1,3}\text{CS}$ state with the energetically next lying singlet or triplet states N_n are divided by the vertical energy separation $\Delta G_{1,3\text{CS}-N_n}$ between these states. In this way, those states that are close in energy to the $^{1,3}\text{CS}$ state have the strongest influence. For the evaluation all conceivable singlet and triplet CT states, all locally excited (TAA, NDI) triplet states and the CS states have been taken into account (see Figures 55 and 57). For all the electronic ET couplings, $V_{1,3\text{CS}-N_n} = 80 \text{ cm}^{-1}$ (the average value for all couplings, see above) were used, for the determination of ΔG the adiabatic state energies (see Figure 57) corrected by the reorganization energy $\lambda = 0.34 \text{ eV}$ for all states were utilized. This yields $2J = +3.1 \text{ cm}^{-1}$ for both **A** and **B**, which means that the triplet CS state is lower in energy than the singlet state. Clearly, the term which couples the triplet CS state to the locally excited NDI triplet state dominates $2J$ because it is next to the CS state in energy. The $2J$ coupling appears to be relatively large, because, as it has been mentioned above, the energy spacing to the locally excited NDI triplet state is small and because the electronic ET coupling is unusually large for systems with broken conjugation.

$$2J = E_S - E_T = \left[\sum_n \frac{V_{3CS-N_n}^2}{\Delta G_{3CS-N_n}} \right]_T - \left[\sum_n \frac{V_{1CS-N_n}^2}{\Delta G_{1CS-N_n}} \right]_S = 3.1 \text{ cm}^{-1} \quad (8)$$

Following a strategy developed by Paddon-Row^[144], time dependent density functional theory calculations on the gas phase optimized structure of the singlet CS state of **B** at CAM-B3LYP/6-31G* level of theory using Gaussian09^[96] also yield a sizable singlet-triplet splitting of the CS state (see Figure 57) of 0.54 cm^{-1} . While this value is an order of magnitude smaller than the one obtained by perturbation theory (see above), it is nevertheless two orders of magnitude larger than the usually observed splittings^[122, 136, 151] but similar to that in a small NDI containing dyad for which Wasielewski et al. recently suggested spin-orbit ISC to be the dominant mechanism.^[153] Nevertheless, the large $2J$ values determined by both approaches appear to be reasonable and the S-T interconversion falls into the spin-lattice relaxation time domain. While this reasoning appears to be plausible, it has to be stated that it is no proof for the spin-lattice relaxation mechanism and further experiments, such as time resolved EPR or magnetic field dependent pump-probe measurements, are necessary to determine the exact values for $2J$ splitting.

Thus, it is concluded that the overall dynamics of **A–C** are governed by a delicate balance of electronic coupling V and exchange interaction $2J$, which makes ET processes fast, but singlet-triplet interconversion slow.

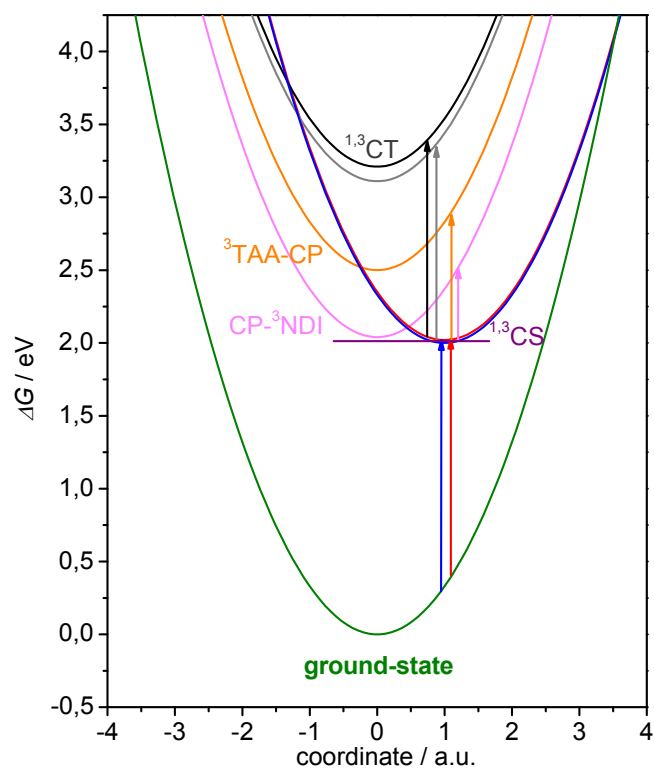


Figure 57. Singlet and triplet CS, CT and local states that are taken into account for second order perturbation interaction to estimate the $2J$ coupling by eq. 3. The red and blue arrows correspond to the TD-DFT calculations of excitation energies with GAUSSIAN09^[96] at CAM-B3LYP/6-31G* level of theory whose difference yields the $2J$.

5 SUMMARY AND CONCLUSION

Regarding mixed valence compounds, the present study focuses on bistriarylamine radical cation \mathbf{F}^+ , which contains the [3.3]paracyclophane bridge unit. The results were compared to the, except for the bridge units, identical literature known compounds \mathbf{G}^+ and \mathbf{N}^+ with [2.2]paracyclophane and *p*-xylene bridges respectively. This led to the conclusion that slightly different bridge units can induce substantial changes to the internal reorganization energy. This is especially noteworthy since it is usually believed that structural adaption limited to the redox centers taking part in the charge transfer dominates the internal reorganization energy.^[38] Furthermore, the application of the two-state Mulliken-Hush approach^[98, 99] shows that compounds \mathbf{F}^+ and \mathbf{G}^+ have near identical couplings and similar thermal barriers. Confirmation of the latter finding as well as near identical thermal electron transfer rates for both compounds were provided via a cooperation project by *Grampp et al.*^[25] in which these values were directly extracted from temperature dependent electron paramagnetic resonance measurements. These results are quite unexpected since the “through-space” distances of the stacked π -systems in the paracyclophane bridges differ significantly. They are well within the sum of the *van der Waals* radii in \mathbf{G}^+ and barely within them in compound \mathbf{F}^+ . In addition, these findings weaken the common assumption of the ethylene bridges in \mathbf{G}^+ substantially adding to the electronic coupling,^[1, 3, 4, 7] since then, in \mathbf{F}^+ , due to its propylene linkers, the coupling should be substantially reduced. Finally, relying on the fact that the electronic couplings are only three times higher and the thermal electron transfer rates are only one order of magnitude higher for \mathbf{N}^+ than for compounds \mathbf{F}^+ and \mathbf{G}^+ shows that intermolecular electron transfer in solid state materials can remain efficient, if the interacting π -systems stay within the sum of *van der Waals* radii of their carbons.

Concerning the donor-acceptor dyads, the current investigation centers on triarylamine-cyclophane-naphthalene diimide (TAA-CP-NDI) compounds which display almost complete photoinduced charge separation. Furthermore, their singlet charge separated states show lifetimes of hundreds of nanoseconds, which is rarely found in such simple dyads. In the present case they can be attributed to the particular amount of electronic coupling V (on the order of 100 cm^{-1}), which is brought about by incorporation of the smallest model systems for π -stacks, the CPs, together with the nodes on the NDI lowest unoccupied molecular orbital,^[40, 58] which electronically decouples the central NDI from its nitrogen substituents. In agreement with studies of [2.2]- and [3.3]paracyclophane bridged mixed valence compounds (see above), the cyclophane bridged dyads show very similar electronic coupling when

dealing with ground state processes like charge recombination. However, when investigating excited state processes, like charge separation in the TAA-CP-NDI dyads, one has to bear in mind that the CP orbitals are involved in the formation of intermediate states that likely possess charge transfer character. In this case, the [2.2]paracyclophane bridge obviously induces a stronger coupling than the [3.3]paracyclophane. Another interesting property of the dyads studied here is the substantial population of the triplet charge separated (CS) state of ca. one third regarding both CS states, which is brought about by singlet-triplet interconversion from the singlet CS state. Thus, the triplet CS state with a lifetime of several microseconds acts as a kind of buffer for the CS state before recombining to the ground state and, thus, leads to distinctly prolonged overall lifetimes of the charge separated states. Thus it can be concluded that the intersystem crossing and charge recombination (CR) processes of the CS states are governed by a delicate balance of a large electronic coupling V and a large exchange interaction $2J$ (both with regard to systems containing a through-space pathway). The latter appears to be induced by second order interaction with a local triplet state lying close in energy to the CS state. This balance results in slow CR- and singlet-triplet- interconversion rates, which differ only by one order of magnitude. Compared to the many NDI containing dyads studied so far, these features of the dyads studied here are, to the best of our knowledge, unique. Especially the combination of high quantum yield of charge separation, long lifetimes and high energy of the charge separated state make the investigated systems interesting for practical applications. Furthermore, the presented unraveling of the underlying mechanisms is of substantial value for the future design of dyads for practical applications regarding the implementation and adjustment of these favorable properties.

6 EXPERIMENTAL SECTION

6.1 PREPARATIVE AND ANALYTICAL METHODS

SYNTHESES

All reactions were carried out in standard glassware. All commercial compounds, including solvents, were purchased from Merck, Acros, Avocado, Chempur, Sigma-Adrich or ABCR and used without further purification. The reactions specified as being performed under nitrogen atmosphere were performed in air-free conditions (nitrogen, dried with Sicapent® from Merck, oxygen was removed by copper oxide catalyst PuriStar® R3-11 from BASF) using solvents freshly dried by standard procedures.^[154]

CHROMATOGRAPHY

Flash column chromatography was performed on standard silica gel, 40–63 μm (Merck or MACHEREY-NAGEL). If specified, products were purified by preparative size exclusion gel permeation chromatography with two sequential columns 10 μm , 50 Å and 500 Å (PSS) in a recycling set-up.

NMR SPECTRA

The ^1H and ^{13}C NMR spectra were recorded at the given temperature either on an AVANCE 400 FT-NMR spectrometer (^1H : 400 Mhz, ^{13}C : 101 MHz) or a Bruker AVANCE DMX 600 FT-NMR Spectrometer (^1H : 600 Mhz, ^{13}C : 151 MHz). The residual signal of the respective solvent was used as the internal reference and the chemical shifts are given in ppm on a δ -scale. The coupling constants (J) are expressed in Hertz [Hz]. The apparent spin multiplicities are denoted as: s = singlet, d = doublet, dd = doublet of doublets, t = triplet, m = multiplet, AA' = $[\text{AB}]_2$ -spin-system ($>$ ppm), BB' = $[\text{AB}]_2$ -spin-system ($<$ ppm). NMR spectroscopic data are quoted as follows: chemical shift (multiplicity, coupling constants, number of protons, assignment).

MASS SPECTROMETRY

The exact masses (ESI) were recorded on a Finnigan MAT 90, a Bruker Daltonik microTOF focus and a Bruker Daltonik autoflex II at the Institute of Organic Chemistry, University of Würzburg.

CRYSTALLOGRAPHY

The crystal data were collected on a Bruker X8APEX diffractometer with a CCD area detector and multi-layer mirror monochromated $\text{MoK}\alpha$ radiation by *Braunschweig et al.* at the Institute of Inorganic Chemistry, University of Würzburg. The structures were solved using direct methods, refined with the Shelx software package^[155] and expanded using Fourier techniques. All non-hydrogen atoms were refined anisotropically. Hydrogen atoms were assigned to idealized positions and were included in structure factors calculations.

CYCLIC VOLTAMMETRY

All measurements were performed using a BAS CV-50 W electrochemical workstation or a GAMRY INSTRUMENTS potentiostat/galvanostat/ZRA model REFERENCE 600 workstation. All electrochemical experiments were performed using a platinum or, if specified, a carbon disk working electrode, an Ag/AgCl reference electrode and a helical platinum counter electrode. In all cases ferrocene/ferrocenium redox couple was used as an internal reference. All experiments were performed in a sealed glass vessel under argon atmosphere (dried with Sicapent® from Merck and traces of oxygen removed with a copperoxide catalyst PuriStar® R3-11 from BASF). Acetonitrile or dichloromethane with tetrabutylammonium hexafluorophosphate as the supporting electrolyte were used. All solvents and supporting electrolytes used were purified, dried and/or degassed according to established procedures.^[154]

STEADY STATE ABSORPTION SPECTROSCOPY

These measurements were performed in 1 cm quartz cuvettes using a JASCO V-570 UV/Vis/NIR spectrometer. The substances were dissolved in Uvasol solvents from Merck and the pure solvent was used as a reference. Absorption spectra were recorded in toluene within a concentration range from 1×10^{-5} to 3×10^{-5} M.

STEADY STATE SPECTROELECTROCHEMISTRY

These measurements were performed in a cylindrical quartz cell with an optically flat cell bottom in which the three electrode set-up consisted of a platinum disc working electrode (6 mm diameter), a gold-coated metal plate as counter electrode and an Ag/AgCl pseudo-reference electrode. Measurements were performed under argon atmosphere with the same solvent and supporting electrolyte as in the cyclic voltammetry. The potentials were applied using an EG&G Princeton Applied Research Model 283 Potentiostat with potential steps of either 25 mV, 100 mV or 250 mV. UV/Vis/NIR spectra were recorded using a JASCO V-570 spectrometer in reflection at the polished working electrode which was adjusted to ca. 100 μm above the cell bottom by using a micrometer screw.

STEADY STATE FLUORESCENCE SPECTROSCOPY

These measurements were performed using a Photon Technology International (PTI) QM fluorescence spectrometer. Cuvettes (1 cm) were used and spectra recorded in Uvasol solvents from Merck after purging the samples for 30 min with argon. The lifetimes were measured using a PTI TM fluorescence lifetime spectrometer with a 340 nm laser diode for excitation. Colloidal silica in de-ionized water was used as a scatterer to determine the instrumental response function. Lifetimes were determined by fitting the decay curves (deconvolution with the instrument response function) with a single-exponential decay function.

FEMTOSECOND-TRANSIENT ABSORPTION SPECTROSCOPY

The pump-probe experiments were performed in a 2 mm quartz cuvette equipped with a micro-stirrer. The target compounds were dissolved in Uvasol solvents from Merck and purged with argon for 30 min. The laser system consists of an ultrafast Ti:Sapphire amplifier (Newport-Spectra-Physics, Solstice) with a central wavenumber of $12\,500\text{ cm}^{-1}$ (800 nm), a pulse length of 100 fs and a repetition rate of 1 kHz. One part of the output beam was used to seed an optical parametric amplifier (Newport-Spectra-Physics, TOPAS) as the source for the pump pulse with an attenuated energy of 150–210 nJ, a wavenumber of $28\,200\text{ cm}^{-1}$ (355 nm) and a pulse length of 140 fs. A small fraction of the Ti:sapphire output was focused into a moving calcium fluoride plate to produce a white light continuum between $12\,500\text{ cm}^{-1}$ (800 nm) and $24\,000\text{ cm}^{-1}$ (417 nm), which acted as the probe pulse. The depolarized excitation pulse was collimated to a spot, which is at least 2 times larger than the diameter of the spatially overlapping linearly polarized probe pulse. After passing the sample, the probe pulses were detected via a transient absorption spectrometer with a CMOS sensor (Ultrafast Systems, Helios). Part of the probe light pulse was used to correct for intensity fluctuations of the white light continuum. A mechanical chopper, working at 500 Hz, blocks every second pump pulse in order to measure I and I_0 . By comparing the transmitted spectral intensity of consecutive pulses $[I(\lambda, \tau), I_0(\lambda)]$, the photoinduced change in the optical density can be recorded as $\Delta\text{OD} = -\log[(I(\lambda, \tau)/I_0(\lambda))]$. The relative temporal delay between pump and probe pulses was varied over a maximum range of 8 ns with a motorized, computer-controlled linear stage. The delay interval between two consecutive data points was 13.3 fs for small delay times and was increased up to 200 ps for very large delay times. The stability of the samples was verified by recording the absorption spectra before and after the time-resolved measurements. The transient spectra recorded with the above outlined set-up were free of interfering absorption signals in the ps time domain as has been detected for a number of aromatic solvents by Masuhara and Mataga.^[156] Furthermore, exciplex formation of NDI with toluene as was found by Barros et al was not observed.^[157]

The time resolved spectra were analyzed by global fitting with GLOTARAN^[101] employing a sequential model (i. e. unbranched unidirectional model) modeling the IRF, the white light dispersion (chirp), and the coherent artifact at time zero to yield the evolution associated spectra (EAS) and their corresponding time constants. The number components and quality of the fits was estimated by singular value decomposition.

NANOSECOND-TRANSIENT ABSORPTION SPECTROSCOPY

The pump-probe experiments were performed in a 1 cm quartz cuvette. The target compounds were dissolved in Uvasol solvents from Merck and purged with argon for 30 min. The laser system consists of a Nd:YAG laser (Continuum, Minilite II) with a repetition rate of 10 Hz. As source for the pump pulse, either the third harmonics of the 1064 nm fundamental ($28\,200\text{ cm}^{-1}$, 355 nm) was used directly or shifted by a Raman shifter (hydrogen, 50 cm path length, 50 bar) to $24\,000\text{ cm}^{-1}$ (416 nm) and selected by a Pellin-Broca prism. The laser pulse energy was varied between 0.20 to 5.2 mJ with a pulse length of 5 ns. As the probe light source (xenon arc lamp), sample chamber and detector (photomultiplier tube) a modular system from Edinburgh Instruments (LP 920-K Laser Flash spectrometer) was used. In general, the recorded transient signal consists of transient absorption, fluorescence and ground state bleaching. The detected transient signal intensity ($I(\lambda, \tau)$) with pump pulse and probe light is corrected by the fluorescence intensity ($I_F(\lambda, \tau)$) measured without the probe light. From the corrected transient signal intensity in combination with the intensity ($I_0(\lambda)$) without the pump pulse, the optical density can be recorded as $\Delta OD = -\log[(I(\lambda, \tau) - I_F(\lambda, \tau))/I_0(\lambda)]$. The instrument response function of the set-up was determined with an empty cuvette. The stability of the samples was verified by recording the absorption spectra before and after the time-resolved measurements. As in the fs-experiments, no transient absorption of toluene could be observed as has been detected for a number of aromatic solvents by Masuhara and Mataga.^[156, 158]

For the lifetime fits, a parallel model (independent exponential decays) was assumed. Long lifetimes ($> 100\text{ ns}$) were determined by a tail fitting routine of the decay curves while shorter ones ($< 100\text{ ns}$) were determined by deconvolution fitting routine taking into account the IRF of the set-up using the corresponding spectrometer software. Residuals and autocorrelation function (without any significant structure) served as the main criteria in the evaluation of the fit. Rate constants for ISC and CR were determined by numerical fitting of the decay curves with TENUA^[106] by applying the appropriate kinetic model (target analysis/time-invariant compartmental model) on the baseline corrected normalized decay curves. The following script (used for **A**) was adapted for each compound. SCS is the concentration of the singlet charge separated state, TCS the concentration of the triplet charge separated state, A1 the overall starting concentration of the CS states and S0 the concentration of the ground state. Starting values for the rate constants were estimated from the reciprocal values of the lifetimes of the long and short component of the biexponential fits ($k(+1) = 1/(\tau_{\text{long}}) \times 3$ and $k(+2) = 1/\tau_{\text{short}}$). A1 and the ratio of the starting concentrations of SCS and TCS were fitted manually.

Script:

SCS<->TCS; SCS<->S0;

k(-1)=A2*k(+1);

k(+1) : 4.3E5;

k(+2) : 2.9E6;

A1 : 0.97;

S0 : 0.01;

A2 : 1/3;

TCS : 0.25*(A1);

SCS : 0.75*(A1);

*output

sum(SCS+TCS); sum2=TCS;

*script ("sum"), ("normalizeddecaycurve");

go varying k(+1), k(+2)

Time Constants:

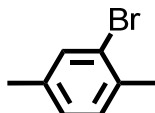
startTime : 0; endTime: 3.65E-5; timeStep: 1.0E-7; time: 0; epsilon: 1.0E-4

The quantum yield for the charge separation ϕ_{CS} of the dyad was determined by relative actinometry, i.e., comparison of the transient absorption signal ΔOD_{CS} of the dyad at $20\,900\text{ cm}^{-1}$ (478 nm) in toluene with the signal ΔOD_{ref} of benzophenone at $18\,900\text{ cm}^{-1}$ (530 nm) in benzene both excited by a laser pulse at $28\,200\text{ cm}^{-1}$ with pulse energies low enough to ensure direct proportionality to the transient absorption signals. The following equation was used: $\phi_{CS} = \phi_{ref} \times ((\Delta OD_{CS} \times \epsilon_{ref}) / (\Delta OD_{ref} \times \epsilon_{CS}))^{[103]}$ where $\phi_{ref} = 1$ and $\epsilon_{ref} = 7220\text{ M}^{-1} \times \text{cm}^{-1}$ ^[159]– $7630\text{ M}^{-1} \times \text{cm}^{-1}$ ^[160] are the quantum yield and extinction coefficient of the triplet state of benzophenone and ϵ_{CS} is the extinction coefficient of the charge separated state of the dyad, which was extracted from spectroelectrochemistry measurements.^[104, 105]

6.2 SYNTHESIS

6.2.1 SYNTHESIS OF PARACYCLOPHANE PRECURSOR 2

2-Bromo-1,4-dimethylbenzene (1)



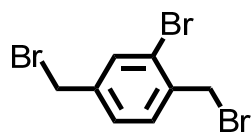
CAS: 553-94-6.

Bromine (416 ml, 8.17 mol) was added dropwise to a suspension of 1,4-dimethylbenzene (1.00 l, 8.17 mol) and *ferrum reductum* (7.99 g, 143 mmol) within 7 h at 10–15°C. The mixture was stirred for 16 h at rt. The crude product was purified by fractional distillation under reduced pressure using a Vigreux column (15 cm).

Yield: 942 g (5.09 mol, 62.3 %) colorless liquid (0.34 mbar, 86°C) C₈H₉Br [185.1 g/mol].

¹H-NMR (400 MHz, CDCl₃, 300 K): δ / ppm = 7.37–7.34 (m, 1H, CH_{arom.}), 7.12–7.08 (m, 1H, CH_{arom.}), 7.02–6.98 (m, 1H, CH_{arom.}), 2.35 (s, 3H, CH₃), 2.29 (s, 3H, CH₃)

2-Bromo-1,4-bis(bromomethyl)benzene (2)



CAS: 19900-52-8

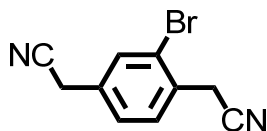
2-Bromo-1,4-dimethylbenzene (**1**) (206 g, 1.11 mol) was added to absolute carbon tetrachloride (1 l) and heated to reflux. *N*-Bromosuccinimide (396 g, 1.29 mol) and azo-bis-isobutyronitrile (1.37 g, 8.34 mmol) were added in small portions during 50 min at reflux. The reaction mixture was stirred for 30 min under reflux. The hot mixture was filtered and the solvent was removed under reduced pressure. The residue was purified by recrystallization (chloroform) and dried in HV.

Yield: 114 g (334 mmol, 30%) colorless solid C₈H₇Br₃ [342.9 g/mol].

¹H-NMR (400 MHz, CDCl₃, 300 K): δ / ppm = 7.63–7.60 (m, 1H, CH_{arom.}), 7.45–7.41 (m, 1H, CH_{arom.}), 7.34–7.30 (m, 1H, CH_{arom.}), 4.58 (s, 2H, CH₂), 4.41 (s, 2H, CH₂)

6.2.2 SYNTHESIS OF PARACYCLOPHANE PRECURSOR 7

2,2'-(2-Bromo-1,4-phenylene)diacetonitrile (3)



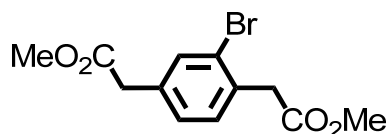
CAS:56403-39-5

2-Bromo-1,4-bis(bromomethyl)benzene (**2**) (80.0 g, 233 mmol) and potassium cyanide (39.6 g, 583 mmol) were suspended in a mixture of ethanol (800 ml) and water (400 ml) and stirred at 70°C for 3.5 h. More water was added and the reaction mixture was extracted with dichloromethane. The combined organic phases were washed with water and dried over magnesium sulfate. The solvent was removed *in vacuo* and the yellowish solid (46.1 g) dried in HV. An analytical sample was purified by flash chromatography (dichloromethane) and dried in HV to yield a colorless solid.

¹H-NMR (400 MHz, CDCl₃, 300 K): δ / ppm = 7.64–7.60 (m, 1H, CH_{arom.}), 7.59–7.53 (m, 1H, CH_{arom.}), 7.38–7.32 (m, 1H, CH_{arom.}), 3.84 (s, 2H, CH₂), 3.76 (s, 2H, CH₂).

¹³C-NMR (101 MHz, CDCl₃, 300 K) δ / ppm = 132.6 (tert.), 132.2 (quart.), 130.4 (tert.), 130.3 (quart.), 127.9 (tert.), 124.4 (quart.), 116.9 (quart.), 116.6 (quart.), 24.7 (2C, sec.), 23.0 (2C, sec.)

Dimethyl 2,2'-(2-bromo-1,4-phenylene)diacetate (4)



CAS: /

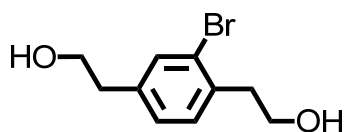
Crude 2,2'-(2-Bromo-1,4-phenylene)diacetoneitrile (**3**) (46.1 g, 156 mmol) was dissolved in dry methanol (500 ml). Sulfuric acid (107 ml, 1.96 mol, 98% in water) was added dropwise within 30 min. Then the solution was stirred for 2 d under reflux conditions. The mixture was hydrolyzed with water and extracted with dichloromethane. The combined organic phases were dried over magnesium sulfate and the solvent was removed *in vacuo*. The residue was purified by fractional distillation (124°C, 0.01 mbar) to yield a yellowish solid (30.1 g). An analytical sample was purified by recrystallization (methanol) to yield a colorless solid.

$^1\text{H-NMR}$ (400 MHz, acetone, 300 K): δ / ppm = 7.58–7.55 (m, 1H, $\text{CH}_{\text{arom.}}$), 7.38–7.34 (m, 1H, $\text{CH}_{\text{arom.}}$), 7.31–7.26 (m, 1H, $\text{CH}_{\text{arom.}}$), 3.81 (s, 2H, CH_2), 3.68 (s, 2H, CH_2), 3.661 (s, 3H, CH_3), 3.658 (s, 3H, CH_3).

$^{13}\text{C-NMR}$ (101 MHz, CDCl_3 , 300 K) δ / ppm = 171.4 (quart.), 171.0 (quart.), 135.0 (quart.), 133.7 (tert.), 133.2 (quart.), 131.6 (tert.) 128.7 (tert.), 125.1 (quart.), 52.33 (prim), 52.32 (prim.), 41.2 (2C, sec.), 40.4 (2C, sec.).

High Resolution Mass (EI): calc.: 221.08084 $[\text{M}-\text{Br}]^+$
 found: 221.08077 $[\text{M}-\text{Br}]^+$
 Δ : 0,29 ppm

2,2'-(2-bromo-1,4-phenylene)diethanol (5)



CAS: /

Lithium aluminum hydride (4.93 g, 130 mmol) was suspended in tetrahydrofuran (400 ml). The crude dimethyl-2,2'-(2-bromo-1,4-phenylene)diacetate (**4**) (30.1 g, 90.5 mmol) dissolved in tetrahydrofuran (80 ml) was added dropwise within 1 h to the suspension at rt. The reaction mixture was heated to 50°C and further lithium aluminum hydride (986 mg, 26.0 mmol) was added. The suspension was stirred for 1h at rt. The reaction mixture was hydrolyzed by slowly adding water. The solution was concentrated to 100 ml by removing the solvent *in vacuo*. Sulfuric acid (400 ml, 5% in water) was slowly added and the product extracted with dichloromethane. The combined organic phases were dried over magnesium sulfate and the solvent was removed *in vacuo*. The residue was dried in HV to yield a colorless oil (17.0 g). An analytical sample was purified by flash chromatography (DICHLORMETHANE/EtOAc 1/1) to yield a colorless solid.

¹H-NMR (400 MHz, CDCl₃, 300 K): δ / ppm = 7.47–7.42 (m, 1H, CH_{arom.}), 7.23–7.20 (m, 1H, CH_{arom.}), 7.15–7.10 (m, 1H, CH_{arom.}), 3.89–3.82 (—, 4H, CH₂), 3.00 (t, ³J_H = 6.68 Hz, 2H, CH₂), 2.82 (t, 2H, CH₂).

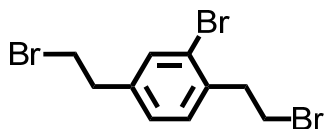
¹³C-NMR (101 MHz, CDCl₃, 300 K) δ / ppm = 139.2 (quart.), 136.0 (quart.), 133.5 (tert.), 131.4(tert.), 128.4 (tert.), 124.9 (quart.), 63.5 (sec.), 62.3 (sec.), 39.1 (sec.), 38.4 (sec.).

High Resolution Mass (EI): calc.: 244.00934 M⁺

found: 244.00939 M⁺

Δ : 0.20 ppm

2-Bromo-1,4-bis(2-bromoethyl)benzene (6)



CAS: /

In three batches the crude 2,2'-(2-bromo-1,4-phenylene)diethanol (**5**) (16.7 g, 59.0 mmol) was added to hydrogen bromide (47.0 ml, 273 mmol, 33% in acetic acid) and stirred for 16 h in a high pressure glass tube at 110°C. The reaction mixture was hydrolyzed with water and extracted with dichloromethane. The combined organic phases were washed with water and dried over anhydrous magnesium sulfate. The solvent was removed *in vacuo*. The residue was purified by flash chromatography on silica gel (dichloromethane/petroleum ether 5:95 → dichloromethane/petroleum ether 8:92).

Yield: 15.8 g (42.5 mmol, 18 % over the last 4 steps) colorless solid C₁₀H₁₁Br₃ [370.9 g/mol].

¹H-NMR (400 MHz, CDCl₃, 300 K): δ / ppm = 7.44–7.41 (m, 1H, CH_{arom.}), 7.24–7.20 (m, 1H, CH_{arom.}), 7.15–7.10 (m, 1H, CH_{arom.}), 3.61–3.52 (—, 4H, CH₂), 3.27 (t, ³J_H = 7.52 Hz, 2H, CH₂), 3.12 (t, ³J_H = 7.45 Hz, 2H, CH₂).

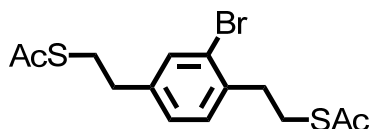
¹³C-NMR (101 MHz, CDCl₃, 300 K) δ / ppm = 139.9 (quart.), 136.8 (quart.), 133.3 (tert.), 131.3 (tert.), 128.0 (tert.), 124.5 (quart.), 39.3 (sec.), 38.5 (sec.), 32.3 (sec.), 31.1 (sec.)

High Resolution Mass (EI): calc.: 367.84054 M⁺

found: 367.84028 M⁺

Δ : 0.71 ppm

S,S'-(2-Bromo-1,4-phenylene)bis(ethane-2,1-diyl) diethanethioate (7)



CAS: /

Under nitrogen atmosphere potassium thioacetate (4.90 g, 42.9 mmol) was added to a suspension of 2-bromo-1,4-bis(2-bromoethyl)benzene (5.71 g, 14.3 mmol) (**2**) in tetrahydrofuran (250 ml). The reaction mixture was stirred for 16 h at 40°C. The solvent was removed *in vacuo*. The residue was extracted with dichloromethane (200 ml) at 40°C and filtered. The solvent was removed from the filtrate *in vacuo*. The resulting product was dried in HV.

Yield: 5.47 g (14.1 mmol, 98 %) white solid C₁₄H₁₇BrO₂S₂ [361.3 g/mol].

¹H-NMR (400 MHz, CDCl₃, 300 K): δ / ppm = 7.44–7.39 (m, 1H, CH_{arom.}), 7.21–7.17 (m, 1H, CH_{arom.}), 7.12–7.08 (m, 1H, CH_{arom.}), 3.15–3.05 (—, 4H, CH₂), 3.00–2.94 (m, 2H, CH₂), 2.84–2.78 (m, 2H, CH₂), 2.34 (s, 3H, CH₃), 2.33 (s, 3H, CH₃).

¹³C-NMR (101 MHz, CDCl₃, 300 K) δ / ppm = 195.7 (quart.), 195.6 (quart.), 140.5 (quart.), 137.5 (quart.), 133.0 (tert.), 130.9 (tert.), 127.9 (tert.), 124.5 (quart.), 35.7 (sec.), 35.1 (sec.), 30.81 (prim.), 30.79 (prim.), 30.3 (sec.), 29.0 (sec.)

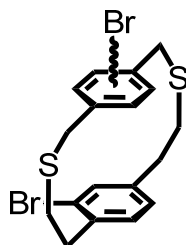
High Resolution Mass (ESI): calc.: 382.97455 [M+Na]⁺

found: 382.97455 [M+Na]⁺

Δ : 0.00 ppm

6.2.3 SYNTHESIS OF DIBROMO-PARACYCLOPHANE 10

Dithia-cyclophane (8)



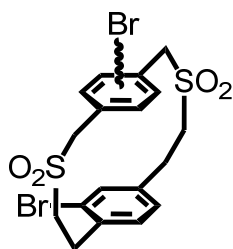
CAS: /

Under nitrogen atmosphere potassium hydroxide (12.2 g, 187 mmol) was dissolved in methanol (1 l) and tetrahydrofuran (1 l). A solution of 2-bromo-1,4-bis(bromomethyl)benzene (**2**) (12.8 g, 37.4 mmol) and *S,S'*-[(2-bromo-1,4-phenylene)bis(ethane-2,1-diyl)] diethanethioate (**7**) (13.5 g, 37.4 mmol) in tetrahydrofuran (60 ml) was added dropwise via a dilution elbow within 19 h under reflux conditions. Then, the solution was stirred for 3h under reflux conditions.

The solvents were removed *in vacuo* and the residue was purified by flash chromatography on silica gel (petroleum ether/dichloromethane 3:1). The dithia-cyclophane (**8**) containing fraction (9.60 g, colorless solid) was dried in HV.

¹H-NMR (400 Mhz, CD₂Cl₂, 300 K): δ / ppm = 7.27–6.70 (—, 6H, CH_{arom}), 3.80–2.20 (—, 12 H, CH₂)

Bis-sulfone-cyclophane (9)

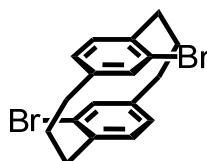


CAS: /

Crude dithia-cyclophane (**8**) (9.44 g) was suspended in acetic acid (150 ml). Then hydrogen peroxide solution in water (220 ml, 2.27 mol, 35%) was added to the suspension within 15 min at 80°C. The reaction mixture was stirred for 16 h at 100°C. The reaction mixture was cooled to rt. The solvent was reduced *in vacuo* to 50 ml. The suspension was filtered. The residue containing the bis-sulfone-cyclophane (**9**) was washed with diethyl ether and then dried in HV (10.5 g, white solid).

MS (EI, 70 eV): m/z (%) = M^+ : 526 (0.2 %), 525 (0.5 %), 524 (2.2 %), 523 (0.9 %), 522 (3.9 %), 521 (0.4 %), 520 (1.9 %)

5,18-dibromo-[3.3]paracyclophane (10)



CAS: /

The crude bis-sulfone-cyclophane (**9**) (10.2 g, 19.5 mmol) was subjected in portions of 230 mg–1300 mg to vacuum flash pyrolysis (550°C, 0.015 mbar).

The resulting condensate was dissolved in dichloromethane and filtered. The solvent was removed *in vacuo* from the filtrate. The residue was purified by flash chromatography (petroleum ether). The product was isolated from the other regioisomers by recrystallization (chloroform) and dried in HV.

Yield: 661 mg (1.68 μmol , (ca. 9%) 5% over the last 3 steps) colorless solid $\text{C}_{18}\text{H}_{18}\text{Br}_2$ [394.1 g/mol].

$^1\text{H-NMR}$ (400 MHz, CDCl_3 , 300K): δ / ppm = 6.98–6.96 (m, 2H, $\text{CH}_{\text{arom.}}$), 6.93–6.87 (m, 2H, $\text{CH}_{\text{arom.}}$), 6.68–6.64 (m, 2H, $\text{CH}_{\text{arom.}}$), 3.15–3.06 (m, 2H, CH_2), 2.84–2.73 (m, 2H, CH_2), 2.69–2.56 (—, 4H, CH_2), 2.40–2.27 (m, 2H, CH_2), 1.98–1.86 (m, 2H, CH_2).

$^{13}\text{C-NMR}$ (101 MHz, CDCl_3 , 300 K): δ / ppm = 141.3 (quart.), 136.9 (quart.), 133.3 (tert.), 132.8 (tert.), 126.9 (tert.), 124.2 (quart.), 35.6 (sec.), 34.8 (sec.), 26.9 (sec.)

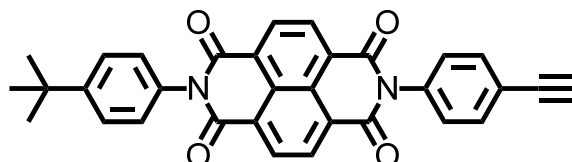
High Resolution Mass (ESI): calc.: 391.97698 M^+

found: 391.97660 M^+

Δ : 0.97 ppm

6.2.4 SYNTHESIS OF NAPHTHALENE BISIMIDE ACCEPTOR 11

NAPHTHALENE BISIMIDE ACCEPTOR 11



CAS: /

Dry pyridine (20 ml) was added to a mixture of 1,4,5,8-naphthalenetetracarboxylic dianhydride (1.61 g, 6.00 mmol) and 4-*tert*-butylaniline (810 μ l, 5.10 mmol). The reaction mixture was stirred in a high pressure glass tube for one hour in a microwave oven at 165°C. The mixture was allowed to cool down to 110°C and 4-ethynylaniline (703 mg, 6.00 mmol) was added. The reaction mixture was stirred for one hour in the microwave oven at 165°C. Subsequently, the mixture was cooled to 110°C and filtered. The solvent of the filtrate was removed *in vacuo*. Acetone (300 ml) was added to the residue and stirred at reflux, allowed to cool to rt and filtered again. The residue was washed with acetone (100 ml). The residue was purified by flash chromatography on silica gel (dichloromethane). The product was dried in HV.

Yield: 700 mg (1.40 mmol, 28%) yellow solid C₃₂H₂₂N₂O₄ [498.5 g/mol].

¹H-NMR (600 MHz, CD₂Cl₂, 298.8 K): δ / ppm = 8.83–8.81 (—, 4H, CH_{naphth.}), 7.71 (AA', 2H, CH_{arom.}), 7.62 (AA', 2H, CH_{arom.}), 7.34(BB', 2H, CH_{arom.}), 7.27 (BB', 2H, CH_{arom.}), 3.26 (s, 1H, CH_{alkin}), 1.43 (s, 9H, CH₃)

¹³C-NMR (151 MHz, CD₂Cl₂, 298.8 K) δ / ppm = 163.5 (2C, quart.), 163.2 (2C, quart.), 152.6 (1C, quart.), 135.7 (1C, quart.), 133.5 (2C, tert.), 132.6 (1C, quart.), 131.7 (2C, tert.), 131.6 (2C, tert.), 129.2 (2C, tert.), 128.4 (2C, tert.), 127.63 (2C, quart.), 127.570 (1C, quart.), 127.566 (1C, quart.), 127.2 (2C, quart.), 126.9 (2C, tert.), 123.4 (1C, quart.), 82.9 (1C, quart.), 78.8 (1C, tert.), 35.1 (1C, quart.), 31.5 (3C, prim.)

High Resolution Mass (ESI):

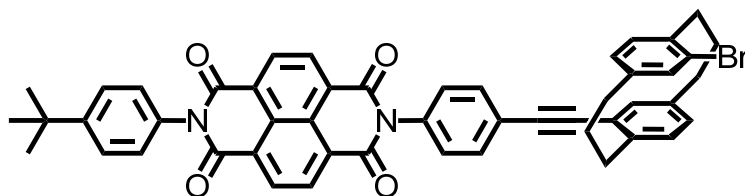
calc.: 499.16523 (M+H)⁺

found: 499.16516 (M+H)⁺

Δ : 0.14 ppm

6.2.5 SYNTHESIS OF NAPHTHALENE BISIMIDE CYCLOPHANES 13 AND E

NAPHTHALENE BISIMIDE CYCLOPHANE 13



CAS: /

Under nitrogen atmosphere absolute dioxane (3 ml) was added to a mixture of compound **11** (116 mg, 232 μmol), 5,18-dibromo-[3.3]paracyclophane **10** (60.9 mg, 155 μmol), bis(benzonitrile)palladium(II)chloride (8.89 mg, 23.2 μmol) and copper(I)iodide (2.94 mg, 15.5 μmol). A solution of tri-*tert*-butylphosphine in toluene (46.4 μl , 155 μmol , 1 M) and triethylamine (43.7 μl , 309 μmol) were added. The reaction mixture was stirred at 25°C for 7 d under exclusion of light. The mixture was hydrolyzed by adding water and extracted with dichloromethane. The combined organic phases were dried over magnesium sulfate. The solvents were removed *in vacuo*. The residue was purified by flash chromatography on silica gel (dichloromethane). The product was rinsed with pentane (3 \times 10 ml) in an ultrasonic bath, and the solvent was removed by centrifugation and decantation. The product was dried in HV.

Yield: 36.3 mg (45 μmol , 29%) yellow solid $\text{C}_{50}\text{H}_{39}\text{BrN}_2\text{O}_4$ [811.8 g/mol].

$^1\text{H-NMR}$ (600 MHz, CD_2Cl_2 , 298.8 K): δ / ppm = 8.86–8.81 (—, 4H, $\text{CH}_{\text{naphth.}}$), 7.81 (AA', 2H, $\text{CH}_{\text{arom.}}$), 7.63 (AA', 2H, $\text{CH}_{\text{arom.}}$), 7.40 (BB', 2H, $\text{CH}_{\text{arom.}}$), 7.28 (BB', 2H, $\text{CH}_{\text{arom.}}$), 7.04–6.98 (—, 3H, CH_{cyc}), 6.95–6.90 (m, 1H, CH_{cyc}), 6.76–6.71 (—, 2H, CH_{cyc}), 3.36–3.29 (m, 1H, $\text{CH}_{2\text{cyc}}$), 3.15–3.06 (m, 1H, $\text{CH}_{2\text{cyc}}$), 2.88–2.58 (—, 6H, $\text{CH}_{2\text{cyc}}$), 2.49–2.29 (—, 2H, $\text{CH}_{2\text{cyc}}$), 2.08–1.93 (—, 2H, $\text{CH}_{2\text{cyc}}$), 1.43 (s, 9H, CH_3)

$^{13}\text{C-NMR}$ (151 MHz, CD_2Cl_2 , 298.8 K) δ / ppm = 163.5 (2C, quart.), 163.3 (2C, quart.), 152.5 (1C, quart.), 141.7 (1C, quart.), 141.1 (1C, quart.), 139.4 (1C, quart.), 137.3 (1C, quart.), 134.9 (1C, quart.), 133.6 (1C, tert.), 133.5 (1C, tert.), 133.0 (1C, tert.), 132.70 (2C, tert.), 132.66 (1C, quart.), 131.7 (2C, tert.), 131.6 (2C, tert.), 131.5 (1C, tert.), 129.2 (2C, tert.), 128.7 (1C, tert.), 128.4 (2C, tert.), 128.1 (1C, tert.), 127.62 (2C, quart.), 127.59 (2C, quart.),

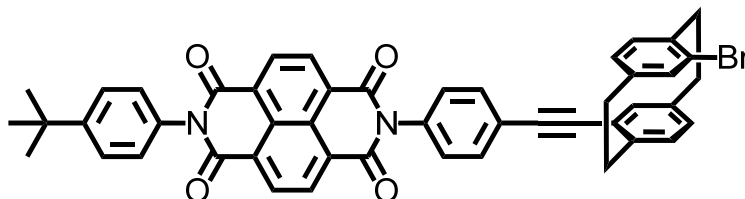
127.3 (2C, quart.), 126.9 (2C, tert.), 125.3 (1C, quart.), 124.3 (1C, quart.), 122.0 (1C, quart.),
91.8 (1C, quart.), 91.2 (1C, quart.), 35.8 (1C, sec), 35.3 (1C, sec.), 35.13 (1C, quart.), 35.11
(1C, sec.), 34.6 (1C, sec.), 31.5 (3C, prim), 28.2 (1C, sec.), 27.1 (1C, sec.)

High Resolution Mass (ESI): calc.: 811.21660 (M+H)⁺

 found: 811.21637 (M+H)⁺

Δ: 0.28 ppm

NAPHTHALENE BISIMIDE CYCLOPHANE E



CAS: /

Under nitrogen atmosphere absolute dioxane (7.5 ml) was added to a mixture of compound **11** (245 mg, 492 μmol), [4,16]-dibromo-paracyclophane **12** (150 mg, 410 μmol), bis(benzonitrile)palladium(II)chloride (23.6 mg, 61.5 μmol) and copper(I)iodide (7.80 mg, 41.0 μmol). A solution of tri-*tert*-butylphosphine in toluene (123 μl , 155 μmol , 1 M) and triethylamine (63.7 μl , 45.6 mg, 451 μmol) were added. The reaction mixture was stirred for 16 h at 25°C under exclusion of light. The mixture was hydrolyzed with water and extracted with dichloromethane. The combined organic phases were dried over magnesium sulfate and the solvents were removed *in vacuo*. The residue was purified by flash chromatography on silica gel (dichloromethane). The product fraction was rinsed with acetone (2 \times 10 ml) in an ultrasonic bath and the solvent was removed by centrifugation and decantation. The product was dried in HV.

Yield: 148 mg (189 μmol , 46%) yellow solid C₄₈H₃₅BrN₂O₄ [783.7 g/mol].

¹H-NMR (600 MHz, CD₂Cl₂, 298.8 K): δ / ppm = 8.87–8.81 (—, 4H, CH_{naphth.}), 7.82 (AA', 2H, CH_{arom.}), 7.63 (AA', 2H, CH_{arom.}), 7.41 (BB', 2H, CH_{arom.}), 7.28 (BB', 2H, CH_{arom.}), 7.22–7.18 (m, 1H, CH_{cyc.}), 7.08–7.04 (m, 1H, CH_{cyc.}), 6.66–6.63 (m, 1H, CH_{cyc.}), 6.58–6.56 (m, 1H, CH_{cyc.}), 6.54–5.51 (—, 2H, CH_{cyc.}), 3.75–3.68 (m, 1H, CH_{2cyc.}), 3.52–3.45 (m, 1H, CH_{2cyc.}), 3.28–3.16 (—, 2H, CH_{2cyc.}), 3.08–2.94 (—, 3H, CH_{2cyc.}), 2.94–2.87 (m, 1H, CH_{2cyc.}), 1.43 (s, 9H, CH₃).

¹³C-NMR (151 MHz, CD₂Cl₂, 298.8 K): δ / ppm = 163.5 (2C, quart.), 163.4 (2C, quart.), 152.6 (1C, quart.), 142.6 (1C, quart.), 142.0 (1C, quart.), 140.0 (1C, quart.), 139.3 (1C, quart.), 137.7 (1C, tert.), 137.6 (1C, tert.), 135.0 (1C, quart.), 134.8 (1C, tert.), 133.4 (1C, tert.), 132.8 (2C, tert.), 132.7 (1C, quart.), 131.7 (2C, tert.), 131.6 (2C, tert.), 129.9 (1C, tert.), 129.7 (1C, tert.), 129.3 (2C, tert.), 128.4 (2C, tert.), 127.64 (2C, quart.), 127.59 (2C, quart.), 127.3 (2C, quart.), 126.94 (1C, quart.), 126.86 (2C, tert.), 125.1 (1C, quart.), 124.8 (1C, quart.), 92.3

(1C, quart.), 91.2 (1C, quart.), 35.7 (1C, sec.), 35.1 (1C, quart.), 34.4 (1C, sec.), 34.0 (1C, sec.), 33.4 (1C, sec.), 31.5 (3C, prim.)

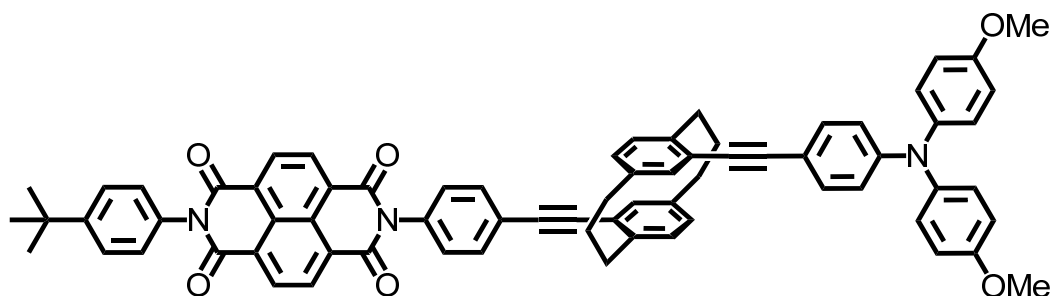
High Resolution Mass (ESI): calc.: 783.18530 (M+H)⁺

 found: 783.18503 (M+H)⁺

Δ: 0.34 ppm

6.2.6 SYNTHESIS OF DONOR-ACCEPTOR DYADS A AND B

DYAD A



CAS: /

Under nitrogen atmosphere dry dioxane (2.5 ml) was added to a mixture of compound **13** (36.3 mg, 44.7 μmol), 4-ethynyl-N,N-bis(4-methoxyphenyl)aniline **14** (58.9 mg, 179 μmol), bis(benzonitrile)palladium(II)chloride (5.15 mg, 13.4 μmol) and copper(I)iodide (1.70 mg, 8.94 μmol). A solution of tri-*tert*-butylphosphine in toluene (26.8 μl , 27.0 μmol , 1.00 M) and triethylamine (316 μl , 2.24 mmol) were added. The reaction mixture was stirred for 10 d at 60°C under exclusion of light. The solvent was evaporated *in vacuo*, the residue hydrolyzed with water and extracted with dichloromethane. The combined organic phases were dried over magnesium sulfate and the solvent was removed *in vacuo*. The residue was purified by flash column chromatography on silica gel (ethyl acetate/dichloromethane 100:1) followed by gel permeation chromatography (chloroform). The product fraction was rinsed with hot acetone (10 ml) in an ultrasonic bath, and the solvent was removed by centrifugation and decantation. This procedure was repeated with cold acetone (10 ml). The product was dried in HV.

Yield: 18.0 mg (17.0 μmol , 38%) yellowish solid $\text{C}_{72}\text{H}_{57}\text{N}_3\text{O}_6$ [1060.2 g/mol].

$^1\text{H-NMR}$ (400 MHz, CD_2Cl_2 , 300 K): δ / ppm = 8.88–8.82 (—, 4H, CH_{naphl}), 7.81 (AA', 2H, $\text{CH}_{\text{arom.}}$), 7.63 (AA', 2H, $\text{CH}_{\text{arom.}}$), 7.43–7.35 (—, 4H, $\text{CH}_{\text{arom.+TAA}}$), 7.28 (BB', 2H, $\text{CH}_{\text{arom.}}$), 7.15–7.07 (—, 4H, CH_{TAA}), 7.03–6.92 (—, 4H, $\text{CH}_{\text{cyc.}}$), 6.91–6.86 (—, 6H, CH_{TAA}), 6.79–6.72 (—, 2H, $\text{CH}_{\text{cyc.}}$), 3.81 (s, 6H, OCH_3), 3.39–3.24 (—, 2H, $\text{CH}_{2\text{cyc.}}$), 2.87–2.60 (—, 6H, $\text{CH}_{2\text{cyc.}}$), 2.51–2.38 (—, 2H, $\text{CH}_{2\text{cyc.}}$), 2.13–1.98 (—, 2H, $\text{CH}_{2\text{cyc.}}$), 1.44 (s, 9H, CH_3).

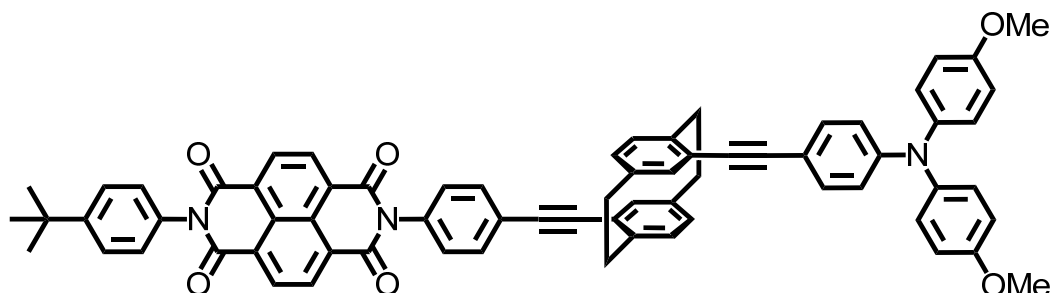
¹³C-NMR (151 MHz, CD₂Cl₂, 298.8 K): δ / ppm = 163.5 (2C, quart.), 163.4 (2C, quart.), 156.9 (2C, quart.), 152.6 (1C, quart.), 149.1 (1C, quart.), 141.2 (1C, quart.), 140.6 (1C, quart.), 140.5 (2C, quart.), 139.5 (1C, quart.), 139.3 (1C, quart.), 134.8 (1C, quart.), 133.6 (1C, tert.), 133.3 (1C, tert.), 132.69 (2C, tert.), 132.67 (1C, quart.), 132.5 (2C, tert.), 131.7 (2C, tert.), 131.6 (2C, tert.), 131.5 (2C, tert.), 129.5 (1C, tert.), 129.2 (2C, tert.), 128.8 (1C, tert.), 128.4 (2C, tert.), 127.62 (2C, quart.), 127.60 (2C, quart.), 127.5 (4C, tert.), 127.31 (2C, quart.), 126.9 (2C, tert.), 125.3 (1C, quart.), 122.8 (1C, quart.), 121.9 (1C, quart.), 119.5 (2C, tert.), 115.1 (4C, tert.), 114.8 (1C, quart.), 93.2 (1C, quart.), 91.7 (1C, quart.), 91.4 (1C, quart.), 88.5 (1C, quart.), 55.8 (2C, prim.), 35.5 (1C, sec), 35.4 (1C, sec.), 35.1 (1C, quart.), 34.7 (2C, sec.), 31.5 (3C, prim.), 28.1 (2C, sec.)

High Resolution Mass (ESI): calc.: 1059.42419 M⁺

 found: 1059.42446 M⁺

Δ : 0.25 ppm

DYAD B



CAS: /

Under nitrogen atmosphere absolute dioxane (2.5 ml) was added to a mixture of compound **E** (30.0 mg, 38.3 μmol), 4-ethynyl-N,N-bis(4-methoxyphenyl)aniline **14** (50.4 mg, 153 μmol), bis(benzonitrile)palladium(II)chloride (4.40 mg, 11.5 μmol) and copper(I) iodide (3.96 mg, 7.66 μmol). A solution of tri-*tert*-butylphosphine (23.0 μl , 23.0 μmol , 1M) in toluene and triethylamine (8.11 μl , 57.4 μmol) were added. The reaction mixture was stirred at 60°C under exclusion of light for 5 d. The mixture was hydrolyzed by adding water and extracted with dichloromethane. The combined organic phases were dried over magnesium sulfate and the solvents were evaporated *in vacuo*. The residue was purified by flash column chromatography on silica gel (gradient: dichloromethane \rightarrow ethyl acetate/dichloromethane 1:100) followed by gel permeation chromatography (chloroform). The product fraction was heated to reflux in acetone (12 ml), cooled to rt and the solvent was removed by decantation. The product was dried in HV.

Yield: 11.0 mg (10.7 μmol , 28%) yellowish solid $\text{C}_{70}\text{H}_{53}\text{N}_3\text{O}_6$ [1032.2 g/mol].

$^1\text{H-NMR}$ (400 MHz, CD_2Cl_2 , 300 K): δ / ppm = 8.87–8.82 (—, 4H, $\text{CH}_{\text{naphth.}}$), 7.82 (AA', 2H, $\text{CH}_{\text{arom.}}$), 7.63 (AA', 2H, $\text{CH}_{\text{arom.}}$), 7.43–7.36 (—, 4H, $\text{CH}_{\text{arom.+TAA}}$), 7.28 (BB', 2H, $\text{CH}_{\text{arom.}}$), 7.13–7.02 (—, 6H, $\text{CH}_{\text{TAA+cyc}}$), 6.91–6.86 (—, 6H, CH_{TAA}), 6.67–6.64 (m, 1H, $\text{CH}_{\text{cyc.}}$), 6.69–6.51 (—, 3H, $\text{CH}_{\text{cyc.}}$), 3.81 (s, 6H, OCH_3), 3.75–3.62 (—, 2H, $\text{CH}_{2\text{cyc.}}$), 3.31–3.19 (—, 2H, $\text{CH}_{2\text{cyc.}}$), 3.12–3.03 (—, 2H, $\text{CH}_{2\text{cyc.}}$), 3.02–2.89 (—, 2H, $\text{CH}_{2\text{cyc.}}$), 1.44 (s, 9H, CH_3).

$^{13}\text{C-NMR}$ (151 MHz, CD_2Cl_2 , 298.8 K): δ / ppm = 163.5 (2C, quart.), 163.4 (2C, quart.), 156.9 (2C, quart.), 152.6 (1C, quart.), 149.2 (1C, quart.), 142.9 (1C, quart.), 142.3.6 (1C, quart.), 140.5 (2C, quart.), 140.2 (1C, quart.), 140.0 (1C, quart.), 137.6 (1C, tert.), 137.3 (1C, tert.), 135.0 (1C, quart.), 133.6 (1C, tert.), 133.5 (1C, tert.), 132.74 (2C, tert.), 132.67 (1C, quart.), 132.5 (2C, tert.), 131.7 (2C, tert.), 131.6 (2C, tert.), 131.0 (1C, tert.), 130.3 (1C, tert.), 129.3

(2C, tert.), 128.4 (2C, tert.), 127.63 (2C, quart.), 127.60 (2C, quart.), 127.58 (4C, tert.), 127.3 (2C, quart.), 126.9 (2C, tert.), 125.6 (1C, quart.), 125.2 (1C, quart.), 124.6 (1C, quart.), 119.3 (2C, tert.), 115.1 (4C, tert.), 114.53 (1C, quart.), 93.9 (1C, quart.), 92.2 (1C, quart.), 91.5 (1C, quart.), 88.7 (1C, quart.), 55.8 (2C, prim), 35.1 (1C, quart.), 34.4 (2C, sec.), 34.3 (1C, sec), 34.2 (1C, sec), 31.5 (3C, prim)

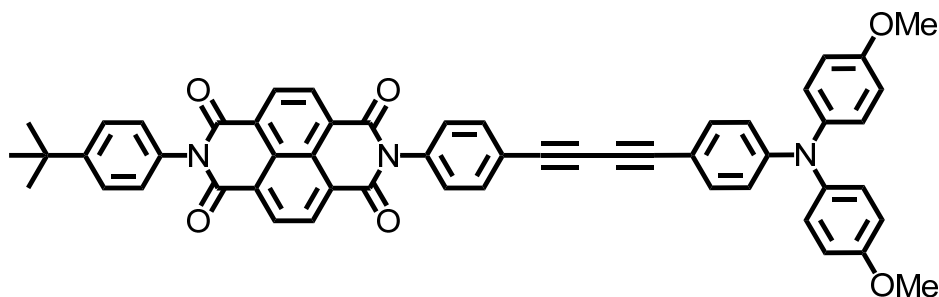
High Resolution Mass (ESI): calc.: 1031.39289 M⁺

 found: 1031.39236 M⁺

Δ: 0.51 ppm

6.2.7 SYNTHESIS OF DONOR-ACCEPTOR DYAD C

DYAD C



CAS: /

Dry dioxane (8 ml) and triethylamine (2 ml) were added to a mixture of compound **11** (75.8 mg, 152 μ mol), 4-ethynyl-N,N-bis(4-methoxyphenyl)aniline **14** (50.0 mg, 152 μ mol), bis(triphenylphosphine)palladium(II) dichloride (7.56 mg, 10.8 μ mol) and copper(I) iodide (2.89 mg, 15.2 μ mol). The mixture was stirred for 3 d at 50°C under atmospheric conditions (oxygen acts as the oxidant) and exclusion of light. The solvent was removed *in vacuo*, the residue was hydrolyzed with water and extracted with dichloromethane. The combined organic phases were dried over anhydrous magnesium sulfate and the solvent was removed *in vacuo*. The residue was purified by flash chromatography on silica gel (dichloromethane) followed by gel permeation chromatography (chloroform). The product was dried in HV.

Yield: 12.0 mg (14.5 μ mol, 10%) yellowish solid C₅₄H₃₉N₃O₆ [825.9 g/mol].

¹H-NMR (600 MHz, CD₂Cl₂, 298.8 K): δ / ppm = 8.83–8.81 (—, 4H, CH_{naphth.}), 7.72 (AA', 2H, CH_{arom.}), 7.62 (AA', 2H, CH_{arom.}), 7.36–7.30 (—, 4H, CH_{arom.+TAA}), 7.27 (BB', 2H, CH_{arom.}), 7.10 (AA', 4H, CH_{TAA}), 6.88 (BB', 4H, CH_{TAA}), 6.77 (BB', 2H, CH_{TAA}), 3.79 (s, 6H, OCH₃), 1.43 (s, 9H, CH₃).

¹³C-NMR (151 MHz, CD₂Cl₂, 298.8 K): δ / ppm = 163.5 (2C, quart.), 163.2 (2C, quart.), 157.3 (2C, quart.), 152.6 (1C, quart.), 150.4 (1C, quart.), 139.8 (2C, quart.), 135.7 (1C, quart.), 133.9 (2C, tert.), 133.7 (2C, tert.), 132.6 (1C, quart.), 131.7 (2C, tert.), 131.6 (2C, tert.), 129.3 (2C, tert.), 128.4 (2C, tert.), 128.0 (4C, tert.), 127.64 (2C, quart.), 127.576 (1C, quart.), 127.572 (1C, quart.), 127.2 (2C, quart.), 126.9 (2C, tert.), 123.4 (1C, quart.), 118.3 (2C, tert.),

115.2 (4C, tert.), 111.0 (1C, quart.), 83.9 (1C, quart.), 80.3 (1C, quart.), 75.9 (1C, quart.),
72.5 (1C, quart.), 55.8 (2C, prim.), 35.1 (1C, quart.), 31.5 (3C, prim.)

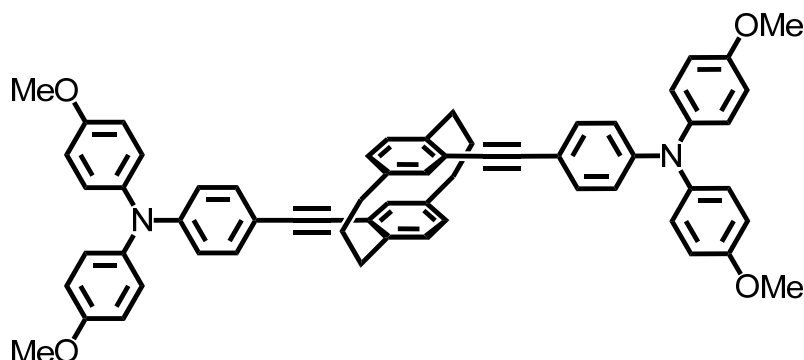
High Resolution Mass (ESI): calc.: 825.28334 M⁺

 found: 825.28313 M⁺

Δ: 0.25 ppm

6.2.8 SYNTHESIS OF MIXED-VALENCE PRECURSOR F

MIXED-VALENCE PRECURSOR F



CAS: /

Under nitrogen atmosphere dry dioxane (1 ml) was added to a mixture of 4-ethynyl-N,N-bis(4-methoxyphenyl)aniline **14** (147 mg, 447 μmol), 5,18-dibromo-[3.3]paracyclophane **10** (40.0 mg, 101 μmol), bis(benzonitrile)palladium(II)chloride (4.67 mg, 12.2 μmol) and copper(I)iodide (1.55 mg, 8.12 μmol). A solution of tri-*tert*-butylphosphine in toluene (24.4 μl , 24.4 μmol , 1.00 M) and diisopropylamine (51.2 μl , 365 μmol) were added. The reaction mixture was stirred for 2 d at 40°C under exclusion of light. The reaction mixture was hydrolyzed with water and extracted with dichloromethane. The combined organic phases were washed with a solution of sodium thiosulfate (5% in water) and water, dried over magnesium sulfate and the solvent was removed *in vacuo*. The residue was purified by column chromatography on aluminum oxide (gradient: dichloromethane/petroleum ether 1:10 \rightarrow 1:3) followed by recrystallization from acetone. The product was dried in HV.

Yield: 14.0 mg (15.7 μmol , 38%) colorless solid $\text{C}_{62}\text{H}_{54}\text{N}_2\text{O}_4$ [891.1 g/mol].

$^1\text{H-NMR}$ (400 MHz, CD_2Cl_2 , 300 K): δ / ppm = 7.37 (AA', 4H, CH_{TAA}), 7.09 (AA', 8H, CH_{TAA}), 6.93–6.84 (—, 16H, CH_{TAA} and CH_{cyc}), 6.73–6.66 (m, 2H, CH_{cyc}), 3.80 (s, 12H, CH_3), 3.31–3.21 (m, 2H, $\text{CH}_{2\text{cyc}}$), 2.82–2.57 (—, 6H, $\text{CH}_{2\text{cyc}}$), 2.47–2.33 (m, 2H, $\text{CH}_{2\text{cyc}}$), 2.07–1.95 (m, 2H, $\text{CH}_{2\text{cyc}}$).

$^{13}\text{C-NMR}$ (101 MHz, CD_2Cl_2 , 300 K): δ / ppm = 156.9 (quart.), 159.2 (quart.), 140.64 (quart.), 140.59 (quart.), 139.3 (quart.), 133.3 (tert.), 132.5 (tert.), 131.4 (tert.), 128.7 (tert.), 127.6 (tert.), 122.8 (quart.), 119.6 (tert.), 115.2 (, tert.), 115.0 (quart.), 93.2 (quart.), 88.7 (quart.), 55.9 (prim), 35.5 (sec.), 34.7 (sec.), 28.0 (sec.)

High Resolution Mass (ESI):

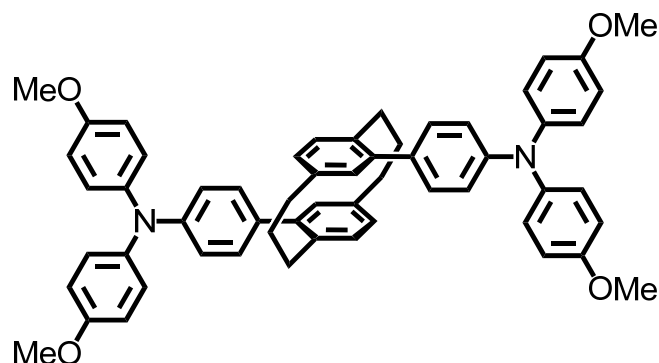
calc.: 890.40781 M⁺

found: 890.40982 M⁺

Δ : 2.26 ppm

6.2.9 SYNTHESIS OF MIXED-VALENCE PRECURSOR J

MIXED-VALENCE PRECURSOR J



CAS: /

Under nitrogen atmosphere dry toluene (7 ml) was added to a mixture of 4-methoxy-N-(4-methoxyphenyl)-N-(4-(4,4,5,5-tetramethyl-1,3,2-dioxaborolan-2-yl)phenyl)aniline **15** (291 mg, 674 μmol), compound 5,18-dibromo-[3.3]paracyclophane **10** (59.0 mg, 150 μmol), Pd(PPh₃)₄ (51.9 mg, 44.9 μmol) and sodium carbonate in water (2.25 ml, 2.25 mmol, 1.00 M). The reaction mixture was stirred for 3 d at 90°C under exclusion of light. The solvent was evaporated *in vacuo*, the residue hydrolyzed with water and extracted with dichloromethane. The combined organic phases were dried over magnesium sulfate and the solvent was removed *in vacuo*. The residue was purified by flash column chromatography on silica gel (toluene) followed by recrystallization from benzene. The product was washed with *n*-hexane and acetone and dried in HV.

Yield: 25.0 mg (29.7 μmol , 20 %) colorless crystals C₅₈H₅₄N₂O₄ [843.1 g/mol].

¹H-NMR (600 MHz, d₈-tetrahydrofuran, 303 K): δ / ppm = 7.27(AA', 4H, CH_{TAA}), 7.09 (AA', 8H, CH_{TAA}), 6.99 (—, 4H, CH_{TAA}), 6.87 (BB', 8H, CH_{TAA}), 6.82–6.76(m, 2H, CH_{cyc.}), 6.76–6.73 (m, 2H, CH_{cyc.}), 6.65–6.57 (m, 2H, CH_{cyc.}), 3.77 (s, 12H, CH₃), 3.25–2.90 (m, 2H, CH_{2cyc.}), 2.80–2.56 (—, 4H, CH_{2cyc.}), 2.56–2.35 (m, 2H, CH_{2cyc.}), 1.97–1.84 (m, 4H, CH_{2cyc.}).

¹³C-NMR (151 MHz, d₈-tetrahydrofuran, 303 K): δ / ppm = 157.0 (4C, quart.), 148.3 (2C, quart.), 141.8 (4C, quart.), 140.9 (2C, quart.), 139.3 (2C, quart.), 135.7 (2C, quart.), 135.3 (2C, quart.), 132.2 (2C, tert.), 130.7 (2C, tert.), 130.5 (4C, tert.), 127.5 (2C, tert.), 127.3 (8C, tert.), 120.6 (4C, tert.), 115.3 (8C, tert.), 55.4 (4C, prim), 36.6 (2C, sec), 34.1 (2C, sec.), 28.7 (2C, sec).

High Resolution Mass (ESI):

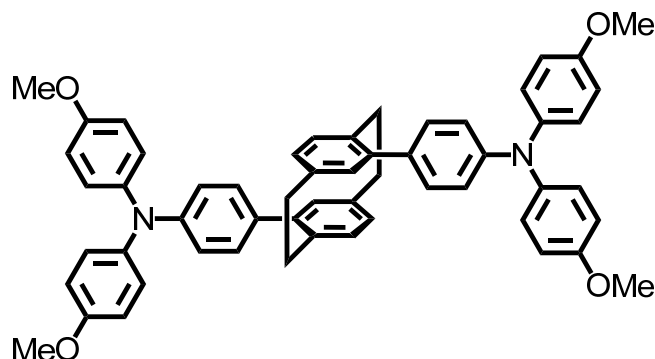
calc.: 842.40781 M⁺

found: 842.40783 M⁺

Δ : 0.02 ppm

6.2.10 SYNTHESIS OF MIXED-VALENCE PRECURSOR K

MIXED-VALENCE PRECURSOR K



CAS: 875709-66-3

Under nitrogen atmosphere toluene (10 ml) was added to a mixture of 4-methoxy-N-(4-methoxyphenyl)-N-(4-(4,4,5,5-tetramethyl-1,3,2-dioxaborolan-2-yl)phenyl)aniline **15** (707 mg, 1.64 mmol), 4,16-dibromo[2.2]paracyclophane (200 mg, 546 μ mol), tetrakis(triphenylphosphine)palladium (126 mg, 109 μ mol) and sodium carbonate in water (8.20 ml, 8.20 mmol, 1.00 M). The reaction mixture was stirred at 90°C under exclusion of light for 5 d. The mixture was hydrolyzed by adding water and extracted with toluene. The combined organic phases were dried over magnesium sulfate and the solvents were evaporated *in vacuo*. The residue was purified by flash column chromatography on silica gel (toluene) followed by recrystallization (benzene). The product was dried in HV.

Yield: 220 mg (270 μ mol, 49%) colorless crystals $C_{56}H_{50}N_2O_4$ [815.0 g/mol].

1H -NMR (400 MHz, d6-tetrahydrofuran, 300 K): δ / ppm = 7.32 (AA', 4H, CH_{TAA}), 7.10(AA', 8H, CH_{TAA}), 6.98 (BB', 4H, CH_{TAA}), 6.87 (BB', 8H, CH_{TAA}), 6.61–6.56 (—, 4H, $CH_{cyc.}$), 6.55–6.50 (m, 2H, $CH_{cyc.}$), 3.76 (s, 12H, OCH_3), 3.54–3.44 (m, 2H, CH_2), 2.99–2.90 (m, 2H, CH_2), 2.87–2.69 (—, 4H, CH_2).

6.3 CALCULATIONS

Absolute energy of the first excited state structure of **B** used for the TD-DFT-calculations in Hartree optimized with Gaussian 09^[96] at CAM-B3LYP/6-31G* level of theory:

$$E_h = -3313.1310703.$$

Cartesian Coordinates of the optimized geometry of the excited state of **B** with Gaussian 09^[96] at CAM-B3LYP/6-31G* level of theory:

C -15.6055 -2.7033 -0.6736	C 7.0443 -1.9363 0.6267	H -9.3307 -1.3187 -1.8139
C -14.4544 -2.7656 0.1263	C 6.5645 0.5203 0.3001	H -8.9170 2.0007 0.8886
C -13.6401 -1.6641 0.2619	O 5.7137 1.4040 0.2442	H -11.3620 2.2068 1.0181
C -13.9532 -0.4693 -0.4042	C 7.9861 0.7457 0.1303	H -2.3777 -1.4217 -2.3209
C -15.1022 -0.4058 -1.1937	O 6.5848 -3.0556 0.8317	H -1.0938 0.0681 -0.8774
C -15.9254 -1.5116 -1.3327	C 8.4566 -1.6521 0.4607	H -4.7069 1.5615 0.8421
C -15.4098 3.2663 1.0641	C 8.4558 2.0495 -0.1157	H -5.8424 -2.3028 1.4655
C -14.9644 4.4042 0.3732	C 9.8020 2.2895 -0.2726	H -4.6819 -0.7490 2.9684
C -13.9039 4.2920 -0.5315	C 10.7295 1.2368 -0.1900	H -2.0703 -3.4962 -0.1711
C -13.3017 3.0605 -0.7357	C 10.2900 -0.0812 0.0532	H -4.1337 -4.1563 -1.3033
C -13.7384 1.9304 -0.0419	C 8.8924 -0.3326 0.2169	H -5.7075 -3.8213 -0.5990
C -14.8079 2.0460 0.8590	C 11.1980 -1.1566 0.1391	H -0.9535 1.3156 1.1634
N -13.1241 0.6717 -0.2586	C 10.7330 -2.4600 0.3829	H -2.3316 2.2076 1.7934
C -11.7471 0.5578 -0.3277	C 9.3875 -2.7042 0.5409	H -1.1592 0.0524 3.0668
C -11.1485 -0.4530 -1.1145	C 12.1482 1.5190 -0.3524	H -2.7964 0.6147 3.3891
C -9.7827 -0.5592 -1.1870	C 12.6265 -0.9260 -0.0254	H -4.5811 -2.5323 -2.8465
C -8.9438 0.3264 -0.4720	N 13.0203 0.4110 -0.2595	H -6.0322 -2.0353 -1.9900
C -9.5494 1.3302 0.3188	O 12.5978 2.6409 -0.5576	H 2.2605 -2.9493 -0.5707
C -10.9142 1.4492 0.3871	O 13.4674 -1.8159 0.0303	H 4.6871 -2.5379 -0.8418
C -7.5483 0.2154 -0.5451	C 14.4239 0.6664 -0.4100	H 4.5695 0.3378 2.3132
C -6.3354 0.1278 -0.6107	C 15.0849 1.5004 0.4838	H 2.1475 -0.0738 2.6122
C -4.9274 0.0660 -0.6842	C 16.4411 1.7424 0.3362	H 7.7269 2.8487 -0.1751
C -4.2786 -0.9130 -1.4773	C 17.1840 1.1606 -0.6965	H 10.1832 3.2859 -0.4611
C -2.9101 -0.7553 -1.6491	C 16.5012 0.3262 -1.5802	H 11.4655 -3.2561 0.4416
C -2.1774 0.0910 -0.8232	C 15.1386 0.0830 -1.4434	H 9.0108 -3.7022 0.7299
C -2.7942 0.8180 0.2034	C 18.6847 1.4514 -0.8138	H 14.5275 1.9689 1.2863
C -4.1751 0.9191 0.1466	C 19.3267 0.7319 -2.0057	H 16.9286 2.4021 1.0478
C -4.0482 -2.9268 0.4509	C 19.3993 0.9843 0.4666	H 17.0265 -0.1539 -2.3972
C -4.7566 -2.2530 1.4463	C 18.9040 2.9639 -0.9949	H 14.6304 -0.5785 -2.1350
C -4.0982 -1.3726 2.2958	O -16.3310 -3.8302 -0.7381	H 19.2295 -0.3552 -1.9235
C -2.7300 -1.1386 2.1768	C -17.5165 -3.8428 -1.5180	H 18.8808 1.0435 -2.9556
C -1.9838 -2.0349 1.3877	O -15.6186 5.5434 0.6455	H 20.3953 0.9678 -2.0471
C -2.6590 -2.9203 0.5369	C -15.2173 6.7400 -0.0039	H 19.0130 1.4938 1.3539
C -4.7311 -3.3790 -0.8193	C -0.5646 -1.9030 1.2892	H 19.2651 -0.0916 0.6165
C -2.0092 1.2277 1.4283	C 0.6292 -1.7433 1.1782	H 20.4742 1.1900 0.4030
C -2.1482 0.1820 2.6215	H -14.2363 -3.6929 0.6430	H 18.5052 3.5347 -0.1516
C -4.9581 -2.1990 -1.8756	H -12.7646 -1.7117 0.9001	H 19.9738 3.1891 -1.0766
C 2.0376 -1.5342 1.0349	H -15.3436 0.5137 -1.7151	H 18.4084 3.3229 -1.9024
C 2.7657 -2.2273 0.0622	H -16.8037 -1.4410 -1.9609	H -17.9293 -4.8449 -1.4134
C 4.1216 -1.9941 -0.0967	H -16.2272 3.3789 1.7666	H -18.2405 -3.1094 -1.1478
C 4.7745 -1.0699 0.7136	H -13.5541 5.1504 -1.0899	H -17.2976 -3.6470 -2.5729
C 4.0588 -0.3858 1.6916	H -12.4952 2.9708 -1.4551	H -15.8733 7.5198 0.3796
C 2.7021 -0.6122 1.8507	H -15.1465 1.1729 1.4053	H -14.1775 6.9881 0.2335
N 6.1704 -0.8214 0.5427	H -11.7760 -1.1226 -1.6894	H -15.3406 6.6608 -1.0891

7 LITERATURE

- [1] E. Heilbronner, J. P. Maier *Helv. Chim. Acta* **1974**, 57, 151–159.
- [2] K. A. Lyssenko, M. Y. Antipin, D. Y. Antonov *ChemPhysChem* **2003**, 4, 817–823.
- [3] *Modern cyclophane chemistry*, (Eds.: R. Gleiter, H. Hopf), Wiley-VCH, Weinheim, **2004**.
- [4] G. F. Caramori, S. E. Galembeck *J. Phys. Chem. A* **2007**, 111, 1705–1712.
- [5] S. Grimme *Chem. Eur. J.* **2004**, 10, 3423–3429.
- [6] H.-C. Lin, B.-Y. Jin *J. Phys. Chem. A* **2008**, 112, 2948–2954.
- [7] S. Amthor, C. Lambert *J. Phys. Chem. A* **2006**, 110, 1177–1189.
- [8] S. M. Bachrach *J. Phys. Chem. A* **2011**, 115, 2396–2401.
- [9] H. Dodziuk, S. Szymański, J. Jaźwiński, M. E. Marchwiany, H. Hopf *J. Phys. Chem. A* **2010**, 114, 10467–10473.
- [10] M. Fujitsuka, S. Tojo, M. Shibahara, M. Watanabe, T. Shinmyozu, T. Majima *J. Phys. Chem. A* **2010**, 115, 741–746.
- [11] M. Fujitsuka, S. Tojo, T. Shinmyozu, T. Majima *Chem. Commun.* **2009**, 1553–1555.
- [12] A. Batra, G. Kladnik, H. Vázquez, J. S. Meisner, L. Floreano, C. Nuckolls, D. Cvetko, A. Morgante, L. Venkataraman *Nat. Commun.* **2012**, 3, 1–7.
- [13] P. Mücke, M. Zabel, R. Edge, D. Collison, S. Clément, S. Záliš, R. F. Winter *J. Organomet. Chem.* **2011**, 696, 3186–3197.
- [14] S. Clément, T. Goudreault, D. Bellows, D. Fortin, L. Guyard, M. Knorr, P. D. Harvey *Chem. Commun.* **2012**, 48, 8640–8642.
- [15] A. M. Soliman, D. Fortin, E. Zysman-Colman, P. D. Harvey *Chem. Commun.* **2012**, 48, 6271–6273.
- [16] K. Kameyama, M. Morisue, A. Satake, Y. Kobuke *Angew. Chem., Int. Ed.* **2005**, 44, 4763–4766.
- [17] N. Kobayashi, T. Fukuda, D. Lelièvre *Inorg. Chem.* **2000**, 39, 3632–3637.
- [18] Y. Asano, A. Muranaka, A. Fukasawa, T. Hatano, M. Uchiyama, N. Kobayashi *J. Am. Chem. Soc.* **2007**, 129, 4516–4517.
- [19] A. Tsuge, T. Hara, T. Moriguchi *Tetrahedron Lett.* **2009**, 50, 4509–4511.
- [20] A. Tsuge, T. Hara, T. Moriguchi, M. Yamaji *Chem. Lett.* **2008**, 37, 870–871.
- [21] L. Lin, Y. Morisaki, Y. Chujo *Int. J. Polym. Sci.* **2010**, 1–9.
- [22] Y. Morisaki, Y. Chujo *Polym. Chem.* **2011**, 2, 1249–1257.
- [23] P. J. Ball, T. R. Shtoyko, J. A. Krause Bauer, W. J. Oldham, W. B. Connick *Inorg. Chem.* **2004**, 43, 622–632.
- [24] G. C. Bazan *J. Org. Chem.* **2007**, 72, 8615–8635.

- [25] D. R. Kattnig, B. Mladenova, G. Grampp, C. Kaiser, A. Heckmann, C. Lambert *J. Phys. Chem. C* **2009**, 113, 2983–2995.
- [26] H. Hope, J. Bernstein, K. N. Trueblood *Acta Crystallogr., Sect. B* **1972**, B 28, 1733–1743.
- [27] P. K. Gantzel, K. N. Trueblood *Acta Crystallogr.* **1965**, 18, 958–968.
- [28] P. G. Jones, H. Hopf, Z. Pechlivanidis, R. Boese *Z. Kristallogr.* **1994**, 209, 673–676.
- [29] D. J. Cram, R. A. Reeves *J. Am. Chem. Soc.* **1958**, 80, 3094–3103.
- [30] Y. Shirota, H. Kageyama *Chem. Rev.* **2007**, 107, 953–1010.
- [31] M. Thelakkat *Macromol. Mater. Eng.* **2002**, 287, 442–461.
- [32] D. S. Weiss, J. Robin Cowdery, R. H. Young *Electrophotography*, (Ed. V. Balzani), Wiley-VCH Verlag GmbH, Weinheim, **2001**, pp.379–471.
- [33] R.-J. Bushby *Magnetism: Molecules to Materials II*, (Eds.: J. S. Miller, M. Drillon), Wiley-VCH, Weinheim, **2001**, pp.149–187.
- [34] Z. Ning, H. Tian *Chem. Commun.* **2009**, 37, 5483–5495.
- [35] H.-J. Yen, G.-S. Liou *Polym. Chem.* **2012**, 3, 255–264.
- [36] S. Amthor, B. Noller, C. Lambert *Chem. Phys.* **2005**, 316, 141–152.
- [37] S. Dapperheld, E. Steckhan, K.-H. G. Brinkhaus, T. Esch *Chem. Ber.* **1991**, 124, 2557–2567.
- [38] A. Heckmann, C. Lambert *Angew. Chem., Int. Ed.* **2012**, 51, 326–392.
- [39] H. E. Katz, A. J. Lovinger, C. Kloc, T. Siegrist, W. Li, Y.-Y. Lin, A. Dodabalapur *Nature* **2000**, 404, 478–481.
- [40] P. Gawrys, D. Djurado, J. Rimarčík, A. Kornet, D. Boudinet, J.-M. Verilhac, V. Lukeš, I. Wielgus, M. Zagorska, A. Pron *J. Phys. Chem. B* **2010**, 114, 1803–1809.
- [41] P. Gawrys, D. Boudinet, M. Zagorska, D. Djurado, J.-M. Verilhac, G. Horowitz, J. Pécaud, S. Pouget, A. Pron *Synth. Met.* **2009**, 159, 1478–1485.
- [42] F. Würthner, M. Stolte *Chem. Commun.* **2011**, 47, 5109–5115.
- [43] B. A. Jones, A. Facchetti, T. J. Marks, M. R. Wasielewski *Chem. Mater.* **2007**, 19, 2703–2705.
- [44] B. A. Jones, A. Facchetti, M. R. Wasielewski, T. J. Marks *J. Am. Chem. Soc.* **2007**, 129, 15259–15278.
- [45] P. Ganesan, J. Baggerman, H. Zhang, E. J. R. Sudhölter, H. Zuilhof *J. Phys. Chem. A* **2007**, 111, 6151–6156.
- [46] S. Green, M. A. Fox *J. Phys. Chem.* **1995**, 99, 14752–14757.
- [47] J. E. Rogers, L. A. Kelly *J. Am. Chem. Soc.* **1999**, 121, 3854–3861.
- [48] S. I. van Dijk, C. P. Groen, F. Hartl, A. M. Brouwer, J. W. Verhoeven *J. Am. Chem. Soc.* **1996**, 118, 8425–8432.

- [49] S. R. Greenfield, W. A. Svec, D. Gosztola, M. R. Wasielewski *J. Am. Chem. Soc.* **1996**, 118, 6767–6777.
- [50] G. P. Wiederrecht, M. P. Niemczyk, W. A. Svec, M. R. Wasielewski *J. Am. Chem. Soc.* **1996**, 118, 81–88.
- [51] M. P. Debreczeny, W. A. Svec, E. M. Marsh, M. R. Wasielewski *J. Am. Chem. Soc.* **1996**, 118, 8174–8175.
- [52] D. Gosztola, M. P. Niemczyk, W. Svec, A. S. Lukas, M. R. Wasielewski *J. Phys. Chem. A* **2000**, 104, 6545–6551.
- [53] S. E. Miller, A. S. Lukas, E. Marsh, P. Bushard, M. R. Wasielewski *J. Am. Chem. Soc.* **2000**, 122, 7802–7810.
- [54] A. S. Lukas, P. J. Bushard, E. A. Weiss, M. R. Wasielewski *J. Am. Chem. Soc.* **2003**, 125, 3921–3930.
- [55] S. Chopin, F. Chaignon, E. Blart, F. Odobel *J. Mater. Chem.* **2007**, 17, 4139–4146.
- [56] F. Chaignon, M. Falkenström, S. Karlsson, E. Blart, F. Odobel, L. Hammarström *Chem. Commun.* **2007**, 64–66.
- [57] F. Würthner, A. Shahadat, C. Thalacker, T. Debaerdemaeker *Chem. Eur. J.* **2002**, 8, 4742–4750.
- [58] J. E. Bullock, M. T. Vagnini, C. Ramanan, D. T. Co, T. M. Wilson, J. W. Dicke, T. J. Marks, M. R. Wasielewski *J. Phys. Chem. B* **2010**, 114, 1794–1802.
- [59] C. Thalacker, C. Röger, F. Würthner *J. Org. Chem.* **2006**, 71, 8098–8105.
- [60] C. Röger, S. Ahmed, F. Würthner *Synthesis* **2007**, 1872–1876.
- [61] C. Röger, F. Würthner *J. Org. Chem.* **2007**, 72, 8070–8075.
- [62] N. Sakai, J. Mareda, E. Vauthey, S. Matile *Chem. Commun.* **2010**, 46, 4225–4237.
- [63] S. V. Bhosale, C. H. Jani, S. J. Langford *Chem. Soc. Rev.* **2008**, 37, 331–342.
- [64] S. Bhosale, A. L. Sisson, P. Talukdar, A. Fürstenberg, N. Banerji, E. Vauthey, G. Bollot, J. Mareda, C. Röger, F. Würthner, N. Sakai, S. Matile *Science* **2006**, 313, 84–86.
- [65] C. J. Zhong, W. S. V. Kwan, L. L. Miller *Chem. Mater.* **1992**, 4, 1423–1428.
- [66] S. Alp, Ş. Erten, C. Karapire, B. Köz, A. O. Doroshenko, S. İçli *J. Photochem. Photobiol., A* **2000**, 135, 103–110.
- [67] F. Chaignon, F. Buchet, E. Blart, M. Falkenström, L. Hammarström, F. Odobel *New J. Chem.* **2009**, 33, 408–416.
- [68] H. Langhals, P. von Unold *Angew. Chem., Int. Ed.* **1995**, 34, 2234–2236.
- [69] H. Langhals, S. Demmig, H. Huber *Spectrochim. Acta, Part A* **1988**, 44, 1189–1193.
- [70] S. Takahashi, K. Nozaki, M. Kozaki, S. Suzuki, K. Keyaki, A. Ichimura, T. Matsushita, K. Okada *J. Phys. Chem. A* **2008**, 112, 2533–2542.
- [71] L. Flamigni, E. Baranoff, J.-P. Collin, J.-P. Sauvage *Chem. Eur. J.* **2006**, 12, 6592–6606.

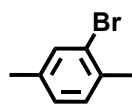
- [72] A. Heckmann, S. Amthor, C. Lambert *Chem. Commun.* **2006**, 2959–2961.
- [73] C. Lambert, C. Risko, V. Coropceanu, J. Schelter, S. Amthor, N. E. Gruhn, J. C. Durivage, J.-L. Bredas *J. Am. Chem. Soc.* **2005**, 127, 8508–8516.
- [74] A. V. Szeghalmi, M. Erdmann, V. Engel, M. Schmitt, S. Amthor, V. Kriegisch, G. Noll, R. Stahl, C. Lambert, D. Leusser, D. Stalke, M. Zabel, J. Popp *J. Am. Chem. Soc.* **2004**, 126, 7834–7845.
- [75] P. J. Low, M. A. J. Paterson, H. Puschmann, A. E. Goeta, J. A. K. Howard, C. Lambert, J. C. Cherryman, D. R. Tackley, S. Leeming, B. Brown *Chem. Eur. J.* **2004**, 10, 83–91.
- [76] C. Lambert, S. Amthor, J. Schelter *J. Phys. Chem. A* **2004**, 108, 6474–6486.
- [77] V. Coropceanu, N. E. Gruhn, S. Barlow, C. Lambert, J. C. Durivage, T. G. Bill, G. Nöll, S. R. Marder, J.-L. Brédas *J. Am. Chem. Soc.* **2004**, 126, 2727–2731.
- [78] V. Coropceanu, C. Lambert, G. Nöll, J. L. Brédas *Chem. Phys. Lett.* **2003**, 373, 153–160.
- [79] C. Lambert, G. Nöll, J. Schelter *Nat. Mater.* **2002**, 1, 69–73.
- [80] C. Lambert, G. Noll *J. Chem. Soc., Perkin Trans. 2* **2002**, 2039–2043.
- [81] C. Lambert, G. Nöll *J. Am. Chem. Soc.* **1999**, 121, 8434–8442.
- [82] Z. Pechlivanidis, H. Hopf, L. Ernst *Eur. J. Org. Chem.* **2009**, 223–237.
- [83] M. Rudolph, S. W. Feldberg *Digisim, Version 3.05*, Bioanalytical Systems Inc., West Lafayette.
- [84] A. J. Bard, L. R. Faulkner, *Electrochemical Methods*, John Wiley & Sons, New York, **2001**.
- [85] Y. Tanaka, T. Ozawa, A. Inagaki, M. Akita *Dalton Trans.* **2007**, 928–933.
- [86] A. R. Wartini, J. Valenzuela, H. A. Staab, F. A. Neugebauer *Eur. J. Org. Chem.* **1998**, 139–148.
- [87] A. R. Wartini, J. Valenzuela, H. A. Staab, F. A. Neugebauer *Eur. J. Org. Chem.* **1998**, 221–227.
- [88] A. R. Wartini, H. A. Staab, F. A. Neugebauer *Eur. J. Org. Chem.* **1998**, 1161–1170.
- [89] D. E. Richardson, H. Taube *Coord. Chem. Rev.* **1984**, 60, 107–129.
- [90] Y.-C. Lin, W.-T. Chen, J. Tai, D. Su, S.-Y. Huang, I. Lin, J.-L. Lin, M. M. Lee, M. F. Chiou, Y.-H. Liu, K.-S. Kwan, Y.-J. Chen, H.-Y. Chen *Inorg. Chem.* **2009**, 48, 1857–1870.
- [91] F. Barrière, N. Camire, W. E. Geiger, U. T. Mueller-Westerhoff, R. Sanders *J. Am. Chem. Soc.* **2002**, 124, 7262–7263.
- [92] D. M. D'Alessandro, F. R. Keene *Dalton Trans.* **2004**, 3950–3954.
- [93] D. E. Richardson, H. Taube *Inorg. Chem.* **1981**, 20, 1278–1285.
- [94] A. Weller *Z. Phys. Chem.* **1982**, 133, 93–98.
- [95] *ChemBio3D Ultra 3.0, Version 12.0.2.1076*, CambridgeSoft, Cambridge, **2010**.

- [96] M. J. Frisch, G. W. Trucks, H. B. Schlegel, G. E. Scuseria, M. A. Robb, J. R. Cheeseman, G. Scalmani, V. Barone, B. Mennucci, G. A. Petersson, H. Nakatsuji, M. Caricato, X. Li, H. P. Hratchian, A. F. Izmaylov, J. Bloino, G. Zheng, J. L. Sonnenberg, M. Hada, M. Ehara, K. Toyota, R. Fukuda, J. Hasegawa, M. Ishida, T. Nakajima, Y. Honda, O. Kitao, H. Nakai, T. Vreven, J. Montgomery, J. A., J. E. Peralta, F. Ogliaro, M. Bearpark, J. J. Heyd, E. Brothers, K. N. Kudin, V. N. Staroverov, R. Kobayashi, J. Normand, K. Raghavachari, A. Rendell, J. C. Burant, S. S. Iyengar, J. Tomasi, M. Cossi, N. Rega, N. J. Millam, M. Klene, J. E. Knox, J. B. Cross, V. Bakken, C. Adamo, J. Jaramillo, R. Gomperts, R. E. Stratmann, O. Yazyev, A. J. Austin, R. Cammi, C. Pomelli, J. W. Ochterski, R. L. Martin, K. Morokuma, V. G. Zakrzewski, G. A. Voth, P. Salvador, J. J. Dannenberg, S. Dapprich, A. D. Daniels, Ö. Farkas, J. B. Foresman, J. V. Ortiz, J. Cioslowski, D. J. Fox *Gaussian 09, Version B.01*, Gaussian, Inc., Wallingford CT, **2009**.
- [97] G. Angulo, G. Grampp, A. Rosspeintner *Spectrochim. Acta, Part A* **2006**, 65, 727–731.
- [98] R. J. Cave, M. D. Newton *J. Chem. Phys.* **1997**, 106, 9213–9226.
- [99] R. J. Cave, M. D. Newton *Chem. Phys. Lett.* **1996**, 249, 15–19.
- [100] J. B. Birks, *Photophysics of Aromatic Molecules*, John Wiley & Sons, New York, **1970**.
- [101] I. H. M. van Stokkum, D. S. Larsen, R. van Grondelle *Biochim. Biophys. Acta* **2004**, 1657, 82–104.
- [102] B. M. Aveline, S. Matsugo, R. W. Redmond *J. Am. Chem. Soc.* **1997**, 119, 11785–11795.
- [103] C. V. Suneesh, K. R. Gopidas *J. Phys. Chem. C* **2009**, 113, 1606–1614.
- [104] I. Carmichael, G. L. H. Hug *J. Phys. Chem. Ref. Data* **1986**, 15, 1–250.
- [105] R. Bonneau, I. Carmichael, G. L. Hug *Pure Appl. Chem.* **1991**, 63, 289–299.
- [106] D. Wachsstock *Tenua, Version 2.1*, **2007**.
- [107] J. W. Verhoeven *J. Photochem. Photobiol., A* **2006**, 7, 40–60.
- [108] U. Werner, Y. Sakaguchi, H. Hayashi, G. Nohya, R. Yoneshima, S. Nakajima, A. Osuka *J. Phys. Chem.* **1995**, 99, 13930–13937.
- [109] U. E. Steiner, T. Ulrich *Chem. Rev.* **1989**, 89, 51–147.
- [110] A. Heckmann, C. Lambert *J. Am. Chem. Soc.* **2007**, 129, 5515–5527.
- [111] W. J. Oldham, Jr., Y.-J. Miao, R. J. Lachicotte, G. C. Bazan *J. Am. Chem. Soc.* **1998**, 120, 419–420.
- [112] G. C. Bazan, W. J. Oldham, Jr., R. J. Lachicotte, S. Tretiak, V. Chernyak, S. Mukamel *J. Am. Chem. Soc.* **1998**, 120, 9188–9204.
- [113] S. Wang, G. C. Bazan, S. Tretiak, S. Mukamel *J. Am. Chem. Soc.* **2000**, 122, 1289–1297.
- [114] G. P. Bartholomew, G. C. Bazan *Acc. Chem. Res.* **2001**, 34, 30–39.

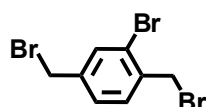
- [115] A. M. Moran, G. P. Bartholomew, G. C. Bazan, A. M. Kelley *J. Phys. Chem. A* **2002**, 106, 4928–4937.
- [116] A. Ruseckas, E. B. Namdas, J. Y. Lee, S. Mukamel, S. Wang, G. C. Bazan, V. Sundström *J. Phys. Chem. A* **2003**, 107, 8029–8034.
- [117] W. Leng, J. Grunden, G. P. Bartholomew, G. C. Bazan, A. M. Kelley *J. Phys. Chem. A* **2004**, 108, 10050–10059.
- [118] H.-G. Hong, W. Park *Electrochim Acta* **2005**, 51, 579–587.
- [119] H. Hayashi, S. Nagakura *Bull. Chem. Soc. Jpn.* **1984**, 57, 322–328.
- [120] T. Klumpp, M. Linsenmann, S. L. Larson, B. R. Limoges, D. Bürssner, E. B. Krissinel, C. M. Elliott, U. E. Steiner *J. Am. Chem. Soc.* **1999**, 121, 1076–1087.
- [121] M. T. Rawls, G. Kollmannsberger, C. M. Elliott, U. E. Steiner *J. Phys. Chem. A* **2007**, 111, 3485–3496.
- [122] Y. Mori, Y. Sakaguchi, H. Hayashi *J. Phys. Chem. A* **2002**, 106, 4453–4467.
- [123] K. P. Ghiggino, J. A. Hutchison, S. J. Langford, M. J. Latter, M. A.-P. Lee, M. Takezaki *Aust. J. Chem.* **2006**, 59, 179–185.
- [124] H. Mauser, *Formale Kinetik*, Bertelsmann Universitätsverlag, Düsseldorf, **1974**.
- [125] D. Kuciauskas, P. A. Liddell, A. L. Moore, T. A. Moore, D. Gust *J. Am. Chem. Soc.* **1998**, 120, 10880–10886.
- [126] H. J. Ramesdonk, B. H. Bakker, M. M. Groeneveld, J. W. Verhoeven, B. D. Allen, J. P. Rostron, A. Harriman *J. Phys. Chem. A* **2006**, 110, 13145–13150.
- [127] L. E. Ebersson *Electron Transfer Reactions in Organic Chemistry, Vol. 25*, Springer-Verlag, Berlin, **1987**, pp.48–53.
- [128] M. Malagoli, J. L. Brédas *Chem. Phys. Lett.* **2000**, 327, 13–17.
- [129] Y. Geng, S.-X. Wu, H.-B. Li, X.-D. Tang, Y. Wu, Z.-M. Su, Y. Liao *J. Mater. Chem.* **2011**, 21, 15558–15566.
- [130] S. P. Adiga, D. Shukla *J. Phys. Chem. C* **2010**, 114, 2751–2755.
- [131] I. R. Gould, D. Noukakis, L. Gomez-Jahn, R. H. Young, J. L. Goodman, S. Farid *Chem. Phys.* **1993**, 176, 439–456.
- [132] J. Cortés, H. Heitele, J. Jortner *J. Phys. Chem.* **1994**, 98, 2527–2536.
- [133] M. Bixon, J. Jortner *J. Chem. Phys.* **1968**, 48, 715–726.
- [134] J. Jortner *J. Chem. Phys.* **1976**, 64, 4860–4867.
- [135] R. A. Marcus *J. Phys. Chem.* **1989**, 93, 3078–3086.
- [136] E. A. Weiss, M. A. Ratner, M. R. Wasielewski *J. Phys. Chem. A* **2003**, 107, 3639–3647.
- [137] D. Veldman, S. M. A. Chopin, S. C. J. Meskers, R. A. J. Janssen *J. Phys. Chem. A* **2008**, 112, 8617–8632.
- [138] D. B. MacQueen, K. S. Schanze *J. Am. Chem. Soc.* **1991**, 113, 7470–7479.

- [139] M. D. Newton *Chem. Rev.* **1991**, 91, 767–792.
- [140] A. L. Thompson, T.-S. Ahn, K. R. J. Thomas, S. Thayumanavan, T. J. Martínez, C. J. Bardeen *J. Am. Chem. Soc.* **2005**, 127, 16348–16349.
- [141] D. González-Rodríguez, T. Torres, M. Á. Herranz, L. Echegoyen, E. Carbonell, D. M. Guldi *Chem. Eur. J.* **2008**, 14, 7670–7679.
- [142] S. Shaikov, T. Galili, E. Stavitski, H. Levanon, A. Lukas, M. R. Wasielewski *J. Am. Chem. Soc.* **2003**, 125, 6563–6572.
- [143] K. Schulten, A. Weller *Biophys. J.* **1978**, 24, 295–305.
- [144] M. N. Paddon-Row, M. J. Shephard *J. Phys. Chem. A* **2002**, 106, 2935–2944.
- [145] B. Brocklehurst *J. Chem. Soc., Faraday Trans.* **1976**, 72, 1869–1884.
- [146] P. W. Anderson *Phys. Rev.* **1950**, 79, 350–356.
- [147] P. W. Anderson *Phys. Rev.* **1959**, 115, 2–13.
- [148] R. Haberkorn, M. E. Michel-Beyerle, R. A. Marcus *Proc. Natl. Acad. Sci. U. S. A.* **1979**, 76, 4185–4188.
- [149] M. Y. Okamura, R. A. Isaacson, G. Feher *Biochim. Biophys. Acta* **1979**, 546, 394–417.
- [150] S. F. Nelsen, R. F. Ismagilov, Y. Teki *J. Am. Chem. Soc.* **1998**, 120, 2200–2201.
- [151] A. M. Scott, T. Miura, A. B. Ricks, Z. E. X. Dance, E. M. Giacobbe, M. T. Colvin, M. R. Wasielewski *J. Am. Chem. Soc.* **2009**, 131, 17655–17666.
- [152] A. M. Scott, M. R. Wasielewski *J. Am. Chem. Soc.* **2011**, 133, 3005–3013.
- [153] M. T. Colvin, A. B. Ricks, A. M. Scott, D. T. Co, M. R. Wasielewski *J. Phys. Chem. A* **2012**, 116, 1923–1930.
- [154] J. Salbeck, PhD thesis, Universität Regensburg, **1988**.
- [155] G. M. Sheldrick *Acta Crystallogr., Sect. A* **2008**, 64, 112–122.
- [156] H. Miyasaka, H. Masuhara, N. Mataga *J. Phys. Chem.* **1990**, 94, 3577–3582.
- [157] T. C. Barros, S. Brochsztain, V. G. Toscano, P. B. Filho, M. J. Politi *J. Photochem. Photobiol., A* **1997**, 111, 97–104.
- [158] H. Miyasaka, H. Masuhara, N. Mataga *Chem. Phys. Lett.* **1985**, 118, 459–463.
- [159] J. K. Hurley, N. Sinai, H. Linschitz *Photochem. Photobiol.* **1983**, 38, 9–14.
- [160] R. Bensasson, E. J. Land *J. Chem. Soc., Faraday Trans.* **1971**, 67, 1904–1915.

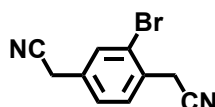
8 STRUCTURAL FORMULA TABLE



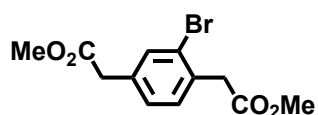
1



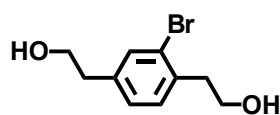
2



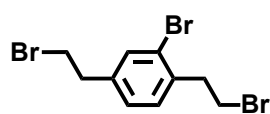
3



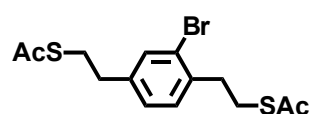
4



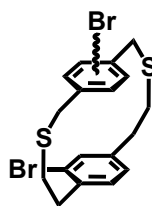
5



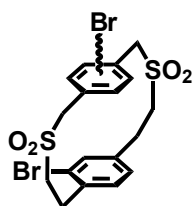
6



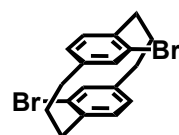
7



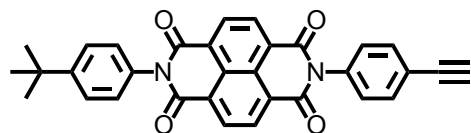
8



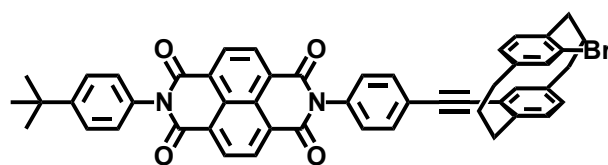
9



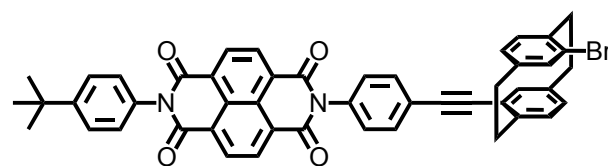
10



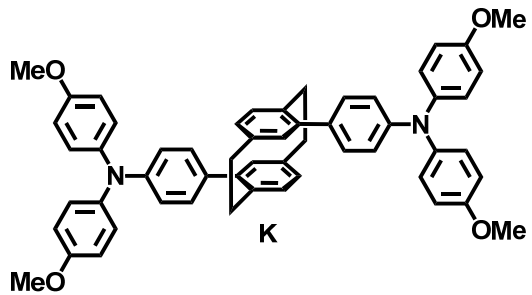
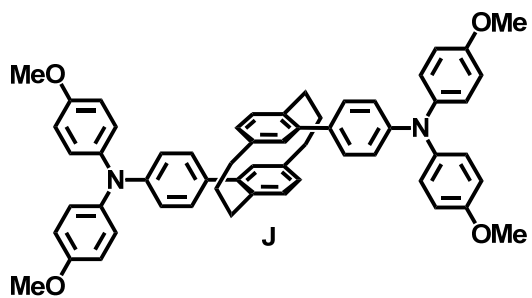
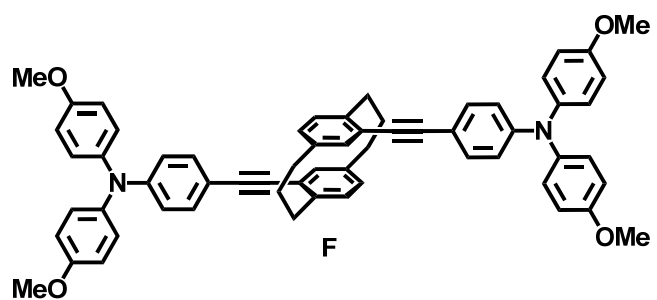
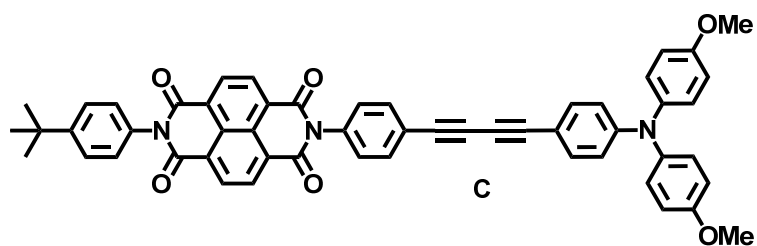
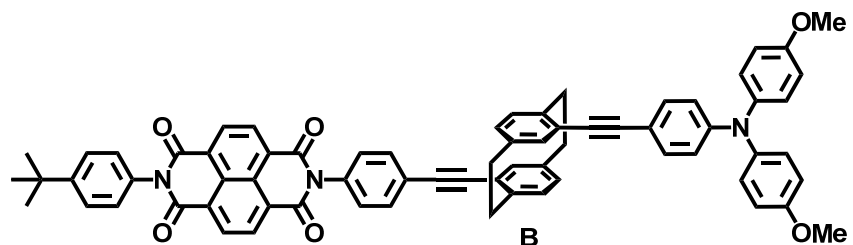
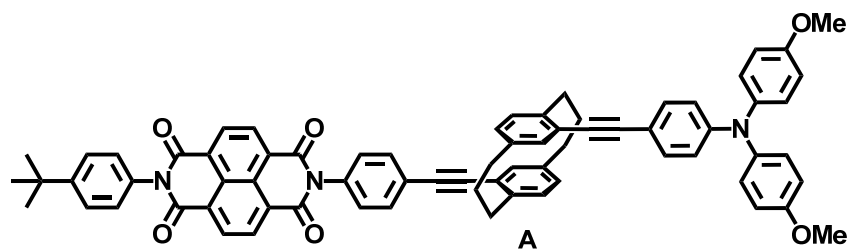
11



13



E



GENERAL SUMMARY (GERMAN)

Im ersten Teil dieser Arbeit wurde der Einfluss der Veränderung der Energetik von Brückeneinheiten auf Elektronentransferprozesse in Donor-Brücke-Akzeptor Modellsystemen in einer Monolagenumgebung untersucht.

Dies wurde mittels speziell dafür entworfener Moleküle mit Ferrocencarbonsäureester Donoren und Hydrochinonderivaten als Brückeneinheiten und durch Verwendung einer Goldelektrode als Akzeptor verwirklicht. Die Energetik der Hydrochinonderivate wurde durch synthetische Variation der Substituenten mit der Absicht angepasst, die Geschwindigkeiten und die Mechanismen der Elektronentransferprozesse zu verändern. Dabei basierte die Wahl der Substituenten auf literaturbekannten Halbstufenpotentialen von ähnlichen solvatisierten Hydrochinonderivaten und anschließender Bestimmung der Halbstufenpotentiale der im Rahmen dieser Arbeit synthetisierten solvatisierten Vorläufer der Brückeneinheiten. Dann wurde unter Berücksichtigung der eingeschränkten Stabilität des Ferrocencarbonsäureesters ein Syntheseplan entwickelt und erfolgreich angewendet. Anschließend wurde eine Vorgehensweise zur Herstellung von sehr dichten und hoch geordneten Monolagen aus den Zielmolekülen auf selbst hergestellten Mikroelektroden aus Gold erarbeitet. Ferner wurden verschiedene Elektrolyte getestet, um eine niedrige Empfindlichkeit des Messaufbaus in Bezug auf kleine Änderungen der Elektrodenanordnung und der Messparameter zu gewährleisten und gleichzeitig eine ausreichende Stabilität der Monolagen sicherzustellen. Des Weiteren wurde ein neuer, kommerziell erhältlicher Potentiostat für die Untersuchungen etabliert, der die Belastung für die Monolagen im Vergleich zu den Messapparaturen in vielen bisherigen Studien reduzierte. Bezüglich der Bestimmung der Elektronentransferraten wurde das von *Creager et al.* entwickelte Protokoll geringfügig erweitert, um die Monolagen trotz ihres nicht-idealen Verhaltens untersuchen zu können. Zusätzlich wurde der Einfluss der elektrischen Parameter der Impedanzmessungen untersucht, um den Fehler in den erfassten Daten zu minimieren.

Die elektrochemische Analyse der Monolagen mittels Cyclovoltammetrie bestätigte das Erreichen einer fast idealen Oberflächendeckung und einer außergewöhnlich hohen Ordnung. Die Oberflächendeckung von \mathbf{M}_B und \mathbf{M}_C war, wahrscheinlich aufgrund der raumfüllenden Substituenten der Brückeneinheiten, geringfügig niedriger als die von \mathbf{M}_A . Ferner zeigen die Redoxwellen im Cyclovoltammogramm von \mathbf{M}_A eine Verbreiterung und eine Verschiebung zu höheren Potentialen, was auf die elektrostatischen Wechselwirkungen der terminalen Redoxzentren als Folge der besonders dichten Packung zurückgeführt wurde.

Bei der cyclovoltammetrischen Untersuchung von **M_B** zeigten sich im Gegensatz zu Vorversuchen an Monolagen desselben Typs mit niedriger Oberflächenbelegung jedoch keine der aufgrund der vorhergesagten Energetik erwarteten, scharfen Redoxwellen der Brückeneinheiten. Dies lässt sich wahrscheinlich auf die unterschiedlichen Umgebungen der tief in die sehr dichten Monolagen eingebetteten Brückeneinheiten zurückführen. Im Detail verursachte vermutlich die unterschiedliche Abschirmung gegenüber den einzelnen Gegenionen und Solvensmolekülen eine Verschiebung der oxidierten Brückenzustände zu verschiedenen höheren Potentialen. Das führt zu der Schlussfolgerung, dass die mittels Cyclovoltammetrie bestimmten Halbstufenpotentiale von solvatisierten Brückeneinheiten nicht geeignet sind, um die Energetik der oxidierten Brückenzustände im Innern von sehr dichten Monolagen vorherzusagen.

Bei der Analyse der Monolagen mittels Impedanzspektroskopie zeigte sich, dass die Elektronentransferraten von **M_A** geringfügig höher als die von **M_B** und beide höher als die von **M_C** sind. Im Einklang mit der Literatur befanden sich alle Werte unter Berücksichtigung der Länge und des Konjugationsgrads des Molekülrückrads in der erwarteten Region. Jedoch relativiert sich dieses Bild bei Berücksichtigung der beabsichtigten energetischen Anpassung der Brückeneinheiten. Aufgrund der vermeintlich nur geringfügig höheren Energie der Zustände der oxidierten Brücke und des oxidierten Donors in **M_B** hätte ein Dominieren des „hopping“ Mechanismus zu einer um einige Größenordnungen höheren Elektronentransferrate als in **M_A** und **M_C** führen sollen. Dass dies nicht der Fall war, kann wahrscheinlich auf die Unterschätzung der oxidierten Brückenzustände durch die Bestimmung mittels Cyclovoltammetrie an den solvatisierten Brückeneinheiten zurückgeführt werden (siehe oben). Insgesamt kann aufgrund der eher geringen Unterschiede der Elektronentransferraten für **M_A**, **M_B** und **M_C** von einem dominierenden „superexchange“ Mechanismus ausgegangen werden. Allerdings hätte, sogar bei einer Verschiebung der Potentiale, die vorhergesagte energetische Anordnung der oxidierten Brückenzustände zu einer sich geringfügig verringernden Elektronentransferrate von **M_B** über **M_A** zu **M_C** führen müssen. Der Grund dafür, dass die tatsächliche Elektronentransferrate in **M_A** geringfügig höher als in **M_B** ist, liegt möglicherweise an der dichteren Packung und damit stärkeren elektrostatischen Interferenz der terminalen Redoxzentren in **M_A** (siehe oben).

Schließlich wurden also die anvisierten Modellsysteme hergestellt und deren Elektronentransferraten erfolgreich bestimmt. Die Probleme mit der relativen energetischen Anordnung der Zustände der Molekülteile in den dichten Monolagen verhinderten allerdings die gezielte Veränderung der Geschwindigkeit und des Mechanismus des Elektronentransfers. Dies ist wahrscheinlich im Wesentlichen auf die hohe Dichte und

Ordnung der im Rahmen dieser Arbeit präparierten Monolagen zurückzuführen, die ein Eindringen der Elektrolytbestandteile in die Monolagen hemmen. Dies führt zu unterschiedlichen Abständen der einzelnen Brückeneinheiten zu den Elektrolytbestandteilen und damit, aufgrund unterschiedlicher Abschwächung der Stabilisierung, zu einer Aufspaltung und Verschiebung des oxidierten Brückenzustandes zu höheren Potentialen. Des Weiteren könnte dieser Effekt durch elektrostatische Kräfte von benachbarten, bereits oxidierten Brückeneinheiten verstärkt werden. All dies macht die Vorhersage der Energetik von eingebetteten Brückeneinheiten extrem schwer. Auf der einen Seite kann dieses Verhalten als Hindernis angesehen werden, dass jedoch durch die Entwicklung von Molekülen mit sperrigen Ankergruppen und starren Molekülrückrädern, die eine Anordnung senkrecht zur Oberfläche und damit eine Exposition gegenüber den Elektrolytbestandteilen ermöglichen, vermieden werden könnte. Auf der anderen Seite könnten gerade solch dichte Monolagen eine Möglichkeit zur Erforschung von Einflüssen einer Umgebung ähnlich derer in Festkörpermateriale bieten.

Im zweiten Teil dieser Arbeit wurde der Einfluss verschieden großer Paracyclophane als Brückeneinheiten auf Elektronentransferprozesse in Donor-Brücke-Akzeptor Modellsystemen in Lösung untersucht.

In Bezug auf die gemischt valenten Verbindungen, konzentrierte sich die Studie auf Bistriarylaminradikalkation \mathbf{F}^+ , welches über eine [3.3]Paracyclophan Brückeneinheit verfügt. Die Ergebnisse wurden mit den bis auf die Brückeneinheiten identischen literaturbekannten Verbindungen \mathbf{G}^+ und \mathbf{N}^+ mit [2.2]Paracyclophan bzw. *p*-Xylen Brücken verglichen. Dies führte zu der Schlussfolgerung, dass bereits sehr kleine Veränderungen der Brückeneinheiten bedeutende Änderungen der internen Reorganisationsenergie bewirken können. Das ist besonders bemerkenswert, da allgemein angenommen wird, dass fast ausschließlich die strukturelle Anpassung der Redoxzentren die Größe der internen Reorganisationsenergie bestimmt. Ferner zeigte die Anwendung des Mulliken-Hush-Ansatzes für zwei Zustände, dass Verbindung \mathbf{F}^+ eine nahezu gleich große Kopplung und eine ähnliche thermische Barriere wie \mathbf{G}^+ aufweist. Dies wurde im Rahmen eines Kooperationsprojekts von *Grampp et al.* bestätigt, bei dem entsprechende Werte sowie fast identische thermische Elektronentransferraten direkt aus temperaturabhängigen Elektronenspinresonanzmessungen extrahiert wurden. Das ist bemerkenswert, da sich die Entfernungen der gestapelten π -Systeme in den Paracyclophanbrückeneinheiten stark unterscheiden. Sie sind deutlich innerhalb der *Van der Waals* Radien der integralen Kohlenstoffe in \mathbf{G}^+ und nur gerade noch innerhalb in Verbindung \mathbf{F}^+ . Ferner schwächen

diese Erkenntnisse die allgemeine Annahme, dass die Ethylenbrücken in \mathbf{G}^+ stark zur elektronischen Kopplung beitragen, da unter dieser Annahme in \mathbf{F}^+ , wegen der Propylenbrücken, die Kopplung deutlich geringer ausfallen müsste. Dass die Kopplung nur dreimal höher und die thermischen Elektronentransferraten nur eine Größenordnung höher für \mathbf{N}^+ sind als für \mathbf{F}^+ und \mathbf{G}^+ , zeigt schließlich, dass intermolekularer Elektronentransfer in Festkörpermateriale sehr effizient sein kann. Dies gilt insbesondere, wenn sich *van der Waals* Radien der Kohlenstoffe der interagierenden gestapelten π -Systeme überlappen.

Hinsichtlich der Donor-Akzeptor Dyaden, liegt der Fokus auf Triarylamin-Cyclophan-Naphthalin Diimide (TAA-CP-NDI) Verbindungen, die nahezu vollständige photoinduzierte Ladungstrennung zeigen. Des Weiteren zeigen deren ladungstrennte Zustände Lebenszeiten von Hunderten von Nanosekunden, was selten für solch einfache Dyaden ist. Im aktuellen Fall kann dies auf die Höhe der elektronischen Kopplung V (ca. 100 cm^{-1}) zurückgeführt werden. Diese kann vor allem auf die Integration der kleinsten Modellsysteme für π -stacks, die CPs und die Knoten im niedrigsten unbesetzten Molekülorbital des NDI, die das Zentrum des NDI von seinen Stickstoffsubstituenten entkoppelt zurückgeführt werden. In Übereinstimmung mit den Studien über [2.2]- und [3.3]Paracyclophanbrücken beinhaltende, gemischt valente Verbindungen (siehe oben), weisen die hier untersuchten paracyclophanverbrückten Dyaden eine sehr ähnliche Kopplung auf, wenn es sich um Grundzustandsprozesse wie Ladungsrekombination handelt. Wenn allerdings Prozesse im angeregten Zustand, wie die Ladungstrennung in den TAA-CP-NDI Dyaden, betrachtet werden, muss berücksichtigt werden, dass die CP Orbitale an der Entstehung von Zwischenzuständen beteiligt sind, die wahrscheinlich Ladungstransfercharakter besitzen. In diesem Fall, ermöglicht das [2.2]Paracyclophan offensichtlich eine stärkere Kopplung als das [3.3]Paracyclophan. Eine weitere interessante Eigenschaft der hier untersuchten Dyaden ist die hohe Population des ladungstrennten Tripletzustands von etwa einem Drittel bezogen auf beide ladungstrennten Zustände, die durch die Singulett-Triplett-Umwandlung vom ladungstrennten Singulettzustand erfolgt. Folglich agiert der Tripletzustand mit einer Lebenszeit von einigen Mikrosekunden als eine Art Puffer für den ladungstrennten Zustand, bevor eine Rekombination in den Grundzustand stattfindet und daher zu einer stark verlängerten Lebenszeit der gesamten ladungstrennten Zustände führt. Daher kann geschlussfolgert werden, dass das *intersystem crossing* und die Ladungsrekombinationsprozesse der ladungstrennten Zustände durch ein empfindliches Gleichgewicht von großer elektronischer Kopplung und großer Austauschwechselwirkung $2J$ (beides in Bezug auf Systeme mit einem Wechselwirkungspfad durch den Raum) bestimmt werden. Die letztere wird vermutlich durch eine Wechselwirkung zweiter Ordnung mit dem lokalen Tripletzustand, der energetisch nah am ladungstrennten Zustand liegt, bedingt.

Diese Balance resultiert in langsamen Ladungsrekombinations- und Singulett-Triplett-Umwandlungsraten, die sich nur um eine Größenordnung unterscheiden. Verglichen mit den vielen bisher untersuchten Dyaden, die NDI beinhalten, sind diese Eigenschaften der hier untersuchten Dyaden, soweit mir bekannt, einzigartig. Vor allem die Kombination aus hoher Quantenausbeute des ladungstrennten Zustands, die langen Lebenszeiten und die ausreichende Energie des ladungstrennten Zustands machen das untersuchte System interessant für praktische Anwendungen. Des Weiteren ist die Aufschlüsselung der zugrunde liegenden Mechanismen von bedeutendem Wert für das zukünftige Design von Dyaden für praktische Anwendungen betreffs der Integration und Anpassung dieser vorteilhaften Eigenschaften.